Low Peclet Number Mixing Behavior at Fracture Junctions

by

Chunhong Li

Submitted in partial fulfillment of the requirements for the degree of the Doctor of Philosophy in Hydrology

Department of Geoscience

New Mexico Institute of Mining and Technology

Socorro, New Mexico

June 1995

ACKNOWLEDGEMENTS

I would like to express my profound gratitude to my adviser, Dr. John L. Wilson, for all his guidance and encouragement in my research.

I would also like to thank other committee members for their contributions to my research. Dr. Robert S. Bowman offered technical advise on tracer sample analyses in my laboratory experiments. Dr. Allan Gutjahr, Dr. Jan Hendricxk, and Dr. Steve Schaffer acted as committee members.

Thanks to all my friends at Tech. for sharing the good and bad times together with me, without friends around life at Socorro would be like still water. Especially my good friend Paul Hofmann who helped me improve my english and in physical experiments. Thanks are also to Ms. Edith Montoya, she is always helpful. I am also grateful to Ms. Maggie Taylor for her technical editing work on my dissertation.

Finally, I would like to thank my wife Hua Wu and our families back in China for all their support through my years at New Mexico Tech.

The research was funded by the U.S. Department of Energy, through the New Mexico Waste–management Education & Research Consortium (WERC) and National Science Foundation (NSF).

Abstract

Numerical simulations of solute transport in discrete fracture networks commonly employ one of two mixing rules at fracture junctions: diffusion controlled complete mixing or advection controlled streamline routing. These rules lead to different transport behavior in the networks [Hull et al., 1987; Robinson and Gale, 1990]. Although twenty years of research has been directed toward determining these mixing rules, there is still uncertainty as to which rule is correct and under what conditions.

To address these uncertainties, lattice gas automata (LGA) numerical simulations and physical experiments were performed to investigate the mixing behavior at idealized fracture junctions in the low to middle range of fracture junction Peclet numbers (1–200). In the LGA simulations, a new tracer particle algorithm was developed and applied to simulate the transport of dilute solutions. Applications of the new algorithm in various transport problems were successful. The LGA simulations of the mixing behavior at fracture juncions predict that for Peclet numbers smaller than 1, diffusion dominates the transport process, and complete mixing occurs. For Peclet numbers larger than 1, both diffusion and advection play important roles in the mixing process. A comparison between the LGA simulations and the recently published simulations of Berkowitz et al. [1994] shows large differences.

To test the numerical results, a lucite physical model was constructed with the same geometry as used in the LGA simulations. The physical model had an aperture of 500 microns and a depth of 1.85 cm, and thus a fracture depth to width ratio of 37. Cl^- and Br^- solutions were used as tracers to indicate mixing behavior at the junction of the physical model. The concentration data from the two outlet fractures were analyzed by HPLC. Experiments were conducted in the Peclet number range of 1–170. The experimental results reveal that for Peclet numbers smaller than 1, diffusion dominates the transport process resulting in complete mixing at the junction. For Peclet numbers in the range of 1 to 170,

both diffusion and advection are important. Mixing in this Peclet number range is referred to as transition zone mixing; Although our experiments did not reach Peclet numbers larger than 200, the experimental results of Hull and Koslow [1986] show that the mixing behavior will be advection controlled, and streamline routing will be appropriate.

A comparison among the experimental results, the LGA simulations, and the simulations of Berkowitz et al. [1994] shows that the LGA simulations are basically correct. The results of Berkowitz et al. do not represent the mixing behavior at middle and low Peclet numbers (200–1), and thus, their conclusion that complete mixing within a fracture intersection did not properly represent the mass transfer process at any value of Peclet number is invalid.

The results of this research clarify previous arguments on mixing rules at fracture junctions. Streamline routing, suggested by Hull and Koslow's [1986] and Robinson and Gale's [1990] experiments, was shown to be valid only at Peclet numbers larger than 200; it can not be generalized to represent mixing behavior at small or middle Peclet numbers (P_e in the range of 1–200). The LGA simulations indicate that the proportional streamline routing proposed by Hull and Koslow [1986] for predicting concentrations in outlet fractures fails to predict the mixing behavior at Peclet numbers below 5 because of the effect of diffusive mixing at fracture junctions.

Finally, a heuristic mixing zone concept and model, based on the physical process governing solute transport at fracture junctions, were developed to provide a physical explanation for the diffusive mixing behavior observed in the experiments and the LGA simulations. A heuristic formula is proposed for predicting diffusive mixing behavior at continuous fracture junctions under equal and non-equal flow rate conditions. The LGA simulations indicate that predictions from this formula are reasonably accurate when the differences between the two inflow rates and the two outflow rates are relatively small, but significant errors can arise otherwise.

Table of Contents

List of Figures

List of Tables

Chapter 1: Introduction

Groundwater flow and contaminant transport in fractured systems are encountered in the study of water supply, groundwater protection and remediation, and nuclear waste repository design. There are basically two approaches to modeling these systems: the equivalent porous media approach and the discrete fracture network approach. A necessary condition for the former approach is that the equivalent parameters describing flow and transport inside fractures can be defined on an REV (Representative Elementary Volume) scale; this approach is appropriate when the scale of the problem is large and the fracture density is high [Long et al. 1982]. However, when the fracture density is low (so that the equivalent porous media approach is not valid), and yet the fractures play an important role, the discrete fracture network approach becomes necessary [Schwartz et al, 1983; Smith and Schwartz, 1984; Andersson and Thunvik, 1986; Huang and Evans, 1985; Cacas et al, 1990; Sudicky and McLaren, 1992].

In numerical models of contaminant transport in discrete fracture networks, mixing rules are applied at fracture junctions to redistribute the inflowing contaminant to the outflowing fractures. There are basically two types of fracture junctions: continuous junction and discontinuous junction, as shown in Figure 1.1. A continuous junction is characterized by

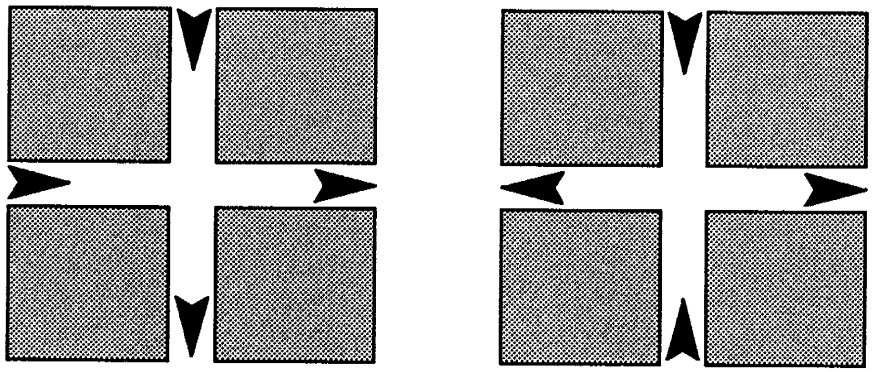

(a) continuous junction (b) discontinuous junction

Figure 1.1. Schematic of continuous and discontinuous fracture junctions.

continuous inflow channels. No exit channel breaks the sequence of inflow channels [Hull and Koslow, 1986]. On the other hand, a discontinuous junction has exit branches interspersed among the inflow channels. In this thesis, only solute mixing behavior at a continuous junction is considered because most of the fracture junctions in the field are this type.

An idealized continuous orthogonal fracture junction with equal fracture apertures is shown in Figure 1.2. Flow enters the junction from top and left with equal flow rates Q, and leaves the junction through right and bottom branches also with the same equal flow rates. The dividing stream line that separates the two flow regions is also shown in the figure. Suppose the top fracture carries a solute of concentration $C_1=C_0$, while the left inflow fracture has no solute with $C_2=0$. The question which arises is what happens to the solute when the two inflows meet at the junction. In general, the solute redistribution process is described by a mixing rule. Depending on the transport mechanism at the junction, the mixing rule used in the numerical simulations of contaminant transport in discrete fracture networks can be classified into two main categories: diffusion controlled complete mixing

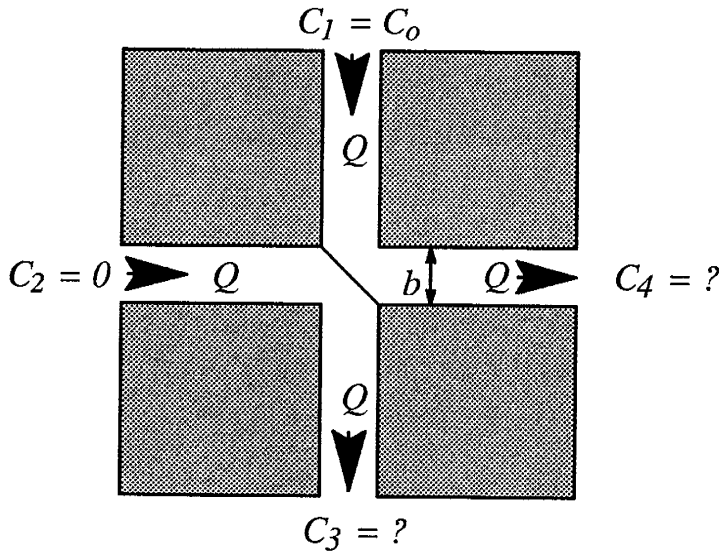

Figure 1.2. Flow intersecting at an idealized fracture junction.

and advection controlled streamline routing. The complete mixing rule assumes a diffusion dominated process around the fracture junction. It states that due to complete mixing at the fracture junction, the flow leaving the junction through the bottom and right fractures has equal concentrations, i.e. $C_3=C_4=0.5C_0$, as illustrated in Figure 1.3(a). On the contrary, the streamline routing assumes an advection dominated process at the fracture junction, allowing no diffusive mixing across streamlines at the junctions. In the case of Figure 1.2, flow in the top inflow fracture carries contaminant directly into the right fracture. The concentration in the right outflow fracture is $C_4=C_1=C_0$, while the concentration in the bottom outflow fracture is $C_3=C_2=0$, as shown in Figure 1.3(b). In the case of non-equal flow rates at the fracture junction, additional mixing occurs in the system simply due to the redistribution of flow as shown in Figure 1.3(c). Such mixing has been called forced mixing [Robinson and Gale, 1990]. It is obvious that depending on flow conditions, diffusion can also play a role in a forced mixing process.

Most models of contaminant transport in fracture networks use the complete mixing rule [Schwartz et al., 1983, Travis, 1984, Huang and Evans, 1985]. But recently there has been a shift to advection controlled streamline routing [Wilson and Witherspoon, 1976; Hull and Koslow, 1986; Robinson and Gale, 1990]. Implementing different mixing rules in numerical

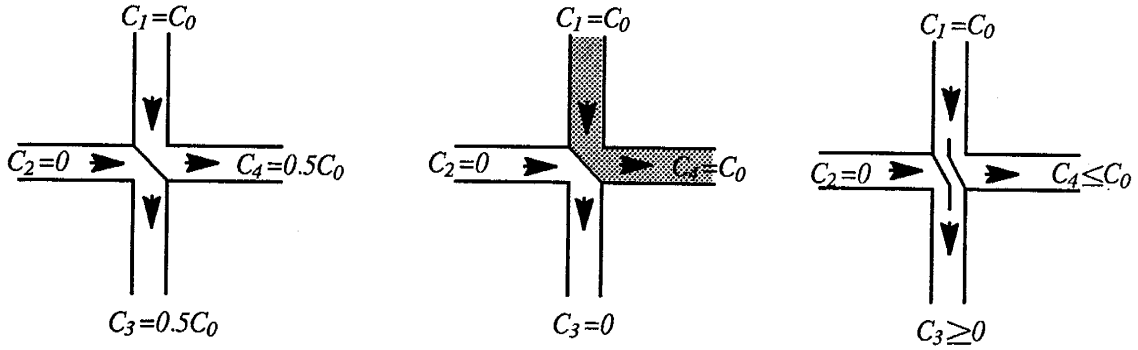

(a) Complete mixing (b) Streamline routing (c) Forced mixing

Figure 1.3. Schematic of mixing behavior at a fracture junction. (a) Diffusion controlled complete mixing. (b) Advection controlled streamline routing. (c) Forced mixing.

simulations of miscible contaminant transport in discrete fracture networks yields a different spatial distribution of the contaminant in the system [Endo et al., 1984; Hull et al., 1987; Robinson and Gale, 1990].

The question arises as to which mixing rule should be used in the numerical simulation of solute transport in discrete fracture networks and under what conditions. Unfortunately, the scale of the mixing problem precludes field experiment, and only a few laboratory experiments have been carried out using physical models with geometries similar to the one shown in Figure 1.2. Krizak et al. [1972] conducted experiments on a single fracture junction with one inlet fracture and two or three outlet fractures. Tracers carried in by the inflow fracture were found in all of the outlet fractures. This phenomenon was explained by complete mixing at the junction although in their experimental design there was only one inlet fracture. What they called complete mixing was actually the result of flow redistribution at the fracture junction instead of diffusive mixing. Wilson and Witherspoon [1976], Hull and Koslow [1986], and Robinson and Gale [1990] carried out physical experiments to study mixing behavior at fracture junctions and concluded that transport at fracture junctions is advection controlled and, therefore, streamline routing is appropriate in discrete fracture network models. Based on their experimental observations and the principle of mass balance, Hull and Koslow [1986] derived a formula for predicting concentrations in each outflow fracture. Later on, Philip [1988] derived approximate analytical solutions for Stokes flow around discontinuous fracture junctions. He concluded that the proportional streamline routing proposed by Hull and Koslow [1986] for forced mixing was inadequate for cases involving large uneven inflow rates and large uneven outflow rates.

In order to compare different experimental and numerical results, we introduce the Peclet number P_e to represent the relative importance of advection and diffusion,

$$P_e = \frac{\frac{\sqrt{2}}{2} b \overline{V}}{D} \qquad 1.1$$

where $\overline{V}$ is the average flow velocity at the fracture junction, $(\sqrt{2}/2)b$ is the half diagonal length of the junction (it is also the half length of the dividing streamline at the junction), and D is the molecular diffusion coefficient of the solute. As flow velocity increases, the Peclet number increases, and the influence of diffusion decreases. On the other hand, as velocity decreases, the Peclet number decreases, and diffusion begins to play an important role in the transport process. Using the data provided in the papers of Hull and Koslow [1986], Robinson and Gale [1990], and Wilson and Witherspoon [1976], we estimate that the Peclet numbers at the fracture junctions in their experiments were larger than 200, 3,000, and 10,000, respectively. At such high Peclet numbers, the transport process at fracture junctions is certainly advection controlled, which explains why they did not observe diffusion controlled mixing in their experiments.

Instead of using mixing rules in their numerical simulation of tracer transport in fracture networks, Hull et al. [1987] explicitly considered both advection and diffusion at a fracture junction in their particle tracking technique, a method rarely used in large networks because of its high computation time. Their results indicated that, even at relatively high flow rates, diffusion plays a significant role in the dispersion of solute in fracture networks, and streamline routing does not provide a realistic prediction of tracer migration in the system.

To determine the range of mixing rules at a fracture junction, Hull et al. [1987] directly applied the analytical results of solute transport in a single fracture to an idealized fracture junction. They predicted that for advection controlled mixing to occur at the junction the residence time of solute particles $b/\overline{V}$ should be smaller than $(0.003b^2)/D$; for diffusion controlled complete mixing, the residence time $b/\overline{V}$ should be bigger than $(0.5b^2)/D$; otherwise, the mixing behavior is controlled by both advection and diffusion. If the above relationships are expressed in terms of the dimensionless Peclet number defined in equation (1.1), we have that advection controlled streamline routing corresponds to Peclet numbers larger than 235; diffusion controlled complete mixing corresponds to Peclet numbers

smaller than 1.414; and transition zone mixing corresponds to Peclet numbers in the range of 1.414 to 235.

Berkowitz et al. [1994] applied a random walk particle tracking technique to study mixing behavior at an idealized junction. The flow field around the junction was computed following Philip's [1988] method. They concluded that streamline routing provides an adequate approximation for contaminant transport at fracture junctions with Peclet numbers greater than 1. For cases with equal inlet and outlet flow rates (Figure 1.2), they showed that even when the Peclet numbers were lower than 10^{-2} at the junction, diffusion controlled complete mixing could not be reached. But there is no experimental data available to verify their numerical results, which clearly disagree with Hull et al. [1987].

Although research on mixing behavior at fracture junctions has been conducted for about twenty years and several mixing rules have been proposed: complete mixing, streamline routing, and some combination, there is still no certain answer as to which rule is correct and under what conditions. We believe that the mixing rule depends on the range of Peclet numbers in a fracture network. Figure 1.4 is a random fracture network generated by Arnold and Bahr [1993]. The fractures have a mean aperture of 10 microns, and the standard deviation of the natural log of the aperture is 0.70. The hydraulic gradient is 0.01 from bottom to top. They computed the Peclet number for each fracture and performed some averaging at each junction to yield an effective junction Peclet number. The resulting histogram, shown in Figure 1.5, spans over five orders of magnitude. In this simulation, the Peclet numbers are low, but we can easily increase them by scaling up the aperture, or more easily the gradient. Thus, a single mixing rule may not be adequate to describe solute mixing behavior in a fracture network with junction Peclet numbers spanning several orders of magnitude.

Stimulated by previous research and prior to our own work, we hypothesized that there should be a continuum of mixing rules, centered somewhere near a Peclet number of 1.

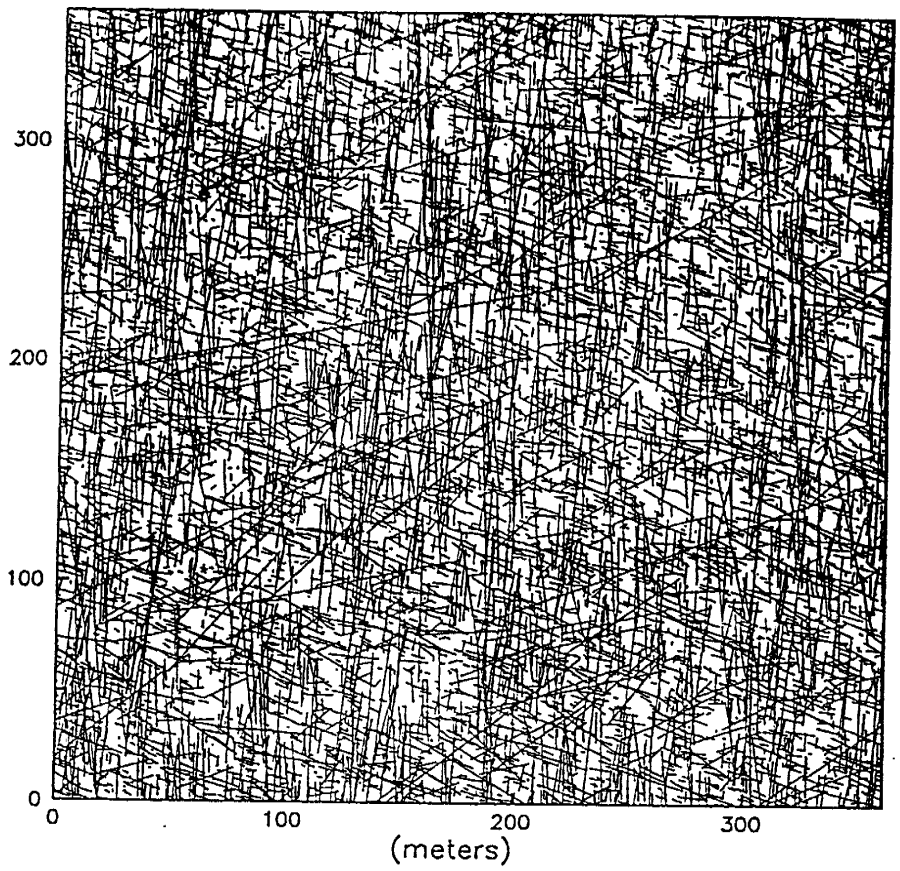

Figure 1.4. Fracture network model from Arnold and Bahr [1993].

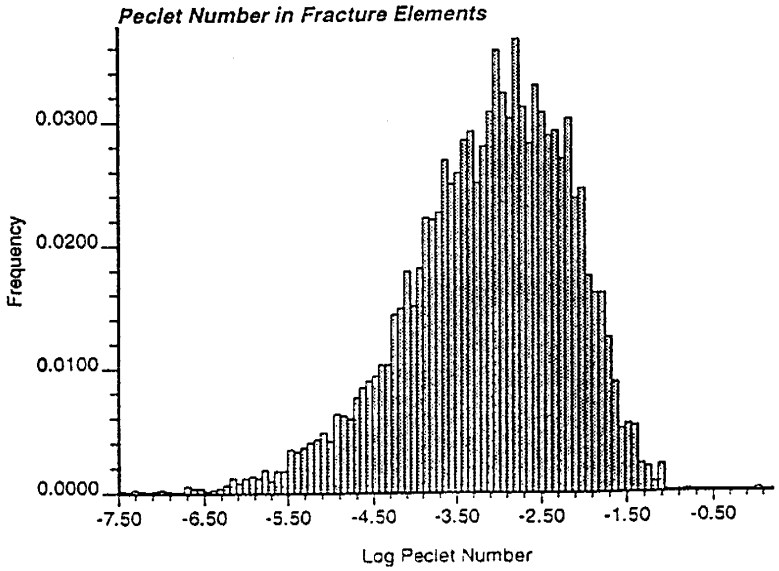

Figure 1.5. Fracture element Peclet number histogram for the network model in Figure 1.5.

Above this Peclet number, a transition zone exists between complete mixing and streamline routing. As the Peclet number decreases, the mixing process is diffusion dominated, and the complete mixing rule is appropriate. When the Peclet number increases, the mixing process as the junction is advection controlled, and there will be little or no diffusive mixing. The upper limit for the streamline routing should be around a Peclet number of 10.

The objective of our research was to investigate the hypothesized relationship between the mixing behavior and the junction Peclet number. The nature and scale of the problem precluded any attempt of direct field research. Thus, numerical simulations and laboratory physical experiments were conducted to investigate mixing behavior at an idealized fracture junction. The LGA (Lattice Gas Automata) method, which was first developed about ten years ago, was used to simulate flow and transport behavior across the fracture junction. A new algorithm, the tracer particle algorithm, was developed in this dissertation to allow the LGA method to simulate advection and diffusion processes more efficiently for trace constituents in the fluid system. The LGA simulation results were compared with previous numerical and experimental results.

A physical fracture junction model was constructed, experiments were conducted with the physical model to investigate mixing rules over reasonable values of Pe. The results from the physical experiments were used to test the LGA simulation results and the results of Berkowitz et al. [1994]. Finally, a heuristic new mixing zone theory was developed to account for the mixing behavior observed in both LGA simulations and the experiments.

References

Andersson, J. and R. Thunvik, Predicting mass transport in discrete fracture networks with the aid of geometrical field data, *Water Resour. Res.*, 22(13), 1941–1950, 1986.

Arnold, B.W. and J.M. Bahr, Spatial distribution of groundwater flow and transport characteristics in a fracture network, abstract, *EOS*, 74(16), 143, 1993.

Berkowitz, B., C. Naumann, and L. Smith, Mass transfer at fracture intersections: An evaluation of mixing models, *Water Resour. Res.*, 30(6), 1765–1773, 1994.

Cacas, M.C., E. Ledoux, G. deMarsily, and B. Tillie, Modeling fracture flow with a stochastic discrete fracture network: Calibration and validation, 1, The flow model, *Water Resour. Res.*, 26(3), 479–489, 1990.

Endo, H.K., J.C.S. Long, C.R. Wilson, and P.A.Witherspoon, A model for investigating mechanical transport in fracture networks, *Water Resour. Res.*, 20(10), 1390–1400, 1984.

Hull, L.C. and K.N. Koslow, Streamline routing through fracture junctions, *Water Resour. Res.*, 22(12), 1731–1734, 1986.

Hull, L.C., J.D. Miller and T.M. Clemo, Laboratory and simulation studies of solute transport in fracture networks, *Water Resour. Res.*, 23(8), 1505–1513, 1987.

Huang, C. and D.D. Evans, A three–dimensional computer model to simulate fluid flow and contaminant transport through a rock fracture system, *Rep. NUREG/CR–4042*, Univ. of Ariz., Tucson, 1985.

Krizek, R.J., G.M. Karadi, and E. Socias, Dispersion of a contamination in fissured rock, Proceedings of Symposium on Percolation Through Fissure Rock, Int. Soc. of Rock Mech., Stuttgart, Germany, 1972.

Long, J.C.S., J.S. Remer, C.R. Wilson, and P.A. Witherspoon, Porous medias equivalents for networks of discontinuous fractures, *Water Resour. Res.*, 18(3), 645–658, 1982.

Philip, J.R., The fluid mechanics of fracture and other junctions, *Water Resour. Res.*, 24(2), 239–246, 1988.

Robinson, J.W., and J.E. Gale, A laboratory and numerical investigation of solute transport in discontinuous fracture systems, *Groundwater*, 28(1), 25–36, 1990.

Smith, L., and F.W. Schwartz, An analysis of the influence of fracture geometry on mass transport in fractured media, *Water Resour. Res.*, 20(9), 1241–1252, 1984.

Schwartz, F.W., L. Smith, and A.S. Crowe, A stochastic analysis of macroscopic dispersion in fractured media, *Water Resour. Res.*, 19(5), 1253–1265, 1983.

Sudicky, E.A. and G.G. McLaren, The Laplace Transform Galerkin technique for large scale simulation of mass transport in discretely fractured porous formations, *Water Resour. Res.*, 28(2), 499–514, 1992.

Travis, B.J., TRAC3D: A model of flow and transport in porous fractured media, *Rep. LA-9667-MS*, Los Alamos National Lab., Los Alamos, NM, 1984.

Wilson, C.R. and P.A. Witherspoon, Flow interference effects at fracture intersections, *Water Resour. Res.*, 12(1), 102-104, 1976.

Chapter 2: The Lattice Gas Automata Method and the Tracer Particle Algorithm

2.1 Introduction

In the last ten years, lattice gas automata (LGA) have been developed as an alternative to molecular dynamics for simulating macroscopic fluid dynamics on the basis of microscopic behavior. Compared to the traditional numerical methods, like finite difference and finite element methods, the LGA method has the following advantages: (1) The LGA simulations have the same speed and efficiency when applied in simulating flow/transport problems with complex geometries, while the speed and efficiency of the traditional methods under this condition decreases; thus the LGA method is more suitable for simulating flow/transport problems in complicated geometries. (2) Boundary conditions can be easily implemented in the LGA method. (3) The LGA method can simulate flow and transport processes simultaneously. (4) The LGA codes are usually easier and faster to develop than the traditional methods. (5) The LGA which are discrete analogues of molecular dynamics can give insight into the process on a macroscopic scale. In this dissertation, we choose to use the LGA method in our research because of the above advantages.

In this chapter, we first introduce the LGA method and then the new tracer particle algorithm for simulating solute transport with the LGA method.

2.2 The Lattice Gas Automata Method

2.2.1 Introduction

On a microscopic level, fluids consist of particles, but upon defining an REV, the fluids can be treated as continuous. Partial differential equations can then be developed to describe the movement of the fluids. The basic idea of LGA (Lattice Gas Automata) is to simulate large scale flow and transport behavior from the movement of particles on a microscopic

level (discrete level). The LGA are discrete analogues of molecular dynamics, in which particles with discrete velocities populate the links of a fixed array of sites [Wolfram, 1986]. Sufficiently large lattice gas automata can reflect flow behavior on the continuous level.

Wolfram [1986] developed the theoretical work for lattice gas automata, in which he showed how the movement of particles on lattice grids can result in continuum scale behavior based on averaging on a relatively large scale. He also proved that in two dimensions, only the hexagonal lattice is isotropic. Wolfram's work laid the theoretical basis for the application of lattice gas automata in fluid dynamics. The first lattice gas automata model capable of simulating the Navier–Stokes flow equations in two dimensions was developed by Frisch, Hasslacher, and Pomeau (the FHP model) in 1986. Since then, lattice gas automata have been widely used in numerical simulations of fluid dynamics.

2.2.2 Theoretical Basis of Lattice Gas Automata

The theory behind lattice gas automata is molecular dynamics, kinetic theory, and statistical mechanics. To run a lattice gas model, particles are introduced onto a lattice field. The most commonly used lattice grid in two dimensions is the hexagonal lattice, as shown in Figure 2.2.1. At each node or site of the hexagonal lattice, there are six links connecting the neighboring nodes. Particles can freely move along the links with the constraint that there can only be one particle moving in each direction. Thus, there is a maximum of six moving

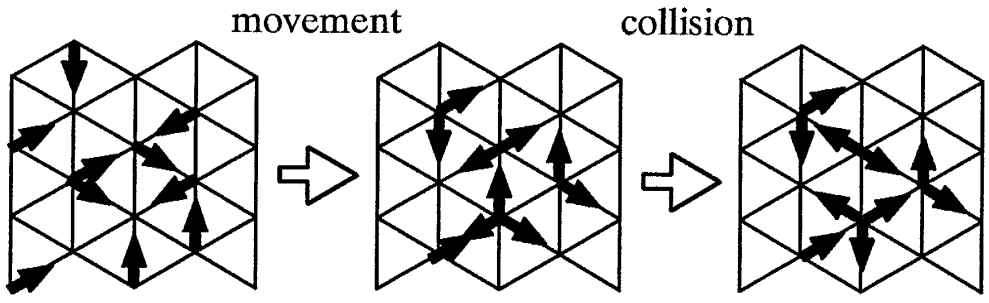

Figure 2.2.1. Lattice gas field and the evolution of particles in the field. Collision rules are illustrated only for simple two and three body collisions.

particles at each site. In models which involve zero–velocity particles, the maximum number of particles that a site can hold is six moving particles plus one static particle. The evolution of LGA follows two steps. First, each particle moves one step along the link to the neighboring site. Second, collisions occur at sites with two or more particles. Collision rules are chosen such that mass and local momentum are conserved at each site. The microdynamic equation that governs the movement of particles in the lattice field can be written as

$$N_j(x_i + e_j,\ t + 1) = N_j(x_i, t) + \Omega_j \tag{2.2.1}$$

where N_j is the number of particles moving in direction j which varies from 1 to 6 in a hexagonal lattice field. N_j is a boolean variable; it equals 1 when a particle is moving in direction j, yet zero when no particle is present in direction j; x_i is the spatial location of particles at site i; t is time; Ω_j represents the collision rules; e_j is the directional velocity vector of a particle moving in direction j

$$e_j = \{cos[\frac{2\pi(j-1)}{6}],\ sin[\frac{2\pi(j-1)}{6}]\} \qquad j = 1, 2, \cdots \cdot 6 \tag{2.2.2}$$

To conserve mass and momentum, respectively, in the field, the collision term in equation (2.2.1) must satisfy the following constraints

$$\sum_j \Omega_j = 0 \tag{2.2.3}$$

$$\sum_j \Omega_j e_j = 0 \tag{2.2.4}$$

The simplest collision rules that conserve mass and momentum and yet are able to simulate Navier–Stokes flow in two dimensions are the two and three body head–on collision rules [Frisch et al., 1986] depicted in Figure 2.2.1. In the two body head–on collision case, where two particles moving head–on collide at the site, there are two possible moving directions for the two particles to be redistributed. A uniform random number generator is used to choose one of the two possibilities. In three body head–on collisions,

each particle is bounced back. The status of the particles is upgraded after each movement and collision in the field. The process continues until equilibrium is reached.

In order to bring the microscopic result up to a continuum scale, averaging is applied to the lattice field. The two most important quantities on the continuum scale are fluid density and velocity. They can be evaluated by spatially averaging individual particle locations and velocities. To obtain representative results, the size of the averaging window needs to be bigger than the particle mean free path in the field. Once the averaging scale is chosen, the mean particle density n and mean fluid velocity, respectively, can be estimated at location $\boldsymbol{x}$ and time t:

$$n = \sum_j f_j \tag{2.2.5}$$

$$n\boldsymbol{u} = \sum_j f_j \boldsymbol{e}_j \tag{2.2.6}$$

where f_j is a neighborhood average of N_j, representing the probability of finding a particle with velocity $\boldsymbol{e}_j$ at position $\boldsymbol{x}$ and time t. $n\boldsymbol{u}$ is the mean momentum density.

The governing equations on the continuum scale can now be derived from the Boltzmann transport equation. In 1872 Boltzmann proposed a transport equation for describing the evolution of the density of similar particles. The Boltzmann transport equation in its discrete form can be written as [Wolfram, 1986]

$$\frac{\partial f_j}{\partial t} + \boldsymbol{e}_j \cdot \nabla f_j = \Omega_j \tag{2.2.7}$$

Summing over all directions j, with equation (2.2.3), leads to

$$\frac{\partial}{\partial t}\left(\sum_j f_j\right) + \sum_j \boldsymbol{e}_j \cdot \nabla f_j = 0 \tag{2.2.8}$$

which can be rewritten in terms of the mean properties of the fluid by using equation (2.2.5) and (2.2.6)

$$\frac{\partial n}{\partial t} + \nabla \cdot (n\boldsymbol{u}) = 0 \tag{2.2.9}$$

Equation (2.2.9) is the continuity equation of the lattice fluid on a continuum scale.

The continuum governing equation for the conservation of momentum can be derived in the similar way [Wolfram, 1986], yielding

$$\frac{\partial}{\partial t}(\sum_j f_j \boldsymbol{e}_j) + \sum_j \boldsymbol{e}_j \cdot (\boldsymbol{e}_j \cdot \nabla f_j) = 0 \tag{2.2.10}$$

There is no simple macroscopic result for the second term in equation (2.2.10). Defining the momentum flux density tensor, Π_{kl}, as

$$\Pi_{kl} = \sum_j (\boldsymbol{e}_j)_k (\boldsymbol{e}_j)_l f_j$$

equation (2.2.10) can then be rewritten as

$$\frac{\partial (nu_k)}{\partial t} + \frac{\partial \Pi_{kl}}{\partial l} = 0 \tag{2.2.11}$$

Frisch et al. [1986] applied the Chapman–Enskog expansion to equation (2.2.11) and derived

$$\frac{\partial (nu_k)}{\partial t} + \frac{\partial [ng(n)u_k u_l]}{\partial x_l} = -\frac{\partial p}{\partial x_l} + \frac{\partial}{\partial x_l}[\mu \frac{\partial u_k}{\partial x_l}] \tag{2.2.12}$$

where μ is the shear viscosity of the fluid, and p is pressure. The appearance of $g(n)$ in the equation arises from the finite discretization of particle velocities in the lattice field. It should be 1 in order to simulate a physical continuum system. The presence of $g(n)$ causes the LGA model to lack Galilean invariance, such that vorticity in the field moves with a velocity different from the fluid velocity. In two dimensions, for the simple two and three body collision FHP model [Frisch et al., 1986]

$$g(n) = \frac{3-n}{6-n} \tag{2.2.13}$$

A general formula for calculating $g(n)$ can be found in the paper by d'Humieres and Searby [1987]. The lack of Galilean invariance has little significance in one phase flow at small Mach numbers where the higher order terms in the momentum equation can be ignored.

For an incompressible fluid, equation (2.2.9) reduces to

$$\nabla \cdot \boldsymbol{u} = 0 \tag{2.2.14}$$

and equation (2.2.12) becomes

$$\frac{\partial \boldsymbol{u}}{\partial t} + g(n)\boldsymbol{u} \cdot \nabla \boldsymbol{u} = -\nabla P + \nu(n)\nabla^2 \boldsymbol{u} \tag{2.2.15}$$

where P is the rescaled pressure. Except the extra factor $g(n)$, equation (2.2.15) is very similar to the usual Navier–Stokes equation. The kinematic viscosity for the FHP model [Frisch et al, 1987] is

$$\nu = \frac{1}{12d(1-d)^3} - \frac{1}{8} \tag{2.2.16}$$

where $d=n/6$ is the number of particles per link per site. Equation (2.2.15) can be rescaled in time and viscosity to restore Galilean invariance [Frisch et al., 1987]

$$t' = t \cdot g(n), \quad \nu' = \frac{\nu}{g(n)} \qquad P' = \frac{P}{g(n)}$$

After rescaling, the resulting governing equation has the same form as the usual Navier–Stokes equation.

Apart from applications in fluid dynamics, the LGA method has also been used to study solute transport processes in fluids. In the case of fluid self diffusion, colored particles, usually labeled black and white, are introduced onto the lattice field [d'Humieres et al., 1987 and 1988]. The colored particles have the same properties; the only difference is that they are labeled with different colors. The collision rules are independent of particle colors. Chen and Matthaeus [1987] used the perturbation of colored particle densities to develop an LGA advection–diffusion equation for a pure fluid. They also derived a theoretical formula for the self diffusion coefficient of the fluid (See equation 2.3.6, below). Besides applications in self diffusion, the LGA method is also applied to study chemical reaction and solute transport process. Wells et al. [1991] applied the LGA method to simulate diffusion controlled chemical reactions at mineral surfaces and in pore networks. Holme and Rothman [1991] developed an algorithm to produce a lattice gas with lower diffusivity in two

dimensions. Their method maximizes the projection of color flux in the direction of the color field. Chen et al. [1993] applied both lattice gas and lattice Boltzmann methods to chemically reacting systems. More detailed information about the applications of LGA method in studying transport process in fluids can be found in §2.3 of this chapter.

This review of theory simply illustrates that the LGA method simulate fluid flow and transport processes based on the microscopic movement of particles, recovering the macroscopic flow and transport behavior upon averaging.

2.2.3 Discussion

Several advantages that relate to the LGA method make it a useful tool in studying complex flow phenomena. From a numerical simulation point of view, the most prominent features of lattice gas automata come from the fact that LGA are discrete both in time and space. As LGA operate on a discrete lattice grid, one can make a lattice field to fit any shape; thus, they can easily handle problems with complex geometries. Since LGA only use Boolean variables, they are numerically stable. The algorithm for LGA is completely parallel, making it more suitable for parallel computing. Physically, the LGA method simulates continuum scale flow and transport behavior based on the movement of particles on discrete (lattice gas) scale. Thus, it can provide insight into the continuum scale processes.

None of the numerical methods used in computational fluid dynamics is perfect. The LGA method requires significant computer time. The computational burden arises from the collision rules and the large number of sites in the field. It increases sharply when there are extensive collision rules involved in the simulations. Another disadvantage the LGA method inherits is the noise of the numerical results. One way of smoothing the results is to carry out averaging in both time and space domains. Recently, an improved version of the LGA method, called the lattice Boltzmann approach, was developed to reduce noise and improve the efficiency of the LGA method. The lattice Boltzmann (LB) method directly uses the discrete Boltzmann equation to determine an average particle density in the field. Instead of

using Boolean variables, the LB method uses real numbers to represent the particle density distributions in the field. Perturbations are then applied to drive flow in the field. As the LB method directly uses the Boltzmann transport equation, it preserves the Galilean invariance automatically and greatly reduces the noise.

Since the development of the first successful LGA model in 1986, research interest in the applications of this numerical technique has been increasing. Numerical simulations have been carried out to study hydrodynamic phenomena, multiphase flow, transport behavior, temperature related flow phenomena, single and multiphase flow in porous media, water–rock interactions, and flow in fractured porous media. In this dissertation, a tracer particle algorithm is developed to simulate the solute mixing process at fracture junctions with the LGA method.

2.3 A Tracer Particle Algorithm for Simulating Solute Transport With Lattice Gas Automata

2.3.1 Introduction

The lattice gas automata (LGA) method has been used to study diffusion and transport processes in fluids. An important advantage of this approach is that it simulates continuum scale flow and transport phenomena based on the microscopic behavior of particles. To simulate diffusion behavior with the LGA method, colored particles are usually introduced into the field [d'Humieres et al., 1987 and 1988]. Chen and Matthaeus [1987] used the perturbation of colored particle densities to obtain an LGA advection–diffusion equation for a pure liquid. Boon and Noullez [1989] applied the extended FHP (Frisch, Hasslacher, and Pomeau) model in a study of self–diffusion coefficients and long time correlations. Bernardin and Sero–Guillaume [1990] generalized earlier lattice gas mixture models for mass diffusion by introducing particles with different speeds and masses. They applied the Chapman–Enskog expansion to derive the dissipative properties of mixture models. The diffusion coefficients and viscosities of non–reactive gases were derived mathematically. Sero–Guillaume and Bernardin [1989] introduced an energy level method to simulate heat transfer and reaction with lattice gas. Bernardin et al. [1991] extended the energy level method to multispecies in two dimensions. Wells et al. [1991] studied diffusion controlled chemical reactions at mineral surfaces and in pore networks. In their model, a method similar to the energy levels approach was used to simulate diffusion processes in the liquids. Holme and Rothman [1991] included a non–local interaction in lattice gas to produce a lattice gas with lower diffusivity in two dimensions. This method maximizes the projection of color flux in the direction of the color field. They also developed a lattice Boltzmann model with non–local interaction. Dawson et al. [1993] developed an algorithm for simulating reaction–diffusion equations with the lattice Boltzmann method. Chen et al. [1993] applied both lattice gas and lattice Boltzmann methods to chemically reacting systems.

The above algorithms involve collisions of all the particles in the field. Since different diffusion coefficients require different collision rules, the simulations can be complicated by these nontrivial rules and require significantly long computer times. Most of these algorithms were developed for studying diffusion related processes. The movement of particles in the field was only related to the concentration gradient of each species in the field and had nothing to do with the local momentum of the field. Therefore, the influence of advection on transport was neglected. However, the movement of particles in the field is determined by both diffusion and advection processes; advection plays an especially important role at high flow velocities. When these colored particle algorithms are applied in simulating transport behavior in a complex flow field, some of the particles can move upstream even though the velocity is quite high.

In this paper we develop a tracer particle algorithm to simulate transport of dilute solutes using the lattice gas approach. A dilute solution consists of bulk fluid particles which act as a solvent, and solute particles. In general, the movement of a solute particle is mainly influenced by forces acting on it from the surrounding bulk fluid particles and by the energy of the solute particle itself. It is assumed that solute particles do not interact with each other because of their low concentrations. In the dilute solution, fluid properties and the flow characteristics of the solution are not significantly affected by the presence of the solute, while the solute particles act as tracers to indicate the flow and transport behavior of the bulk fluid. With these thoughts in mind, we suggest a new algorithm using so-called "tracer particles" for the study of solute transport phenomena with the lattice gas approach. The new tracer particle algorithm does not require collision rules for the tracer particles, so it can be easily implemented in any lattice gas model studying solute transport processes. The new algorithm is computationally efficient since each tracer particle acts independently of the others. It also can easily simulate solute diffusion processes with low diffusion coefficients. We first describe the new algorithm; then we show some of the numerical results for solute diffusion and for dispersion processes in a moving fluid.

2.3.2 The Tracer Particle Algorithm

The tracer particle algorithm is based on the analog to solute particle movement at the lattice gas level. Considering the fact that in a diffusion process the bulk fluid particles acting as solvent move randomly in the field, the direction of the local momentum of the bulk fluid particles also changes randomly. When flow is involved, at an REV (Representative Element Volume) scale, the flow field has a certain pattern; there is no randomness. But at the lattice gas (discrete) scale, depending on fluid velocity, the movement of fluid particles from site to site still involves some random movement, as does the local momentum. As flow velocity increases, the relative randomness of the fluid particles decreases, the local momentum has a prevalent direction, and diffusion becomes less important. While, as flow velocity decreases, the randomness of the fluid particles and the direction of the local momentum increases at local scale, and diffusion begins to play an important role. Thus, local net momentum alone could act as an indicator for the transport of tracer particles in the field. In the current algorithm, only the local net momentum of the bulk fluid particles is used to direct the moving direction of the tracer particles. The tracer particles do not participate in the collisions involving bulk particles, nor do they interact with each other. The tracer particles are independent of each other. The introduction of tracer particles in the lattice field does not change the bulk fluid properties and the flow characteristics of the field. As a result, the mass and momentum of the fluid particles are conserved during the simulations. Although the tracer particle momentum is not strictly conserved, this loss is not significant because the density of the tracer particle is very low.

In the tracer particle algorithm, the fluid lattice field is computed in the standard way, with bulk fluid particles of mass m moving from site to site and colliding with each other every simulation time step. The tracer particles are moved only every k time steps. The length of the waiting period k is proportional to the 'diameter' of the tracer particle. The bigger the diameter of a tracer particle, the larger the value k, which means that as the diameter of a tracer particle increases, its moving velocity decreases. Once a tracer particle reaches a site,

it rests at that site for $k-1$ time steps before moving again. A new moving direction j is computed, and the tracer particle moves in that direction with velocity $u_j = 1/k$ (*lu/sts*), where *lu* is the length of the hexagonal lattice links, *sts* represents simulation time step, and for a hexagonal lattice field, j=1, ...6. The process is then repeated. The length of the waiting period k determines the tracer particle diffusion coefficient. Unlike the commonly used colored particle algorithm, the tracer particle algorithm allows a tracer particle and a bulk particle to have the same moving direction at one site. The bulk particles are allowed to pass through the (usually) slow moving tracer particles.

The new moving direction of a tracer particle is computed in the following way. Suppose a tracer particle is located at site i with moving direction in j at time t. The tracer particle remains at site i until some later time $t+k$. During this period it accumulates additional momentum from the surrounding bulk fluid particles which is used to determine the new moving direction. At the end of the period, the tracer particle moves to a neighboring site and the direction of its movement is a weighted function of the accumulated momentum. The momentum the tracer particle "obtains" from the bulk particles at a later time $t+k$ is given by

$$\boldsymbol{J}_{i,t+k} = \sum_{t}^{t+k} \sum_{j} m\boldsymbol{e}_j \qquad (2.3.1)$$

where $\boldsymbol{e}_j$ is the velocity (1 *lu/sts*) of a bulk fluid particle at site i moving in direction j after collision among bulk fluid particles at time t. The terms on the right hand side of equation (2.3.1) represent the accumulation of net local momentum at the lattice site from time t to $t+k$.

The actual moving direction of the tracer particle at time step $t+k$ must still be calculated from the particle momentum described by equation (2.3.1). In the two dimensional case with a hexagonal lattice, there are only six possible moving directions in the lattice field. If the net local momentum $\boldsymbol{J}_{i,t+k}$ is zero, the moving direction of the tracer particle at the ith site

is selected randomly with equal probability in all six directions. For non-zero $\boldsymbol{J}_{i,t+k}$ the direction of the net local momentum at site i is calculated as

$$\alpha_i = \arctan(\frac{J_{iy}}{J_{ix}}) \tag{2.3.2}$$

where α_i is the direction of the local net momentum; and J_{ix} and J_{iy} are the cartesian x and y components of the local net momentum $\boldsymbol{J}_{i,t+k}$. For a hexagonal lattice, the direction of each link can be written as $\pi(j-1)/3$, where j varies from 1 to 6, representing all the six possible moving directions in a lattice field. If α_i is in a lattice link direction, then the tracer particle will exactly follow the direction of α_i. When α_i is not in a lattice link direction, the moving direction of a tracer particle must be decided by some rule. In this paper, we introduce an increment δ around the moving directions $\pi(j-1)/3$. Then α_i satisfies one of the following equations

$$\frac{\pi(j-1)}{3} - \delta < \alpha_i \leq \frac{\pi(j-1)}{3} + \delta \ , \ \text{or} \tag{2.3.3}$$

$$\frac{\pi(j-1)}{3} + \delta < \alpha_i \leq \frac{\pi j}{3} - \delta \tag{2.3.4}$$

When equation (2.3.3) is satisfied, the momentum direction α_i is within a δ value of a link direction $\pi(j-1)/3$ and the tracer particle is directed to move along direction j. If equation (2.3.4) is satisfied, a uniform random number generator is used to choose the moving direction of the tracer particle between the j and $j+1$ directions. As the apparent density of the tracer particles is very low, the probability that two tracer particles could end up at the same site is very small; should this occur, the tracer particles will move along their previous directions. Thus, the movement of the tracer particles in the field is an uncorrelated random walk in time and space.

Within the colored particle algorithm, the self-diffusion coefficient D_s of a fluid can be calculated from the theoretical analysis of certain collision rules. For example Chen and Matthaeus [1987] used the perturbation of colored particle densities to obtain an LGA

advection–diffusion equation for pure fluid. When the velocity of the fluid is zero, the governing equation describes a diffusion process, yielding Fick's second law

$$\frac{\partial C}{\partial t} = \nabla \cdot (D_s \nabla C) \tag{2.3.5}$$

where D_s is the self–diffusion coefficient with units of lu^2/sts. For simple FHP two and three body head–on collision rules, the self–diffusion coefficient is given by

$$D_s = \frac{3}{n}(1 - \frac{n}{6})^{-3} \tag{2.3.6}$$

where $n/6$ is the number of particles per link per site.

A current weakness of the tracer particle algorithm is that we have not been able to theoretically calculate its diffusion coefficient. In this paper, numerical simulations inside a rectangular domain with a known analytical diffusion solution on the continuum scale were carried out, and an analytical solution was used to fit the numerical simulation results to estimate the diffusion coefficients of the tracer particles.

2.3.3 Diffusion Results and Discussion

Consider a rectangular domain in the x and y plane. Two kinds of colored particles are introduced into the field, black and white. They are identical in properties and behavior, differing only in their labels and initial locations. The relative concentration is defined as the ratio of the number of black particles over the total number of particles in the averaging space. The white particles are initially distributed in the right part of the domain from $x>l/2$ to $x=l$, the length of the domain, with a relative concentration of zero. The black particles are initially located in the left part of the field from $x=0$ to $x<l$ with a relative concentration of unity (C/C_0=1). No–flow boundary conditions are maintained along the borders of the domain. The analytical solution for a y–direction averaged diffusion process inside this domain is given by Crank [1970]

$$C = C_0\left[\frac{h}{l} + \frac{2}{\pi}\sum_{n=1}^{n=\infty}\frac{1}{n}\ sin\frac{n\pi h}{l}\ cos\frac{n\pi x}{l}\ exp\left(\frac{-Dn^2\pi^2 t}{l^2}\right)\right] \tag{2.3.7}$$

with the initial condition

$$C = C_0 \qquad 0 < x < h$$
$$C = 0 \qquad h < x < l$$

and boundary conditions

$$\frac{\partial C}{\partial x} = 0 \qquad x = 0$$
$$\frac{\partial C}{\partial x} = 0 \qquad x = l$$

where h is the initial domain length of the solution with assumed concentration C_0, and D is the diffusion coefficient of black particles. This continuum solution predicts mean concentration over a transect of the rectangular domain.

To test the numerical code, the LGA model was first run with the colored particle algorithm for self diffusion of the fluid particles. In equation (2.3.7), D was replaced with the self-diffusion coefficient of black and white particles. For simple two and three body head-on collision rules, D_s is given by (2.3.6). In the simulation, the mean density of the bulk fluid was n=1.5 particles per site, with a theoretical self diffusion coefficient D_s=4.74(lu^2/sts). The rectangular shaped field had x and y dimensions of 240x84 (sites). The fluid particles had a unit mass of m=1, and a unit velocity of 1 *lu/sts*. In the first step, black fluid particles were randomly distributed only in the left half of the field, and white fluid particles were randomly distributed only in the right half. The momentum of the particles was distributed such that the total momentum of the field was zero. Thus, the macroscopic velocity of the bulk fluid was zero. As the simulation proceeded, particles moved freely along the lattice links. We examined the y-directional averaged relative concentration in the field using (2.3.7). The averaging window used to compute the y averaged colored concentrations in the simulation was 12x84 over one simulation time step. The simulated relative concentration distribution for the black particles reproduces the analytical relative concentration distribution calculated from equation (2.3.7), as shown in Figure 2.3.1.

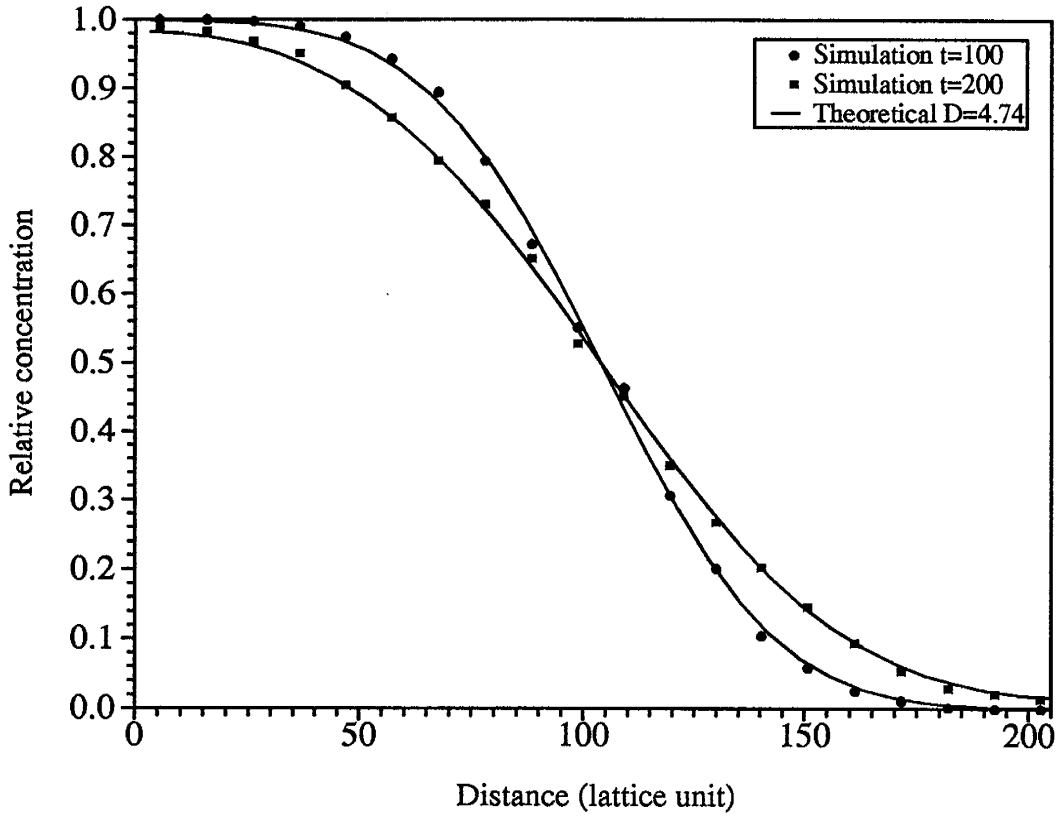

Figure 2.3.1. Relative concentration distribution for self-diffusion in bulk solution, theoretical self-diffusion coefficient D_s=4.74 (lu^2/sts). The time t represents the number of simulation time steps.

The same solution (2.3.7) was also used to examine the diffusion of tracer particles, representing the diffusion of a solute. In the tracer particle method, black tracer particles were initially distributed at the left half side of the field, again with a relative concentration of 1, and white tracer particles were on the right half side of the field with relative concentration zero. In this case, D was the tracer particle diffusion coefficient to be determined. There are two approaches in determining the tracer particle diffusion coefficient D. First, we can introduce just one tracer particle into the field and then measure the distance X traveled by the tracer particle in time t. We then repeat this procedure for many tracer particles to get a statistical relationship between X and t. The tracer particle diffusion coefficient can be determined from the classical Fickian relationship $X=\sqrt{(2Dt)}$. The second approach used in this paper is to put many tracer particles into the field but also to

ensure that the probability that two tracer particles can meet at the same site be close to zero. Since the tracer particles are independent of each other, the results can be regarded as an ensemble average over many individual tracer particle excursions. We used the second method because it is far more efficient. The diffusion coefficient in equation (2.3.7) was adjusted to match the analytical solution to the y-direction averaged tracer particle concentrations.

In the following simulations, the lattice field had dimensions of 480x36 (sites). The average number of bulk particles per site was, n=1.5, the same as for the bulk fluid self-diffusion case. The number of tracer particles introduced onto the the lattice field was 10% of the total number of sites. Tests were run to check the possibility that two tracer particles could meet at the same site, and the results showed that the probability was very low; in 5,000 simulation time steps, only two cases were found involving two tracer particles at the same site. The initial positions of the tracer particles inside the field were randomly distributed by using a uniform random number generator, so that the diffusion process started from an initially stable condition. The δ value used to determine tracer particle moving directions was $\delta = 2.78x10^{-2}$ radians which corresponds to 5 degrees.

We first started with the case $k=1$. The tracer particles moved at the same velocity as the bulk fluid particles. The simulated and fitted relative concentration curves for the tracer particles are plotted in Figure 2.3.2 The tracer particle concentrations are consistent with a Fickian molecular diffusion process described by equation (2.3.7); thus the algorithm appears to be working. The tracer particles have a diffusion coefficient of D=0.88 (lu^2/sts), substantially lower than the bulk fluid self-diffusion coefficient, a situation that arises from the fact that the tracer particles do not take part in the two and three body collisions with the bulk fluid particles. Increasing the waiting time period k has the effect of decreasing the diffusion coefficient, as shown in Figure 2.3.3 for k=6. The tracer diffusion coefficient is D=0.085 (lu^2/sts), an order of magnitude lower than that with waiting period k=1.

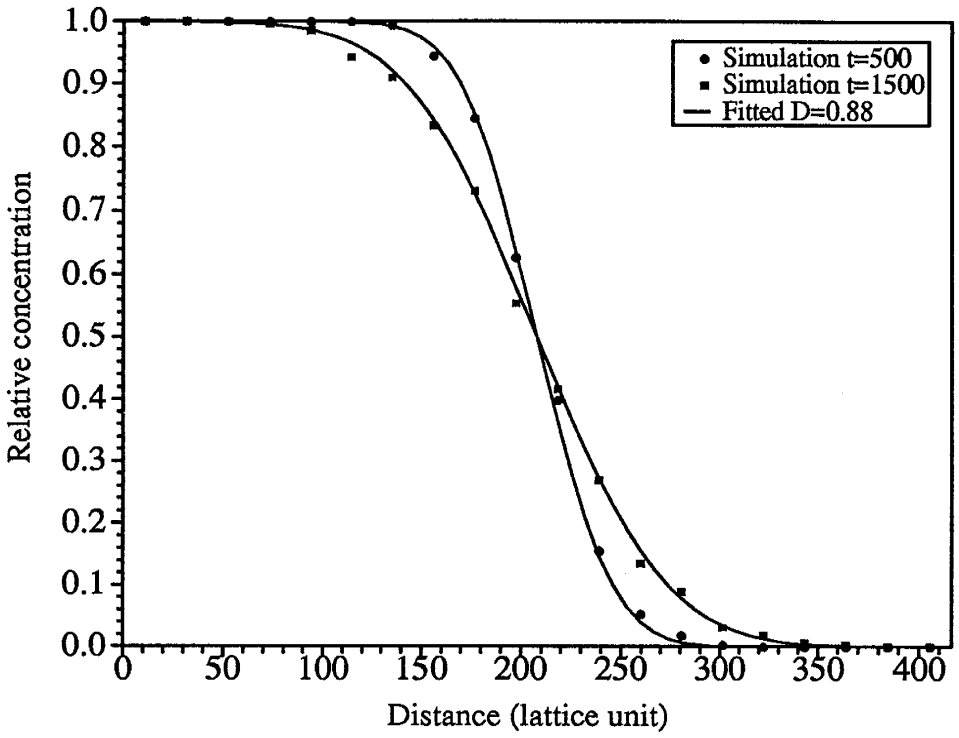

Figure 2.3.2. Relative concentration distribution of tracer particles. The fitted diffusion coefficient D=0.88 (lu^2/sts).

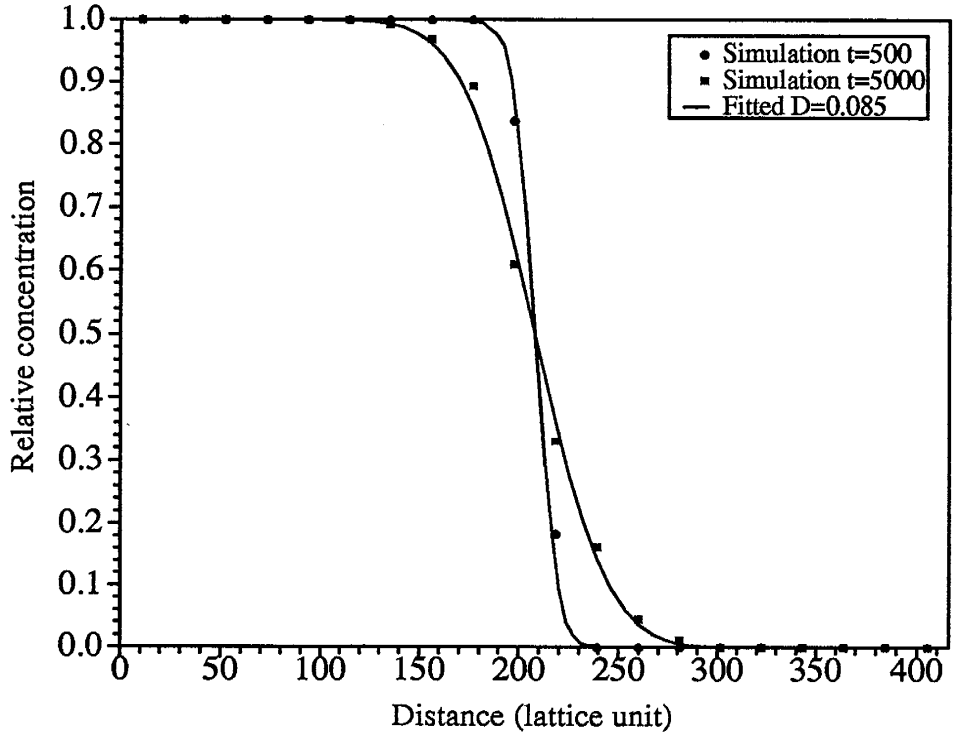

Figure 2.3.3. Relative concentration distribution of tracer particles with a waiting period k=6. The fitted diffusion coefficient D=0.085 (lu^2/sts).

Additional simulations were run with different k values to investigate the influence of waiting period k on tracer diffusion coefficients. Figure 2.3.4 shows the relationship between log$D$ and log$k$, for k ranging from 1 to 200. The simulated data shows that for constant bulk fluid density, tracer particle diffusion coefficient D is inversely proportional to k, the waiting period. A linear regression of the tracer particle simulation results revealed that the slope of the fitted line is around –1 if the point at k=1 is ignored. Recall that we suggested that the waiting period k is proportional to the size of the tracer particles. Thus, the tracer particle diffusion coefficient is inversely proportional to the radius of the tracer particles. Einstein [1908] derived a theoretical formula for calculating the diffusion coefficient of dilute suspended particles in a liquid. He showed that the diffusion coefficient is inversely proportional to the radius of the suspended particles.

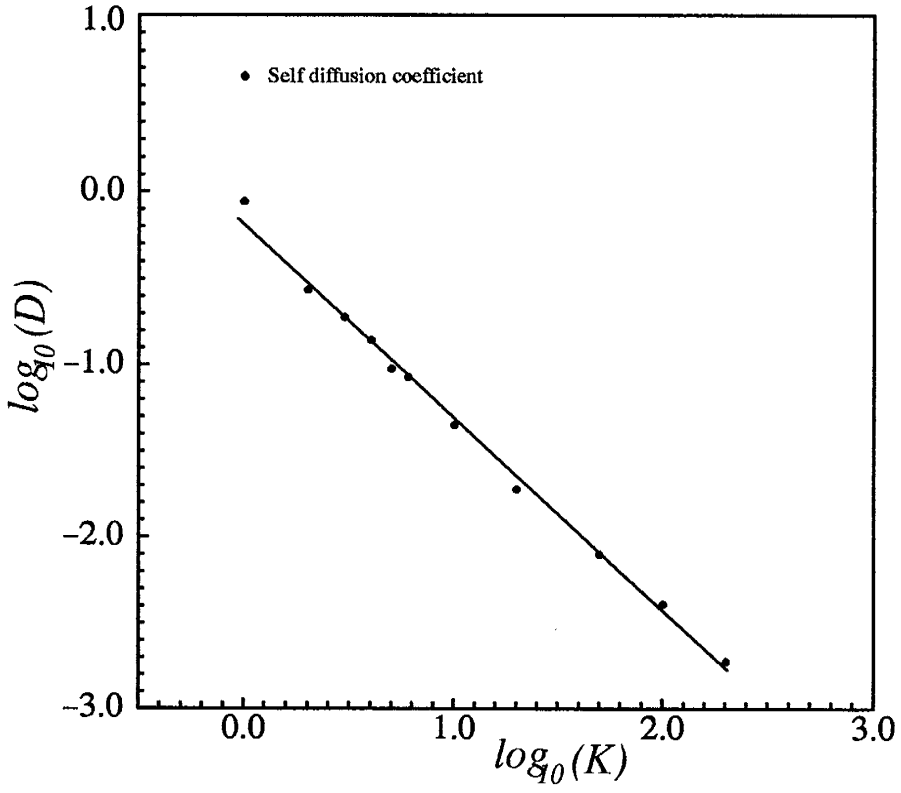

Figure 2.3.4. Variation of tracer diffusion coefficient, D, with waiting period, k.

In these simulations, only the local net momentum was used for directing the movement of the tracer particles and the memory of the tracer particle was ignored. The memory can be easily added in the current algorithm, but must be done carefully. If the memory is too large, tracer particles basically follow their previous moving directions, and the influence of local net momentum is ignored. Computationally, adding memory in the simulations increases the computation time. Physically, the tracer particle algorithm without memory appears to posses the desired diffusion behavior. Thus, we do not consider the memory in simulations presented here. Further research is necessary to investigate the influence of the tracer particle memory on the diffusion coefficients.

The numerical simulation results illustrate that with the tracer particle algorithm, the lattice gas automata method can be easily applied to simulate diffusion transport processes with low diffusion coefficients.

2.3.4 Taylor Dispersion Results and Discussion

One purpose for developing the tracer particle algorithm was to study solute transport processes in a flowing fluid. The algorithm was tested for solute transport behavior during flow between two parallel plates. The solution for the averaged concentration distribution in the direction of flow can be easily derived from Taylor–Aris dispersion theory [Aris, 1955]

$$\frac{C}{C_0} = \frac{1}{2}[1 \mp erf(\frac{x-\overline{V}t}{2\sqrt{D_l t}})] \tag{2.3.8}$$

$$D_l = D + \frac{\overline{V}^2 l^2}{210\ D} \tag{2.3.9}$$

where x is the distance from the source, $\overline{V}$ is the average flow velocity, l is the width of the channel, erf is the error function, and D_l is the longitudinal dispersion coefficient.

To test the tracer particle algorithm for the Taylor dispersion problem, a steady state flow field was first formed and then tracer particles were injected into the field. The field had

dimensions of 460x35 sites. In the numerical simulation, the mean density of bulk fluid particles was n=1.91. The averaging window for flow estimation was 115x7 sites. The average flow velocity in the field was 0.055 lu/sts. Tracer particles with the waiting period k=1 were used in the simulation. The tracer particle diffusion coefficient was 0.68 lu^2/sts which was determined by running the diffusion problem described in equation (2.3.7) with the mean bulk fluid particle density of n=1.91. The tracer particles were injected at a distance of 174 lu from the upstream flow boundary to ensure a fully developed velocity profile, which was checked by using a small averaging window for the flow field in the test runs. When a tracer particle reached the downstream boundary, it was removed from the field. The size of the averaging window used in the numerical experiments for estimating tracer concentrations was 10x35. The reason for choosing a small averaging size for tracer particles in x direction was that a large averaging size in x direction would smooth the concentration profile. The averaging window for tracer particle concentrations was applied from the injection boundary of tracer particles then down stream. The injection boundary of the tracer particles was taken as the origin of the dispersion problem. The simulated relative concentration curves of tracer particles at times 600, 1,000, and 2,000 simulation time steps are plotted in Figure 2.3.5 and compared to those calculated from equation (2.3.8). Notice that at 2,000 sts, the tracer particles have already reached the down stream boundary. This test shows that the tracer particle algorithm can simulate transport processes involving both diffusion and advection.

In the case of waiting period k>1, the tracer particle moves at a velocity slower than the fluid. The dispersion behavior can no longer be simply described by the Taylor-Aris dispersion theory. Thus, the algorithm needs to be further developed for simulating dispersion problems with low diffusion coefficients (waiting period k>1). In the fracture junction problem we are thus required to use k=1 and to change fluid density n in order to change the velocity, tracer diffusion coefficient, and Peclet number.

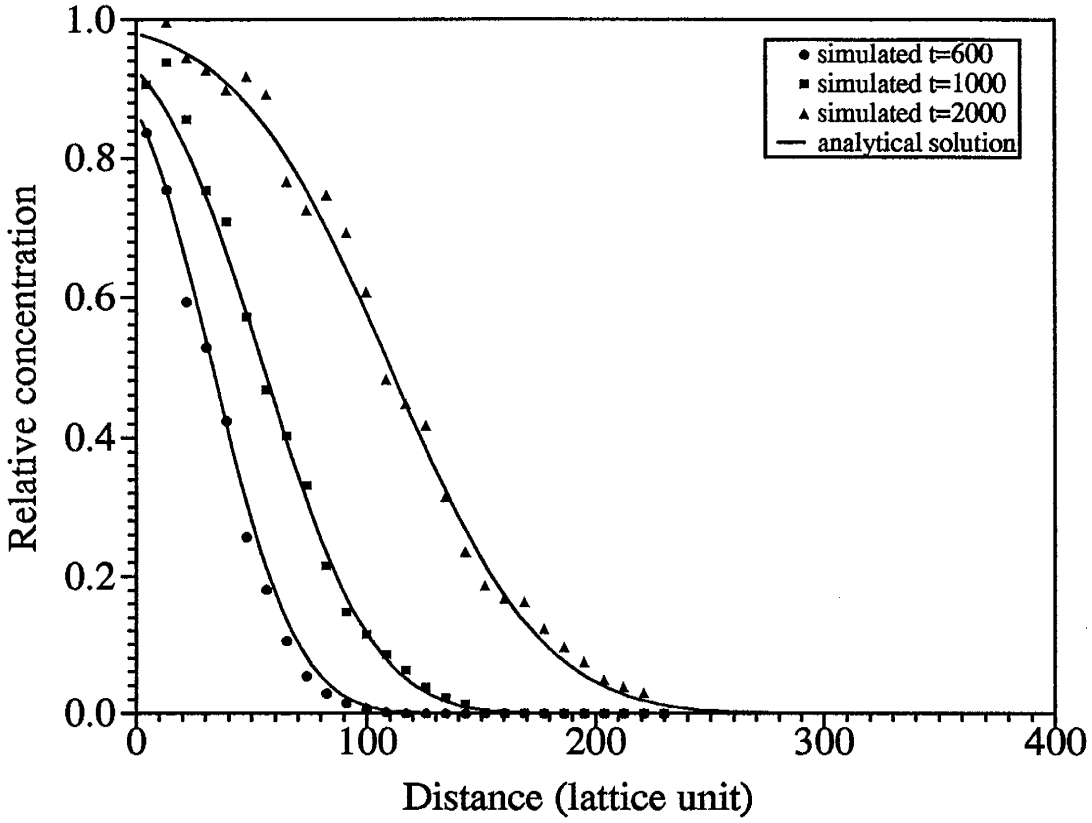

Figure 2.3.5. Comparison between simulated concentration profiles and the theoretical results.

2.3.5 Conclusions

The tracer particle algorithm simulates diffusion and advection processes properly. By varying the waiting period of the dilute tracer particles, the effective diffusion coefficient can be controlled over a wide range without changing the properties of the bulk fluid particles. One important feature of this new algorithm is that it relates the local momentum of the bulk fluid lattice field to the moving processes of tracer particles, reflecting the dynamic transport process of solute particles in the flow field. This new method can be easily extended to higher dimensions and multiple species. Unlike the colored particle methods, the tracer particle algorithm does not involve collisions between tracer particles and bulk particles nor among tracer particles themselves. The computational burden is reduced greatly. Thus, the algorithm is more efficient. But the algorithm needs to be further developed for simulating dispersion behavior involving waiting period $k>1$.

References

Aris, R., On the dispersion of a solute in a fluid flowing through a tube, *Proc. Roy. Soc. A.* 235, 67–77, 1956.

Boon, J.P., and A. Noullez, Lattice gas diffusion and long time correlations, Proceedings of the Workshop on Discrete Kinetic Theory, Lattice Gas Dynamics and Foundation of Hydrodynamics, World Scientific Publishing Co., Singapore, 1989.

Bernardin, D., and O.E. Sero-Guillaume, Lattice gases mixtures models for mass diffusion, *Eur. J. Mech., B/Fluids,* 9, 21–46, 1990.

Bernardin, D., O.E. Sero-Guillaume, and C.H. Sun, Multispecies 2D lattice gas energy level: Diffusive properties, *Physica D*, 47, 169–188, 1991.

Chen, H., and W.H. Matthaeus, Cellular automata formulation of passive scalar dynamics, *Phys. Fluids*, 30, 1235–1237, 1987.

Chen, S., S. P. Dawson, G. D. Doolen, D. R. Janecky, and A. Lawniczak, Lattice methods and their applications to reaction systems, submitted to Computer and Chemical Engineering, Los Alamos National Laboratory, New Mexico 87545, 1993.

Crank, J., The Mathematics of Diffusion, Oxford at the Clarendon Press, 1970.

Dawson S. P., S. Chen, and G. D. Doolen, Lattice Boltzmann computations for reaction-diffusion equations, *J. Chem. Phys.*, 98(2), 1514–1523, 1993

d'Humieres, D., P. Lallemand, and G. Searby, Numerical experiments on lattice gases: Mixtures and Galilean invariance, *Complex Systems*, 1, 633–647, 1987.

d'Humieres, D., P. Lallemand, J.P. Boon, D. Dab and A. Noullez, Fluid dynamics with lattice gases, Chaos and Complexity, 278–301, World Scientific, Singapore, 1988.

Einstein, A. Investigations of the Theory of the Brownian Movement (the original paper was published in 1905 in German), edited by R. Furth, translated by A.D. Cowper, Dover Publications, Inc, New York, 1956.

Frisch, U., B., Hasslacher, and Y. Pomeau, Lattice gas automata for the Navier-Stokes equation, *Phys. Rev. Lett.*, 56(14), 1505–1508, 1986.

Frisch, U., D. d'Humieres, B. Hasslacher, P. Lallemand, Y. Pomeau, and J. Rivet, Lattice gas hydrodynamics in two and three dimensions, *Complex Systems,* 1, 649–707, 1987.

Holme, R. and D.H. Rothman, Lattice-gas and lattice-Boltzmann models of miscible fluids, MIT Porous Flow Project, Report No. 4, 70–95, MIT, 1991.

Sero-Guillaume, O.E., and D. Bernardin, A lattice gases model for heat transfer and chemical reaction, *Eur. J. Mech., B/Fluids,* 9, 177–196, 1989.

Wells, J.T., D.R. Janecky and B.J. Travis, A lattice gas automata model for heterogeneous chemical reactions at mineral surfaces and in pore networks, *Physica D*, 47, 115–123, 1991.

Wolfram, S., Cellular automata fluids 1: Basic theory, *J. Stat. Phys.*, 45, 471–526, 1986.

Chapter 3: Mixing Behavior at Fracture Junctions: The Numerical Simulation Results

3.1 Introduction

Past research on mixing behavior at fracture junctions has been focused on determining mixing rules applied in numerical simulations of solute transport in discrete fracture networks (see Chapter 1). Several mixing rules have been proposed: complete mixing, streamline routing, and some combination. However, there is still no certain answer as to which rule is correct and under what conditions.

Stimulated by previous research [Hull et al., 1987; Berkowitz, et al., 1994] we hypothesized a mixing rule at idealized fracture junctions. There should be a continuous mixing rule started somewhere near a Peclet number of 1. Above this Peclet number, a transition zone exists between complete mixing and streamline routing (see Figure 3.1). As the Peclet number decreases, the mixing process is diffusion dominated, and the complete mixing rule is appropriate. When the Peclet number increases, the mixing process at the junction is advection controlled, and there will be little or no diffusive mixing. The upper

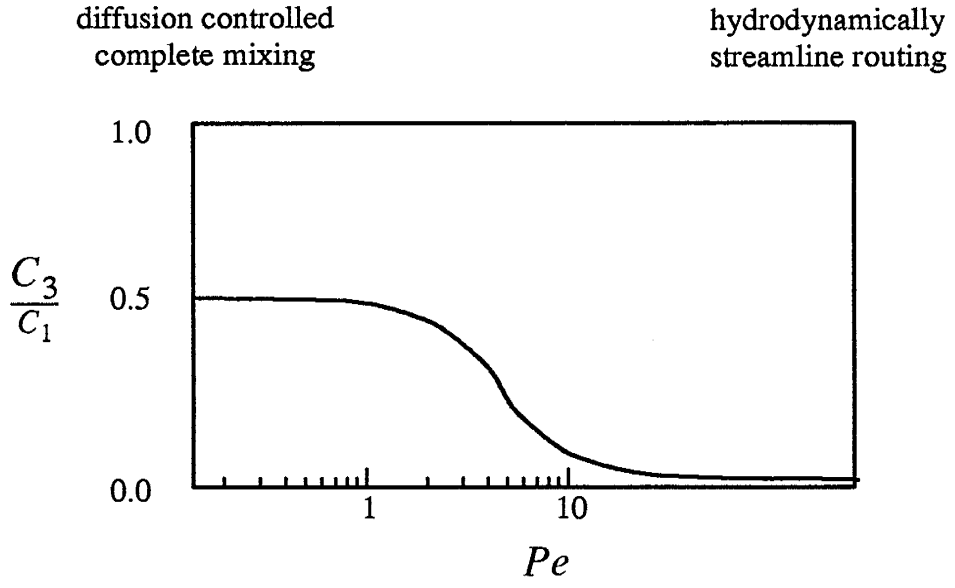

Figure 3.1 Hypothesized mixing rule at the idealized fracture junction of Figure 3.2.

limit for the streamline routing should be somewhere around a Peclet number of 10. If the transition zone between the two limiting cases is narrow, then either the diffusion controlled complete mixing rule or the advection controlled streamline routing can be used. If the transition zone is broad, then an adaptive mixing rule is required, and it depends on local conditions around each fracture junction in a network. Hull et al. [1987] had a similar hypothesis, but with a higher estimate for the upper limit.

Of the very few attempts to study mixing behavior at fracture junctions, Hull et al. [1987] implicitly considered this transitional hypothesis by creating a heuristic hybrid mixing rule but never explicitly studied it. Berkowitz et al. [1994] applied a random walk particle tracking technique to study mixing behavior at an idealized continuous junction as shown in Figure 3.2. The flow field at the junction was computed following Philip's [1988] method. They concluded that streamline routing provides an adequate approximation for contaminant transport at fracture junctions with Peclet numbers greater than 1; there is a transition zone between diffusive mass transfer and advective mass transfer; and complete mixing does not properly represent mixing behavior at any Peclet number. Berkowitz et al. [1994] never observed diffusion controlled complete mixing in the simulations even at junction Peclet numbers as low as $3x10^{-3}$. There are no other numerical simulations or experimental results available to verify their numerical results.

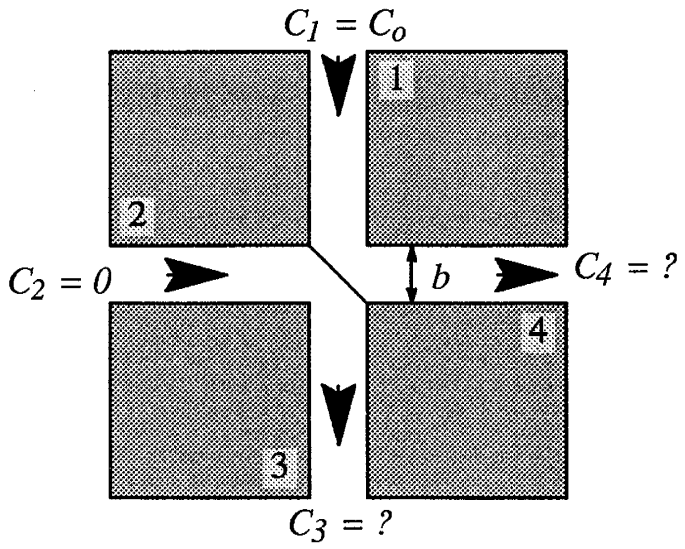

Figure 3.2. Mixing at an idealized continuous fracture junction.

In the current research, we use the lattice gas automata (LGA) method to investigate this hypothesis and other issues concerning mixing behavior at fracture junctions. The numerical results from the LGA simulations are then compared with those of Berkowitz et al. [1994]. Under non-equal flow rate conditions, the proportional routing proposed by Hull and Koslow [1986] for predicting concentrations in outlet fractures is tested with the LGA simulations.

3.2 Numerical LGA Model of Mixing at a Fracture Junction

The idea of the LGA method is to simulate macroscopic flow and transport behavior from the movement of particles on microscopic level (discrete level). Macroscopic fluid behavior can be recovered after one defines average particle densities and velocities over suitable regions of the lattice. Frisch et al. [1986] were the first to apply the LGA method to the numerical simulation of the Navier-Stokes equation. The first step of the method is to construct a lattice field. In two dimensions, a hexagonal lattice is isotropic and widely used in the simulations of fluid dynamics (see Figure 2.2.1). To simulate a fluid in equilibrium, particles are initially distributed in the field at random. Each fluid particle has unit mass and moves with unit speed in one of the six possible directions. For the two dimensional hexagonal lattice, the velocity vector in direction j ($j=1, 2, \ldots 6$) is

$$e_j = \{cos[\frac{2\pi(j-1)}{6}],\ sin[\frac{2\pi(j-1)}{6}]\} \qquad (3.1)$$

At each site of the lattice, no more than one fluid particle can move in the same direction, so each site can have up to six moving particles.

The evolution of particles follows two steps. First, each particle moves one step along the link to the neighboring site. Second, collisions occur at each site with two or more particles. Collision rules are chosen such that mass and momentum are conserved after each collision. In the current study, two, three, and four body head-on collision rules are used, as illustrated in Figure 2.2.1 and Figure 3.3. When a fluid particle hits the fracture wall, it is bounced back to preserve a non-slip boundary along the wall. Frisch et al. [1986] proved that such collision rules can reproduce the Navier-Stokes equation on a macroscopic scale. The macroscopic

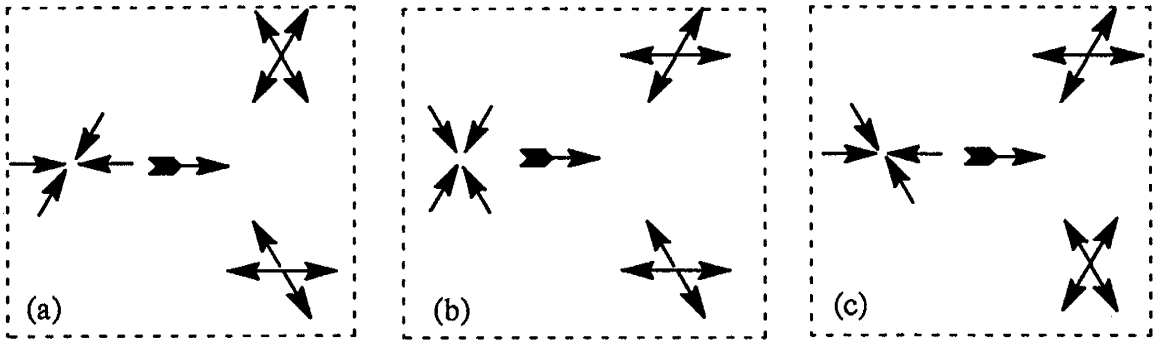

Figure 3.3. Four body head–on collision rules used in the numerical simulations. There are three possible configurations a, b and c. In each configuration, the left side refers to the state before the collision. The right side refers to the state after the collision. A uniform random number generator was used to choose one of the two possibilities.

mean density, d, and velocity, $\boldsymbol{u}$, of the field are defined as

$$d = \frac{2}{\sqrt{3}}\frac{1}{M}\sum_i(\sum_j N_j) \tag{3.2}$$

$$\boldsymbol{u} = \frac{2}{\sqrt{3}}\frac{1}{dM}\sum_i(\sum_j N_j \boldsymbol{e}_j) \tag{3.3}$$

where M is total number of sites, N_j is the number of fluid particles at site i moving in direction j; $\boldsymbol{e}_j$ is the particle velocity vector in direction j. The relationship between macroscopic mean fluid density d and mean fluid particle density n is $d=2n/\sqrt{3}$. The ratio $2/\sqrt{3}$ comes from the fact that in a hexagonal lattice the number of nodes per unit area is $2/\sqrt{3}$ instead of 1.

The LGA method simulates flow and transport processes simultaneously, and it can handle problems with complex geometries. In our LGA simulations, the fracture junction model has an uniform aperture of 35 lu (lattice unit) with total length of 398 lu in each direction. The total number of nodes in the field was 31,212. The numerical simulations were run on a SUN SPARC–2 and a SPARC–IPX with a Wetek power up™ chip.

To simulate flow around the fracture junction, fluid particles were injected at each end of the fracture. Only at the downstream outflow boundaries could fluid particles move freely out of the field. In this way, a pressure gradient and flow field were established. The number

of injected particles at both inflow and outflow boundaries were adjusted to create the desired discharge and mean flow velocity in each fracture. Figure 3.4 shows the simulated velocity profile around a fracture junction with equal discharge in each fracture, simulating the situation shown in Figure 3.2. The mean fluid particle density n=2.67, and the average velocity was 0.140 *lu/sts* (lattice unit/simulation time step) in each fracture. The averaging window used for deriving velocity profiles in this and all the later simulations was 10x7 along and perpendicular to flow direction, respectively. It is clear that a dividing streamline exists that separates the flow from fracture 1 and that from fracture 2 at the junction. In the case of an advection controlled transport process, solute carried in from fracture 1 will follow

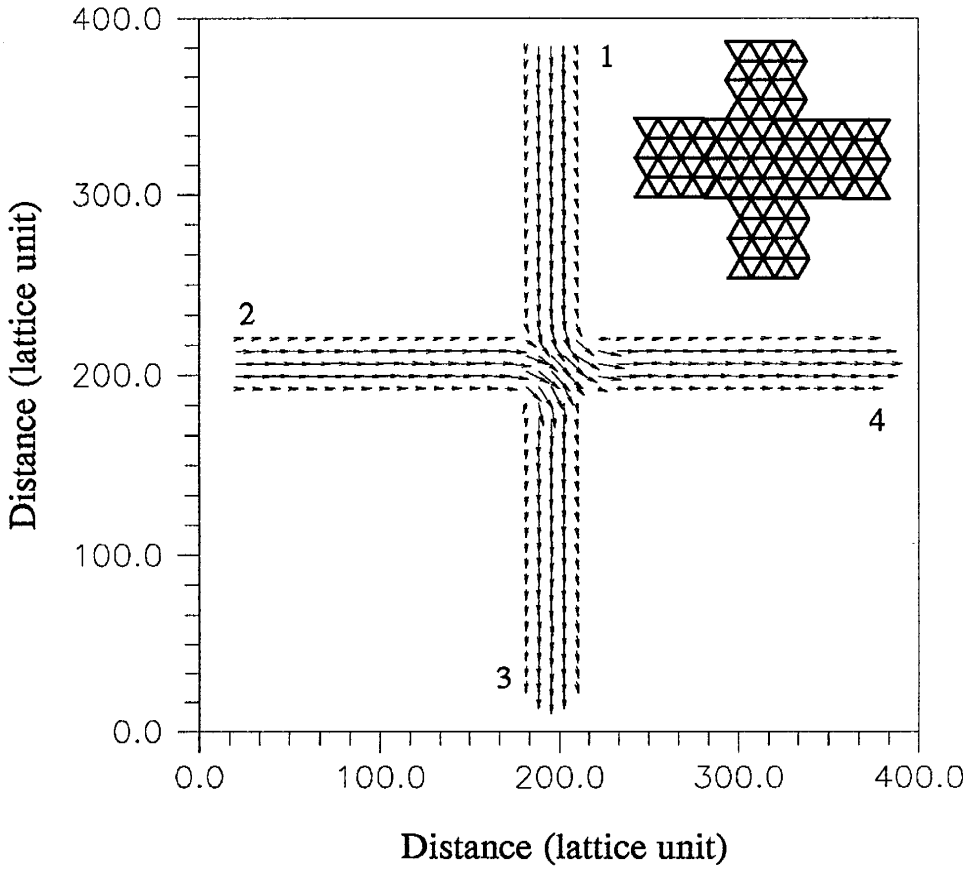

Figure 3.4. Velocity distribution at the fracture junction. A dividing streamline separates flow from top and left. A schematic of the grid orientation is shown in the upper right corner for illustrative purpose at a much reduced grid density.

the streamline directly into fracture 4 (see Figure 1.3b). Only diffusion can cause solute to move across the dividing streamlines to enter the flow region formed by fractures 2 and 3.

In order to simulate the mixing process at the fracture junction with the LGA method more efficiently, a new algorithm, called the tracer particle algorithm, was developed (refer to §2.3 for details) and used in the current research. The algorithm takes into account the influences of both diffusion and advection on the transport of solute particles in the field. As the word "tracer" implies, the introduction of tracer particles will not alter the flow field, nor will it change the transport properties of the field. Thus, no collision rule is involved for the tracer particles, and the computation burden is greatly reduced. In LGA simulations of mixing behavior at fracture junctions, tracer particles were introduced onto the lattice field as an indicator for flow and transport in the system, and they moved with the same velocity as the fluid particles (the waiting period of the tracer particle was 1; see §2.3). The density of tracer particles in the lattice field was kept very low to reduce the probability of two or more tracer particles meeting at the same site, in such a case, each tracer particle would move along its original direction.

The diffusion coefficient of tracer particles was estimated by running a self-diffusion problem in a rectangular domain and fitting the numerical results with a known analytical solution (refer to §2.3 for details). The tracer diffusion coefficient D depends on the fluid particle density n which also determines the fluid pressure and viscosity. Numerical simulations were run to estimate tracer particle diffusion coefficients for different particle densities n. Figure 3.5 shows the relationship between particle density n and tracer particle diffusion coefficient D for two, three, and four body fluid particle head-on collision rules. As the fluid particle density increases, the tracer particle diffusion coefficient decreases, but at a decelerating rate. The simulated average flow velocity, the tracer particle diffusion coefficient corresponding to the fluid particle density in the field, and the half diagonal

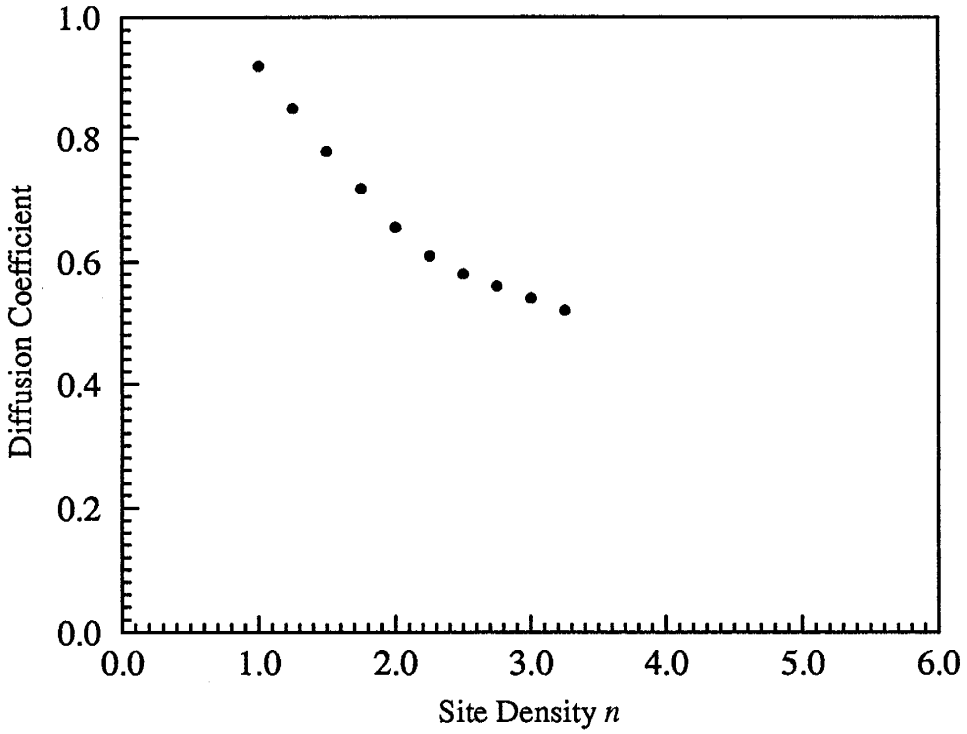

Figure 3.5. Relationship between tracer particle diffusion coefficient and fluid particle density for two, three, and four body head–on collisions.

length of the junction were used to calculate the junction Peclet number defined in equation (1.1).

In the numerical simulations, tracer particles were injected at the top boundary of fracture 1 as indicators for the movement of a solute through the junction. The tracer particles were labeled black to distinguish from the white fluid particles. A constant mass flux boundary condition was maintained at the top boundary by injecting tracer particles at certain time intervals. To conserve the total mass of tracer particles injected, any injected tracer particle that hit the entries of the two inflow boundaries was bounced back. Tracer particles could only leave the system through outflow fractures 3 and 4. Once a tracer particle reached one of the outflow boundaries, it was removed from the field, which is similar to a first type boundary condition with zero concentration in a continuum model. The total number of particles injected and the total number of particles flowing out of the system were counted at the top, right, and bottom boundaries of the junction. Equilibrium was reached when the

total number of particles injected equaled the total number of particles flowing out of the system.

The mixing ratio, introduced to indicate the level of diffusive mixing at the fracture junction, is defined as

$$M_r = \frac{C_3}{C_1} \tag{3.4}$$

As shown in Figure 3.2, C_3 is the concentration of contaminant in the outflow fracture 3, and C_1 is the concentration of the original contaminant in the inflow fracture 1. In the LGA simulations, the mixing ratio is redefined in terms of tracer particle numbers. In equation (3.4) the concentration C_3 is replaced by the total number of particles moving out through fracture 3 within a certain number of simulation time steps, and C_1 is replaced by the total number of tracer particles injected at the inflow boundary of fracture 1 during the same period,

$$M_r = \frac{N_3}{N_1} \tag{3.5}$$

Under equal flow conditions, a value of $M_r=0$ indicates an advection controlled process at the fracture junction. While the case of diffusion dominated complete mixing corresponds to a mixing ratio of $M_r=0.5$. Any value of M_r between 0 and 0.5 indicates a transition mixing process in which both advection and diffusion control the solute mixing behavior at the junction.

3.3 Mixing Behavior at a Fracture Junction With Equal Flow Rates

For an idealized fracture junction with equal flow rates, solute transport at the junction is determined by both advection and diffusion. But only diffusion can contribute to the mixing of the solute at the junction. Numerical simulations were run from high Peclet numbers down to low Peclet numbers to simulate a range of mixing behaviors at the fracture junction.

The first case was run with a mean fluid particle density n=2.67 and an average flow velocity of 0.14 lu/sts in each fracture. The velocity profile of the flow field is shown in Figure 3.4. At each simulation time step, one tracer particle was injected at the inflow boundary of fracture 1. The tracer particles had a diffusion coefficient of 0.56 lu^2/sts. Starting from 20,000 sts, the system was at equilibrium with the number of particles moving out of the system equaling the number of injected tracer particles. To obtain a proper estimate of the mixing ratio, only the tracer particle data from 30,000 to 60,000 simulation time steps was used. During this period, a total of 30,000 tracer particles were injected into the inflow fracture 1. Of all the injected tracer particles, 5,135 of them moved out through fracture 3, and 24,840 of them flowed out through fracture 4. The tracer mass balance error was 0.083%. At equilibrium there were, on average, 1,475 tracer particles in the field at any time. Compared to a total of 31,212 sites in the field, the number of tracer particles was very small. In order to get a clear idea about the transport of tracer particles around the junction, a superposed spatial distribution of tracer particles is used to represent the average behavior of the tracer particles. Figure 3.6 shows the superposed spatial distribution of tracer particles, exaggerated in size, in the field from snap shots at 40,000, 50,000, and 60,000 simulation time steps. The tracer particles are shown in exaggerate size. The simulated mixing ratio at the junction is 0.17, which means that of 100 tracer particles injected at the inflow boundary of fracture 1, on average 83 of them left the system through fracture 4, and only 17 of them moved across the dividing streamline under the influence of diffusion and left the system through fracture 3. The Peclet number at the fracture junction calculated from equation (1.1) is P_e=6.10. It suggests that advection played a more important role than diffusion in the transport process, consistent with the simulation results.

Figure 3.6 also clearly shows the dividing streamline along the diagonal of the fracture junction. When flow from fracture 1 met flow from fracture 2 at the left upper corner of the junction, few particles had a chance to move across the dividing streamline due to the relatively high flow velocity and small residence time. As the flow moved toward the

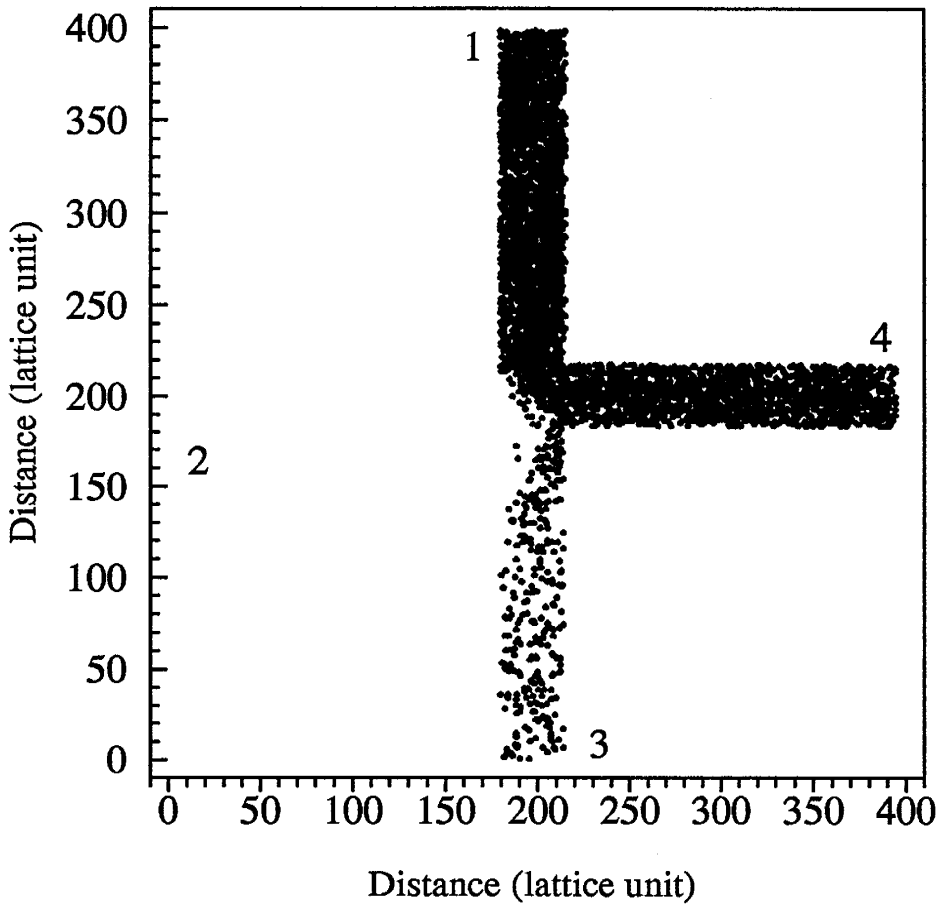

Figure 3.6. Superposed spatial distribution of tracer particles in the field from snap shots at 40,000, 50,000, and 60,000 simulation time steps for n=2.67, P_e=6.10, and M_r=0.17.

outflow fractures, the residence time of tracer particles increased, which in turn increased the chance for a tracer particle moving adjacent to the dividing streamline to diffuse across it and into the lower left flow domain. That is why the number of scattered tracer particles increased from the upper left corner down to the lower right corner at the junction. Those particles were then carried downstream into the lower outflow fracture 3. Once the tracer particles were in the outflow, diffusion played an important role in homogenizing tracer particle distribution downstream in the channel.

As flow velocity decreases, the residence time of tracer particles at the junction increases; thus more tracer particles have the chance to diffuse across the dividing streamline. The second case was run with a mean fluid particle density n=1.78 and an average velocity of

0.105lu/sts in each fracture. At each simulation time step, one tracer particle was injected at the entrance of the the inflow fracture 1. The diffusion coefficient of tracer particles in the field was 0.71 lu^2/sts and the Peclet number was P_e=3.71. Transport equilibrium was established in the system after 20,000 steps. Figure 3.7 shows the superposed spatial distribution of tracer particles in the field with a mixing ratio of M_r=0.25. From 30,000 to 60,000 sts, a total of 30,000 tracer particles were injected, with 22,520 of them flowing out through fracture 4, and 7,484 of them moving out through fracture 3. The mass balance error of the tracer particles was 0.013%. At equilibrium, the average number of tracer particles in the field was 2,465, almost 1,000 more than the previous case. Comparing to previous case in Figure 3.6, the spatial distribution of tracer particles in Figure 3.7 clearly shows that as the average velocity decreases, more tracer particles cross the dividing streamline into the

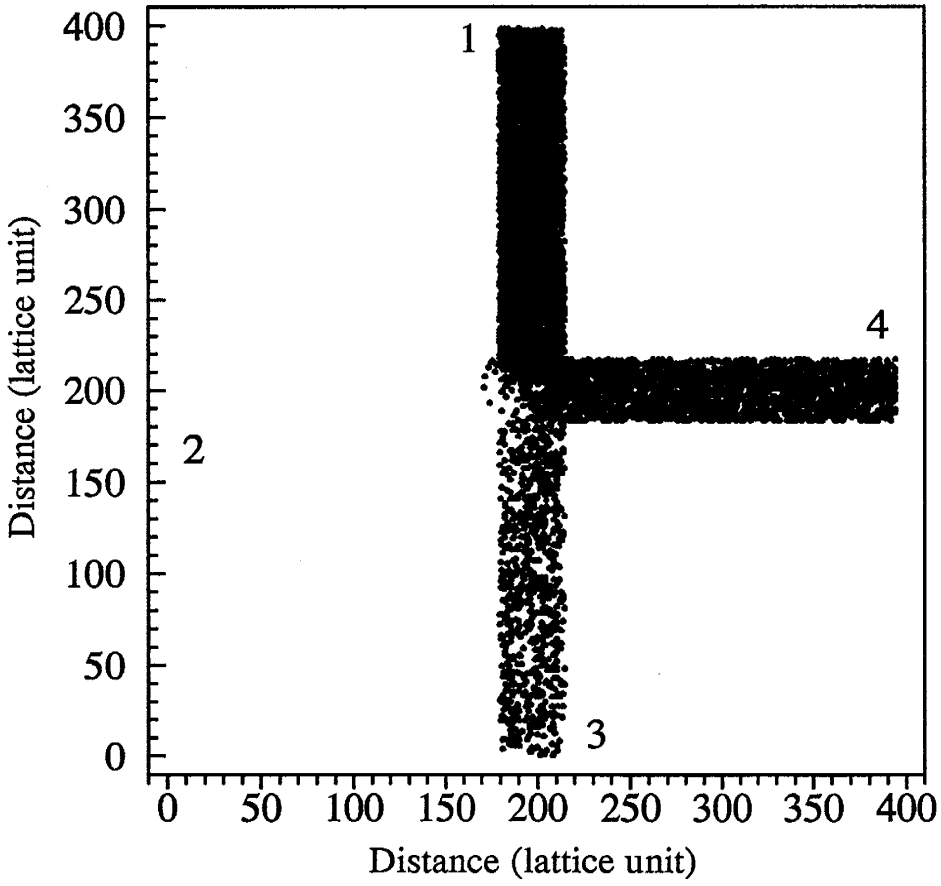

Figure 3.7. Superposed spatial distribution of tracer particles in the field from snap shots at 40,000, 50,000, and 60,000 simulation time steps for n=1.78, P_e=3.71, and M_r=0.25.

lower flow region formed by fractures 2 and 3. As a result, there is more diffusive mixing at the junction.

A further decrease of flow velocity results in a much larger tracer particle residence time in the junction, and thus an even higher mixing ratio. Figure 3.8 shows the snap shot of tracer particle locations in the field at 80,000 simulation time steps. The average velocity in each fracture is 0.05lu/sts with a mean bulk fluid particle density of 1.60 and a tracer diffusion coefficient of $0.75 lu^2/sts$. The junction had a Peclet number of P_e=1.67 and a mixing ratio of M_r=0.37. The numerical simulation was run for a total of 80,000 time steps to make sure equilibrium was established in the field. A mass balance check on tracer particles indicated that the system was at equilibrium after 30,000 steps. In a test run, one tracer particle at each

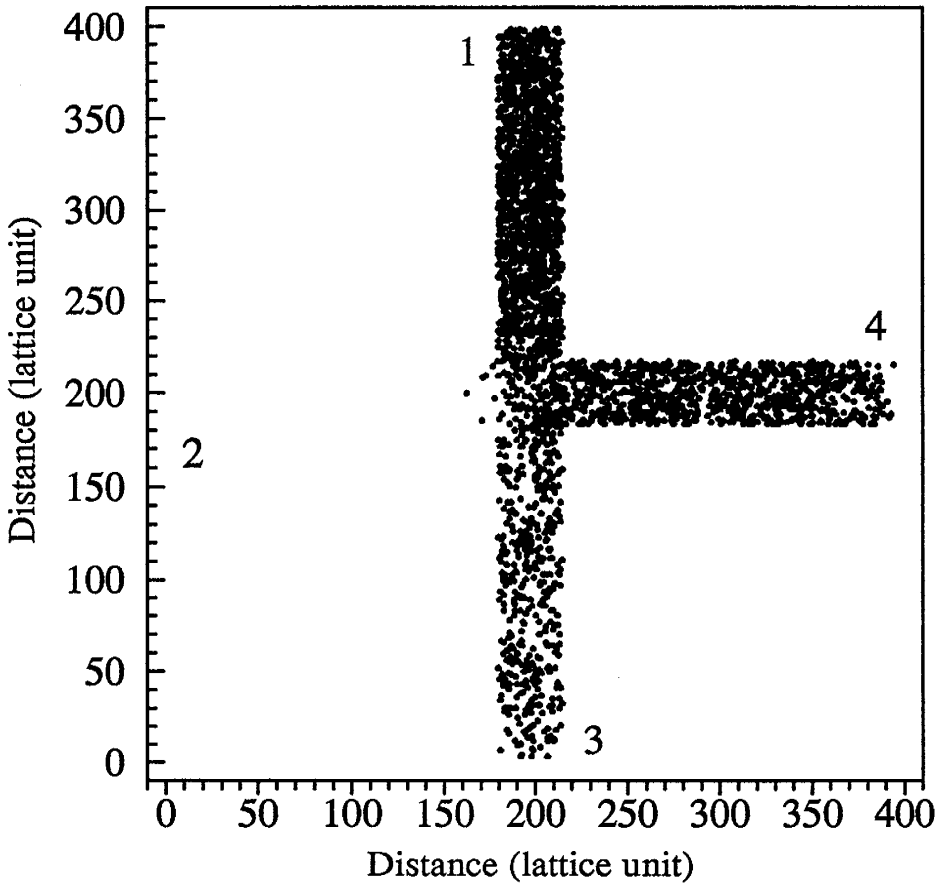

Figure 3.8. Snap shot of tracer particle distributions in the field at 80,000 simulation time step for n=1.60, P_e=1.67, and M_r=0.37.

simulation time step was injected at the inflow boundary of fracture 1. The test result showed a mixing ratio of 0.38 at the junction. An examination of the number of tracer particles per site showed that some sites had more than one tracer particle. At a low flow velocity, the injected tracer particles were not quickly carried out by the flow and the number of tracer particles built up, exceeding the assumed maximum one tracer particle per site restriction imposed to ensure statistical independence. In this case, the algorithm simply directs the tracer particles to move in their original directions, which causes artificial mixing at the junction. To eliminate this problem, the numerical simulation was rerun for the same flow field but with a reduced number of tracer particles. Instead of injecting one tracer particle at each time step, a tracer particle was injected every two simulation time steps. Thus, the number of tracer particles in the field was greatly reduced. This the case shown in Figure 3.8. From time step 50,000 to 80,000, a total of 15,000 tracer particles were injected with 9,366 of them moving out through fracture 4 and 5,591 flowing out through fracture 3. The mass balance error of the tracer particles was 0.28%. At equilibrium, on average, there were 2,800 tracer particles in the field. The mixing ratio dropped slightly from 0.38 to 0.37. Figure 3.9 shows the superposed spatial distribution of tracer particles in the field from the snap shots at 60,000, 70,000, and 80,000 simulation time steps. Compared with previous relatively high Peclet number cases, it is easy to see that as velocity decreases, more and more tracer particles cross the dividing streamline, and the magnitude of diffusive mixing increases. Another feature shown in both Figures 3.8 and 3.9 is that, due to diffusion, some of the tracer particles moved upstream into inflow fracture 2.

We expect that when the velocity is reduced below a certain limit, complete mixing should occur. Increased residence time of tracer particles at the junction should allow diffusion to dominate the mixing process. The next simulation in Figure 3.10 illustrates this case. The average velocity in each fracture was 0.02 lu/sts with a mean fluid particle density of n=1.64. One tracer particle was injected at the inflow boundary of fracture 1 in every 10 simulation steps. The tracer particles had a diffusion coefficient of 0.74 lu^2/sts. The Peclet number at

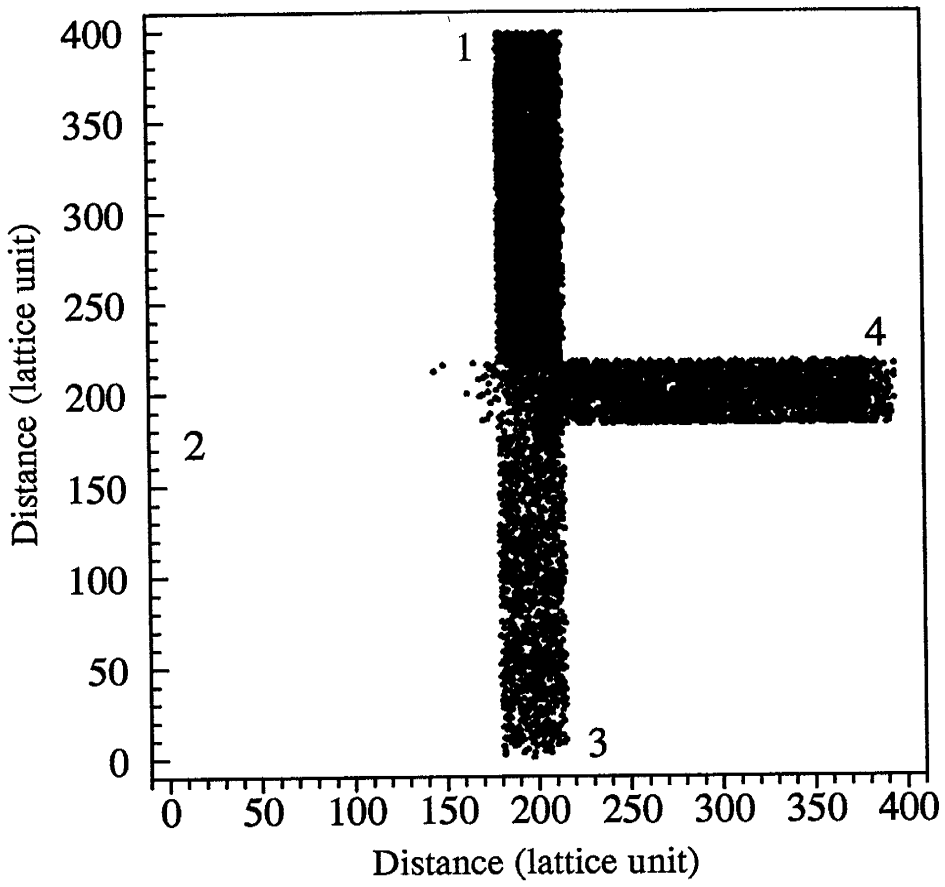

Figure 3.9. Superposed tracer particle locations in the field from snap shots at 60,000, 70,000, and 80,000 simulation time steps for n=1.60, P_e=1.67, and M_r=0.37.

the junction was 0.68. The simulation was run for a total of 200,000 sts. The locations of tracer particles in the field were output every 20,000 sts. A mass balance check of tracer particles showed that equilibrium was established after 80,000 sts. Figure 3.10 presents the superposed tracer particle distribution in the field from the snap shots at 160,000, 180,000, and 200,0000 simulation time steps. It is apparent that complete mixing occurred. The tracer particle data from 140,000 to 200,000 sts was used to calculate the mixing ratio at the junction. During this period, a total of 6,000 tracer particles were injected into the field. Of all of them, 3,047 moved out through fracture 3 and 2,950 moved out through fracture 4. The mass balance error of the tracer particles is 0.05%. On the average, there were 2,145 tracer particles in the field at equilibrium. The mixing ratio at the junction was 0.508, slightly larger

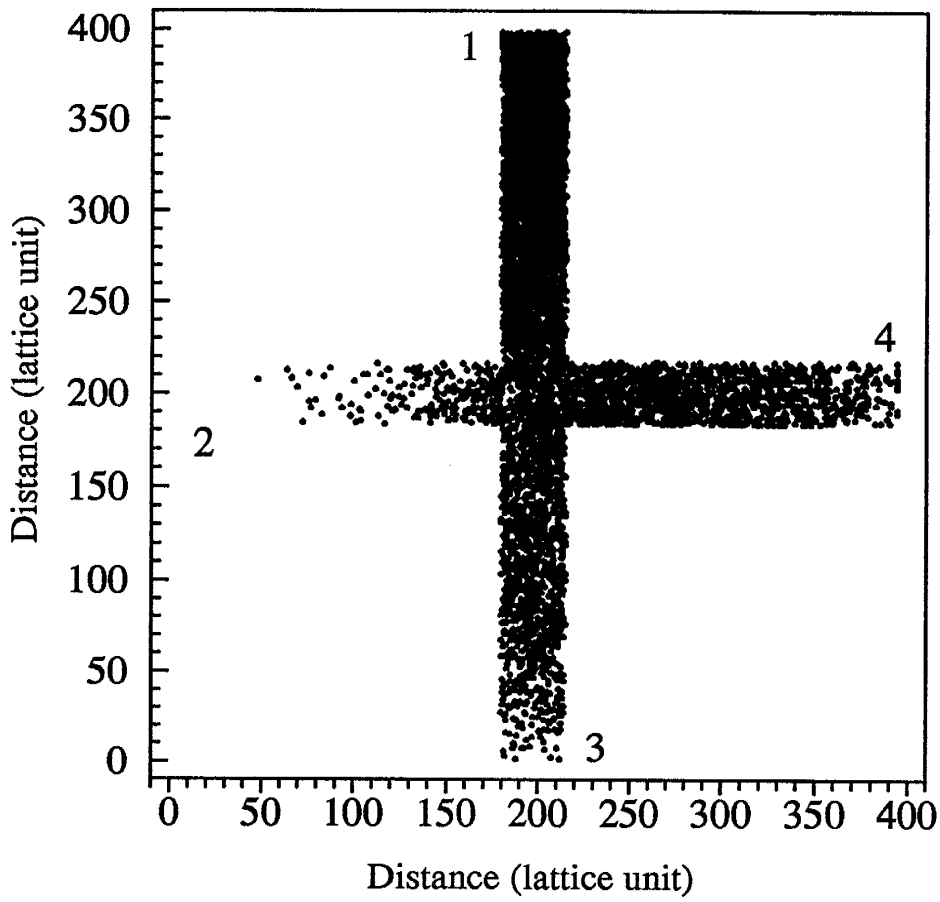

Figure 3.10. Superposed spatial tracer particle distribution in the field at 160,000, 180,000 and 20,0000 simulation time steps for n=1.64, P_e=0.68, and M_r=0.508.

than 0.50, but within the statistical error of the method. At low velocity, due to the noise of the flow field, the tracer particles move more randomly. Thus, the number of tracer particles moving out from the outflow boundaries varies from time to time, which results in an estimation error in the mixing ratio. Figure 3.10 also shows that under the influence of diffusion, many of the tracer particles have migrated upstream into the left inflow fracture 2. The relatively low tracer particle densities around the outlet boundaries of fracture 3 and 4 were caused by the imposed zero concentration boundary condition at each end.

Other numerical simulations were run for Peclet numbers ranging from 0.37 to 6.10. The detailed information on the average velocity, mean bulk fluid particle density, tracer particle

diffusion coefficient, Peclet number, and mixing ratio for each case is listed Table A.1 of Appendix A.

The results are plotted in Figure 3.11, demonstrating that in this model there is a transition zone for mixing behavior at the fracture junction, in support of our hypothesis. As the Peclet number decreases, the transport process becomes more and more diffusion controlled. As a result, there is more diffusive mixing at the junction, and the mixing ratio increases toward an asymptotic value of M_r=0.5. When the Peclet number is smaller than 0.68, there is complete mixing. For a Peclet number larger than 0.68, the transport process is both advection and diffusion controlled. The maximum Peclet number reached in the numerical simulation was 6.10, corresponding to a mixing ratio of 0.17. We expect that as Peclet

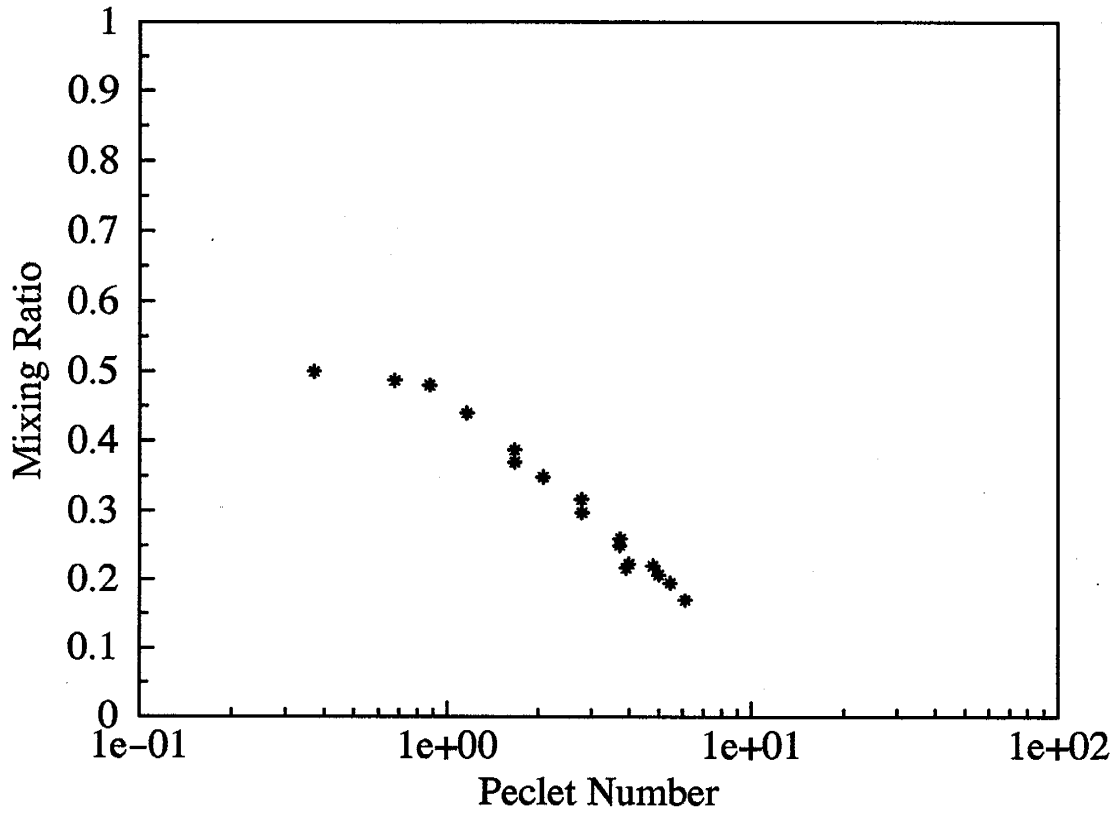

Figure 3.11. Relationship between mixing ratios and Peclet numbers at the fracture junction.

numbers further increase, the mixing ratio will approach zero. The transport process at the junction should be dominated by advection only, with no diffusive mixing in the junction. Thus, somewhere above a Peclet number of 10, streamline routing should become appropriate.

We were not able to generate flow fields with high average velocity and high Peclet numbers because of limitations with the LGA method. In the LGA method, flow properties (density, viscosity, pressure, etc.) and flow velocity in the field are directly related to the fluid particle density. The most difficult aspect in the LGA simulation of the fracture junction problem is that there is no systematic way to determine how many particles should be injected at the boundaries to obtain the desired evenly balanced flows. Thus, the numerical simulations boil down to trial and error until balanced velocity profiles are established, thus making the LGA method less efficient. When simulating flow at high velocity, a large pressure gradient must be built up in the field. Due to the relatively low fluid particle densities around each outflow boundary, the bulk fluid velocity tends to increase as it moves downstream. To balance the flow, more fluid particles should be injected at the outflow boundaries, but doing so also reduces the velocity inside the fracture and the Peclet number at the junction.

On the other hand, simulating transport behavior at Peclet numbers much lower than 1 was also very difficult due to the noise of the velocity field. Thus, a better method must be developed in order to overcome this difficulty and simulate transport at high Peclet numbers.

3.4 Comparison With Previous Numerical Results

Berkowitz et al. [1994] applied a random walk particle tracking technique to simulate mixing behavior at an idealized fracture junction with the same geometry as shown in Figure 3.2. Their numerical results for the equal flow rate case studied here are plotted in Figure 3.12 and compared to the LGA simulation results. It is clear that both numerical results suggest a transition zone for the mixing process, but with a significant difference in the

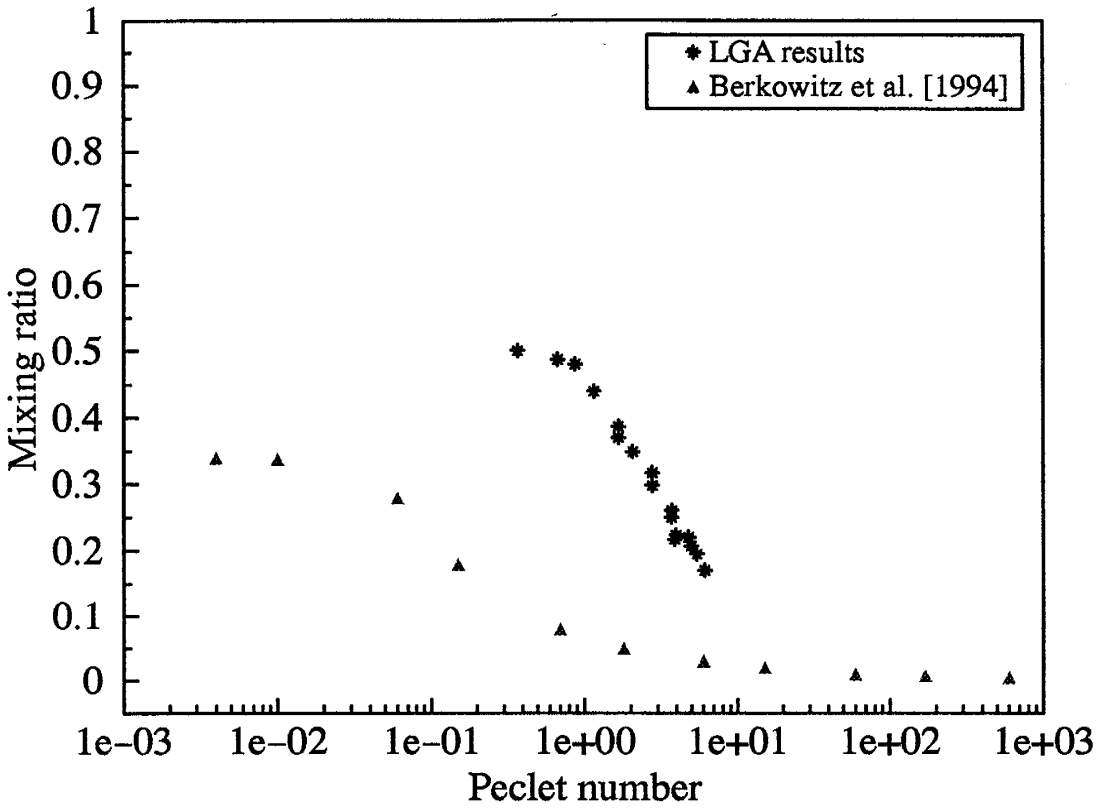

Figure 3.12. Comparision between the LGA simulation results and the numerical results of Berkowitz et al. [1994].

corresponding range of Peclet numbers. The LGA results indicate the lower limit of the transition zone is around the Peclet number of 1, while the results of Berkowitz et al. suggest a substantially lower limit of about $3x10^{-3}$. At the lower limit, the LGA simulations suggest complete mixing, M_r=0.5, but Berkowitz et al. only reach a mixing ratio of 0.34 even at the Peclet number as low as $3x10^{-3}$. They explained this less complete mixing by noting that particles entering the junction on a path line close to the left side of the wall of fracture 1 have a higher probability of moving across the dividing streamline into the left flow region than remaining inside the original flow domain. The middle line of the inflow branch does not correspond to the position where it was equally probable that particles could exit through the two outflow branches [Berkowitz et al, 1994]. Their explanation is not convincing enough to explain the less complete mixing in their numerical simulations. At their lowest Peclet number, $3x10^{-3}$, the average residence time of the particles in the junction is about 333 times

longer than the time required for the particles entering the junction from fracture 1 along the right side of the wall to diffuse across the dividing streamline. Thus, at a Peclet number well below 1, they should have been able to observe complete mixing at the junction in their numerical simulations.

The results of Berkowitz et al. [1994] suggest that the upper limit of the transition zone is around Peclet number of 1, and the transition zone has a range of about 3 orders of magnitude. The LGA results predict a transition zone of about 1 order of magnitude in the Peclet number, starting near 1 and ending around 10. When the LGA results suggest significant sensitivity of the mixing ratio to the Peclet number, the results of Berkowitz et al. predict advection controlled streamline routing. Although both models show less mixing at the junction as the Peclet number increases, the difference between them is significant (see Figure 3.12).

Efforts were also directed at simulating the numerical results of Berkowitz et al. [1994] by using the same geometry and boundary conditions as in their simulations. The LGA simulations could not reproduce the results of Berkowitz et al. [1994]. Further investigations are required to determine the cause of differences between these two numerical models.

With these two totally different numerical results on the mixing behavior around the fracture junction, a decision has to be made as to which one, if either, is correct and represents the physical process occurring at fracture junctions. To address this problem, physical experiments under the same model conditions must be carried out to test the numerical results. That is the second goal of this research and is addressed in the next chapter.

3.5. Mixing Behavior at a Fracture Junction: The Influence of Non-equalFlow Rates

In the case of equal inflow and equal outflow, solute particles that move across the dividing streamline by diffusion are carried out through fracture 3. In nature, the flow rates in each fracture are most likely different due to differences in fracture geometries and

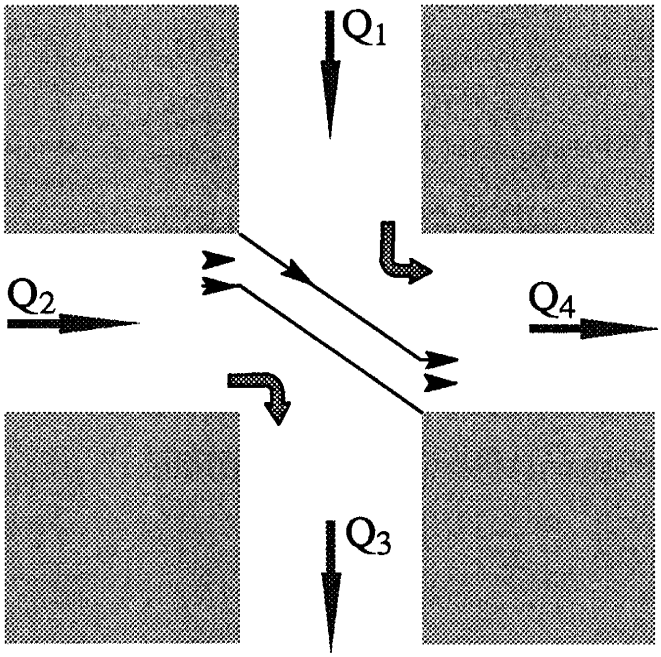

Figure 3.13. Schematic of the flow field around the fracture junction with equal inflow but non-equal outflow velocities.

hydraulic gradients. Figure 3.13 is a schematic sketch of the dividing streamlines for equal inflow but non-equal outflow in the system. Part of the water from fracture 2 crosses the junction and joins the flow from fracture 1, and then flows out through fracture 4. Thus, the outlet flow rate Q_4 is larger than Q_3. The upper dividing streamline in the figure separates the inflows while the lower one separates the outflows. Some of the solute particles that are carried into the junction through fracture 1, diffuse across the upper dividing streamline. But only a small portion of these solute particles move far enough to escape the cross flow region (the region between the two dividing streamlines in the figure), and eventually flow out through fracture 3. The particles remaining in the cross flow region are carried back into fracture 4 to join the original solute stream. Thus, the mixing process at the junction in the case of non-equal flow rates includes two parts: diffusive mixing and forced mixing due to cross flow [Robinson and Gale,1990]. It is almost impossible to separate the effects of diffusive mixing from forced mixing, so in the remainder of this chapter, unless specified, the term "mixing" includes both diffusive mixing and forced mixing. The influence of

non-equal outlet flow rates on mixing depends on the difference in magnitude between the outlet flow rates Q_3 and Q_4. The mixing behavior at the junction is still characterized by the Peclet number. The mean fracture velocity is used in equation (1.1) to calculate the Peclet number. Several numerical simulations were performed to investigate the influence of non-equal flow rates on mixing behavior.

3.5.1 Equal Inflow but Non-equal Outflow Rates

Based on their experimental results on mixing behavior at an idealized fracture junction, Hull and Koslow [1986] suggested that streamline routing be used to describe mixing process at the fracture junction. Using mass balance and ignoring diffusion, they developed a simple formula for predicting the concentrations in each outlet fracture. This forced mixing formula is also called proportional routing because the predicted concentrations in the outlet fractures are proportional to the magnitude of the flow rates. For equal inflow but non-equal outflow rates, with $Q_1=Q_2$ and $Q_4 \geq Q_1$, the formula predicts

$$C_4 = C_1 \cdot \frac{Q_1}{Q_4} + C_2 \cdot (1 - \frac{Q_1}{Q_4})$$
$$C_3 = C_2 \qquad (3.6)$$

Since $C_2=0$, we get $C_3=0$. Thus, the equal flow rate mixing ratio, defined as C_3/C_1, is 0, implying no mixing at the junction; but this definition can not reflect the influence of non-equal flow rate on mixing behavior at the junction. Due to non-equal outlet flow rates, there is forced mixing in fracture 4. In order to provide a better description of the mixing process at the junction, we introduce a mixing ratio for fracture 4. It is defined as the ratio C_4/C_1. In this case, the mixing ratio in fracture 3 is 0, which indicates that there is no mixing (diffusive/forced) while the mixing ratio in fracture 4 is Q_1/Q_4, larger than 0, indicating mixing occurs at fracture 4.

A numerical simulation of this situation was run with a mean fluid particle density of n=2.86 and an average inflow velocities in fractures 1 and 2 of 0.130 lu/sts. The velocity

profile through the junction is plotted in Figure 3.14, showing significant cross flow. With 26% of the fluid from fracture 2 joins the flow from fracture 1 and moves into fracture 4, the average outlet flow velocities in fractures 3 and 4 were 0.096 lu/sts and 0.170 lu/sts, respectively. The flow had a mass balance error of 2.3%. To simulate the mixing process at the junction, one tracer particle was injected at the inflow boundary of fracture 1 at each time step. The tracer particles had a diffusion coefficient of 0.545 lu^2/sts. The Peclet number at the junction was 5.99. System equilibrium was established after 20,000 sts with an average of 1,320 tracer particles in the field. From 30,000 to 60,000 sts, a total of 30,000 tracer particles were injected. The total number of particles moving out through fractures 3 and 4 during the same period are 1,499 and 28,486, respectively, with a relative mass balance error

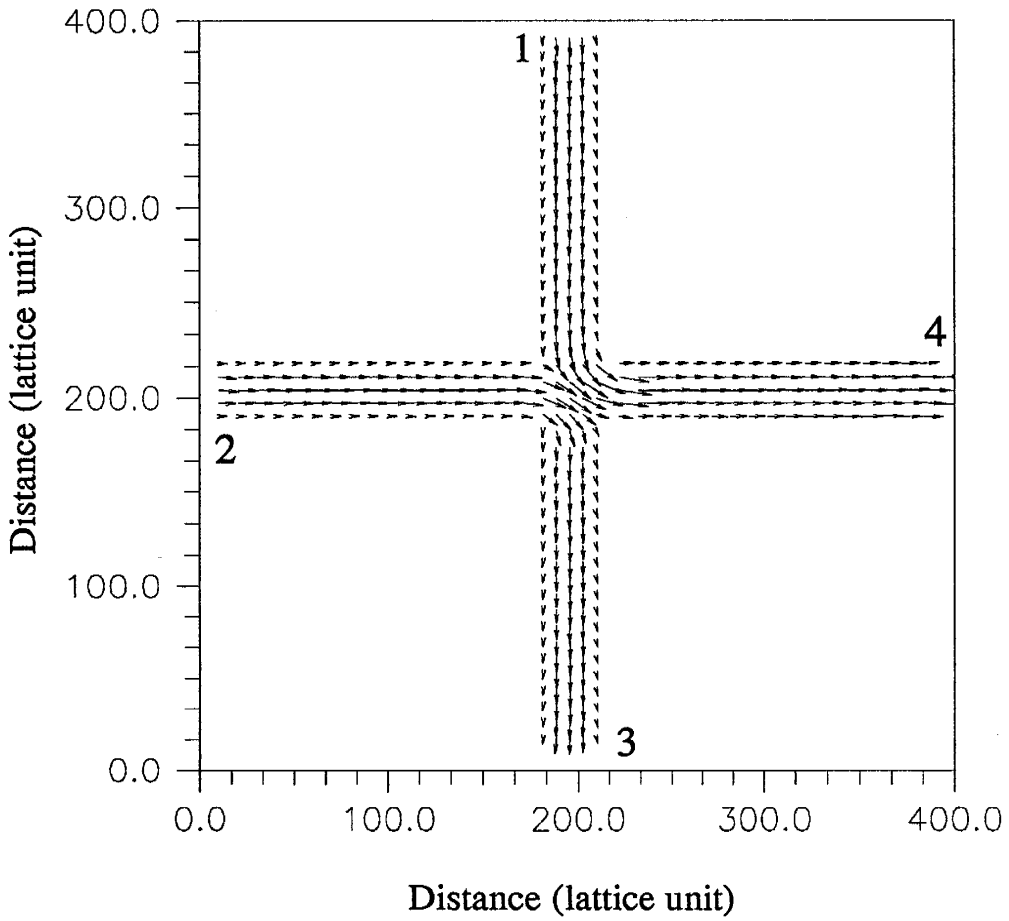

Figure 3.14. Velocity profile for moderate cross-flow with non-equal outflow but equal inflow at the fracture junction.

of 0.05%. The superposed spatial distribution of tracer particles in the field from snap shots at 40,000, 50,000 and 60,000 sts is plotted in Figure 3.15. Clearly, there is diffusive mixing at the junction. Using equation (3.5) to estimate the mixing ratio at the junction gives a mixing ratio of 0.05 for fracture 3. However, this mixing ratio does not properly represent the real mixing level at the junction because it neglects the influence of non-equal outflow rates on the mixing process. The mixing ratio for the case of non-equal flow rates can not be directly estimated from equation (3.5) by using only the number of particles flowing out of the system. It must account for the influence of different flow rates. The concentration in each fracture is

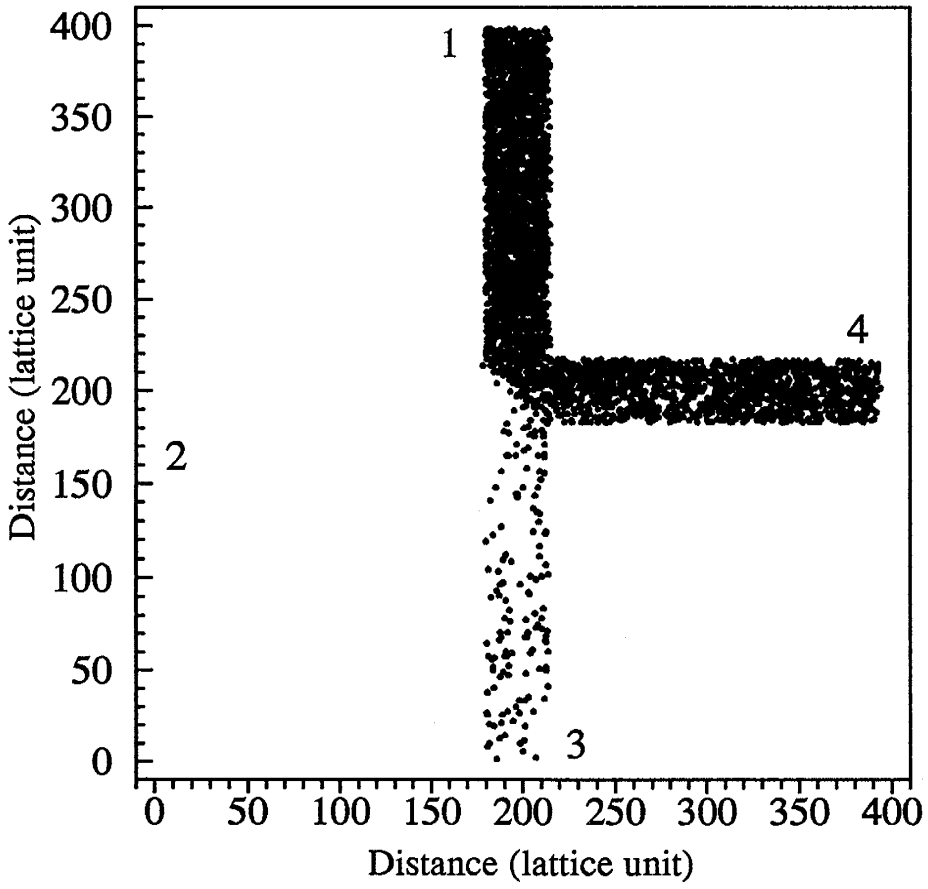

Figure 3.15. Superposed tracer particles for moderate cross-flow (2 to 4) and median Peclet number from snap shots at 40,000, 50,000 and 60,000 simulation time steps for n=2.86, P_e=5.99, M_{r3}=0.07, and M_{r4}=0.73. The corresponding flow field is shown in Figure 3.14.

$$C_i = \frac{N_i}{\overline{V}_i \cdot t \cdot b_i} \tag{3.7}$$

where N_i is the number of particles which flow out of the outlet fracture i during time period t, $\overline{V}_i$ is the average flow velocity in fracture i, and b_i is the width of the corresponding outlet fracture. Substituting equation (3.7) into equation (3.4), the mixing ratio for fracture i now becomes

$$M_{ri} = \frac{N_i \cdot \overline{V}_1 \cdot b_1}{N_1 \cdot \overline{V}_i \cdot b_i} \tag{3.8}$$

The calculated mixing ratio for fracture 3 is M_{r3}=0.07, and for fracture 4 is M_{r4}=0.73, further indicating diffusive mixing at the fracture junction. The proportional routing of Hull and Koslow predicts mixing ratios of M_{r3}=0 and M_{r4}=0.76.

The predicted lower mixing ratio for fracture 3 and higher mixing ration for fracture 4 are the result of diffusive mixing at the junction. Under the influence of diffusion, some of the tracer particles that diffused across the upper dividing streamline moved far enough to escape from the cross flow region into the flow discharging into fracture 3. This process increased the concentration in fracture 3, while it decreased the concentration in fracture 4. The mixing ratios for the corresponding equal flow rate case are about 0.19 and 0.81 (extrapolated from Figure 3.11) for fracture 3 and 4, respectively. Compare the spatial distribution of tracer particles in Figure 3.15 to a similar equal flow rate case in Figure 3.6 (Peclet number of 6.10 and mixing ratio 0.17). The influence of diffusive mixing at the junction is greatly reduced by the cross flow.

A second phenomenon shown in Figure 3.15 relates to both diffusion and cross flow. In the absence of diffusion, we would expect to find no tracer in the lower part of fracture 4, which should be occupied by cross flow from fracture 2. Instead, we see tracer particles. Although the density is initially somewhat lower than that at the upper corner of the entrance, further downstream they fully mix across the fracture 4 under the influence of diffusion.

A second simulation was run with a relatively low Peclet number of 1.42 and more cross flow, with a mean fluid particle density of n=1.66. The inlet flow rates were 0.042lu/sts in fractures 1 and 2, while the outlet flow rates in fractures 3 and 4 were 0.011lu/sts and 0.072lu/sts, respectively. Only 26% of the original flow in fracture 2 discharged into fracture 3; the other 74% crossed the junction flowed into fracture fracture 4. One tracer particle was injected in every ten simulation time steps at the inflow boundary of fracture 1 to prevent the build up of tracer particles in the field. The tracer particles had a diffusion coefficient of $0.74lu^2/sts$. The simulation was run for a total of 80,000 simulation time steps. Equilibrium was established after 30,000 steps. The spatial distribution of the tracer particles in the field is plotted in Figure 3.16 by superposing snap shots of tracer particles in the field at 60,000,

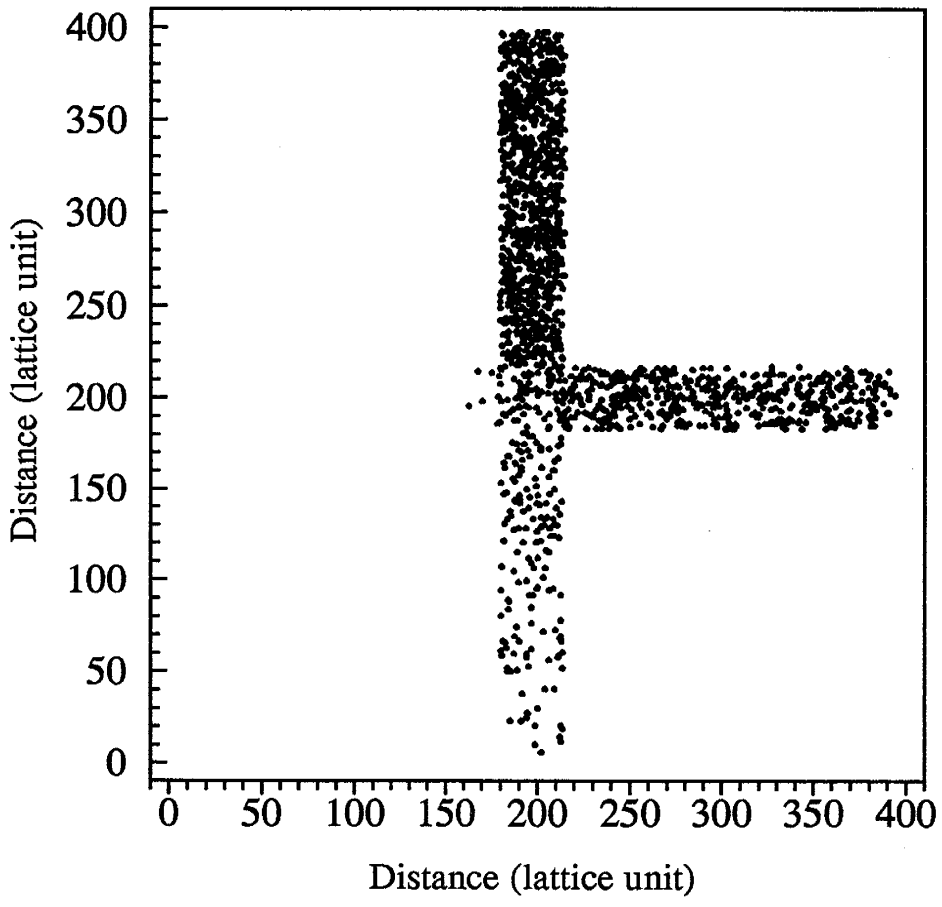

Figure 3.16. Superposed tracer particles for high cross-flow (2 to 4) and low Peclet number from snap shots at 60,000, 70,000, and 80,000 simulation time steps for n=1.66, P_e=1.42, M_{r3}=0.34, and M_{r4}=0.53.

70,000, and 80,000 sts. A total of 3,000 tracer particles were injected during this period. With 270 tracer particles leaving through fracture 3, and 2,734 leaving through fracture 4, the total number of particles which left the field was 3,004 during the same period, indicating a mass balance error of 0.13%. From equation (3.8), we have mixing ratios M_{r3}=0.34 and M_{r4}=0.53. The mixing ratios predicted by the proportional routing of Hull and Koslow [1986] are M_{r3}=0 and M_{r4}=0.58. The large difference for fracture 3 is caused by the presence of greater diffusive mixing at the junction due to this relatively low Peclet number. The mixing ratios for the corresponding equal flow rate case are roughly 0.39 and 0.61 for fracture 3 and 4, respectively. Compared with this case, although the mixing ratios are similar, the actual number of tracer particles that were carried by the flow in each outlet fracture differs significantly due to the difference in flow rates.

These two examples illustrate that even with cross flow at the fracture junction, diffusion can play an important role in the mixing process, depending on the Peclet number at the junction and the magnitude of the difference in outlet flow rates. The diffusive mixing process is more sensitive to the difference in outlet flow rates at middle range of Peclet numbers than at low Peclet numbers. In our case, at the Peclet number 5.99, with only 26% cross flow in fracture 4, the diffusive mixing ratio for fracture 3 decreases from 0.19 to 0.067, while at the low Peclet number of 1.42, with much more (74%) cross flow, the mixing ratio for fracture 3 decreased only slightly from 0.39 to 0.34. In both cases, proportional routing predicted concentrations for fracture 4 that were close to the simulated results but failed in fracture 3. Using proportional streamline routing at low to middle Peclet numbers could result in large errors for the predicted concentrations in the outlet fracture without cross flow.

3.5.2 Non-equal Inflow Rates but Equal Outflow Rates

The mixing process of non-equal inflow but equal outflow has a similar behavior as the equal inflow but non-equal outflow cases. As an example, Figure 3.17 shows the velocity profile around a junction with a mean fluid particle density of n=2.60. The average flow

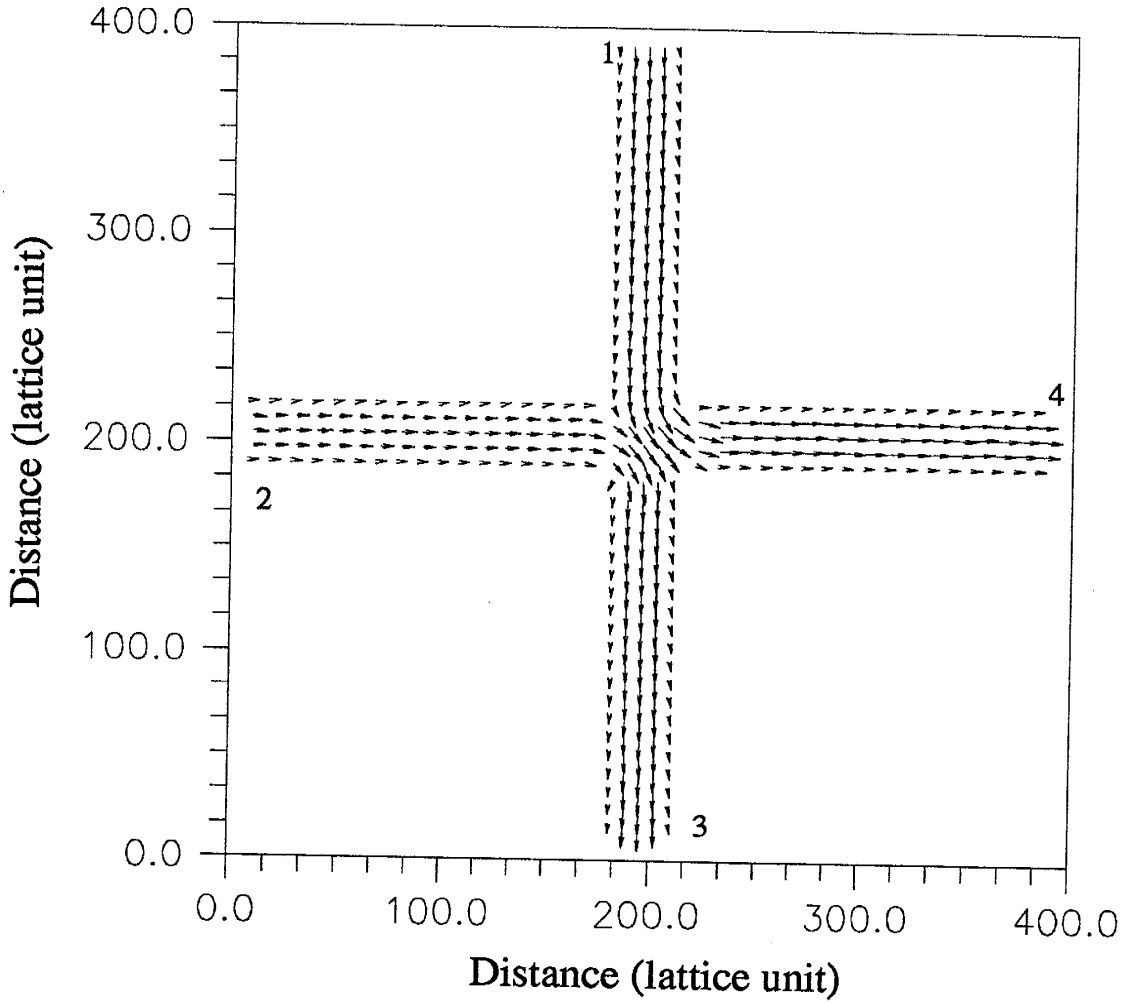

Figure 3.17. Velocity profile for the non–equal inflow but equal outflow case with moderate cross–flow from fracture 1 to 3.

velocities in the inflow fractures 1 and 2 were 0.14lu/sts and 0.076lu/sts, respectively. The cross flow was from fracture 1 to fracture 3, with 21% of the fluid from fracture 1 joining the fluid from fracture 2, then moving out through fracture 3. The remaining 79% of the fluid in fracture 1 moved out through fracture 4. The average outlet flow velocities in fracture 3 and 4 were 0.11lu/sts.

The proportional routing developed by Hull and Koslow [1986] for predicting tracer concentrations in the outlet fractures with $Q_4 \leq Q_1$ now is

$$C_3 = C_2 \cdot \frac{Q_2}{Q_3} + C_1 \cdot (1-\frac{Q_2}{Q_3})$$

$$C_4 = C_1 \qquad (3.9)$$

Since C_2=0, the forced mixing ratios are $M_{r3}=C_3/C_1=(1-Q_2/Q_3)$ and $M_{r4}=1$.

The LGA simulation was run to test the formula for a Peclet number of 4.84. At each simulation time step only one tracer particle was injected at the entrance of the inflow fracture 1. The tracer particles had a diffusion coefficient of 0.5711u^2/sts. From simulation time steps 30,000 to 60,000, a total of 30,000 tracer particles were injected at the top boundary of fracture 1. Of these injected tracer particles, 20,514 of the them left through fracture 4, and 9,490 left through fracture 3. The total number of particles leaving the system was 30,004, suggesting a mass balance error of 0.013%. Figure 3.18 shows the superposed spatial distribution of tracer particles in the field from snap shots at 40,000, 50,000, and 60,000 simulation time steps. The mixing ratio calculated from equation (3.8) is 0.39 for fracture 3, and 0.88 for fracture 4. Using the proportional streamline routing proposed by Hull and Koslow [1986], we have mixing ratios of 0.31 and 1 for fractures 3 and 4, respectively. The difference between the numerical simulation results and that predicted by proportional routing is caused by diffusive mixing; the concentration in fracture 4 is lower and the concentration in fracture 3 is higher. Comparing the distribution of tracer particles in Figure 3.18 to the velocity field in Figure 3.17, it is clear that mixing occurred along the boundary of the cross flow region. Figure 3.18 also shows the diffusion homogenized concentration profile further downstream in fracture 3.

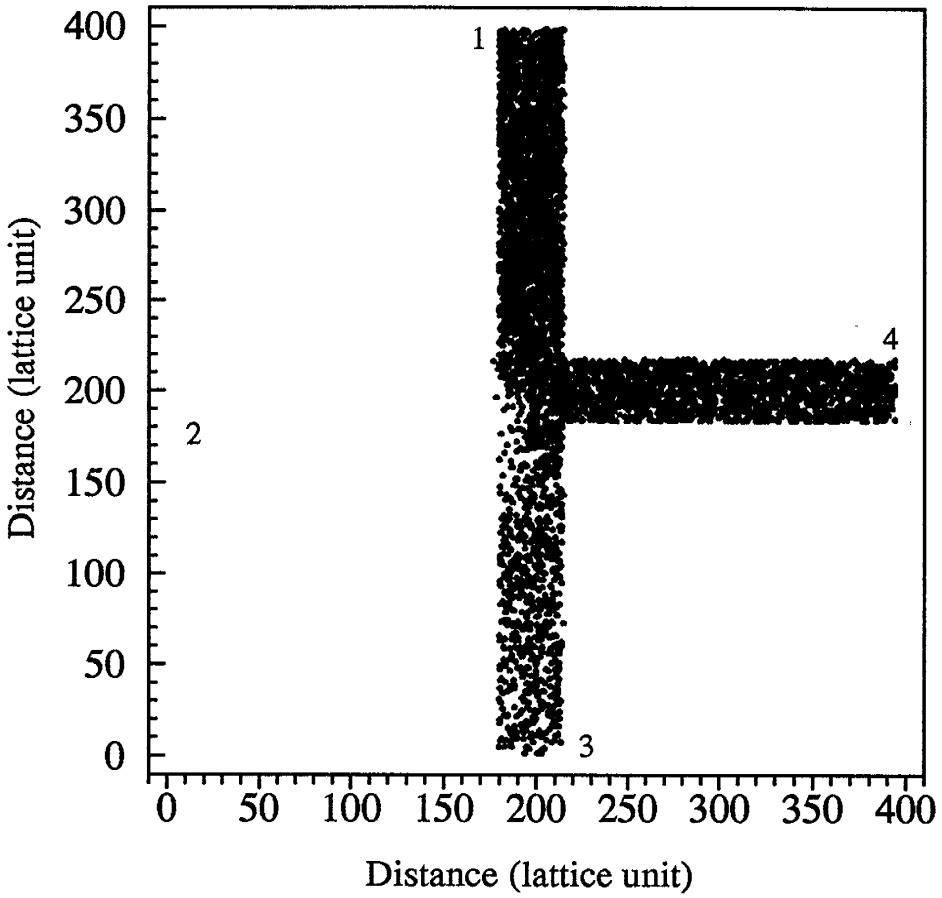

Figure 3.18. Superposed spatial distributions of tracer particles in the field under non-equal inflow rates, moderate cross-flow (1 to 3), and medium Peclet number from snap shots at 40,000, 50,000, and 60,000 simulation time steps for n=2.60, P_e=4.84, M_{r3}=0.39, and M_{r4}=0.88. The velocity profile is shown in Figure 3.17.

3.5.3 Non-equal Flow Rates in all Fractures

Around a natural fracture junction, flow rates are usually not equal in the fractures. Figure 3.19 shows the flow field at an example fracture junction with non-equal flow rates and a mean fluid particle density of n=2.13. The average velocities in the system were 0.082lu/sts in fracture 1, 0.041lu/sts in fracture 2, 0.034lu/sts in fracture 3, and 0.089lu/sts in fracture 4. Most of the flow entered in fracture 1 and departed via fracture 4. 17% of the fluid from fracture 2 crossed the junction into fracture 4, accounting for only 7% of the total flow in that fracture. At each simulation step, one tracer particle was injected at the inflow boundary of fracture 1. The tracer particles had a diffusion coefficient of 0.63lu^2/sts, leading to a Peclet

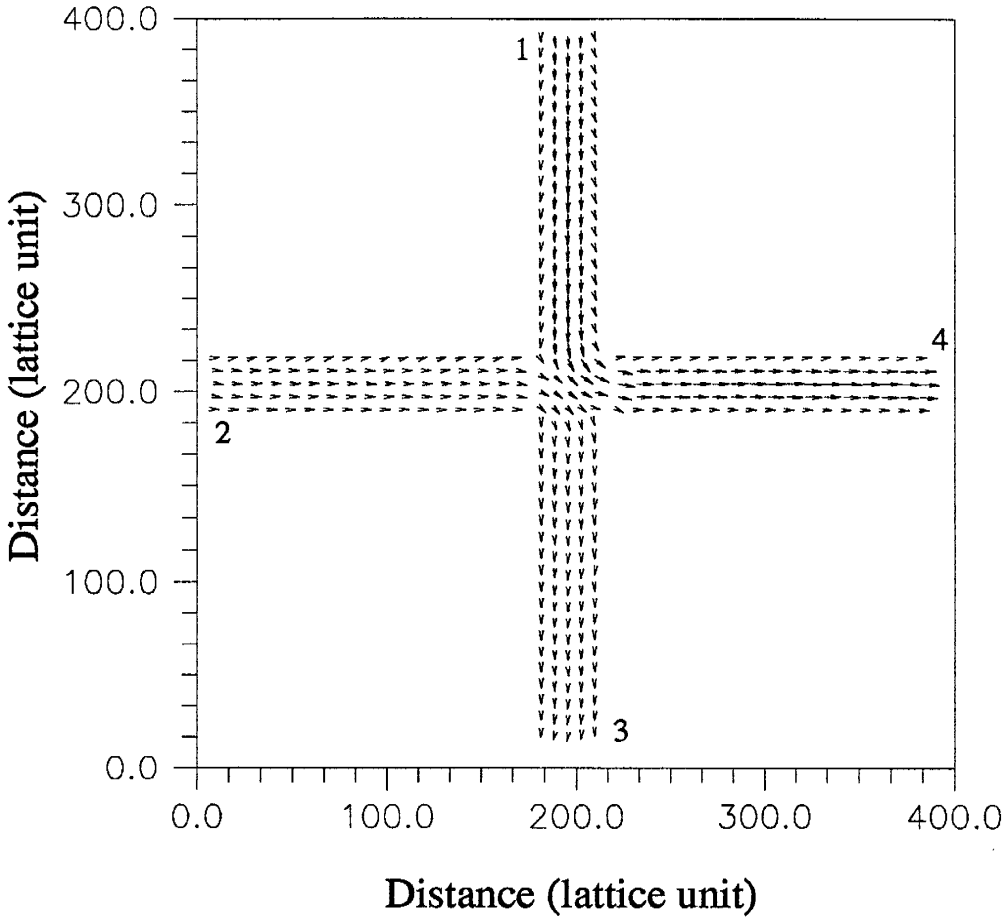

Figure 3.19. Velocity profile at the fracture junction with non-equal flow rates. Most of the flow moves from fracture 1 to fracture 4.

number of 2.43 at the junction. The superposed spatial distribution of tracer particles in the field from snap shots at 50,000 and 60,000 simulation time steps is shown in Figure 3.20. From 40,000 to 60,000 sts, a total of 20,000 tracer particles were injected into the field. With 16,208 of them moving out through fracture 4 and 3,789 moving out through fracture 3, the mass balance error of the tracer particles was 0.015%. At equilibrium, on average there were 2,990 tracer particles in the field.

The mixing ratios calculated from equation (3.8) are M_{r3}=0.46 and M_{r4}=0.75, while the $Q_4 \geq Q_1$ proportional routing in equation (3.6) would yield equivalent mixing ratios of 0 and 0.92, respectively. Note, the high mixing ratio M_{r3}=0.46 arises from the effect of the uneven flow in the system; in the even flow case we would only have M_{r3}=0.31 (see Figure 3.11).

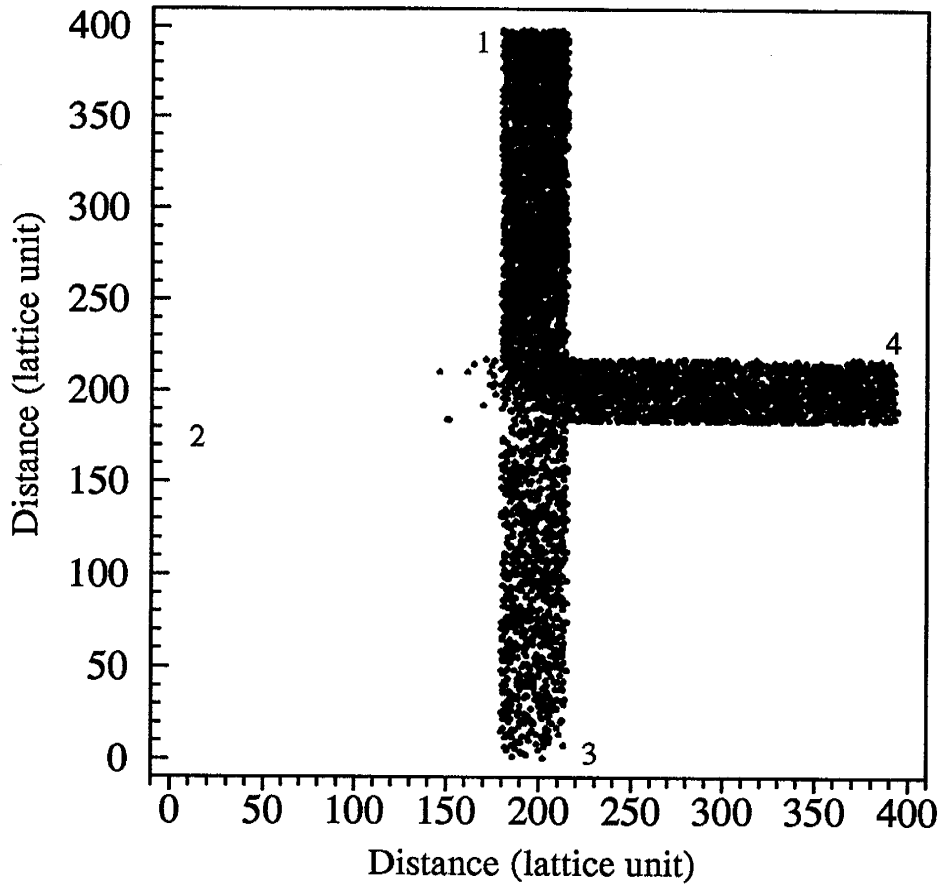

Figure 3.20. Superposed tracer particles in the field for non-equal flows and a moderate to low Peclet number from snap shots at 50,000 and 60,000 simulation time steps for n=2.13, D=0.63 lu^2/sts, M_{r3}=0.46, and M_{r4}=0.75. The velocity profile is shown in Figure 3.19.

Since the cross flow only accounted for 7% of the flow in fracture 4, the width of the cross flow region is small. Many of the tracer particles that diffused across the dividing streamline could escape from the cross flow region into the low velocity zone formed by the flow moving from fracture 2 to fracture 3. The tracer particles in the flow region of fracture 3 were not advected away quickly because of the low flow velocity; during the same time, tracer particles continuously moved in under the influence of diffusion. As a result, the concentration of tracer particles in fracture 3 built up, causing a relatively high concentration in fracture 3. As illustrated by these numbers and Figure 3.20, diffusive mixing is amplified by the low flow rate in fracture 3.

The spatial distribution of tracer particles in Figure 3.20 also clearly show diffusive mixing along the dividing streamline. As the lower left corner of the junction is far away from the dividing streamline, the density of tracer particles around this corner of the junction is relatively low.

3.5.4 Summary

These examples illustrate that non-equal flow rates (inflow/outflow or both) can have a significant influence on mixing (diffusive/forced mixing) behavior at fracture junctions. For junctions with low Peclet numbers, diffusive mixing plays a more important role than forced mixing, thus the mixing ratios are less sensitive to the non-equal flow rates. However, at middle Peclet numbers, diffusive mixing combining with forced mixing complicates the mixing mechanism at the junction, particularly for the lower flow rate outlet fractures. The proportional routing proposed by Hull and Koslow [1986] for predicting concentrations in each outlet fracture only works for junctions with very high Peclet numbers. When the Peclet numbers are low or in the middle range, using proportional routing can cause large errors in predicted concentrations.

3.6 Conclusions and Discussion

In general, the LGA results support our hypothesis that there is a continuous mixing rule starting somewhere near a Peclet number of 1. The following conclusions can be drawn:

(1) For Peclet numbers smaller than 1, the transport process at the junction is diffusion controlled, and the complete mixing rule is appropriate. The prediction made by Hull et al. [1987] about complete mixing occurs at Peclet numbers smaller than $\sqrt{2}$ is reasonably good. In the Peclet number range of 1 to some value above 10, both advection and diffusion play important roles in the mixing process. This Peclet number range we call the transition zone. Although we were not able to simulate the mixing behavior at Peclet number larger than 10, we expect that advection will eventually dominate the transport process, and thus streamline routing will be the right choice for describing the mixing behavior.

(2) The streamline routing suggested by Hull and Koslow [1986] and Robinson and Gale [1990] based on experimental results at Peclet numbers larger than 200 (Hull and Koslow) and 3,000 (Robinson and Gale) can not be generalized to represent mixing behavior at low Peclet numbers (P_e less than 10).

(3) A comparison between the LGA simulations and the numerical results of Berkowitz et al. [1994] shows significant disagreement about the range of Peclet numbers that correspond to complete mixing and to the transition zone. Physical experiments should be carried out to test these two numerical models.

(4) The mixing process at a fracture junction with non-equal flow rates is sensitive to the magnitude of the non-equal flow rates at middle Peclet numbers but less sensitive at low Peclet numbers. The effect of diffusive mixing is amplified in the low flow rate outflow fractures.

(5) The proportional routing proposed by Hull and Koslow [1986] for predicting forced mixing concentrations in outflow fractures is adequate only at high Peclet numbers. When the junction Peclet number is in the lower range (less than 5), diffusive mixing at the junction plays an important role. The error of the proportional routing can be quite large.

Berkowitz et al. [1994] generated a 2-D (x-y) discrete fracture network using a stochastic approach. A uniform hydraulic gradient was applied to the field in the x-direction, and Peclet numbers were calculated using the average flow velocity at each fracture junction. The Peclet numbers varied from 10^{-6} to 1, spanning 6 orders of magnitude. The distribution of Peclet numbers showed a log-normal pattern with a mean of -2. Under this condition, the LGA results suggest a complete mixing rule could be used at all fracture junctions when simulating solute transport in the discrete fracture network, while the results of Berkowitz et al. [1994] suggest that transition zone mixing should be used even at Peclet numbers smaller than 10^{-2}. Previous numerical simulations have shown that when different mixing rules are applied in discrete fracture networks, they result in different spatial distributions

of the solute [Hull et al, 1987; Robinson and Gale, 1990]. We can expect that applications of these two different mixing rules to solute transport in discrete fracture networks will generate different estimations of the strength of the solute.

The question still remains as to which mixing rule, if either, is correct and represents the physical process occurring at fracture junctions. To answer this question, physical experiments under the same model conditions must be carried out to test the numerical results. That is the second goal of this research and is addressed in the next chapter.

References

Berkowitz, B., C. Naumann, and L. Smith, Mass transfer at fracture intersections: An evaluation of mixing models, *Water Resour. Res.*, 30(6), 1765–1773, 1994.

Frish, U., Hasslacher,B., and Pomeau, Y., Lattice-gas automata for the Navier-Stokes equation, *Phys. Rev. Ltrs.*, 56, 1505–1508, 1986.

Hull, L.C. and K.N. Koslow, Streamline routing through fracture junctions, *Water Resour. Res.*, 22(12), 1731–1734, 1986.

Hull, L.C., J.D. Miller and T.M. Clemo, Laboratory and simulation studies of solute transport in fracture networks, *Water Resour. Res.*, 23(8), 1505–1513, 1987.

Philip, J.R., The fluid mechanics of fracture and other junctions, *Water Resour. Res.*, 24(2), 239–246, 1988.

Robinson, J.W., and J.E. Gale, A laboratory and numerical investigation of solute transport in discontinuous fracture systems, *Groundwater*, 28(1), 25–36, 1990.

Chapter 4: Physical Experiments on Mixing Behavior at the Fracture Junction

4.1 Introduction

As presented in Chapter 3, the LGA (Lattice Gas Automata) simulations of mixing behavior at an idealized fracture junction support our hypothesis that there is a transition zone between diffusion controlled complete mixing and advection controlled streamline routing (refer to Chapter 3). Contrary to the earlier numerical results of Berkowitz et al. [1994], the LGA simulations suggest that the transition zone corresponds to Peclet numbers larger than 1, which is consistent with our hypothesis and that of Hull et al. [1987]. When the Peclet number is less than 1, diffusion dominates the mixing process, and complete mixing occurs at the junction. Berkowitz et al. [1994] did not observe complete mixing in their simulations even at the Peclet number as low as $3x10^{-3}$. Thus, they concluded that complete mixing at a fracture junction did not properly represent the transport process at any value of the Peclet number.

With two sets of contradicting numerical simulation results on mixing behavior at fracture junctions, the question has arisen as to which, if either, is correct and under what conditions? All previous physical experiments were performed at very high Peclet numbers, in the range of 200–10,000 (refer to Chapter 1). Yet, no physical experiment has ever been carried out on mixing behavior in the low to middle range of Peclet numbers (1–200). The physical experiments in this research focus on this range, using an idealized junction model under equal inflow and outflow rate conditions. The objectives of the physical experiments are (1) to determine the mixing rule and its corresponding Peclet numbers; (2) to test the LGA results, the numerical results of Berkowitz et al. [1994], and our hypothesis (refer to §3.1); and (3) to provide additional background information on the mixing process at fracture junctions.

4.2 The physical Fracture Junction Model

To test the numerical results and the hypothesis, we used a physical model with two orthogonal channels of uniform width (aperture) b, and depth d (see Figure 4.1). The depth d was sufficient ($d>>6b$) to ensure Stokes flow in the channels. Even flow rate Q entered the model from channels 1 and 2, and left through channels 3 and 4, as shown in Figure 4.1. The channel length L leading into and out of the junction was sufficient to ensure fully developed flow in each fracture, thus minimizing effects of boundary conditions at the end of each channel. Subsequently, we refer to the channels as fractures.

Under equal inflow and outflow conditions, only diffusive mixing can occur at the junction. To detect such mixing behavior, two different tracers, A and B, with concentrations C_{A1} and C_{B2} were introduced into fractures 1 and 2, respectively. The magnitude of mixing was monitored by measuring tracer concentrations in both outflow fractures as they left the model. Four measurements were available: concentrations of tracer A, C_{3A} and C_{4A}, in fractures 3 and 4, respectively; and concentrations of tracer B, C_{3B} and C_{4B}, in fractures 3 and 4, respectively. From these data, the mass balance of each tracer was checked and four mixing ratios were estimated. Theoretically, under equal inflow and outflow conditions, if

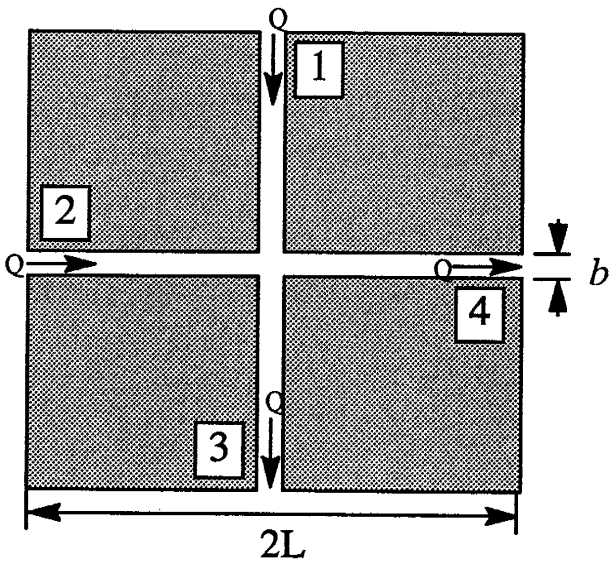

Figure 4.1 Schematic of the physical fracture junction model (not to scale).

mass is conserved and the measurement error is negligible, we would expect that

$$M_{rA} = \frac{C_{3A}}{C_{1A}} = 1 - \frac{C_{4A}}{C_{1A}}, \qquad M_{rB} = \frac{C_{4B}}{C_{2B}} = 1 - \frac{C_{3B}}{C_{2B}} \tag{4.1}$$

The mixing ratios combined with the Peclet numbers described the mixing behavior at the junction.

The physical model was designed to obtain Peclet numbers in the range of 1 to 200, by carefully selecting a carrier fluid (gas or liquid), a fracture aperture b, and a fracture depth d. At the fracture junction, with a discharge Q [L^3/T] in each fracture, the Peclet number is defined as

$$P_e = \frac{\overline{V} \cdot b \cdot \frac{\sqrt{2}}{2}}{D} = \frac{Q \cdot \frac{\sqrt{2}}{2}}{dD} \tag{4.2}$$

where $(\sqrt{2}/2)b$ [L] is the half diagonal length of the fracture junction (it also equals the width of the flow region from fracture 1 to fracture 4 at the junction), $\overline{V}$ is the mean fracture velocity [L/T], and D [L^2/T] is the solute molecular diffusion coefficient. From equation (4.2), for a physical model, we can only change flow rate Q, fracture depth d, and diffusion coefficient D to achieve different Peclet numbers.

One concern that relates to the flow rate in a physical model was ensuring laminar flow in the fracture. The flow conditions in a system can be expressed in terms of the Reynolds number, which in a fracture is defined as

$$R_e = \frac{\overline{V} \cdot b}{\nu} = \frac{Q}{d\nu} = \frac{\sqrt{2} D \cdot P_e}{\nu} \tag{4.3}$$

where ν is the fluid kinematic viscosity. For flow between two parallel plates, the upper limit of laminar flow corresponds to a Reynolds number of 2,000. In equation (4.3), for a gas $D/\nu = O(10^0)$ while for a liquid $D/\nu = O(10^{-3})$, indicating that in the range of $1 \leq P_e \leq 200$, the Reynolds number for water (our typical liquid) is clearly in the laminar flow range (eg, $P_e < 1{,}000$, $R_e < 1.4 \ll 2{,}000$). For a gas, R_e and P_e are roughly equal; and the Reynolds numbers are also in the laminar range. Therefore, for Peclet numbers in the desired range,

the flow will be laminar for a liquid or a gas. We chose to perform the experiment with water because it is the fluid of interest in nature, and it is the same fluid used by previous researchers.

Another consideration in the model design was the time required for establishing equilibrium in the model. One measure of the equilibrium time is the solute diffusion time across the fracture or fracture junction, which is on the order of

$$t_d \approx \frac{b^2}{4D} \tag{4.4}$$

For a liquid with tracer diffusion coefficient on the order of 10^{-5} cm^2/sec, equation (4.4) implies a limitation on fracture aperture $b \leq \sqrt{(4Dt_d)}$. If the maximum desired diffusion time is 1 day, then the fracture aperture b must be less than 1.86 cm, a size which is obviously not a serious constraint for model construction.

A second measure of equilibrium is the time for tracer concentrations to reach equilibrium throughout the model, in particular at its outlets. Advection and Taylor diffusion are the active transport processes in the fractures leading away from the junction. If these fractures are of length L, then the time for piston displacement is $t'_f = L/\overline{V}$. Dispersion adds to this time. For example, the time t_f necessary for the concentration at the end of the fracture to reach 99.7% of its equilibrium can be estimated from Taylor–Aris dispersion theory (see §4.3.4):

$$\frac{x - \overline{V} \cdot t_f}{2\sqrt{D_l t_f}} = 2 \tag{4.5}$$

where D_l is the Taylor–Aris dispersion coefficient

$$D_l = D + \frac{\overline{V}^2 \cdot b^2}{210 \cdot D} = D\left(1 + \frac{P_e^{\,2}}{105}\right) \tag{4.6}$$

The longest displacement time of interest is when $P_e \approx 1$, for which $D_l \approx D$. In order to ensure developed flow, we also want $L \geq 5d = 5b(d/b)$, where d/b is the fracture x-section aspect ratio. Solving equation (4.5) for maximum aperture b in terms of a desired displacement time t_f, leads to

$$b \leq \{(4Dt_f)^{\frac{1}{2}} + [4Dt_f + 5\sqrt{2}DP_e t_f\, d/b]^{\frac{1}{2}}\} \frac{1}{5(d/b)}$$

For $P_e \geq 1$ and $d \gg b$, we have

$$b \leq [\frac{\sqrt{2}D\ P_e\ t_f}{5(d/b)}]^{\frac{1}{2}}$$

For example, using a displacement time of 1 day and a typical tracer ($D \approx 10^{-5}$ cm^2/sec) requires that the maximum aperture $b \leq [4.4/\sqrt{(d/b)}]$ mm; for example, if d/b=16, then $b \leq$ 1.11 mm. Considering the equilibrium time and problems involved in building the model, we selected d/b=37, so that $b \leq$ 740 μm. Because in the experiments tracer concentrations were not measured directly at the junction model outlets but further downstream, the displacement time increased further, which suggested an even smaller aperture.

In designing the model, flow rate measurement problems limited the size of the fracture. The lowest flow rate occurs around a P_e=1, for which equation (4.2) gives $Q=dD\sqrt{2}$. Using water with a desired tracer requires a low flow rate around $Q=1.414d\text{x}10^{-5}$ cm^3/sec$=5.09d\text{x}10^{-2}$ cm^3/hr when the fracture depth is measured in cm. Recalling that d/b=37, the low flow rate becomes $1.88b$ cm^3/hr. From a displacement time perspective, a maximum aperture size of around 0.075 cm indicates a low flow rate of about 0.14 cm^3/hr=110 μl/hr. Thus, we have to control a low flow rate on the order of 100 μl/hr.

On the basis of the above analyses, the actual model was designed with an aperture of b=500 μm and a fracture depth of d=1.85 cm, for an aspect ratio of d/b=37. Each fracture had a length of L=10cm. Water was the carrier fluid, and dilute KBr (potassium bromide) and KCl (potassium chloride) were selected as the tracers for inflow fractures 1 and 2, respectively. The diffusion coefficient for a KBr solution is around $D=1.87\text{x}10^{-5}$ cm^2/sec at 25°C [Weast et al., 1987], while for KCl it is around $D=1.917\text{x}10^{-5}$ cm^2/sec at 25°C [Weast et al., 1987]. The KBr solution strength was $C_{kBr}=1.01\text{x}10^{-3}$ mol/l=120 mg/l, and the KCl solution had a strength of $C_{KCl}=1.61\text{x}10^{-3}$ mol/l=120mg/l. For these concentrations, the water density and viscosity were not significantly affected by the

presence of the two dissolved tracers. In order to improve control, the experiments were run at only slightly elevated pressures and temperature described in §4.3.4. Under these conditions, a Peclet number in the range of 1 to 200 required that the fracture flow rates vary from 0.179 ml/hr to 35.90 ml/hr.

The fracture junction model was constructed of lucite, with two rectangular cross-section channels intersecting at right angles (see Figure 4.1.). The model was constructed by bonding 3 layers of plexiglass together, as shown in Figure 4.2. Layer-1 was a 8 mm thick 20 cm x 20 cm rigid sheet which formed the bottom of the model. Layer-2, consisting of four 10 cm x 10 cm blocks of plexiglass with a uniform thickness of 18.5 mm, formed the main body of the fracture junction. Layer-2 was glued to layer-1 with a solvent. Layer-3 was shaped like the fracture junction with a uniform thickness of 2 mm and was glued on the top

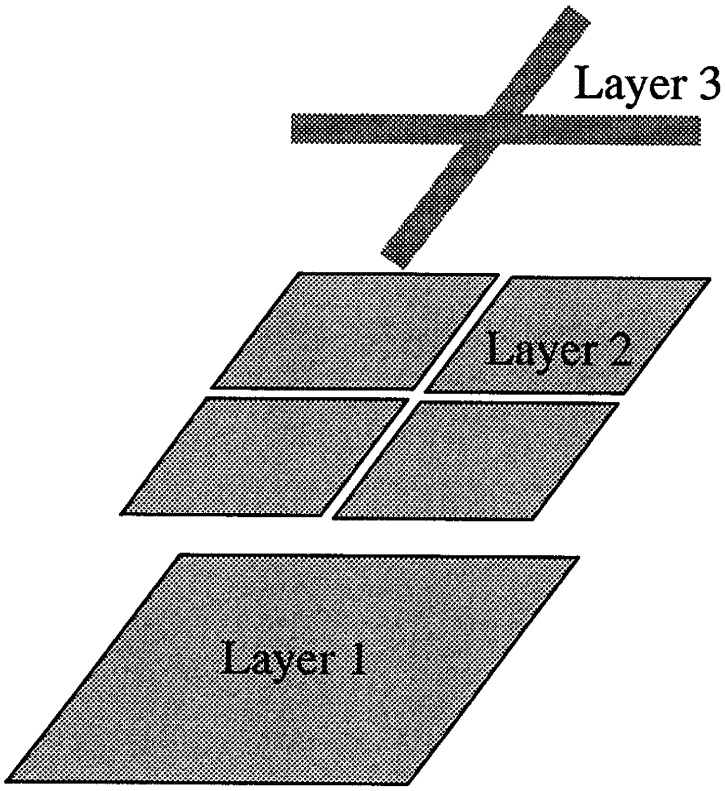

Figure 4.2 Schematic of the structure of the physical fracture junction model.

of layer 2, covering the channels. To reduce head loss between the fractures and connected flow tubes due to the sudden change in the geometry, a 1 cm long, smooth transition was fitted inside the end openings of each channel (see Appendix B, Figure B.1). Tube fittings were then attached to the ends of the four fractures to conduct water to and from the model.

4.3 Experiment set up

The model was connected to an external plumbing system designed to monitor and control the flow rates. With two inflow lines and two outflow lines, controlling and balancing the flow rates was difficult. To address this problem, positive displacement piston pumps were used to inject tracer solutions into each inflow fracture. The discharge from these pumps was independent of constant back pressure and provided positive control over the inflows. The outflow rates were controlled by metering needle valves and monitored by a flow meter. Adjusting the valve on one outflow line affected discharge in both outflow lines. Balancing flows took some time, particularly at the lowest flow rates (*Pe* around 1). Once the concentration equilibrium was established, samples were collected from the ends of the outflow tubes and analyzed for tracers by HPLC.

A schematic showing how the model was connected to the plumbing system is shown in Figure 4.3. The two positive displacement high precision piston pumps for the injecting of KBr and Kcl solutions are shown on the left. Pump flow rates were controlled by a digital pump controller. A pressure transducer was installed in the KCl inflow channel to monitor system pressure variations. The outlet flow rate in channel 4 was monitored by a flow meter which used a differential pressure transducer to measure the pressure drop along the outflow tube between two points with a known distance. Assuming Hagan–Poiseuille flow in the tube, the flow rate could be easily calculated from the theoretical formula and checked in calibration runs. Signals from the pressure transducers were sent to a current scanner, then to a picoammeter, and finally to a PC for real time data analysis. The system pressure and outlet flow rate data were plotted on the computer screen in real time for flow rate control.

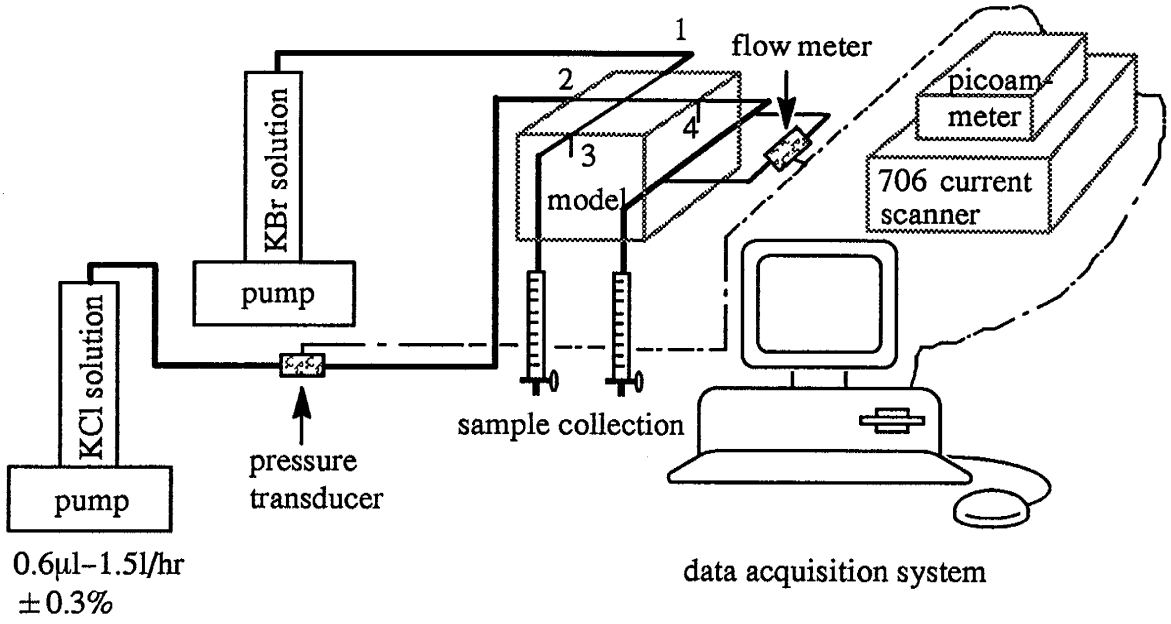

Figure 4.3. Experiment set up for flow connections and flow control.

The experiment was sensitive to temperature fluctuations, particularly at low flow rates. The primary problem was thermal expansion of the water, which could induce flow in the system. To control this problem, the physical fracture junction model was placed horizontally in a constant temperature cabinet, as illustrated in Figure 4.4. A constant temperature bath (CTB) was used to circulate water through pump jackets and the model cabinet throughout the experiment. To monitor temperature variations, temperature probes were installed in the lab, inside the cabinet, and in the water circulation tube of the pump jackets. Signals from the temperature probes were sent to a data logger and then transferred to the computer for analysis.

Essentially, the experimental system can be organized in four subsystems: tracer solution injection and inlet flow rate control; system pressure and flow rate monitoring; outlet flow rate control; sample collection and sample analysis; and temperature control. The detailed information on each of subsystems is given below.

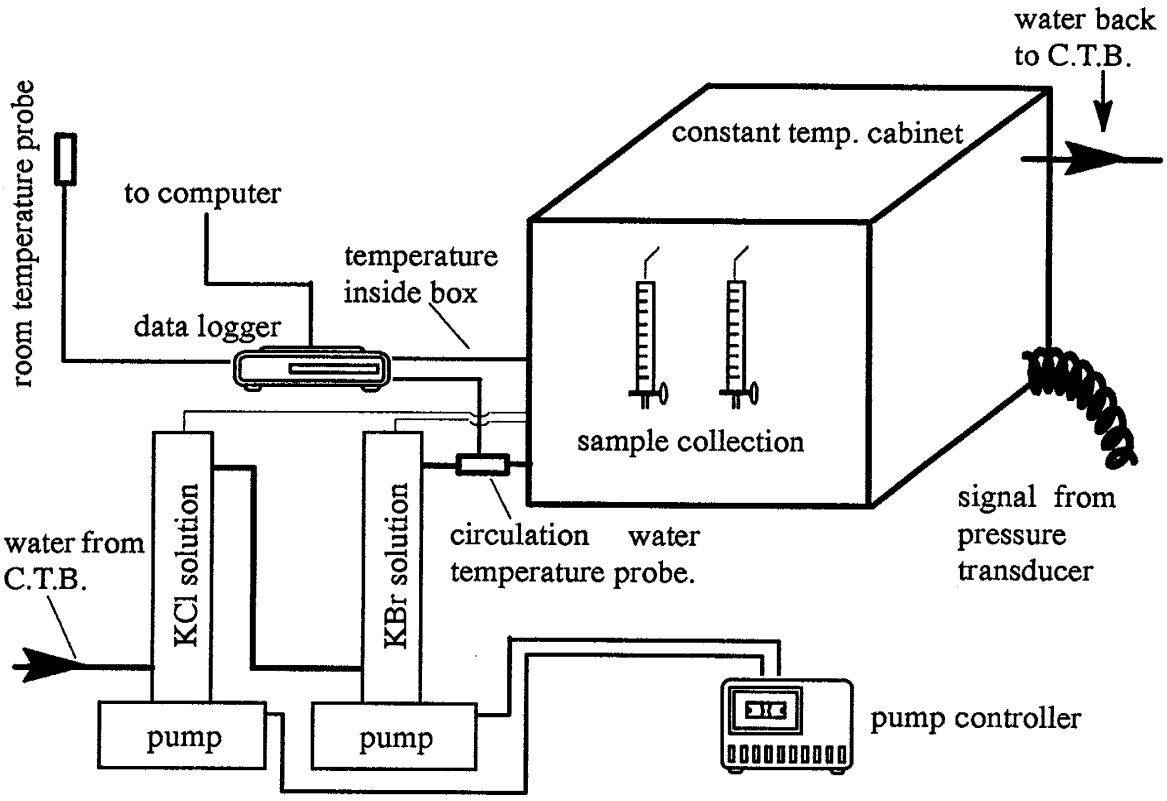

Figure 4.4. Experiment set up for instrument control and temperature control.

4.3.1 Tracer Solution Injection and Input Flow Rate Control

Two high-precision ISCO 100DM syringe pumps were used to dispense the aqueous tracer solutions, KCl and KBr, into the two inflow channels of the physical model and to control the injection flow rates. The pump cylinders were made of nitronic alloy and had a capacity of 102.93ml with a dead volume of 1.30 ± 0.020ml. The 100DM pump could be operated at either constant pressure or constant flow mode. However, in our experiments, the pumps were only operated at constant flow rate mode. The 100DM pump had a flow range from 0.6μl/h to 1500ml/h for any pressure up to 10,000 psi and a specified flow rate accuracy of $\pm 0.3\%$. Each pump had a pressure transducer at top of the cylinder to monitor the fluid pressure inside the cylinder. The pressure transducer had a range of 10 psi to 10,000 psi with a specified accuracy of $\pm 2\%$ full scale (± 200 psi). At a low pressure range, this transducer only indicated the relative pressure variation in the cylinder. The ambient

operating temperature of the pump was from 0 to 40°C. To reduce the influence of temperature variation on pump flow rates, cooling/heating jackets were installed for each pump. Water at 26°C from a constant temperature bath was circulated through the pump jackets to keep the tracer solutions inside the cylinders at a constant temperature (see §4.3.5). A Campbell 107B [Campbell Scientific, Inc., Logan, Utah] soil/water temperature probe was used to monitor the circulation water temperature from the pump jackets (see Figure 4.4). At low pump pressure and flow rate, variations in pump pressure can affect the accuracy of the pump flow rate, a problem which was overcome by installing two 100 psi back pressure regulators at the outlet of each pump. To ensure that any solids produced from wear of the pump seals would not clog the flow channels in the system, two tantium $2\ \mu m$ inline filters were connected between the pump outlets and the back pressure regulators.

An ISCO digital pump controller (no model number, specially designed for ISCO pumps) was used to control the pump flow rates. The pump controller had three ports, A, B, and C and could control up to three pumps. The power supply for the pump controller came from the pump connected to port A.

Alltech color-coded PEEK (Poly Ether Ether Ketone) tubing with 0.020" ID was used to conduct the aqueous solution into or from the model (see Figure 4.3). The PEEK tubing is chemically inert, strong (maximum pressure for 1/16" OD and 0.020" ID tubing is 6000 psig), and very flexible. Knurl-Lok™ III wrench/fingertight fittings were used to connect the PEEK tubing to the model (see Appendix B, Figure B.1). The fittings are also made of PEEK material and are chemically inert. One advantage of using PEEK tubing was preventing corrosion in the flow tubes, so that no deposit could be generated and clog flow channels in the system.

The ISCO pumps were calibrated separately by running each pump at a flow rate of 0.020 ml/hour for about 100 hours. Before the tests, each pump was filled with deaired type I water (water was deaired by boiling it for about 30 minutes, then stirring and vacuuming until no

air bubble could be seen) and was operated for a certain time until the pressure in the pump cylinders was constant (typically around 400 psi). During the tests, the CTB was used to circulate water at 26°C through the pump jacket to keep water inside at constant temperature. Water dispensed from each pump was collected in a 2.5 ml vial with a known weight. Once the tests were finished, the amount of water dispensed by each pump was estimated by subtracting the initial weight of the container from the final weight and then dividing by water density (0.997 g/ml, Weast et al., 1987). The flow rate test for the pump later used for KBr injection showed that in 99 hours and 20 minutes, a total of 1.973 ml water was dispensed, which corresponds to a flow rate of 0.0199 ml/hour and a relative error of 0.5%. The test result of the other pump, used later for KCl injection, showed that a total of 1.993ml of water was dispensed in 99 hours and 35 minutes, which corresponds to a pump flow rate of 0.0200ml/hour. These two tests indicated that the ISCO pumps were indeed accurate. Before a series (group) of experiments, the two pumps were also tested at the desired flow rates. All the tests showed that the pumps were accurate.

During the pump flow rate tests, a known amount of mineral oil (Aldrich mineral oil, density 0.838g/ml) was used in the sample vial to prevent the evaporation of water. Since there was no physical data available on the evaporation rate of the oil, a lab test was conducted to determine the evaporation rate. A 2.5 ml HPLC auto sampler vial with 10 mm ID was filled with water and 1 ml of the mineral oil. The sample was weighed on a Mettler AT400 analytical scale with an accuracy of 0.1mg. Before the test, the sample weighed 3.8214g. It was placed close to the model cabinet with the vial open to the air. The test began at 10:00 pm Dec. 27, 1994 and ended at 3:00 pm Jan. 13, 1995. The final weight of the sample was 3.8204g. In a total of 401 hours, the loss of mineral oil due to evaporation was only 0.0010g which corresponds to a volume of 1.2 μl. The evaporation rate of the mineral oil proved to be extremely low and was, therefore, ignored in the calculations.

4.3.2 System Pressure and Outlet Flow Rate Monitoring

Since the model inflow rates could be accurately controlled by the two ISCO 100DM pumps, the primary problem in the experiments was to monitor and control the outlet flow rates. System pressure and outlet flow rate monitoring offered key information for flow rate control in each outlet fracture.

The purpose of the system pressure monitoring was to ensure that during the experiments, the system was under constant pressure and there was no leaking or clogged flow channels in the system. The system pressure was monitored by a SETRA C–206 pressure transducer (Setra Systems, Inc., Acton, Massachusetts) which had a gauge pressure in the range of 0–25 psig and a proof pressure of 100 psi, the maximum pressure that might be applied without changing performance beyond specification (<$\pm$0.5% FS zero shift). The pressure transducer had a specified accuracy of $\pm 0.13\%$ full scale (0–25 psig) at constant temperature. It was factory calibrated with non–linearity of $\pm 0.1\%$ full scale. The transducer was located in the line of the KCl injection tube, just upstream of the model, as shown in Figure 4.3. The excitation for the C–206 is 24 VDC, and the current output from the transducer is in the range of 4–20mA. The relationship between current and pressure is linear

$$P_a = \frac{25}{16}(C-C_0) \tag{4.7}$$

where C is the current output from the transducer, P_a is the pressure measured relative to ambient atmospheric pressure, and C_0 is the base value of the current output under zero gage pressure. If C_0 did not equal 4.0 mA under zero gage pressure, it was reset to 4.0 mA by adjusting the zero adjustment screw under the ambient atmospheric pressure conditions.

The output signals from the pressure transducer were sent to a Keithley Model 706 low current scanner (Keithley Instruments, Inc., Cleveland, Ohio) which was connected to a Keithley model 486 picoammeter and then to a PC. The Model 706 low current scanner could accommodate ten plug–in scanner cards. It could be operated in continuous mode or manual

mode. The selectable scan rate of the Model 706 was in the range of 10 msec to 999,999 sec. Two Keithley Model 7158 low current scanner cards, each with 10 channels, were used with the 706 scanner. The maximum signal level of the card was 100 mA at 30V peak resistive load. The offset current error of the card is less than 1 pA (specified), and typically less than 30 fA. The actuation time of the card was less than 1 ms. Strength of the output signals from the scanner were reduced ten times by adding appropriate resistors in the circuit so that output signals from the scanner were then in the range of 0.4–2.0 mA before they were sent to the picoammeter for data displaying and basic processing. The 486 picoammeter had a current measurement range of 0 to 2.19999 mA at maximum voltage of 50 VDC. The picoammeter also had two built-in filters, digital and analog, to stabilize noisy measurements. In our experiments only the digital filter was selected. Signals from the picoammeter were collected by the computer through an IEEE–488 connector (see Figure 4.3). In the computer, Keithley VIEWDAC software was used for data acquisition and data processing. System pressure data from the C–206 transducer was analyzed according to equation (4.7) and plotted on the computer screen in real time.

To ensure accurate experimental results, the flow rate in each outflow fracture had to be precisely measured and controlled. There were two outlet flow tubes from the physical model. The outlet flow rate in fracture 4 was monitored by a flow meter which measured the pressure drop between two points with a known distance along the flow tube. Since the Reynolds number inside the tube in all the experiments was far below 2,000, the upper limit of laminar flow, the theoretical Hagan–Poiseuille results can be used to estimate average flow rate in the outflow tube. From fluid dynamics, the flow rate through a circular tubing is (Hagan–Poiseuille flow) [Batchelor, 1967]

$$Q = -\frac{\pi R^4}{128\mu} \cdot \frac{dP}{dx} \tag{4.8}$$

where R is the inner diameter of the tube; μ is the dynamic viscosity of water (see Appendix B, equation B.2); and dP/dx is the pressure gradient in the direction of flow. In equation (4.8),

the only unknown is the pressure gradient. Once it was determined, the flow rate in the tube could be easily calculated.

A SETRA C228–1 differential pressure transducer was used to measure pressure drops between two points along the outflow tube from fracture 4 (see Figures 4.3 and 4.5). A 0.02" ID PEEK tubing connected the outlet of the fracture junction model to a 'T' type connector which connected one end to the high pressure port of the C228–1 and the other end to the second in line 'T' type connector for the flow. The second 'T' type connector connected one end to the low pressure port of the C228–1 and the other end to outflow tube. There was no flow through the differential pressure transducer. The C228–1, which had a pressure range of 0–1 psid with a specified accuracy of $\pm 0.15\%$ full scale, measured the pressure drop between the two 'T' connectors. The relationship between differential pressure and the output current is linear

$$P_d = \frac{1}{16}(C\text{-}C_0) \tag{4.9}$$

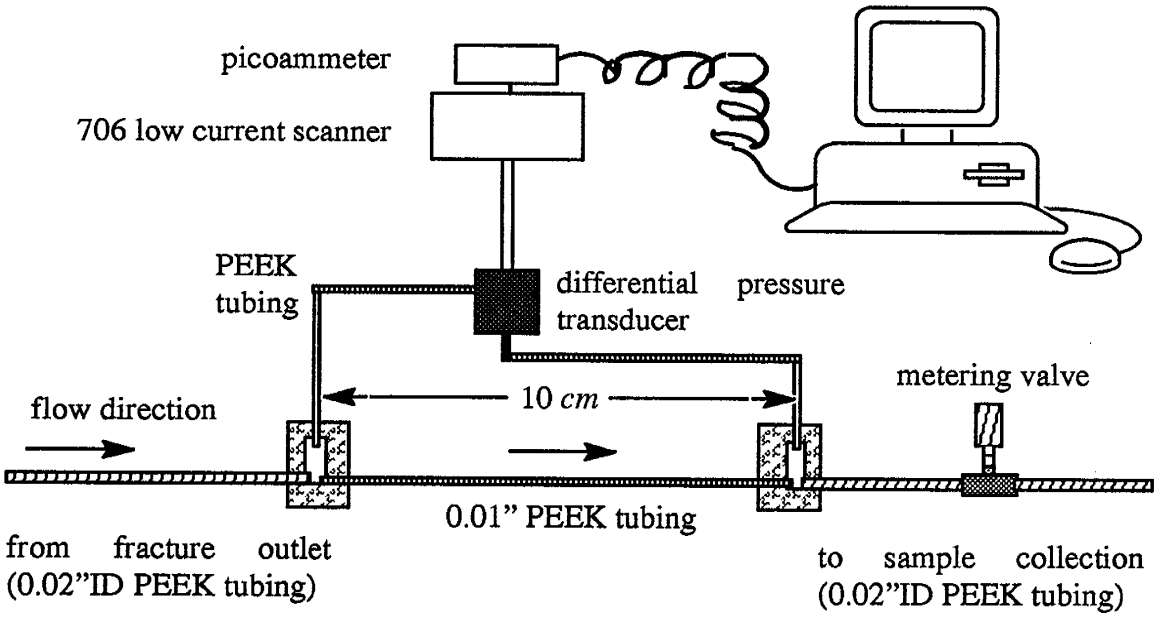

Figure 4.5. Schematic of the connection of C228–1 differential pressure transducer in the system for monitoring flow rate in fracture 4.

where P_d is the pressure difference between the two ports, and C_0 is the base value of the transducer which should be 4.0mA at 0 psid. However, C_0 changed with the line pressure in test runs. The excitation for the C228–1 was also 24 VDC. The output current of the transducer was from 4 to 20 mA. Appropriate resistors were used in the circuit to reduce the strength of the signals to a range of 0.4–2.0 mA before they were sent to the 486 picoammeter. The computer calculated the pressure drop between those two connectors, the pressure gradient, the flow rate in the tube, and plotted the flow rates on the screen in real time.

To ensure accurate flow rate data, the C228–1 was dynamically calibrated each time before experiments were started. During the calibration, only KBr solution was injected into the fracture model through inflow fracture 1, and the system pressure was monitored. The KCl aqueous solution injection pump and the outflow through fracture 3 were shut off. Thus, the KBr solution could only flow out through fracture 4. The metering valve for the flow rate control in fracture 4 (see Figure 4.5 and next section) was adjusted until the desired system pressure was reached. The base value of the C228–1 was then adjusted to match the calculated flow rate from the flow meter to the pump injection rate. Once the C228–1 was calibrated, the setting for the metering valve in fracture 4 was fixed.

Note that only the flow in outflow fracture 4 was monitored. At low Peclet numbers (low flow rate), diffusion into or out of the dead volume in the two 'T' type connectors and adjacent connections to the transducer in fracture 3 could cause additional mixing. By monitoring the flow rate in only one of the outlets and leaving the other undisturbed, we ensured that water samples coming out of the undisturbed channel were free from this possible side effect. The flow rate in fracture 3 was estimated by subtracting the flow rate of channel 4 from the total inlet flow rates.

4.3.3 Output Flow Rate Control

The outlet flow rates from channels 3 and 4 were controlled by 1/16" SWAGELOK 'S' series metering valves. The valve which controlled the flow rate in fracture 4 and the inline flow meter were placed inside the constant temperature cabinet. The valve was adjusted during flow calibration before each experiment (refer to §4.3.2 for details). The valve for flow rate control in fracture 3 was located outside the cabinet for easy access. The body of the metering valve was made of 316 stainless steel. The tapered stem used for flow control in the metering valve was hard chrome plated and the orifice of the metering valve was 0.81mm. Vernier handles were used with the metering valves to facilitate flow adjustments. During the experiments, input flow rates in fractures 1 and 2 were controlled by the two high precision pumps. The system pressure and outlet flow rate in fracture 4 were monitored by the pressure transducer and the flow meter, and the readings were plotted on the computer screen in real time. The discharge rates in the model were adjusted mainly by turning the metering valve which controlled the flow rate in fracture 3. The feed back could be read directly from the computer screen and the valve readjusted as necessary. The above process was repeated until the desired flow rate was reached. At low flow rates (low Peclet numbers), the relationship between the flow rate and the valve opening was nonlinear, making flow adjustments tedious.

4.3.4. Sample Collection and Sample Analysis

In our experiments, under equal inflow and outflow conditions, only diffusion could cause mixing at the junction, and by analyzing the concentrations of Br^- and Cl^- in each outflow channel, the magnitude of diffusive mixing was estimated.

In the model system, outlet flow tubes were connected to fractures 3 and 4 for discharging the aqueous solutions from the model (see Figures 4.3 and 4.4). As described in §4.3.2, in the line of the outlet flow from fracture 4, a flow meter was installed to monitor the flow rate in fracture 4, while the outlet flow tube of fracture 3 was undisturbed. Two metering valves

were used to control outlet flow rate in fractures 3 and 4 (see §4.3.2 and §4.3.3). The outlet tubes were extended to the exterior of the cabinet for sample collections.

Drops of the effluent solutions discharging from the outlet tubes connected to fractures 3 and 4 were collected in two separate polypropylene autosampler vials (0.6 ml), as shown in Figures 4.4 and 4.5. Each sample contained at least 0.1 ml of effluent solution from the corresponding outlet tube. At low flow rates (low Peclet numbers), the time necessary to collect a sample ranged from several minutes to about 30 minutes. Thus, to reduce possible evaporation, the vials were closed with caps between drop collections. Once the sample collections were completed, the vials were sealed with caps and parafilm and stored in a refrigerator until sample analysis.

Representative samples of effluent solution could not be taken until the mixing was at equilibrium and the resulting solution concentration had reached the sampling vial. The waiting time was estimated with a simple model of transport involving mixing at the junction, homogenization inside the outflow fractures, and homogenization inside the outlet flow tubes. The necessary time for each process to reach equilibrium can be estimated independently. Among all the three processes, the equilibrium time for mixing at the junction is negligible and is not considered below.

The time required for diffusion to homogenize the concentration profile in a 10 cm long fracture with an aperture of b can be estimated by the Taylor–Aris dispersion theory which gives the averaged concentration at a cross section of the fracture [Aris, 1956]

$$\frac{C}{C_0} = \frac{1}{2}[1 \mp erf(\frac{x - \overline{V} \cdot t_f}{2\sqrt{D_l t_f}})] \tag{4.10}$$

where t_f is the time the solute has traveled in the fracture, erf is the error function, and D_l is the dispersion coefficient. For transport between two parallel plates D_l is

$$D_l = D + \frac{(\overline{V} \cdot b)^2}{210 \cdot D} \tag{4.11}$$

A stable concentration profile is established in the fracture when C/C_0=1.0 at the end of the fracture outlet. Thus from equation (4.10)

$$erf(z) = erf(\frac{x-\overline{V} \cdot t_f}{2\sqrt{D_l t_f}}) = 1 \tag{4.12}$$

As an approximation, when the relative concentration at the end of the fracture is larger than 0.99, the concentration profile is taken to be at equilibrium. The value of z that makes erf(z)=0.99532 and C/C_0=0.9977 is 2.00 [Abramowitz and Stegun, 1972]. The time t_f required for establishing a stable concentration profile at the end of a 10 cm long outflow fracture can be solved from equations (4.11) and (4.12)

$$\frac{x-\overline{V} \cdot t_f}{2\sqrt{D_l t_f}} = 2 \tag{4.13}$$

The time t_c required for building a stable concentration profile at the end of the outlet tube can also be estimated in a similar way. The only difference is that the longitudinal dispersion coefficient for transport inside a circular tubing is [Aris, 1956]

$$D_l = D + \frac{(\overline{V} \cdot r)^2}{48 \cdot D} \tag{4.14}$$

where r is the radius of the outflow tube, and $\overline{V}$ is the average flow velocity in the tubing.

The summation of t_r, t_f, and t_c gives an estimation of the total elapsed time required before collecting stable samples. For example, at a fracture flow rate of 30ml/hour, the Peclet number at the junction is 170. The time t_f for establishing a stable concentration profile in the outflow fractures is 2.50 minutes; and the necessary time t_c for building a stable concentration profile at the end of a 100 cm long outlet flow tube (the actual length of each outlet flow tube was around 60 cm) is 0.49 minutes. Adding t_f and t_c, the total elapsed time required to establish equilibrium in the system is approximately 3.00 minutes after equal outlet flow rates have been established in each outflow fracture. Mixing at the flow meter

'T' connectors contributed additional apparatus induced mixing, which increased the necessary time for establishing equilibrium in the system.

During the experiments, the sample collection time was first calculated. Then two or more samples (each sample contained at least 0.1 ml of the effluent solution) were collected at intervals to ensure that the concentration profile in the physical model was at equilibrium.

Samples collected during the experiments were analyzed by high-performance liquid chromatography (HPLC). The HPLC instrumentation consisted of a Model 994 programmable photodiodide array detector, a Model U6K syringe injector, and a Model 510 pump, all manufactured by Waters Chromotography Division, Millipore Corporation (Milford, MA). The features of the Waters 994 detector included (1) variable wave length from 190 to 800 nm (2) detection of components absorbing UV/visible light, and (3) peak integration.

The detection mechanism of the Waters 994 detector was based on Beer's law which describes the relationship between absorbance and solute molar concentration

$$A = \varepsilon l C \tag{4.15}$$

where ε is molar absorptivity, l is path length, and C is the molar concentration of the solute. Beer's law is only valid for well-equilibrated dilute solutions, such as in our experiments. It assumes that the sample's refractive index is constant, the light is monochromatic, and that no stray light reaches the detector element.

The wave length of the UV detector was set at 195 nm with a band width of $\pm$3nm for detecting Cl^- and Br^-. At this wave length, the normalized detector response relative to detection at 190 nm for Br^- is close to 90% and around 40% for Cl^- [Bowman, 1984]. The sensitivity of the UV detector was set at 0.01 because of the weak absorbancy of Cl^- to UV light. The analytical column used for sample analysis was a Sphere/5 SAX (Phenomenex, CA, USA) 250x46 mm I.D. The mobile phase was 0.03M KH_2PO_4/H_3PO_4 at pH 2.63 with 18% acetonitrile. In a sample analysis, 25 µl of a water sample was manually injected into

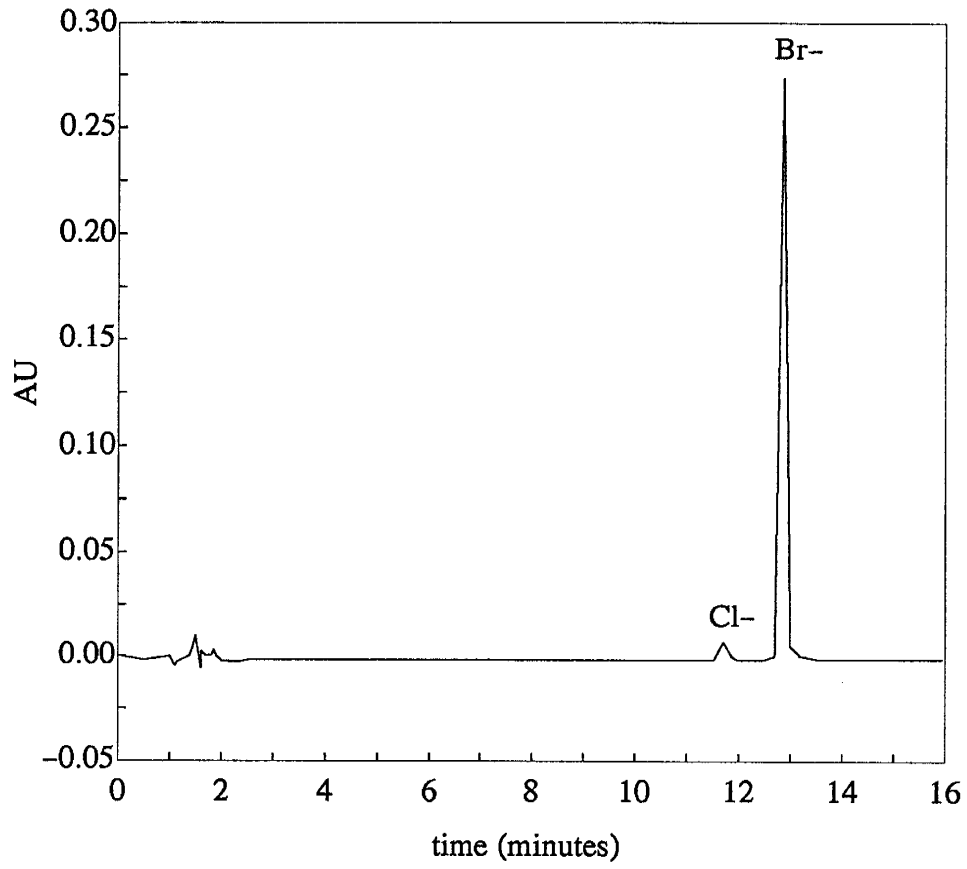

Figure 4.6. Chromatogram, using Phenomenex column, of a standard tracer solution prepared in type I water.

the injector at mobile phase flow rate 2.0 ml/min and a pump pressure of 2750 psi. Figure 4.6 shows the chromatogram of Cl^- and Br^- with concentrations of 0.0008 mol/l and 0.0005 mol/l, respectively. The retention time of Cl^- was 11.71 minutes and 12.87 minutes for Br^-.

Standard samples were used to determine the relationship between concentration and UV absorbance for Br^- and Cl^-, respectively. In each calibration, four to six standard solutions at different concentrations were used. The regression results are shown in Appendix B, Figure B.32–B.43. In all the analyses, the UV absorbance peak height was used to calculate sample concentrations from equation (4.15).

4.3.5 Temperature Control During the Experiments

In general, as temperature increases, the solute diffusion coefficient increase, while the viscosity and density of water decreases. Thus, temperature fluctuations during the experiments would cause both flow rates and solute diffusion coefficients to vary, thereby, reducing the accuracy of the experimental results. To mitigate these effects, the fracture model and most of the plumbing, including the pressure transducers, were placed in an insulated constant temperature cabinet built for the experiment. Coiled copper tubing was placed on the inside walls of the cabinet to circulate water from a CTB (constant temperature bath; Polyscience, model 1166). The CTB has both heating and cooling capabilities with a water temperature control accuracy of 0.1 °C. The water temperature in the CTB was set at 26°C.

Campbell 107 air temperature probes were used to monitor room and model cabinet temperatures during the experiments (see Figure 4.4). The 107 temperature probe had an accuracy of $\pm$0.4°C over the range of –33°C to +44°C. Under normal conditions, the error was typically less than the specification. The major error component was the $\pm$0.2°C offset error of the thermistor from 0°C to 60°C, and the error could be determined with a single point calibration and be compensated for in data analysis. Signals from the temperature probes were sent to a Campbell 21x data logger which was connected to a PC through Campbell RS232 interface (see Figure 4.4). The data logger was controlled by the PC with the Campbell PC208 software. Temperature data was temporarily stored in the 21x data logger and then dumped to the PC for data processing.

Figure 4.7 shows temperature variations in the room and the model cabinet several months before the experiments were run. The room temperature fluctuated periodically with a magnitude of almost 7°C, resulting in a 0.7°C fluctuation of temperature inside the cabinet. During the day, the temperature was relatively stable, but it began to increase at midnight and reached the highest value of 29°C in the early morning around 5:00 am. Such

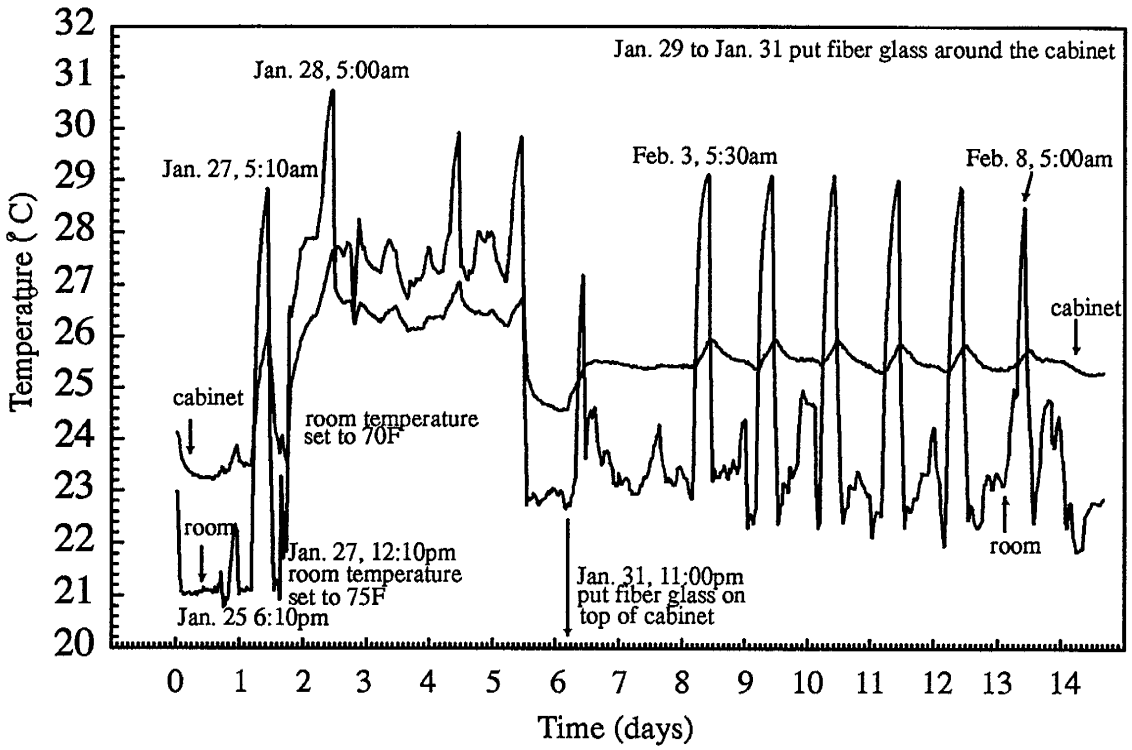

Figure 4.7. Temperature variations in the lab. and the model cabinet from 1/25 to 2/9, 1994.

large variations in room temperature could cause an unacceptably large error in the experiments at low flow rates (low Peclet numbers).

For example, in the worst case, if a pump is filled with water (100.0ml) and operating at a flow rate of 0.2 ml/hr for 6 hours, theoretically, the pump will dispense 1.20 ml water during this period. If the temperature of the water inside the pump cylinder increases 7°C in this period, the actual amount of water dispensed by the pump will increase. Using the relationship between water density and temperature (see Appendix B, equation B.1) and the principle of mass balance, we estimate that the actual volume of water dispensed by the pump to be (1.2+0.183) ml. Thus, the relative error of flow rate is 15.3% under this condition. A similar process occurs in the physical model. Since the total volume of the model is only about 4.0ml, which is 25 times smaller than that in the pump cylinder, the influence of the temperature increase on flow in the model will have an error of less than 1%. The above

calculations illustrate that the temperature variation can cause significant error in pump flow rates but a negligible influence on the model.

Temperature variation also affects the diffusion coefficient of the solute. As the solution temperature increases, the diffusion coefficients of electrolytes increase. The variations of the solute diffusion coefficient in the model due to temperature fluctuation could affect the mixing process (Peclet numbers) at the junction. Theoretically, the diffusion coefficients of strong electrolytes at infinite dilution are proportional to the absolute temperature of the solution [Weast et al., 1987]. Although the tracer solution in our experiments was not at infinite solution, we used this theoretical relationship to estimate the influence of temperature on the solute diffusion coefficient and to obtain some idea about the magnitude of the influence of temperature variation on solute diffusion coefficients. In our estimation, if the solution temperature increases 7 °C and all the other properties (cation and anion limiting equivalent conductances, cation valency, etc.) of the solute remain unchanged, the diffusion coefficient of the solute will increase about 2.3%, which is relatively small.

Another aspect of temperature control during the experiments concerned water viscosity. In general, water viscosity decreases as temperature increases and can affect flow rates in a constant head system but will have little influence on flow rates in a constant flow system. Since our experiments were conducted under constant flow conditions, the influence of viscosity variation with temperature on flow rates in the model was negligible

The above analyses illustrate that temperature variation can cause large errors in pump flow rates but relatively small errors on solute diffusion coefficients and flow rates in the model. We had to determine within what magnitude the temperature variations had to be controlled in order to minimize their influence. We determined that the influence of temperature variation on pump flow rates should be controlled within $\pm 3\%$ of the set values. Then a simple analysis showed that the water temperature inside the pump cylinders should be controlled within a range of $\pm 0.2°C$ of the target temperature. Inside the constant

temperature cabinet, temperature variations of less than ± 1.0 °C would limit the flow rate and diffusion coefficient variations in the model to much less than $\pm 1\%$. Thus, the goal of temperature control during the experiments was to control temperature variations to less than ± 0.2°C in the pump cylinders and ± 1.0 °C in the model cabinet.

An important aspect in controlling temperature variations was reducing room temperature fluctuations. The periodic room temperature fluctuations illustrated in Figure 4.7 occurred because the cooling system for the entire building was shut down during the night. This problem was corrected by leaving the cooling system on continuously. During the fracture junction experiments, the room temperature was set at 25°C. Figure 4.8 shows that the room temperature variations were greatly reduced. The figure also clearly shows that the magnitude of the relative temperature variation inside the model cabinet was much less than ± 1.0°C as a result of room temperature control.

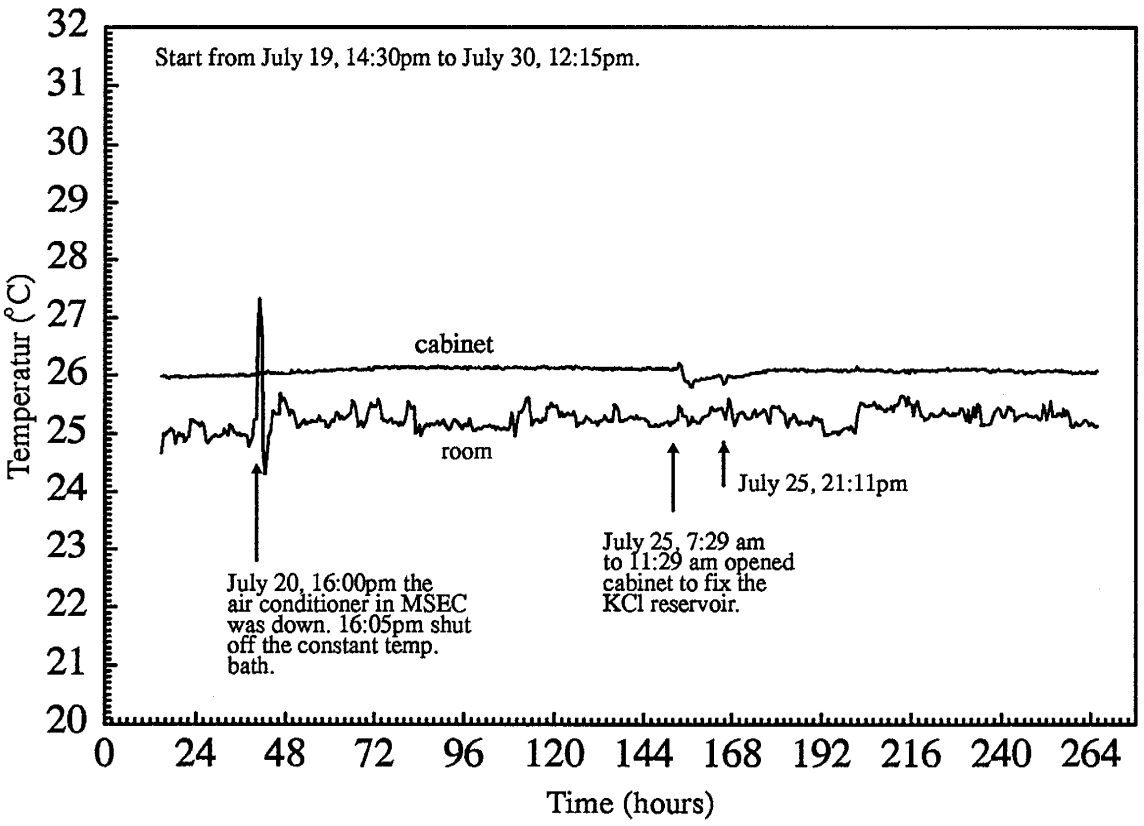

Figure 4.8. Temperature variations with time in the lab and in the model cabinet.

To control the temperature in the pump cylinders, water from the CTB first circulated through the pump jackets of the two ISCO pumps, then through the model cabinet, and finally flowed back to the CTB. The water temperature from the pump jacket was monitored by a Campbell 107B water/soil temperature probe, as shown in Figure 4.4. The water temperature variations in the pump jackets for a period of 12 days are plotted in Appendix B, Figure B.2. The magnitude of the variation was far less than $\pm 0.2\,^{\circ}C$, which would limit the influence of temperature variation on the pump flow rates to less than $\pm 3\%$ of the set values.

In general, by reducing room temperature variations, installing the model system in an insulated cabinet, and using CTB to control temperature in pump cylinders and model cabinet, the temperature in the experiments was well controlled, thus, significantly reducing uncertainty in the experimental results.

4.4 Experimental procedures

The experiments were conducted in descending order from Peclet number 170 to 1. One advantage of this sequence was a reduction of the mixing effects from the previous experiment in the system. Preparation for the experiments included the following steps: (1) preparing tracer solutions, (2) testing pump leakage and flow rate, and (3) removing air from the physical model and filling it with tracer solutions. Then for each experiment at a unique Peclet number, the additional steps were (4) calibrating the flow meter and setting the metering valve for outlet flow rate control in fracture 4, (5) monitoring system pressure and flow rate, (6) running the experiment and collecting samples, (7) analyzing samples. Each of these steps is described below.

1. Preparing tracer solutions. Deaired type I water was used for preparing the KBr and KCl tracer solutions. The purpose of using deaired water was to reduce the possibility of generating air bubbles in the system and to help dissolve CO_2 later used for removing air from the system. 12 mg of KBr (99.99% pure, Aldrich) and KCl (99.99+% pure, Aldrich)

were dissolved in two separate beakers, each containing 100 ml of water. Thus, the concentrations of Br^- and Cl^- were $1.01x10^{-3}$ mol/l and $1.61x10^{-3}$ mol/l, respectively. Standard samples were then taken for use in HPLC analysis.

2. Testing pump leakage and flow rate. Before a group (a series) of experiments could begin, the two ISCO pumps were tested for leakage and corrected for flow rates. A pump leakage test was conducted by running the pump at constant pressure mode. First, the outlet tubing from the pump was removed and replaced with a plug. The pump was then filled with the corresponding tracer solution and set at the normal pump operating pressure (around 400 psi). The leakage rate was estimated by operating the pump for about 12 hours and recording both the initial and end volumes of solution left in the cylinder (the volume of the remaining solution could be directly read from the screen of the pump controller). The initial volume of the solution minus the end volume of the solution gave the total volume of water leaked during the test period. The leakage rate then could be determined and added to the pump flow rate for compensation. Tests showed that the leakage rates increased with the wear of the pump seals. Initially, the leakage rates of both pumps were less than 1 μl/hour. However, by the end of all of the experiments, the leakage rates had increased to around 5μl/hour.

The flow rate of each pump was tested by running the pumps at the desired flow rates for a certain periods (several hours to 10 hours, depending on the flow rates) and collecting the water flowing out of the pumps (see §4.3.1). In general, the two ISCO pumps were very accurate. In all tests, flow rate errors were less than $\pm 2\%$, including measurement errors.

3. Removing air from the system. Air inside the pressure transducer and the model was removed to ensure accurate experimental results. An air bubble inside the transducers or the model could affect the accuracy of the instruments or disturb the flow field in the model. Of special concern were air bubbles around the junction which would change the flow field and affect the mixing process. The following procedures were followed to remove the air in the pressure transducers and the model.

(3a). Removing air from the C-206 pressure transducer. The C-206 was placed in the flow path of KCl injection between the back pressure regulator and the model to monitor system pressure during the experiments (see Figures 4.3 and 4.9). To remove air from the C-206, the 3-way valve controlling KCl injection to the model inflow fracture 2 was shut off. The bleed hole on top of the transducer was opened. KCl solution was injected by the pump through the inflow tube to push air out of the transducer. Once the solution flowed out continuously from the bleed hole, the air was removed. The injection pump was shut off and the bleed hole closed.

(3b). Flushing the physical model with CO_2 gas. The purpose of this step was to use CO_2 to push air out of the model. The relatively high aqueous solubility of CO_2 in water makes it useful in removing gas from the model. The set up for CO_2 flushing is shown in Figure 4.9. CO_2 gas from the supply tank passed through a pressure regulator and a 2 μm inline filter (to remove dirt in the gas phase) to a 3-way valve. By switching the 3-way valve, the two inflow fractures 1 and 2, and the two outflow fractures 3 and 4 could be flushed by CO_2 gas. After CO_2 flushing, the CO_2 3-way switching valve was shut off.

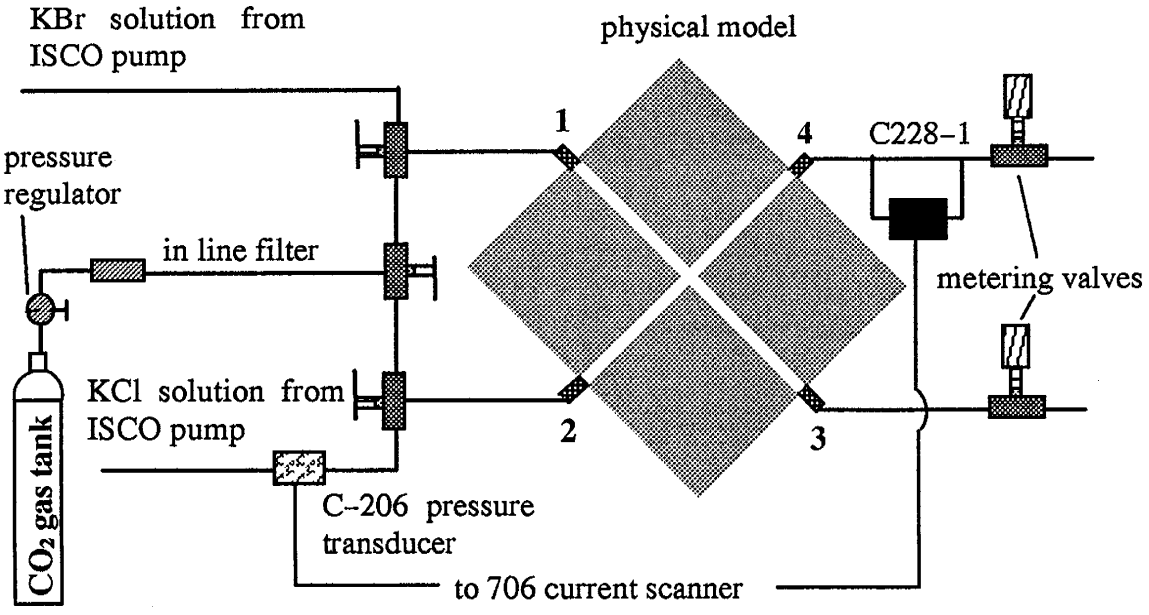

Figure 4.9. Schematic of experimental set up for removing air in the model.

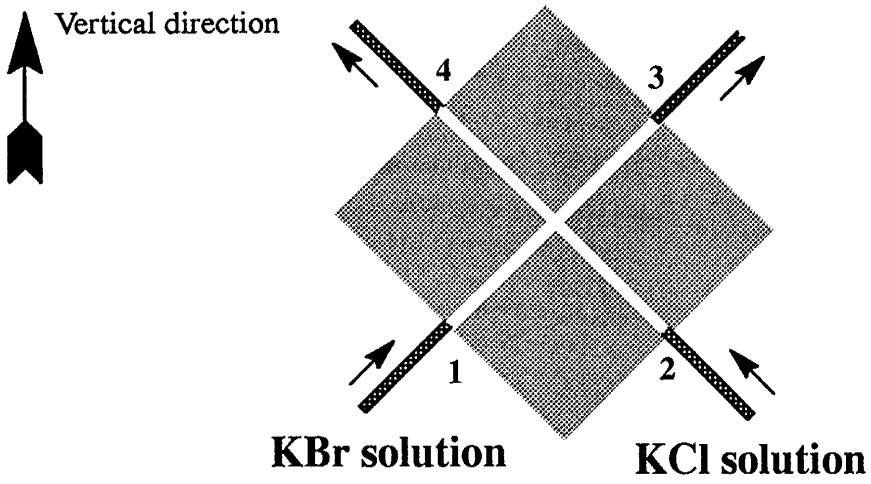

Figure 4.10. Schematic of model position for removing air from the model.

(3c). Removing CO_2 from the model and filling it with tracer solutions. This was the last but the most important step in removing air from the model. The two outflow tubes connected to outlet fractures, 3 and 4, were temporarily removed from the physical model. KBr and KCl aqueous solutions were then injected into the physical model simultaneously. The model was lifted into a vertical position so that the CO_2 inside could be easily pushed out through the outlet fractures by the aqueous solutions, as illustrated in Figure 4.10. Once the model was CO_2 free (it could be easily checked by eye), the two outlet tubes were re-attached to the physical model. The pumps were kept running to push gas out of these outflow tubes until water continuously discharged from the two outlets. Then the pumps were shut off.

(3d). Bleeding air out of the flow meter (C228-1 differential pressure transducer). The differential pressure transducer must be air free to ensure accurate measurements. The location and connections of the C228-1 differential pressure transducer are shown in Figures 4.4, 4.5, and 4.9. There are two bleed holes in the C228-1, one for the high pressure port, the other for the low pressure port. During the bleeding process, all the outflow control

valves were shut off, and only KBr was injected into the model (the pump for KCl injection was shut off). First, the air in the high pressure port was bled out, and then the air in low pressure port.

After removing air from the physical model system, each fracture was flushed thoroughly with the corresponding tracer solution. The purpose of this step was to remove the artificial mixing effect of the two tracers during the pre-experiment set up, so that fractures 1 and 4 were initially filled with KBr solution, and fractures 2 and 3 were filled with KCl solution. To flush fracture 2 and 3 with the KCl tracer solution, the metering valve controlling outlet flow rate in fracture 4, the KBr injection pump, and the 3-way for KBr injection were shut off. Only the metering valve controlling the outlet flow rate in fracture 3 was open. KCl tracer solution was injected into the physical model at a rate of 30ml/h for 10 minutes. The injected KCl solution flowed through fractures 2 and 3 and discharged through the outlet flow tube. The same procedure was repeated to flush fractures 1 and 4 and the connected outflow tubes. Thus, before the experiments, each fracture corresponded to a state of no mixing at the junction, and any artificial mixing during the pre-experiment set up was reduced.

4. Calibrating the flow meter and setting the metering valve for outlet flow rate control in fracture 4. To ensure accurate flow rate data, the C228-1 differential transducer was dynamically calibrated at the desired flow rate (and therefore the desired Peclet number) before each experiment (see §4.3.2 for details). The metering valve for flow rate control in fracture 4 was adjusted until the desired system operating pressure (around 1-2 psi gage pressure) was reached. It was left unaltered during the experiment.

5. Monitoring system pressure and flow rate during the experiment. The real time information on flow rate and system pressure was essential for flow rate control during the experiments. The VIEWDAC data acquisition software was programmed to obtain system pressure data and inline pressure drop data from the C-206 pressure transducer and the

C228-1 differential pressure transducer every 5 seconds. The collected data were analyzed in real time and then plotted on the computer screen as outlet flow rate in fracture 4 vs. time and system pressure vs. time, respectively. VIEWDAC was also programmed to automatically monitor flow rate and system pressure variations in the system. Whenever the flow rate variation was over 3% of the designated flow rate or the system pressure rose above the upper limit or dropped below the lower limit, the computer would beep to warn the operator. Based on the real time flow rate data, outlet flow rates in the system could be maintained at the desired values by mainly adjusting the metering valve controlling flow rate in fracture 3.

6. Running the experiment and collecting samples. After these preparations, we began the experiments by injecting KBr and KCl tracer solutions into fractures 1 and 2 simultaneously. Manual adjustments on system outflow rate were made to ensure equal flow rates in each outlet fracture. Figure 4.11 and Figure 4.12 are plots of flow rate and system pressure variations of the experiment at a high flow rate of 30.000 ml/hour and a Peclet number of 170. The average measured flow rate in fracture 4 was 30.030 ml/hour. The relative error of the flow rate was 0.1%. The average velocity in the fracture was 5.39cm/minute with a Reynolds number of 0.047 which is far below the upper limit (around 2,000) for laminar flow between two parallel plates. The average velocity in the 0.02" ID PEEK flow tubing was 396.43cm/minute with a Reynolds number of 30.017. Figure 4.12 shows that during this experiment, the system was at constant pressure. The estimated time required for establishing a stable concentration profile in the system was about 3.00 minutes (more detailed information on sample collection and sample analysis can be found in §4.3.4). Three effluent water samples (0.5ml each) were taken at elapsed times of 6, 12, and 20 minutes. These times and the estimated times at which the sampled water arrived at the fracture junction are labeled in Figure 4.11.

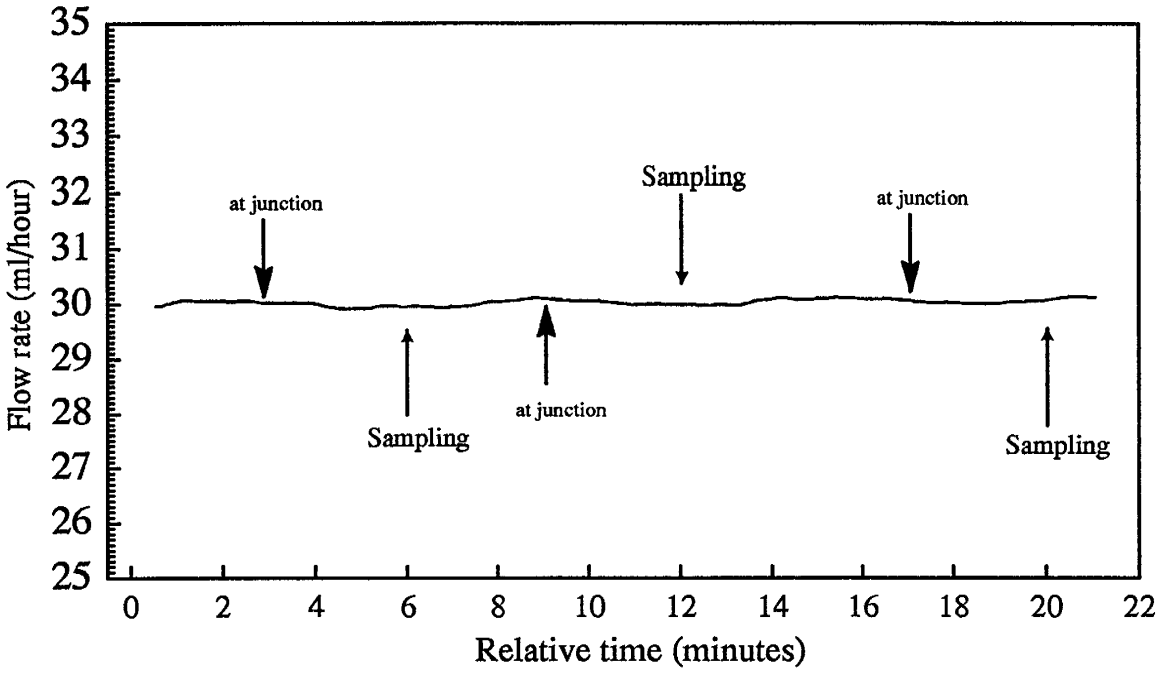

Figure 4.11. Flow rate variations in fracture 4 during the experiment at flow rate 30.0 ml/hour. The average flow rate is 30.03ml/hour.

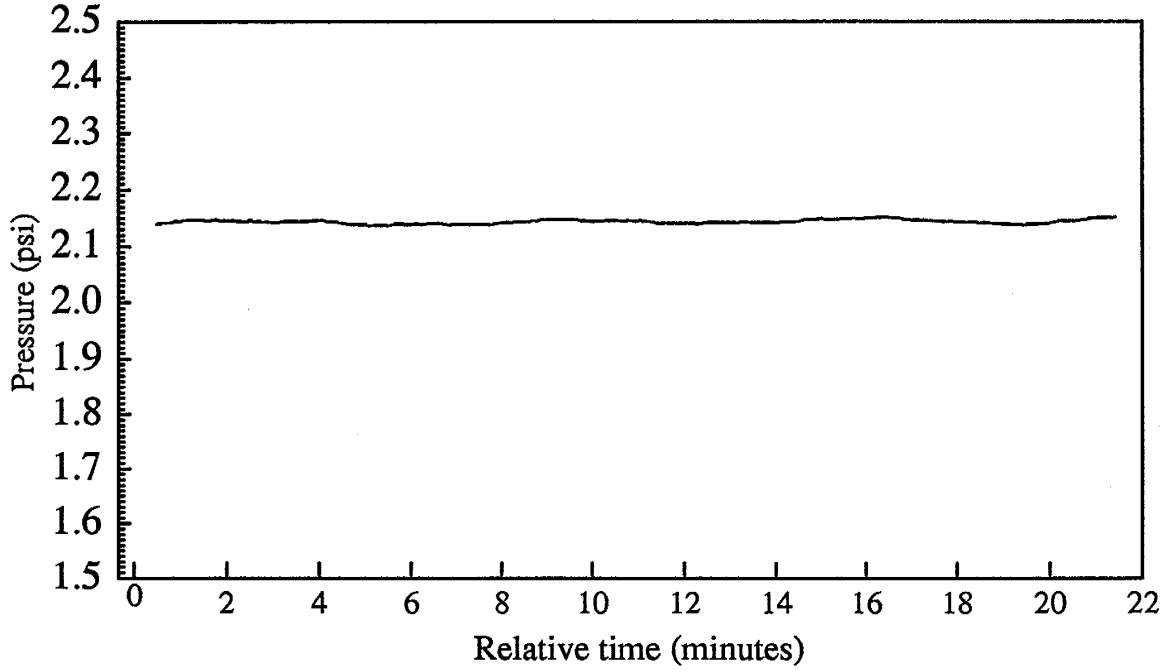

Figure 4.12. Pressure variations during the experiment at flow rate 30.0 ml/hour.

A second example shows the flow rate and system pressure variations of the experiment at a middle flow rate of 1.000 ml/hour and a Peclet number of 5.67 (see Figures 4.13 and 4.14). The average flow rate in fracture 4 was 1.020 ml/hour. The relative error of flow rate was 2%. Figure 4.13 shows a very slow increase in the flow rate from an initial flow rate of 1.00ml/hour to 1.02 ml/hour in 40 minutes. The flow rate then basically stabilized at 1.020 ml/hour. The system pressure also showed a very similar trend. The estimated time required for establishing a stable concentration profile in the system was 71 minutes. Three samples (0.1ml each) were taken at 133, 188, and 208 minutes after the outlet flow rates were balanced.

A third example shows the flow rate and system pressure variations during the experiment at a low flow rate 0.200ml/hour, corresponding to a Peclet number of 1.13 (see Figures 4.15 and 4.16). The average measured flow rate was 0.202 ml/hour. The average flow velocity in each fracture was 3.59×10^{-2}cm/minute with a Reynolds number of 3.143×10^{-4}. Figure 4.15 shows small fluctuations in the flow rate. Those small fluctuations were caused by noise in the differential pressure transducers and small real time adjustments in outlet flow rate control. After the initial adjustment around relative time 2 hours, the system pressure in Figure 4.16 slowly increased by 0.08psi over 10 hours. Due to the adjustments in outlet flow rates at relative time 12 hours, the system pressure showed a quick increase of 0.12psi in 7 hours. The estimated elapsed time required for establishing a stable concentration profile in the system was around 6.5 hours. A total of 6 samples (each contained 0.1 ml of the corresponding effluent solution) were collected during the experiments as shown in Figure 4.16.

Samples collected during the experiments were sealed and temporarily stored in a refrigerator. They were later analyzed by HPLC.

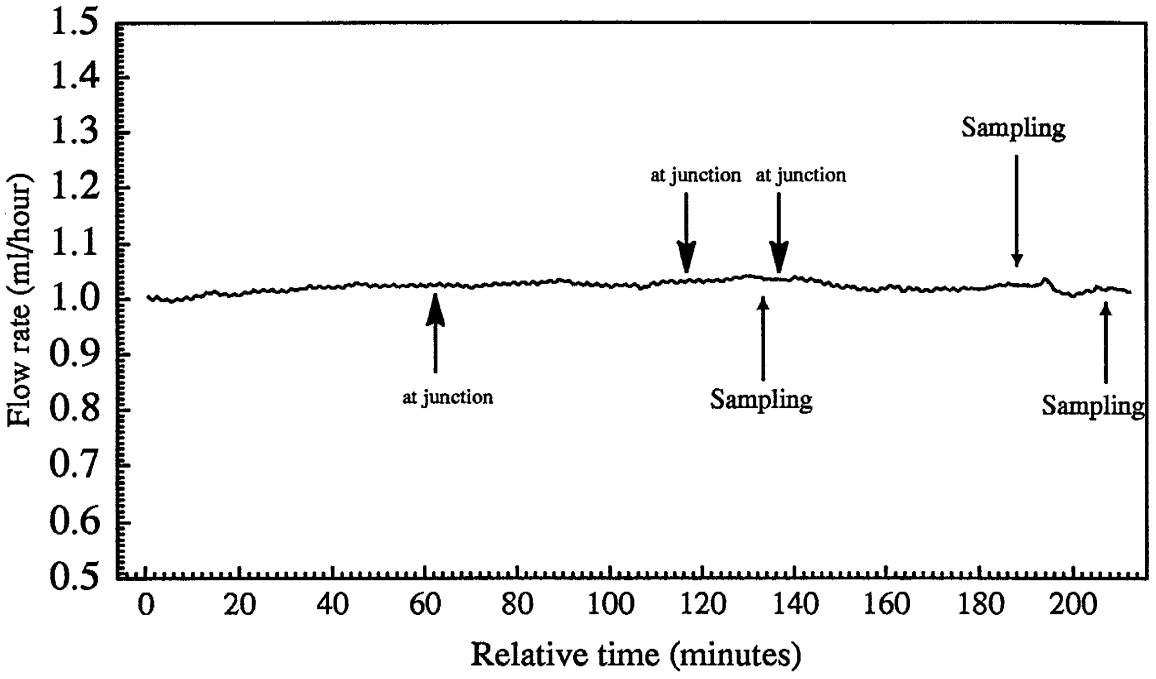

Figure 4.13. Flow rate variations in fracture 4 during the experiment at flow rate 1.00 ml/hour. The average flow rate was 1.02 ml/hour.

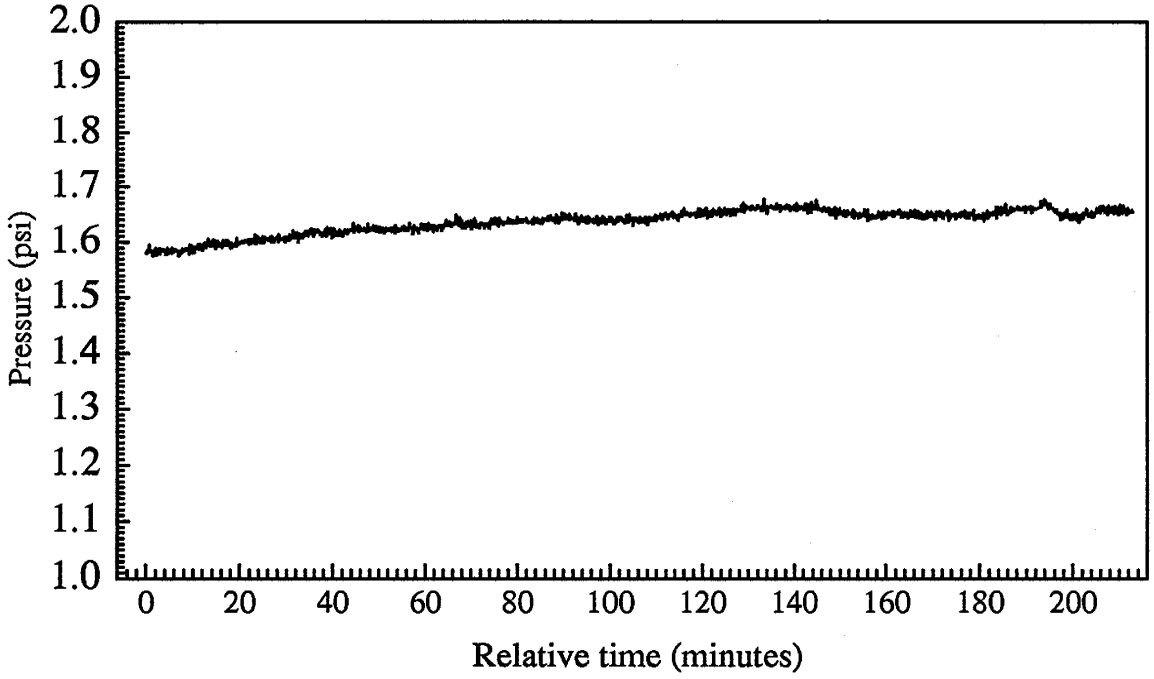

Figure 4.14. Pressure variations with time during the experiment at flow rate 1.0ml/hour.

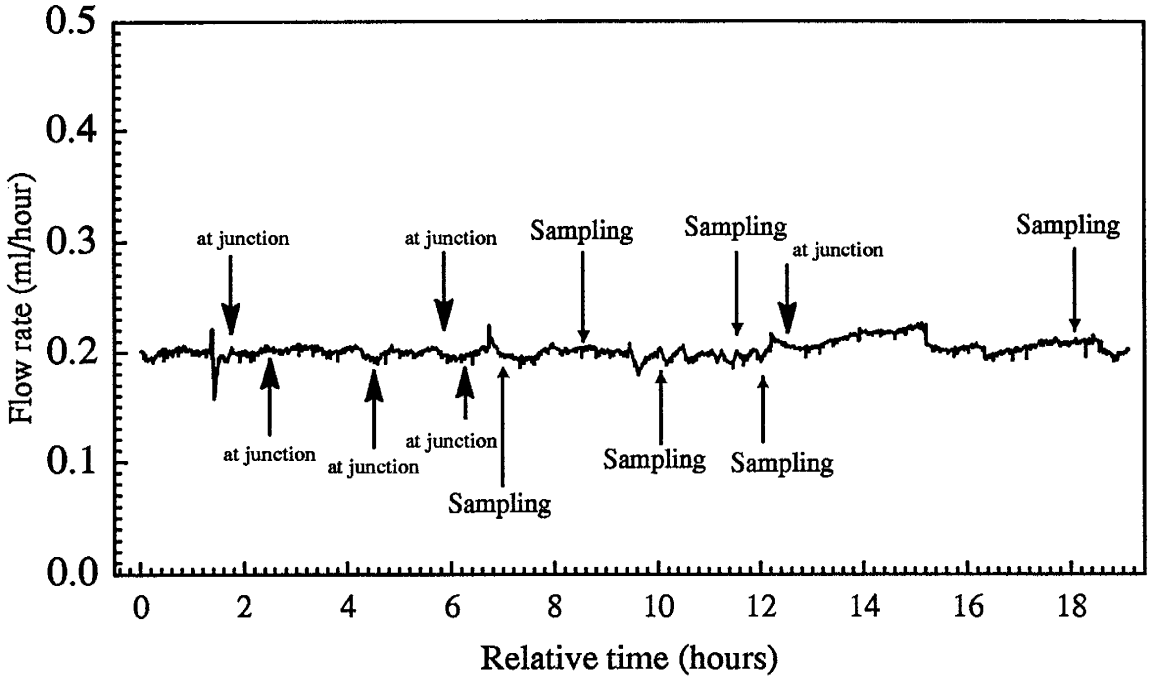

Figure 4.15. Flow rate variations in fracture 4 during the experiment at flow rate 0.200ml/hour. The average flow rate was 0.202ml/hour.

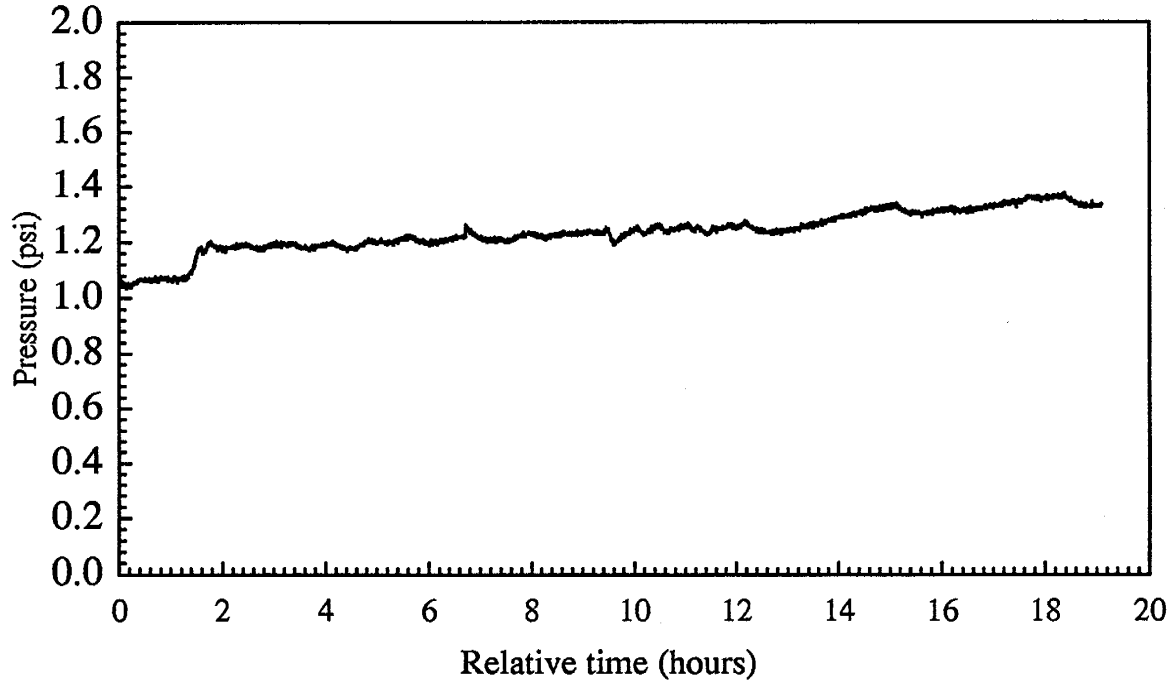

Figure 4.16. Pressure variations with time during the experiment at flow rate 0.200ml/hour.

4.5 Experimental Results and Discussion

A total of 20 experiments were carried out to investigate the mixing behavior at the fracture junction with Peclet numbers ranging from 1.13 to 170. The corresponding Reynolds numbers in the fracture model were in the range of 3.14×10^{-4} to 0.047. 104 samples were collected and analyzed by HPLC for the concentrations of Br^- and Cl^- (the raw data are listed in Appendix B, Table B.1). For some of the experiments, the raw data indicate discrepancies in the concentrations for the Br^- and Cl^- in outlet fracture 3 and 4, respectively. To determine the cause of this problem, the raw data and flow data were examined together. We found that the discrepancies were mainly due to large outlet flow rate variations during the experiments. Those data were then removed from data analysis (see Appendix B).

For the Br^- tracer in outlet fracture 3, the mixing ratio (the same as the normalized concentration) is defined as

$$M_{3Br} = \frac{C_{3Br}}{C_{1Br}} \tag{4.16}$$

where C_{3Br} is the Br^- concentration in the outlet fracture 3, and C_{1Br} is the Br^- source concentration in the inlet fracture 1. A similar mixing ratio, M_{4Cl}, can be estimated from Cl^- tracer concentration data in fracture 4. The expected maximum value of the mixing ratio is 0.5, which represents a diffusion controlled complete mixing process at the junction. The minimum value of the mixing ratio is 0, corresponding to no diffusive mixing at junction, such that the transport process at the junction is advection controlled. Any value of the mixing ratio that is between 0 and 0.5 indicates a diffusion and advection controlled transition zone mixing process.

The Br^- concentration data in fracture 4 can also be used to estimate the mixing ratio at the junction, which is estimated as

$$M_{4Br} = 1 - \frac{C_{4Br}}{C_{1Br}} = 1 - M'_{4Br} \tag{4.17}$$

where C_{4Br} is the Br^- concentration in the outlet fracture 4. Again, similar mixing ratio, M_{3Cl},

can also be estimated from Cl^- concentration data in fracture 3. The primed mixing ratios calculated from equation (4.17) lie between 0.5 and 1, corresponding to complete mixing, transition zone, or streamline routing. Theoretically, the sum of M and M' should be 1.

From the final Br^- and Cl^- concentration data (the data that were seriously affected by large outlet flow fluctuations had been removed, see Appendix B), we calculated four mixing ratios, M_{3Br}, M_{4Br}, M_{3Cl}, M_{4Cl}. These data are listed in Appendix B, Table B.2 and Table B.3 and are plotted in Figure 4.17. The data clearly show that as Peclet numbers decrease, the mixing ratios increase and have larger variations at low Peclet numbers than at high Peclet numbers.

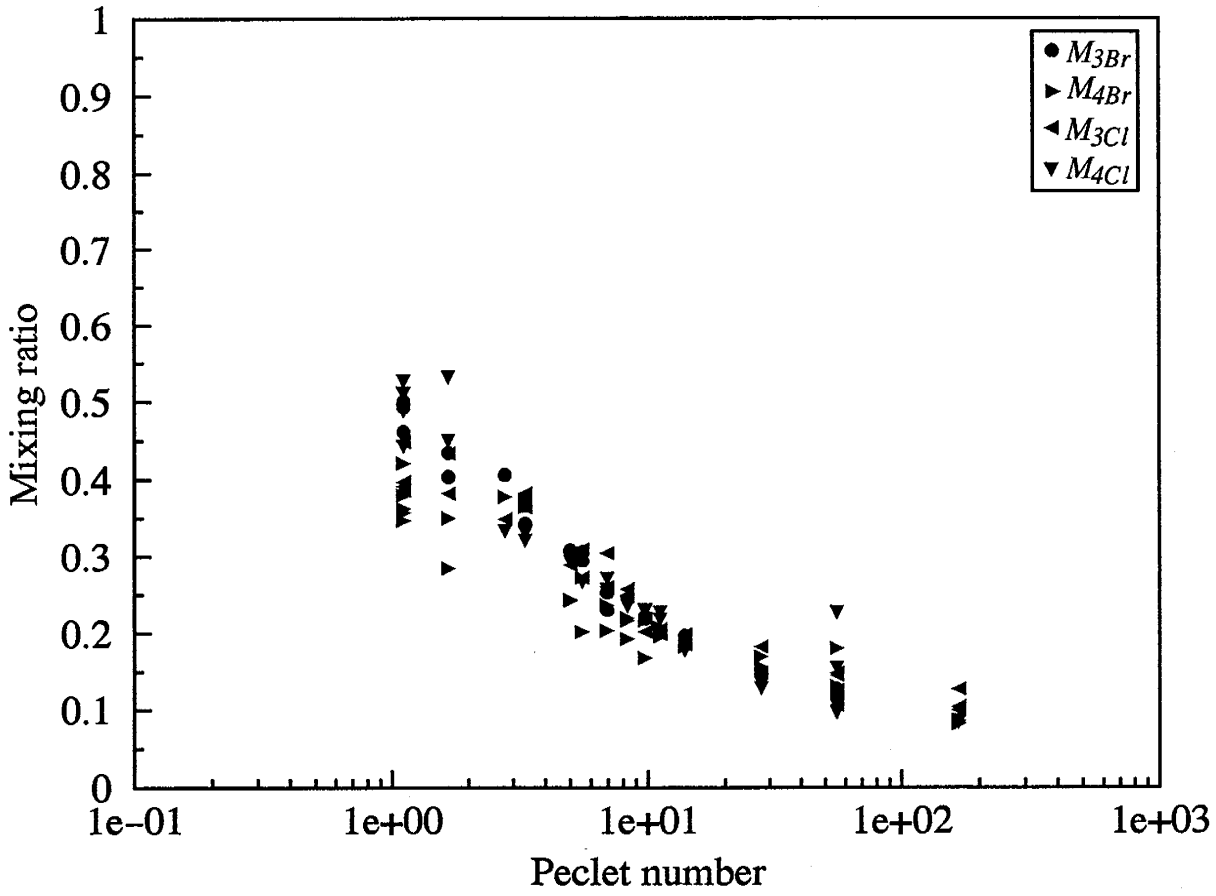

Figure 4.17. Relationship between mixing ratios and Peclet numbers at the junction.

One way to look at the variations of the mixing ratios is to plot the mixing ratios M_{3Br} vs. M'_{4Br} and M_{3Cl} vs. M'_{4Cl}, as shown in Figures 4.18 and 4.19, respectively. Theoretically, the relationship between M and M' should be a straight line with a slope of -1. But due to the influence of outlet flow rates variations during the experiments and errors in sample analysis, the sum of M and M' is rarely 1 (more detailed information on mass balance error for Br^- and Cl^- is listed in Appendix Table B.2 and Table B.3) Figure 4.18 clearly shows

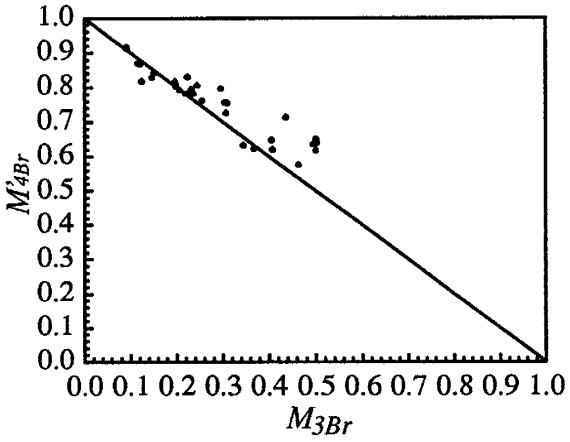

Figure 4.18. Relationship between M_{3Br} and M'_{4Br}

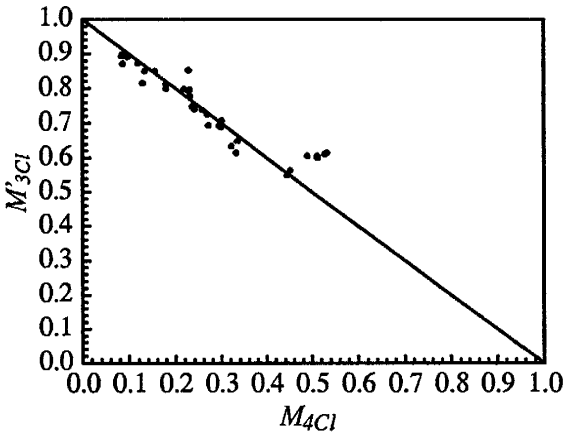

Figure 4.19. Relationship between M_{3Cl} and M'_{4Cl}

that as M_{3Br} increases, some of the data points stray from the straight line, and the variations increase. The mixing ratio data determined from the Cl^- concentrations show relatively small variations except for M_{4Cl} around 0.5. Thus, as a whole, the mixing ratios determined from the Cl^- concentration data have smaller variations than those determined from Br^- concentration data, which does not necessarily mean that both M_{3Cl} and M'_{4Cl} are more reliable than M_{3Br} or M'_{4Br}.

In order to determine which concentration data can give the most reliable estimation of the mixing ratio, the relationships between the mixing ratio and the Peclet number estimated from M_{3Br}, M_{4Br}, M_{3Cl}, and M_{4Cl} are plotted in Figures 4.20–23. It is clear that mixing ratios, M_{3Br}, determined from Br^- concentration data in fracture 3 have the least variation, while the mixing ratios, M_{4Br}, determined from Br^- concentrations in fracture 4 have the largest variation, especially at low Peclet numbers, thus explaining the large variations in Figure

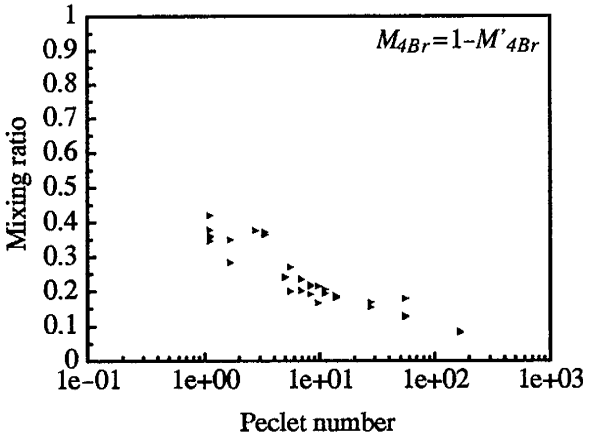

Figure 4.20. Relationship between M_{4Br} and P_e.

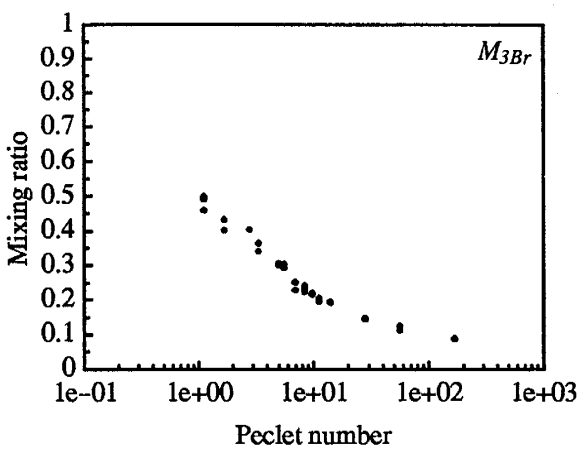

Figure 4.21. Relationship between M_{3Br} and P_e.

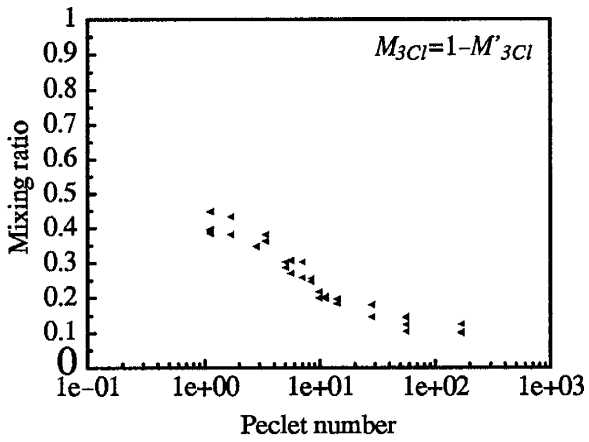

Figure 4.22. Relationship between M_{3Cl} and P_e.

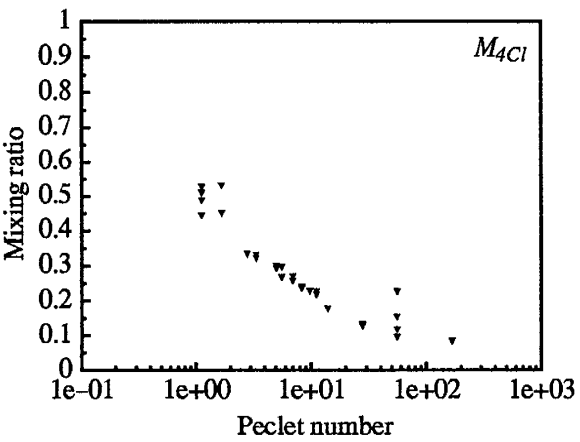

Figure 4.23. Relationship between M_{4Cl} and P_e.

4.18. The mixing ratios determined from Cl^- concentrations in fracture 3 and 4 show relatively small variations except for the M_{4Cl} data around Peclet numbers 50 and 1. To ensure that the mixing ratio (M_{3Br}) data determined from Br^- concentrations in fracture 3 are consistent with M_{3Cl} and M_{4Cl}, the mixing ratio M_{3Br} is compared with M_{3Cl} and M_{4Cl}, respectively, as shown in Figures 4.24 and 4.25. The conformity is obvious. Therefore, the mixing ratio M_{3Br} is reliable and has the least variation.

The large variation of the mixing ratio, M_{4Br}, in Figure 4.20 determined from Br^- concentration data in fracture 4 could be due to additional dispersion caused by the dead volume in the two ports for the inline flow meter's differential pressure transducer (Refer

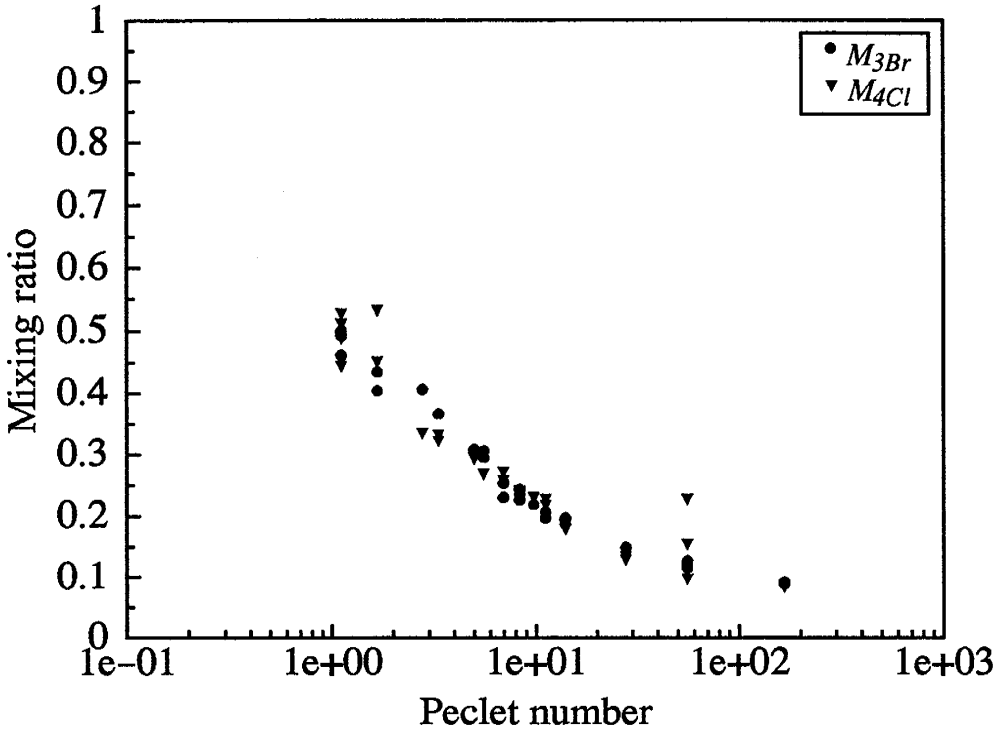

Figure 4.24. A comparison between the mixing ratios M_{3Br} and M_{4Cl}.

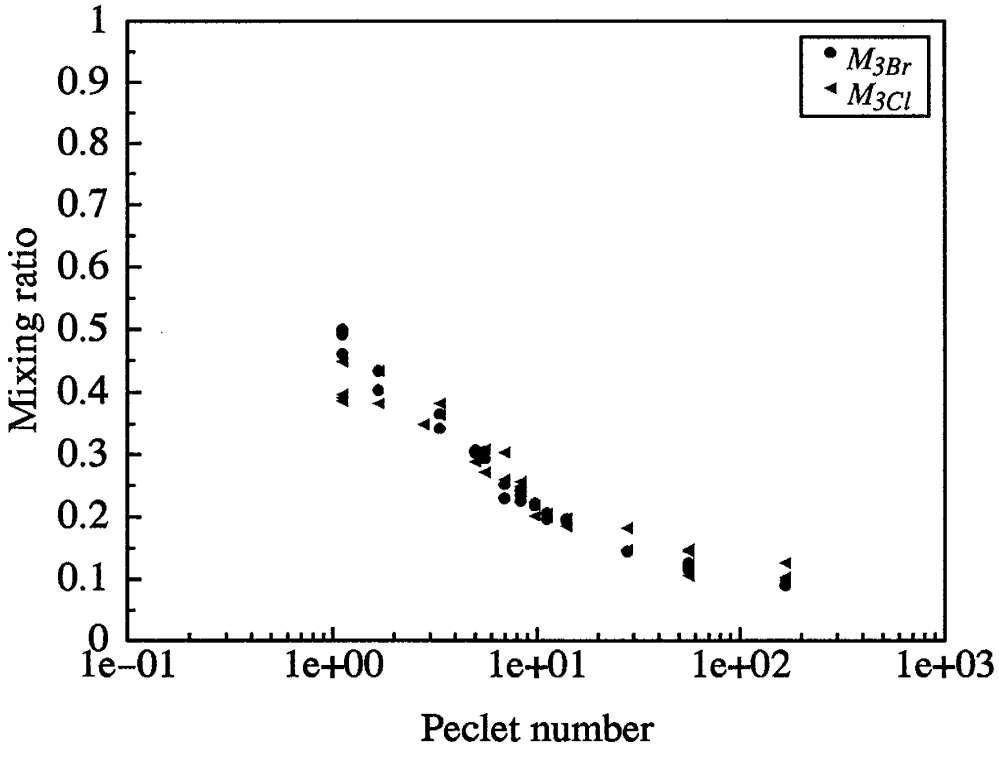

Figure 4.25. A comparison between the mixing ratios M_{3Br} and M_{3Cl}.

to Figure 4.5 and Figure 4.10). The same problem could also affect the mixing ratios determined from Cl^- concentrations in fracture 4. Fortunately, fracture 3 had no flow meter, perhaps explaining the apparent lack of noise in mixing ratios determined on the basis of tracer concentrations in this fracture.

Based on the above analysis, the mixing ratios calculated from Br^- concentrations in fracture 3 were used to represent the magnitude of diffusive mixing at the junction in the following discussion. For most Peclet numbers, there was more than one mixing ratio was estimated from the Br^- concentration data (see Figure 4.21). These mixing ratios were arithmetically averaged and are plotted in Figure 4.26, representing the relationship between the mixing ratio and the Peclet number at the junction.

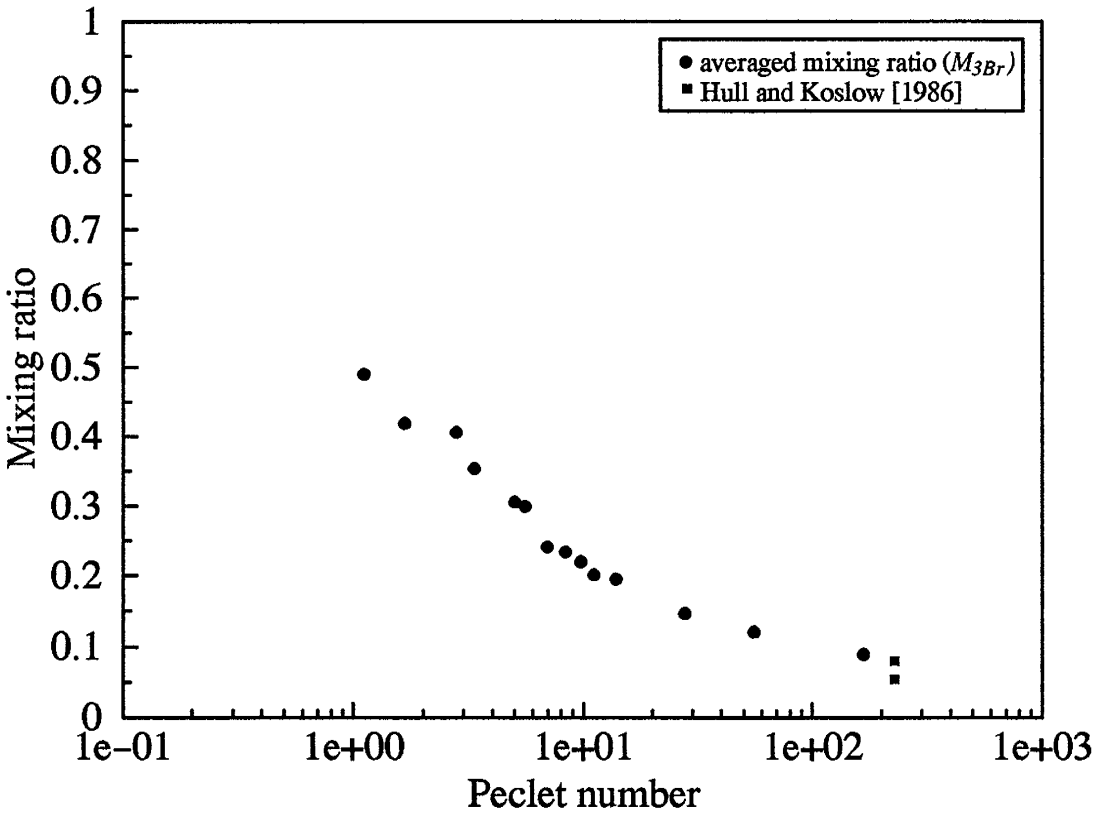

Figure 4.26. Relationship between Peclet numbers and averaged mixing ratios estimated from Br^- concentration data in fracture 3.

The experiment results confirm our hypothesis that there is a transition zone between the advection controlled streamline routing and the diffusion controlled complete mixing. As expected, when the Peclet number is around 1, transport at the junction is diffusion controlled, and complete mixing occurs at the junction. The transition zone corresponds to the Peclet number in the range of 1 to 170. The upper limit is some what arbitrary. Indeed the range is consistent with Hull et al.'s [1987] hypothesis, while our hypothesized upper limit is less than that observed. Within this range both advection and diffusion control the mixing process. We were unable to carry out the experiments at Peclet numbers smaller than 1 because controlling the outlet flow rates became extremely difficult at lower flow rates due to the nonlinear property of the metering valves. On the other hand, experiments at Peclet numbers higher than 170 could not be conducted under current experimental design due to the high flow rates and thus high pressure in the system.

An important feature of the observed mixing process at the junction is that the mixing ratio decreases asymptotically at the the top end of the transition zone. The highest Peclet number in the experiments was around 170, which corresponds to an average flow velocity of 5.39cm/minute, or 77.61m/day in the fractures. Even at this high Peclet number, the mixing ratio at the fracture junction was 0.09 instead of 0. We expect that as the Peclet number further increases, the influence of diffusion will be much less important and eventually stream line routing will become appropriate.

Hull and Koslow [1986] conducted laboratory experiments to investigate mixing behavior at the fracture junction with an idealized physical model. They conducted only one experiment for the equal flow rate case (referred to as D1 in their paper) at Peclet number of 225. Two mixing ratios were determined from their tracer concentration data in each outlet fracture. They were 0.05 with -3.49% error and 0.92 (corresponding to 0.08 in their low concentration fracture) with 8.00% error. This data is also plotted in Figure 4.26 and is consistent with our asymptotic experimental results.

4.6 Comparison Between the Numerical Simulation Results and the Experimental Results

The LGA (Lattice Gas Automata) simulation results in Chapter 3 and the simulation results of Berkowitz et al. [1994] are plotted together with our experimental results in Figure 4.27 for comparison. It is clear that the LGA simulation results are much closer to the experimental results, while the difference between the results of Berkowitz et al. [1994] and the experimental results is very large. For Peclet numbers smaller than 1, both the experimental results and the LGA simulation results indicate complete mixing at the fracture junction while the results of Berkowitz et al. predict a transition zone for Peclet numbers far smaller than 1. More importantly, they never observed complete mixing even at the Peclet numbers as low as $3x10^{-3}$. They also suggest that for Peclet number greater than 1, the

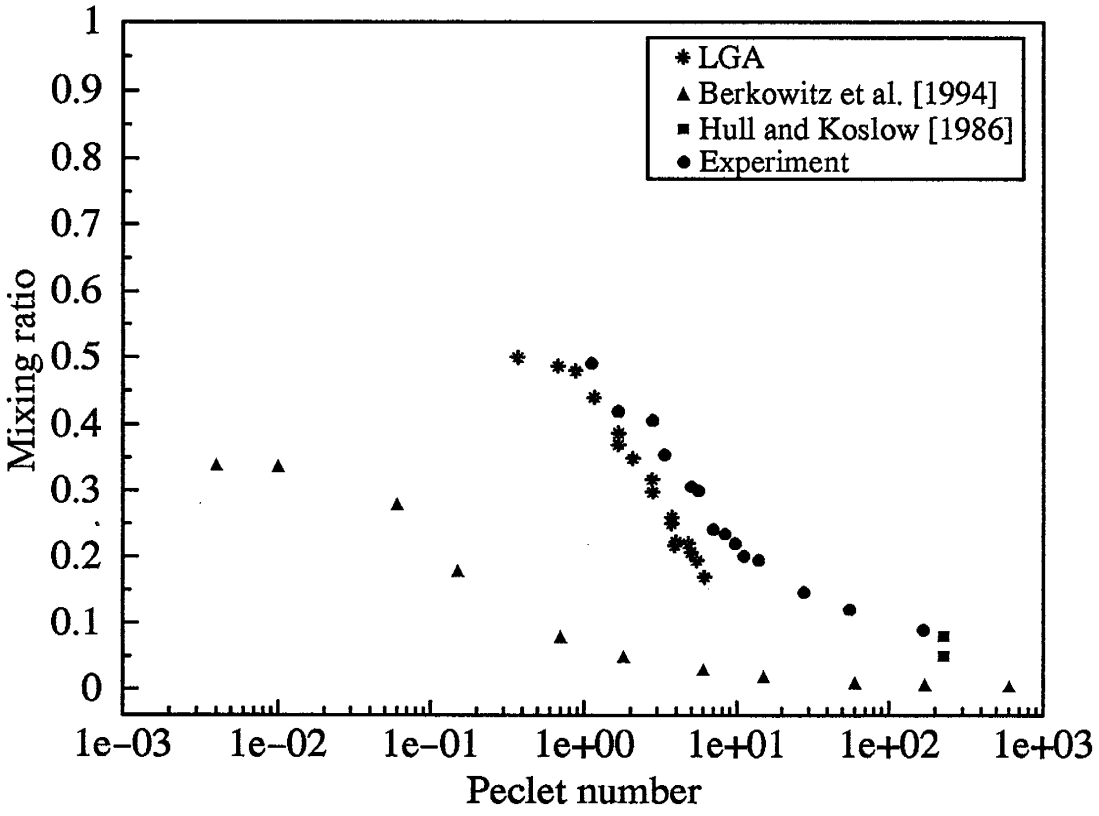

Figure 4.27. Comparisions of the mixing ratios at the fracture junction among the numerical results of Berkowitz et al. [1994], the LGA results, and the averaged experimental results from Br^- concentrations in fracture 3.

transport process at the junction is advection controlled, and streamline routing is appropriate. In contrast, the LGA results and the experimental results show that for Peclet numbers larger than 1, transport at the junction is both advection and diffusion controlled, and the mixing behavior at the junction has a broad transition zone.

The experimental results indicate that the LGA simulation results are basically correct, providing additional evidence that the new tracer particle algorithm is physically correct and can reflect the basic physical processes governing the transport of solute in the flow field. One thing worth mentioning is that the LGA simulations were completed before the experiments began. The agreement between the LGA results and the experimental results shows that the LGA method is capable of predicting macroscopic flow and transport behavior.

The difference between the LGA results and the experimental results is relatively small at low Peclet numbers, but tends to increase as the Peclet number increases. The largest difference is about 0.08 at a Peclet number of 6.10, the largest Peclet number simulated by LGA. This difference could have been caused by a number of influencing factors. First, the LGA simulations have some numerical error. The discreteness of the LGA approximation introduces noise into the simulations which is smoothed with spatial and time averaging. Second, there was some error in the experiments, possibly causing differences in outlet flow rates that might have resulted in forced mixing at the junction, thus affecting the mixing ratios. Third, a post-experiment examination of the model showed that the fracture junction of the physical model was not perfectly symmetric. The apertures of the two outflow fractures were larger than their corresponding inflow fractures, as shown in Figure 4.28. The dividing streamline is about 1.38 times longer than the length of the orthogonal diagonal direction. Although this difference did not affect the Peclet number at the junction under equal flow rate conditions (refer to equation 4.2), the length of flow path at the junction was increased and flow velocity was reduced due to the larger outflow fractures. As a result, solute particle residence time might have increased, allowing more solute particles to diffuse

Figure 4.28. Photo of the physical junction model. Blue dyed water and clear water entered the junction from top and left fractures, respectively, then discharged through right and bottom fractures. The blue dyed water from the top fracture shows the dividing streamline along the diagonal direction of the junction.

across the dividing streamline, increasing the magnitude of diffusive mixing at the junction. Thus, the mixing ratios for this specific geometry could be higher than the corresponding idealized model. These three factors, taken together, can explain the difference between the experiments and the numerical simulations.

To test the influence of this specific geometry on diffusive mixing at the junction. Three LGA simulations were carried out for this specific junction at Peclet numbers of 6.10, 3.71, and 1.67, respectively. The simulated corresponding mixing ratios for these three cases were 0.29, 0.33, and 0.43. Compared to the extrapolated corresponding experimental mixing ratios of 0.27, 0.35, and 0.42, it is clear that the non-perfect geometry of the physical model increased the diffusive mixing at the junction, and could explain all of the difference between experimental and LGA simulated values presented in Figure 4.27.

4.7 Conclusions

All previous experiments on mixing behavior at fracture junctions were conducted at junction Peclet numbers in the range of 200–10,000 [Wilson and Witherspoon, 1976; Hull and Koslow, 1986; Robinson and Gale, 1990]. These studies failed to establish a systematic relationship between the mixing ratio and the junction Peclet number. Our experimental results provided systematic information for junction Peclet numbers in the crucial range of 1–170. On the basis of the experimental results, we concluded that:

(1) The experimental results support our hypothesis (see Chapter 3) that there is a transition zone between diffusion controlled complete mixing and advection dominated streamline routing. The results further indicate that for Peclet numbers around 1, diffusion dominates the transport process resulting in complete mixing at the junction. For Peclet numbers in the range of 1 to 170, both diffusion and advection are important. Mixing in this Peclet number range is referred to as transition zone mixing. Although our experiments did not reach Peclet numbers larger than 200, the experimental results of Hull and Koslow [1986] show that the mixing behavior will be advection controlled, and streamline routing will be appropriate for junction Peclet numbers larger than 200. The experimental results also shows that the prediction made by Hull et al. [1987], about the transition zone corresponding to Peclet numbers in the range of $\sqrt{2}$ to 235, is reasonable.

(2) The streamline routing suggested by Hull and Koslow [1986] and Robinson and Gale [1990] was only valid at Peclet numbers larger than 200; it can not be generalized to represent mixing behavior at small or middle Peclet numbers (P_e in the range of 1–200).

(3) Our experimental results and the LGA simulations indicate that the numerical results of Berkowitz et al. [1994] are invalid, and thus their conclusions that "the concept of complete mixing within a fracture intersection does not properly represent the mass transfer

process at any value of Peclet number...and streamline routing models provided a good approximation for Peclet numbers greater than 1..." are disproved.

(4) The LGA simulations, which preceded the experiments, were basically correct, suggesting that the new tracer particle algorithm is physically correct and can reflect the physical processes governing solute transport, and the LGA can be used to predict previously unobserved experimental phenomena.

(5) The small but systematic differences between the LGA simulations presented in Chapter 3 and the experimental results can be explained by imperfections in the experimental fracture junction geometry. LGA simulations run with this geometry are different from those simulations with the idealized geometry, and are very close to the observed experimental results.

In this research only mixing at an idealized fracture junction with even inflows and outflows was tested. Under natural conditions, fracture junctions are likely to be imperfect and with non–equal flow rates; thus, the mixing behavior at a real fracture junction is more complicated. Nevertheless, results from the current research offer background knowledge for future studies on mixing behavior at real fracture junctions.

References

Abramowitz, M. and I.A. Stegun, Handbook of Mathematical Functions, Dover Publications, Inc., New York, 1972.

Aris, R., On the dispersion of a solute in a fluid flowing through a tube, *Proc. Roy. Soc. A.* 235, 67–77, 1956.

Batchelor, G.K, An Introduction to Fluid Dynamics, Cambridge University Press, London, 1967.

Berkowitz, B., C. Naumann, and L. Smith, Mass transfer at fracture intersections: An evaluation of mixing models, *Water Resour. Res.*, 30(6), 1765–1773, 1994.

Bowman, R.S., Analysis of soil extracts for inorganic and organic tracer anions via high–performance liquid chromatography, *J. Chromatogr.*, 285, 467–477, 1984.

Hull, L.C. and K.N. Koslow, Streamline routing through fracture junctions, *Water Resour. Res.*, 22(12), 1731–1734, 1986.

Robinson, J.W., and J.E. Gale, A laboratory and numerical investigation of solute transport in discontinuous fracture systems, *Groundwater*, 28(1), 25–36, 1990.

Weast, R.C., M.J. Astle, and W.H. Beyer, CRC Handbook of Chemistry and Physics, CRC Press, Boca Raton, Florida, 1987.

Wilson, C.R. and P.A. Witherspoon, Flow interference effects at fracture intersections, *Water Resour. Res.*, 12(1), 102–104, 1976.

Chapter 5: Heuristic Theory on Diffusive Mixing Behavior at Fracture Junctions

5.1 Introduction

The choice of mixing rules at fracture junctions affects the movement and spatial distribution of solute in discrete fracture networks [Hull et al., 1987; Robinson and Gale, 1990]. Laboratory physical experiments have been applied to study these mixing rules. Tracers/dyes were injected into the inflow channels of a physical model, and the mixing behavior at the junction was determined from tracer concentrations in the outflow channels. Experiments, at various levels of sophistication, have been carried out by Wilson and Witherspoon [1976], Hull and Koslow [1986], and Robinson and Gale [1990]. Since diffusive mixing was not observed, they all concluded that streamline routing is appropriate. Hull and Koslow [1986] developed a proportional streamline routing for predicting concentrations in outlet fractures due to forced mixing.

Mathematical/numerical simulations have also been performed to investigate solute mixing behavior at a fracture junction. Philip [1988] studied the advection controlled forced mixing process at an idealized discontinuous fracture junction. He used approximate analytical solutions of Laplace and Stokes flow. He concluded that when the two inlet discharges and the two outlet discharges both differ greatly in magnitude, the proportional routing suggested by Hull and Koslow [1986] for forced mixing at the junction could result in large error. Berkowitz et al. [1994] conducted numerical simulations on mixing behavior at an idealized continuous junction. The flow field in the system was solved following the stream function method suggested by Philip [1988], while a random walk particle tracking method was applied to account for solute diffusion and advection processes. Their results predicted that at Peclet numbers larger than 1, mixing at the junction was advection controlled. Below that there was a diffusion and advection controlled transition zone.

However, under equal flow conditions, they did not observe complete mixing at the junction even at the Peclet number as low as $3x10^{-3}$.

We conducted both numerical simulations and physical experiments to investigate the solute mixing behavior at an idealized fracture junction. Both the LGA simulation results and the experimental results support our hypothesis (see Chapters 3 & 4) that there is a transition zone between diffusion controlled complete mixing and advection dominated streamline routing. The results further indicate that for Peclet numbers smaller than 1, diffusion dominates the transport process, resulting in complete mixing at the junction. For Peclet numbers in the range of 1 to 170, both diffusion and advection are important. Mixing in this Peclet number range is referred to as transition zone mixing. The experimental results show that the streamline routing suggested by Hull and Koslow [1986] and Robinson and Gale [1990] was only valid at Peclet numbers larger than 200 and can not be generalized to represent mixing behavior at small or middle Peclet numbers (P_e in the range of 1-200).

Realizing the impracticality of conducting numerical or physical simulations to investigate the mixing behavior at a junction under all different flow combinations (there are thousands of them), we start from a different point of view to heuristically investigate the mixing behavior. We analyze the physical processes which dominate the mixing behavior and develop a mixing zone concept that appears to explain the solute diffusive mixing behavior at the junction.

5.2 Mixing Behavior at Fracture Junctions: The Physical Process

This heuristic study of mixing behavior around fracture junctions first focuses on the idealized case which has uniform apertures and even flow rates in each fracture. The idealized fracture junction is depicted in Figure 5.1. Flow enters the junction through inflow fractures 1 and 2 and leaves the junction through outflow fractures 3 and 4. The dividing streamline that separates the two inflow regions is along the diagonal of the junction (see Figure 5.1). Supposing that the inflow fracture 1 carries a contaminant with uniform

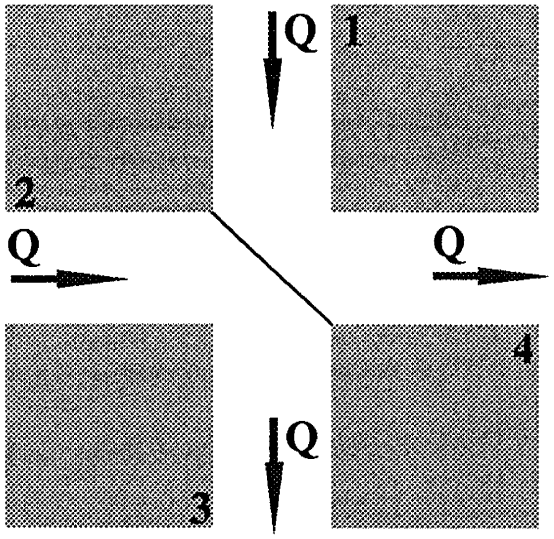

Figure 5.1. Schematic of an idealized fracture junction.

concentration while fracture 2 has no contaminant, when these two inflows meet at the junction, solute mixing occurs. The two processes governing the solute mixing behavior are diffusion and advection. Diffusion causes solute particles to move across the dividing streamline into the flow region formed by fractures 2 and 3, while advection prevents the solute from spreading. Thus, the degree of mixing depends on the strength of each process.

At the idealized junction with equal inflow and outflow, diffusion is the only driving process for mixing at the junction. The magnitude of diffusive mixing depends on how long the solute particles can stay at the junction, i.e., residence time. The solute residence time is determined by the length of the flow path and flow velocity. Instead of calculating the residence time of individual solute particle, we use the average flow velocity, $\overline{V}$, in the inflow fracture 1 and the length of the center streamline at the junction to estimate the representative residence time t_r of the solute

$$t_r = \frac{r}{\overline{V}} \tag{5.1}$$

where r is the length of the center streamline at the junction, measured from the entrance of the junction, and varies from $\sqrt{2} \cdot b/2$ to 0 at the exit of the junction. At high flow velocity

and short residence time, only solute particles that are adjacent to the dividing streamline can move across the dividing streamline into fracture 3 under the influence of diffusion. There is little mixing at the junction. As velocity decreases, solute residence time increases. More solute particles can now diffuse across the dividing streamline, and there is more mixing. When the residence time increases above a certain limit, then all the solute particles entering the junction from fracture 1 can participate in the mixing process. As a result, complete mixing occurs.

Another factor which also plays a key role in the mixing process is the solute diffusion coefficient. It determines how far a solute particle can travel by diffusion in certain time period. The time t_d required for a solute particle to travel a distance of δ and diffuse across the dividing streamline is estimated by

$$t_d = \frac{\delta^2}{D} \tag{5.2}$$

where D is the solute diffusion coefficient. δ varies from 0 to $\sqrt{2} \cdot b/2$ (the width of the flow region formed by flow from fracture 1 to fracture 4 at the junction). Thus, for complete mixing to occur at the junction, all the solute particles entering the junction should have the opportunity to diffuse across the dividing streamline. The minimum residence time required for complete mixing to occur is roughly

$$t_{dc} = \frac{(\frac{\sqrt{2}}{2} \cdot b)^2}{D} = \frac{b^2}{2D} \tag{5.3}$$

If $t_r > t_{dc}$, then the transport process is diffusion controlled, and complete mixing should occur. Otherwise, only part of the solute particles can participate in the mixing process. In the case of $t_r << t_{dc}$, mixing at the junction is dominated by advection, and streamline routing becomes appropriate.

Equations (5.1) and (5.2) state that two competing processes determine the mixing behavior: advection and diffusion. When $t_r < t_d$, only part of the solute particles that are within a distance δ of the dividing streamline can contribute to the mixing process. When

$t_r > t_d$, all of the solute particle that are within δ can take part in the mixing process. Thus, the population of solute particles that can effectively contribute to the mixing process depends of the residence time. We introduce a mixing zone to represent this population. It is defined as a zone inside which there is a high probability that solute particles can diffuse across the dividing streamline to contribute to the mixing process at the junction. The size of the mixing zone is determined by both the residence time and the solute diffusion coefficient. Equating equation (5.1) and (5.2), the mixing zone is described by

$$\delta = \sqrt{\frac{r \cdot D}{\bar{V}}} \tag{5.4}$$

This expression suggests that the size of the mixing zone is proportional to the length of the flow path and the solute diffusion coefficient but inversely proportional to flow velocity. Figure 5.2 is a schematic of mixing zones for different flow velocities. From zone 1 to zone 3, the average velocity in the system decreases. As water flows around the junction from

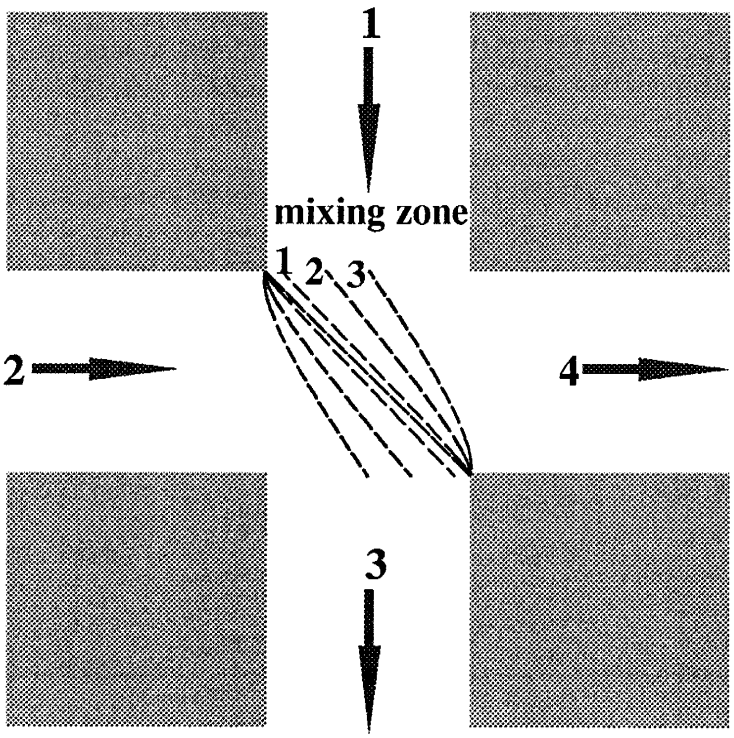

Figure 5.2. Schematic of the mixing zone.

fracture 1 into the junction and toward the outlet fracture 4, the time for a solute particle to stay at the junction decreases; therefore, the size of the mixing zone decreases. The dashed lines in the flow region formed by flow from fracture 2 to fracture 3 represent the corresponding zones of the solute particles that have moved across the dividing streamline. In this flow region, a solute particle tends to move further away from the dividing streamline under the influence of diffusion. The size of the corresponding mixing zones increases as the water flows away from the junction. Figure 5.2 illustrates that as flow velocity decreases, the residence time increases; thus, the size of the mixing zone increases, and more solute particles can take part in the mixing process at the junction.

The Peclet number P_e is used to characterize the transport process mechanism at a fracture junction. It is defined as

$$P_e = \frac{\overline{V} \cdot b\sqrt{2}}{2D} \quad . \tag{5.5}$$

As the Peclet number increases, advection begins to dominate the transport process. On the other hand, as the Peclet number decreases, diffusion begins to play an important role and the influence of advection decreases.

Combining equation (5.4) and equation (5.5), the mixing zone can be rewritten as a function of the Peclet number and the representative flow path r in the junction

$$\delta = \sqrt{\frac{r_{\max} \cdot r}{P_e}} \tag{5.6}$$

where $r_{max}=\sqrt{2} \cdot b/2$. We define the maximum width δ_m of a mixing zone as the value of δ corresponds to $r=r_{max}$

$$\frac{\delta_m}{r_{\max}} = \frac{1}{\sqrt{P_e}} \tag{5.7}$$

The left hand side of equation (5.7) is the ratio of the width of the mixing zone to r_{max}. Equation (5.7) shows that for a fixed value of r_{max}, as the Peclet number decreases, the width of the mixing zone increases; more solute particles can cross the dividing streamline, and

diffusion begins to dominate the transport process. On the contrary, as the Peclet number increases, the width of the mixing zone decreases, and few particles can across the dividing stream line. As a result, the transport process becomes advection controlled.

5.3 Applications of the Mixing Zone Theory in Data Analyses

The experimental relationship between the mixing ratio and the fracture junction Peclet number presented in Chapter 4 (see Figure 4.19) shows that as the Peclet number decreases, the mixing process quickly reaches complete mixing. But it asymptotically approaches advection controlled streamline routing as the Peclet number increases. Why do we see an asymptotic result at high Peclet numbers but not at the lower end? What is the physical process that controls the mixing behavior?

To answer these questions, it is useful to look at the mixing behavior on the basis of the mixing zone concept. The asymptotic character of the mixing ratio can be easily explained by considering the size of the mixing zone at high Peclet numbers. Equation (5.7) indicates that the width of the mixing zone is inversely proportional to the square root of the Peclet number, suggesting that the size of the mixing zone decreases slowly as the Peclet number increases. If the Peclet number P_e=100 at the junction, then the mixing zone width calculated from equation (5.7) is $0.1r_{max}$. As the Peclet number P_e increases to 10,000, the mixing zone width decreases to $0.01r_{max}$. It is clear that although the Peclet number increases 100 times, the width of the mixing zone only decreases 10 times. Thus, even at a Peclet number as high as 10,000, there is still some kind of diffusive mixing occurring at the junction. The mixing ratio asymptotically approaches 0 and advection dominated streamline routing. On the other hand, at relatively low and decreasing Peclet numbers, the size of the mixing zone increases at a much faster rate. The size of the mixing zone soon reaches the limit required for complete mixing to occur at the junction, and the mixing process quickly becomes diffusion controlled.

Using the heuristic mixing zone concept, we can also attempt to explain why complete mixing occurs at the Peclet number around 1. From equation (5.7), the width of the mixing zone is

$$\delta_m = \frac{r_{\max}}{\sqrt{P_e}} = \frac{\frac{\sqrt{2}}{2} \cdot b}{\sqrt{P_e}} \tag{5.8}$$

To achieve complete mixing at the fracture junction, all the solute particles entering the junction from fracture 1 should be included in the mixing zone, which means the width of the mixing zone, δ_m, must be equal to or larger than $\sqrt{2} \cdot b/2$, the half diagonal length of the junction. Thus, complete mixing occurs around P_e=1.

The above examples illustrate that the heuristic mixing zone concept reflects the basic physical processes governing the mixing behavior at the junction. But understanding the physical process is not the only goal of this research; our ultimate goal is to use the mixing zone concept to predict the mixing behavior without conducting numerical simulations or experiments. We use P_{e50} and δ_{m50} to represent the Peclet number and the width of the mixing zone at complete mixing. The width of the diffusive mixing zone can be normalized as

$$M_z = \frac{\delta_m}{\delta_{m50}} = \sqrt{\frac{P_{e50}}{P_e}} \tag{5.9}$$

where M_z is the normalized diffusive mixing zone width. As the size of the mixing zone increases, more solute particles can contribute to the mixing process at the junction. When $M_z \geq 1$, $\delta_m \geq \delta_{m50}$, complete mixing occurs; when M_z=0, δ_m=0, no diffusive mixing can occur; any value of M_z that is in the range of 0 and 1 indicates a diffusion and advection controlled transition mixing zone. Thus, the normalized mixing zone width, M_z, becomes another indicator to represent the magnitude of diffusive mixing at the junction. Because the mixing ratio varies from 0.5 for diffusion controlled complete mixing to 0 for advection controlled streamline routing, to make the normalized mixing zone width comparable with

the mixing ratio, equation 5.9 is rescaled to predict diffusive mixing ratio at the junction

$$M_r = \frac{\delta_m}{2\delta_{m50}} = \frac{1}{2}\sqrt{\frac{P_{e50}}{P_e}} = \begin{cases} 0.5, & M_r \geq 0.5 \\ M_r \end{cases} \qquad 5.10$$

Substituting $P_{e50}=1$ in equation (5.8), the values of M_z are calculated and plotted as the dashed line in Figure 5.3 together with the experimental results of Hull and Koslow [1986], the numerical results of Berkowitz et al. [1994], our LGA results, and our new experimental results. Figure 5.3 clearly shows that the values of (5.10) are very close to the LGA results but below the experimental results. Even with this difference, Figure 5.3 indicates that the heuristic concept of mixing zone is physically correct. The difference between the mixing ratios predicted by the mixing zone and modeled by Berkowitz et al. [1994] is significant for Peclet numbers smaller than 100. The differences between the predicted mixing ratios

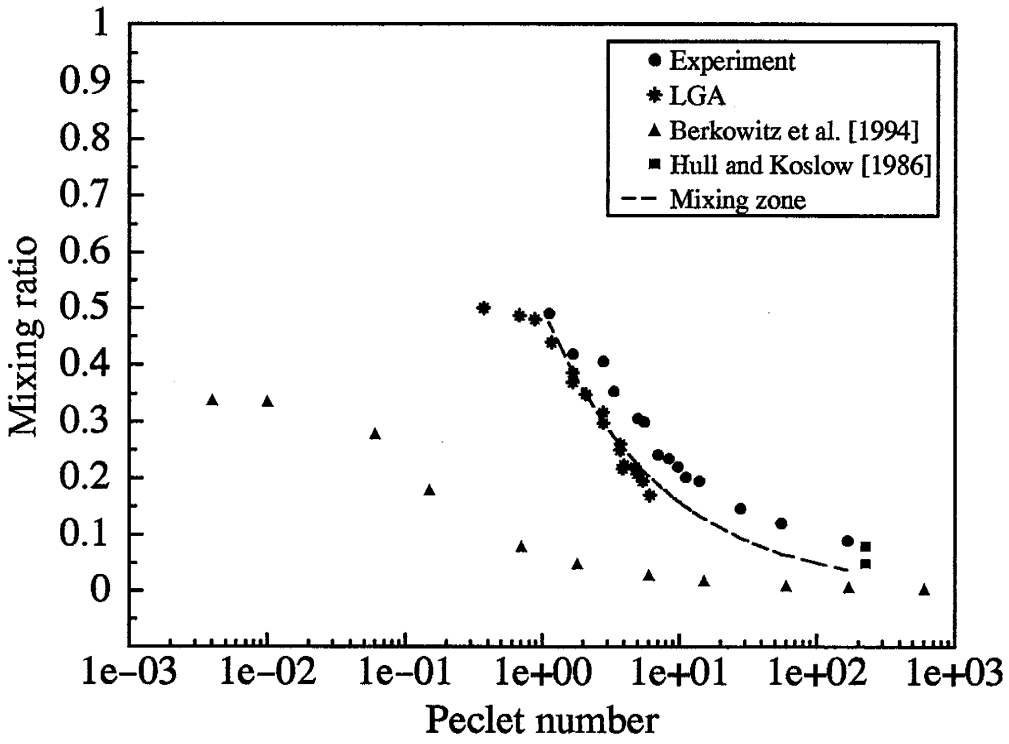

Figure 5.3. Comparision among predicted mixing ratios, the experimental results, and the numerical results.

and the experimental results (refer to Chapter 4) may arise from the following factors. First, the heuristic mixing zone concept is only a rough approximation of the real problem. Second, the physical model used in the experiments was not geometrically perfect, as shown in Figure 4.28 and schematically redrawn in Figure 5.4. Reduced velocity at the junction and the longer flow path can increase the residence time and contribute more mixing at the junction.

Based on the mixing zone concept, we can estimate the influence of the non-perfect junction geometry on the mixing ratios without conducting new numerical simulations or new physical experiments. In Figure 5.4, the apertures of the two outlet fractures are 16% larger than that of their corresponding inflow fractures. The length, $2r'_{max}$, of the dividing streamline that separates the two inflow regions is about 1.38 times longer than the shorter diagonal line, $2r_{max}$. For a perfectly symmetric junction, $r'_{max}=r_{max}=b\sqrt{2}/2$, and the Peclet number is defined in equation (5.5). For the non-perfect physical junction model, the Peclet number is defined as $P_e=\overline{V}r_{max}/D$, and r'_{max} represents the length of the center flow path from the end of inflow fracture 1 to the entrance of the outflow fracture 4. As it is difficult to estimate the change of velocities at the junction, we still use the average inflow velocity

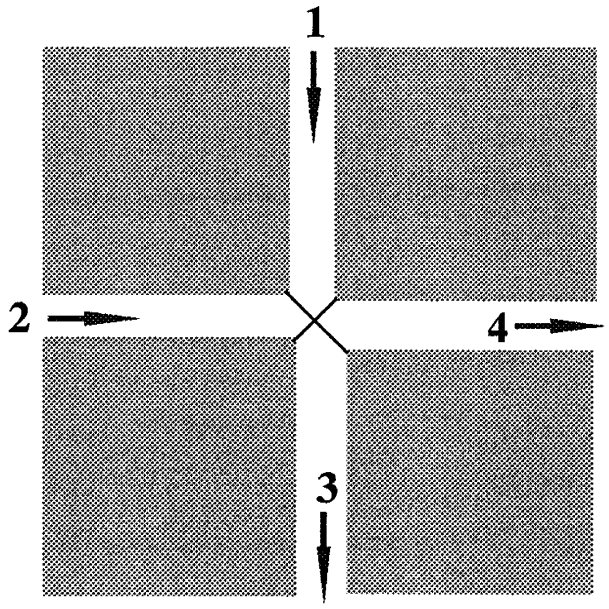

Figure 5.4. Schematic of the real physical model.(not to scale)

in the following calculations. In equation (5.6) with r replaced by r'_{max}, the width of the mixing zone at the real junction is

$$\delta_m = \sqrt{\frac{r'_{\max} \cdot r_{\max}}{P_e}} \qquad 5.11$$

From equation (4.2) in §4.2, we know that junction Peclet numbers does not depend on the apertures of the fractures under equal flow rate conditions. Thus, the non-perfect physical junction model and the idealized model have the same junction Peclet number under the same flow rate condition. Repeating the processes from equations (5.8) to (5.10), the relationship between the mixing ratio at the non-perfect junction and that at the idealized junction is

$$M'_r = \sqrt{\frac{r'_{\max}}{r_{\max}}} \cdot M_r = \begin{cases} 0.5, & M'_r \geq 0.5 \\ M'_r \end{cases} \qquad 5.12$$

Since in the physical model r'_{max}/r_{max}=1.38, equation 5.12 indicates that the mixing ratio at the real physical junction increases systematically. Substituting M_r from equation (5.10) into equation (5.12), the corresponding mixing ratios M'_r at the real physical junction are calculated and plotted in Figure 5.5. Comparing Figures 5.3 and 5.5, we can see that this specific junction geometry can increase diffusive mixing at the junction.

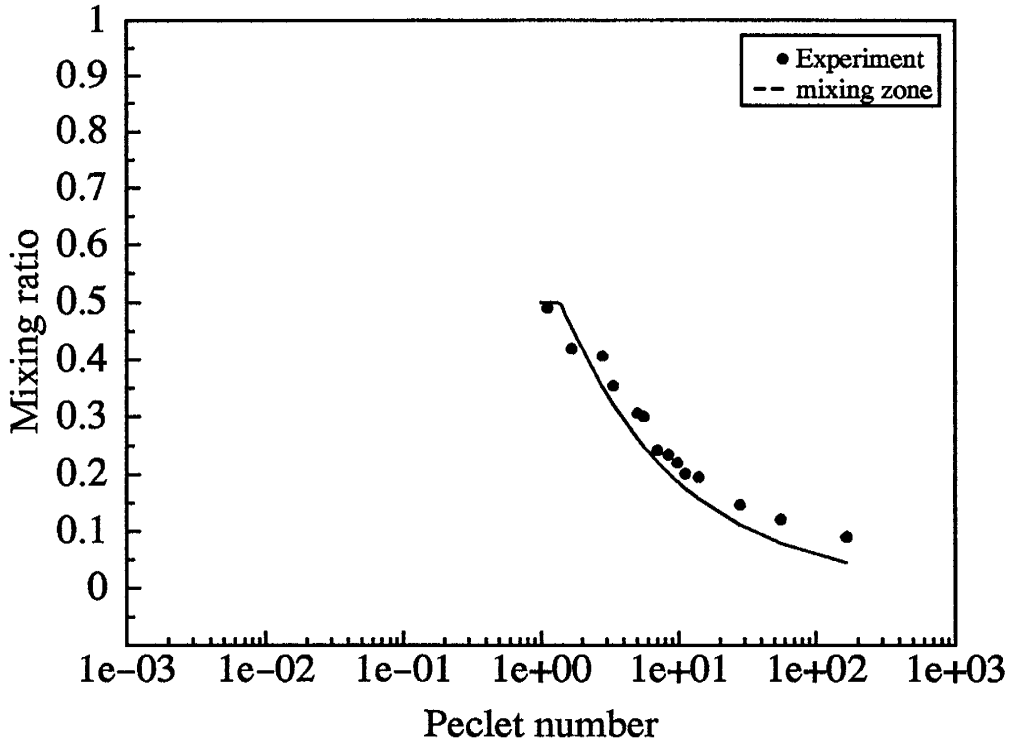

Figure 5.5. Comparison between the experimental results and the predicted mixing ratios for the non-perfect physical junction model.

5.4 Applications of the Mixing Zone Theory to Non-equal Flow Rate Diffusive Mixing Behavior at Fracture Junctions

Under natural conditions due to differences in fracture geometries and hydraulic gradients, the flow rate in each fracture may be different. Figure 5.6 is a schematic of the flow configuration at an idealized fracture junction with non-equal flow rates and the corresponding mixing zones. The inlet flow rates Q_1 and Q_3, are equal, but the outlet flow rates are different with $Q_4 > Q_3$. Some of the water from fracture 2 crosses the junction, joins the flow from fracture 1, and then discharges through fracture 4. Due to the cross flow, the solute concentration in fracture 4 decreases, which is is referred to as 'forced mixing' by Robinson and Gale [1990].

There are two schematic dividing streamlines in the Figure 5.6. The upper one separates inflows coming from fractures 1 and 2. The lower one separates the inflow from fracture 2

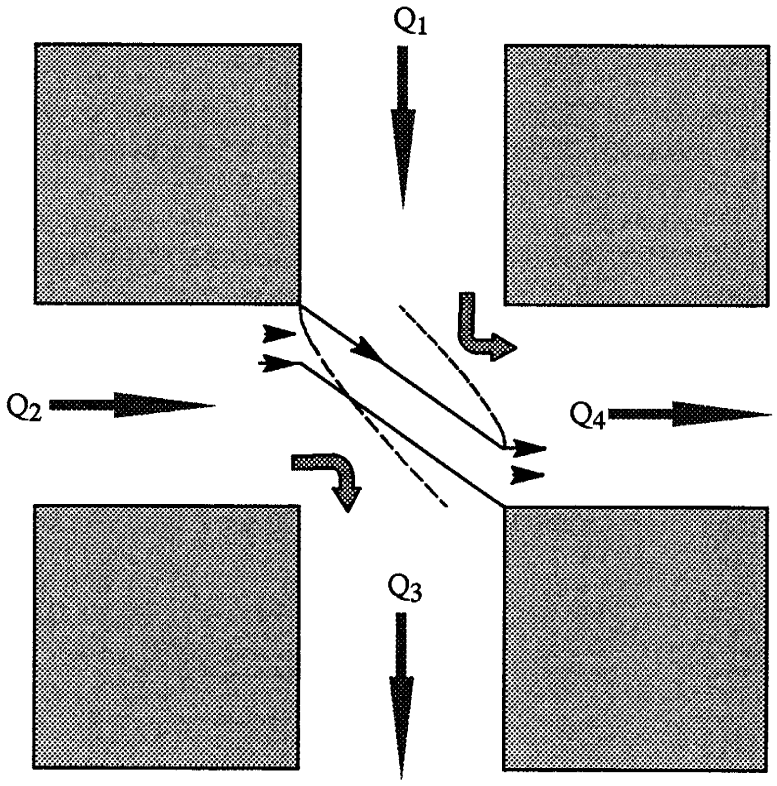

Figure 5.6. Schematic of the mixing zone under non-equal flow rate condition.

into two parts: the cross flow which discharges into outflow fracture 4, and the outflow which discharges into fracture 3. Solute particles that enter the junction from fracture 1 will discharge into fracture 4 unless there is sufficient diffusive mixing to carry some of them across both dividing streamlines. The dashed lines represent the boundary for diffusive mixing in the junction. The upper dashed line represents the region of the solute particles that can diffuse across the upper dividing streamline into the cross-flow region, while the lower dashed line represents the zone that can be occupied by solute particles which have crossed the upper dividing streamline. Because this zone overlaps the cross-flow region, only the particles that are able to diffuse out of the cross-flow region contribute to diffusive mixing in fracture 3. The solute particles which can not escape from the cross-flow region will be carried into fracture 4 to join the main solute body. When the flow velocity is very high or the magnitude of the cross-flow is large, the lower dashed line will be included inside the cross-flow region. Solute particle can not escape from the cross-flow region, and no solute particle in fracture 3 will be found. Thus, cross-flow at the junction reduces the magnitude of diffusive mixing.

Hull and Koslow [1986] developed a formula to predict solute concentrations in the two outflow fractures by assuming that streamlines do not cross (no diffusive mixing in the junction). This formula is also called proportional routing because concentrations in each outlet fracture are proportional to the magnitude of cross flow. In the case shown in Figure 5.4, the proportional routing predicts that concentrations in outflow fractures 3 and 4 are

$$\begin{aligned} C_4 &= C_1 \cdot \frac{Q_1}{Q_4} + C_2 \cdot (1 - \frac{Q_1}{Q_4}) \\ C_3 &= C_2 \end{aligned} \tag{5.13}$$

In our case, let C_2=0 and C_1=1, giving C_3=0, and C_4=$(C_1Q_1)/Q_4$. Proportional routing assumes that only forced mixing occurs. The LGA results presented in Chapter 3 have shown that even with a cross-flow, diffusive mixing can still occur under some conditions. Using

the mixing zone concept, we can estimate the influence of cross-flow on diffusive mixing at the junction.

As the flow at the junction is no longer symmetric, determining the actual dividing streamline and the length of the center flow path for the actual flow field is difficult. As an approximation, we treat the non-equal flow rate system as an equal one for estimating the Peclet number and the size of the mixing zone. We can expect that this kind of approach may induce large error when the magnitude of the cross-flow is large. The Peclet number at the junction can be estimated as

$$\overline{P}_e = \frac{\overline{V} \cdot \frac{\sqrt{2}}{2} b}{D} \tag{5.14}$$

where $\overline{V}$ is the average inflow velocity of the system. Substituting the average Peclet number into equation (5.8), the width of the diffusive mixing zone is estimated by

$$\delta_m = \frac{\frac{\sqrt{2}}{2} \cdot b}{\sqrt{\overline{P}_e}} \tag{5.15}$$

But due to cross-flow from fracture 2, only some of the solute particles can escape from the cross-flow region into fracture 3. The effective size of the mixing zone that can contribute to diffusive mixing in fracture 3 is reduced. The effective size of the mixing zone depends on the width of the cross-flow region which can be estimated by assuming that the width of the cross-flow region is proportional to the relative magnitude of the cross-flow in the outlet fracture 4. The amount of flow from fracture 2 that crosses the junction discharges into fracture 4 is (Q_4-Q_1). The width of the cross-flow region δ_f is

$$\delta_f = \frac{(Q_4 - Q_1) \cdot b}{Q_4} \tag{5.16}$$

From equations (5.15) and (5.16), the actual size of the mixing zone that can contribute to diffusive mixing at the junction becomes

$$\delta_{mix} = \delta_m - \delta_f \tag{5.17}$$

$\delta_{mix}>0$ indicates that the width of the mixing zone is larger than that of the cross-flow region. Under this condition both forced mixing and diffusive mixing occur. When $\delta_{mix}<0$, the width of the diffusive mixing zone is smaller than that of the cross-flow region, and the diffusive mixing zone is included inside the cross-flow region. No effective diffusive mixing can occur, and no solute particle will move into fracture 3.

The mixing ratio determined from the normalized size of the mixing zone in equation (5.10) only corresponds to the equal flow rate case. Under non-equal flow rate conditions, it must be modified. The cross-flow from fracture 2 reduces the magnitude of outflow in fracture 3. The normalized flow in fracture 3 corresponding to the average flow in the system is

$$Q_{n3} = \frac{Q_3}{\frac{1}{2}(Q_2 + Q_1)} \tag{5.18}$$

Under equal flow rate conditions, the normalized flow in fracture 3 is 1. In the case of equal inflows but non-equal outflows, if $Q_3<Q_1=Q_2$, then the normalized flow rate, Q_{n3}, in fracture 3 will be smaller than 1. If the effective diffusive mixing zone is the same for both the equal flow rate case and the non-equal flow rate case, then the non-equal flow rate case will have a large diffusive mixing ratio due to the small flow rate in fracture 3. Thus, the diffusive mixing ratio estimated from the normalized mixing zone has to account for the relative difference in outlet flow rates. On the basis of equation (5.10), the mixing ratio for this non-equal flow case can be estimated by

$$M_r = \frac{1}{2}\frac{\delta_{mix}}{Q_{n3} \cdot \delta_{m50}} \tag{5.19}$$

where δ_{m50} is the width of the mixing zone corresponds to complete mixing at the average Peclet number of 1. From equation (5.15), $\delta_{m50}=\sqrt{2}l(2b)$. A zero or negative M_r indicates that the mixing zone is included inside the cross-flow region, no solute particles can diffuse out from this region into fracture 3, and no effective diffusive mixing occurs at the junction. When $M_r \geq 0.5$, diffusion controlled complete mixing occurs. Substituting δ_{m50} into

equation (5.19) and redefining the range of M_r, we have

$$M_r = \frac{1}{\sqrt{2}} \frac{\delta_{mix}}{Q_{n3} \cdot b} = \begin{cases} 0.5, & M_r > 0.5 \\ M_r, & 0 \leq M_r \leq 0.5 \\ 0, & M_r < 0 \end{cases} \tag{5.20}$$

Equation 5.20 can be used to estimate the diffusive mixing ratios at the fracture junctions under equal inflow rates but non-equal outflow rates conditions with $Q_4 > Q_3$. A similar formula can also be derived for the general cases with non-equal inflow and non-equal outflow rates. As no detailed information on the flow field at the junction is required, equation 5.20 is easy to apply and can offer information about the diffusive mixing behavior.

The heuristic formula (5.20) is tested by comparing the predicted mixing ratios with the simulated ones in Chapter 3. Two LGA simulations were performed in that chapter to investigate the mixing behavior under equal inflow but non-equal out flow conditions. The first case was run with an average inflow velocity of 0.13 lu/sts in fractures 1 and 2, and a Peclet number of 5.45. With 26% of the water from fracture 2 crossing the junction and discharging into fracture 4, the average outflow velocities in fracture 3 and 4 were 0.096lu/sts and 0.170lu/sts, respectively. The width of the cross-flow region estimated from equation (5.16) was $\delta_f = 0.21b$. From equation (5.18), the normalized flow in fracture 3 was $Q_{n3} = 0.74$. The diffusive mixing zone width calculated from equation (5.15) was $\delta_m = 0.28b$. Thus, the effective diffusive mixing zone width that contributed to diffusive mixing at the junction was $\delta_{mix} = 0.07b$. With these values, the heuristic formula predicts a diffusive mixing ratio of $M_{r3} = 0.067$ in fracture 3. The corresponding diffusive mixing ratio determined from the LGA simulation was identical to this estimated value.

The second case was run at a relatively low Peclet number of 1.39. The inflow rate in fractures 1 and 2 was 0.0415lu/sts. Almost 74% of the fluid from fracture 2 crossed the junction and discharged into fracture 4; the outflow rates in fracture 3 and fracture 4 were 0.011lu/sts and 0.072lu/sts, respectively. The width of the cross-flow region was $\delta_f = 0.42b$.

The normalized flow rate in fracture 3 was Q_{n3}=0.27. From equation (5.11), the width of the diffusive mixing zone was δ_m=0.60b. The effective diffusive mixing zone width was δ_{mix}=0.18b. Using equation (5.20), the estimated diffusive mixing ratio was 0.47. The mixing ratio determined from the numerical simulation was 0.34. Compared to the high Peclet number case, we see that in the case of large cross-flow, using equation (5.20) can introduce a large error in the predicted diffusive mixing ratio.

In both the cases, the proportional routing developed by Hull and Koslow predicted a diffusive mixing ratio of M_r=0. It is clear that the proportional routing is only appropriate under very high Peclet number conditions or when the size of the diffusive mixing zone is smaller than the cross-flow region.

Under more general conditions when the flow rates in the inflow outflow fractures are not equal, the mixing process becomes more complicated. An LGA simulation was run with the inflow velocities of 0.082lu/sts and 0.041 lu/sts in fractures 1 and 2, respectively. The average outflow velocity in fractures 3 was 0.034lu/sts and in fracture 4 was 0.089lu/sts. The Peclet number at the junction was 2.49 which corresponds to a diffusive mixing zone width of δ_m=0.448b. The width of the cross-flow region calculated from equation (5.16) was 0.078b, the average flow velocity in the system was 0.0615lu/sts, and the normalized flow in fracture 3 was Q_{n3}=0.55. Under this flow condition, forced mixing occurred in fracture 4 but only diffusive mixing in fracture 3. The mixing ratio C_3/C_1 estimated from the simulation was 0.48. Note, this high mixing ratio was due to the non-equal inflow in the system; it only represents the relative magnitude of the concentration in fracture 3 and does mean mixing at the junction was almost complete. Under non-equal inflow rate conditions, in order to compare the mixing ratio predicted by equation (5.20) with the simulated mixing ratio, the concentrations in fracture 3 needs to be normalized to the complete mixing concentration instead of the source concentration. The flow corrected mixing ratio was $C_3(Q_1+Q_2)/(2C_1Q_1)$=0.36. Using the mixing zone concept, the effective mixing zone width

that contributed to the diffusive mixing in fracture 3 was δ_m=0.37b. The heuristic formula (5.20) predicts a mixing ratio of 0.48. Compared with the simulated mixing ratio of 0.36, the difference is 0.12. This large difference arises mainly from the approximation of using average velocity to represent the flow in the actual system.

5.5 Conclusions and Discussion

The heuristic mixing zone concept and model is shown to be physically correct by the LGA simulations and the experimental results and is able to reflect the physical processes governing solute transport at fracture junctions. The mixing zone concept gives the diffusive mixing behavior under non-equal flow rate conditions a clear physical explanation.

The heuristic formula developed for predicting diffusive mixing ratios under equal flow rate conditions proved to be valid. The generalized formula which takes into account the influence of cross-flow can be used to estimate the diffusive mixing ratios, but the errors increase as the magnitude of the inflows differs largely. Compared to the proportional streamline routing proposed by Hull and Koslow [1986], the heuristic formula is able to take into account the influence of diffusive mixing at a junction.

In this section, we demonstrate the applications of the mixing zone concept in predicting diffusive mixing ratios at an idealized fracture junction, yet the mixing zone concept needs to be further developed to take into account the influence of non-equal apertures on diffusive mixing.

References

Berkowitz, B., C. Naumann, and L. Smith, Mass transfer at fracture intersections: An evaluation of mixing models, *Water Resour. Res.*, 30(6), 1765–1773, 1994.

Hull, L.C. and K.N. Koslow, Streamline routing through fracture junctions, *Water Resour. Res.*, 22(12), 1731–1734, 1985.

Hull, L.C., J.D. Miller and T.M. Clemo, Laboratory and simulation studies of solute transport in fracture networks, *Water Resour. Res.*, 23(8), 1505–1513, 1987.

Philip, J.R., The fluid mechanics of fracture and other junctions, *Water Resour. Res.*, 24(2), 239–246, 1988.

Robinson, J.W., and J.E. Gale, A laboratory and numerical investigation of solute transport in discontinuous fracture systems, *Groundwater*, 28(1), 25–36, 1990.

Wilson, C.R. and P.A. Witherspoon, Flow interference effects at fracture intersections, *Water Resour. Res.*, 12(1), 102–104, 1975.

Chapter 6: Conclusions and Recommendations

The major contributions and conclusions of this work to the research of mixing behavior at fracture junctions can be summarized as follows:

(1) All previous experiments on mixing behavior at fracture junction were conducted at junction Peclet numbers in the range of 200–10,000 [Wilson and Witherspoon, 1976; Hull and Koslow, 1986; Robinson and Gale, 1990]. These studies failed to establish a systematic relationship between the mixing ratio and the junction Peclet number. Our experimental results provided that systematic information for junction Peclet numbers in the crucial range of 1–170.

(2) Both the LGA simulation results and the experimental results support our hypothesis (see Chapters 3 & 4) that there is a transition zone between diffusion controlled complete mixing and advection dominated streamline routing. As suggested by our hypothesis and Hull et al. [1987] the results further indicate that for Peclet numbers smaller than 1, diffusion dominates the transport process resulting in complete mixing at the junction. For Peclet numbers in the range of 1 to 170, both diffusion and advection are important. Mixing in this Peclet number range is referred as transition zone mixing. Although our experiments did not reach Peclet numbers larger than 200, the experimental results of Hull and Koslow [1986] show that the mixing behavior will be advection controlled, and streamline routing will be appropriate for junction Peclet numbers larger than 200. Hull et al.'s [1987] estimate for the upper range of the transition zone, P_e=235, is consistent with our findings.

(3) The experimental results clarified previous arguments on mixing rules at fracture junctions. The streamline routing suggested by Hull and Koslow [1986] and Robinson and Gale [1990] was shown to be only valid at Peclet numbers larger than 200; it can't be generalized to represent mixing behavior at small or middle Peclet numbers (P_e in the range of 1–200).

(4) Our experimental results and the LGA simulations indicate that the numerical results of Berkowitz et al. [1994] are invalid, and thus their conclusions that "the concept of complete mixing within a fracture intersection does not properly represent the mass transfer process at any value of Peclet number...and streamline routing models provided a good approximation for Peclet numbers greater than 1..." are disproved.

(5) The proportional routing proposed by Hull and Koslow [1986] for predicting forced mixing concentrations in outflow fractures was adequate only at very high Peclet numbers. When the junction Peclet number is in the lower range (less than 5), diffusive mixing at the junction play an important role, the error of the proportional routing can be quite large.

(6) A heuristic mixing zone concept and model was developed to provide a physical explanation for the diffusive mixing behavior at fracture junctions. This new concept and model was shown to be consistent with the LGA simulations and the experimental results, and helped to explain the experimental observations. A heuristic formula is proposed for predicting diffusive mixing behavior at continuous fracture junctions under equal and non-equal flow rate conditions. The LGA simulations indicate that predictions from this formula are reasonably good when the differences between the two inflow rates or the two outflow rates are relatively small, but significant errors can arise otherwise. Nevertheless, this formula is useful in offering information on the importance of diffusive mixing at a fracture junction.

(7) A new tracer particle algorithm for simulating solute transport with the LGA method was developed and applied in the research of the mixing behavior at fracture junctions. A series of test problems, and the comparison between fracture junction LGA simulations and experimental results, indicate that the new tracer particle algorithm is basically correct and reflects the physical processes governing the transport of a non-reactive solute.

(8) The LGA simulations [Wilson et al., 1993; Li and Wilson, 1994] which preceded the experiments was shown to be physically correct by the experimental results, suggesting that the LGA method can simulate macroscopic flow and transport behavior properly.

In this research, we only examined the solute mixing behavior at an idealized fracture junction (two orthogonal fractures with equal apertures), still, the primary results from this research offers background knowledge for future research on the mixing behavior at fracture junctions with more complex geometries.

In the field, fractures have different apertures, orientations, rough walls, and non-equal flow rates. Under such conditions, the mixing behavior is much more complicated. On the basis of the current research, the following problems are suggested for future research:

(1) Perform experiments and numerical simulations to investigate the influence of non-equal flow rates on mixing (diffusive mixing and forced forced mixing) behavior at fracture junctions in the Peclet number range of 0.1-200. The results from these experiments can help elucidate the importance of diffusive mixing versus forced mixing under different flow conditions.

(2) Perform experiments and simulations to study the influences of fracture junction geometries (fractures with different apertures, different intersection angles, and wall roughness) on the mixing process at fracture junctions.

(3) Generalize the heuristic mixing zone concept to include cases involving non-equal apertures and non-equal flow rates and seek the possibility of applying the mixing zone concept to predict mixing behavior at non-ideal fracture junctions.

(4) Build a physical fracture network model and perform experiments and numerical simulations to test the new mixing rules.

Appendix A: LGA Simulation Results

Table A.1. LGA simulation results of mixing behavior at an idealized fracture junction.

Mean den. (n)	D (lu^2/sts)	$\overline{V}$ (lu/sts)	P_e	Mixing ratio M_r
1.37	0.81	0.012	0.37	0.500
1.64	0.74	0.020	0.68	0.508
2.03	0.66	0.023	0.88	0.480
2.08	0.65	0.030	1.16	0.440
2.28	0.62	0.041	1.67	0.387
1.60	0.75	0.050	1.67	0.370
2.27	0.62	0.051	2.08	0.349
2.48	0.59	0.065	2.78	0.317
1.73	0.72	0.080	2.79	0.298
2.94	0.54	0.080	3.73	0.260
1.78	0.71	0.105	3.71	0.250
1.84	0.69	0.110	3.97	0.223
1.83	0.70	0.133	4.78	0.220
2.17	0.63	0.098	3.90	0.217
2.19	0.63	0.125	4.99	0.207
2.38	0.60	0.130	5.44	0.195
2.67	0.56	0.137	6.10	0.170

Appendix B: Experimental set up and Results

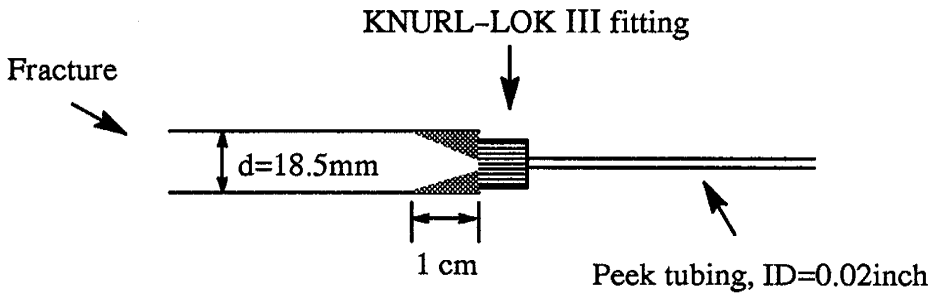

Figure B.1. Cross-sectional schematic of the structure at the inflow/out-flow end of each fracture.

The variations of water density with temperature at 1 atm can be estimated as [Weast et al., 1987]

$$\varrho = (999.83952 + 16.945176t - 7.9870401x10^{-3}t^2 - 46.170461x10^{-6}t^3 + 105.56302x10^{-4}t^4 - 280.54253x10^{-13}t^5)/(1 + 16.879850x10^{-3}t) \quad \text{(B.1)}$$

where t is temperature in degree centigrade.

The changes of dynamic viscosity with temperature is given by Helmholtz equation

$$\mu = \frac{\mu_0}{1 + 0.03368t + 0.00022099t^2} \quad \text{(B.2)}$$

$\mu_0 = 1.783x10^{-3}\ Pa \cdot s$ is the dynamic viscosity of water at 0° C

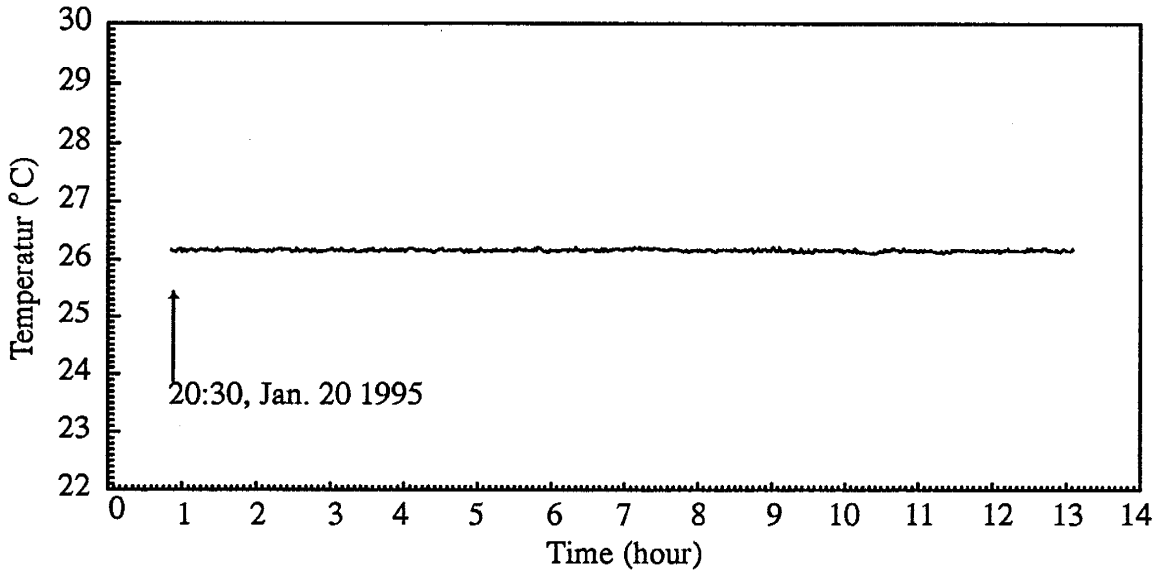

Figure B.2. Circulation water temperature variations in the pump jackets with time.

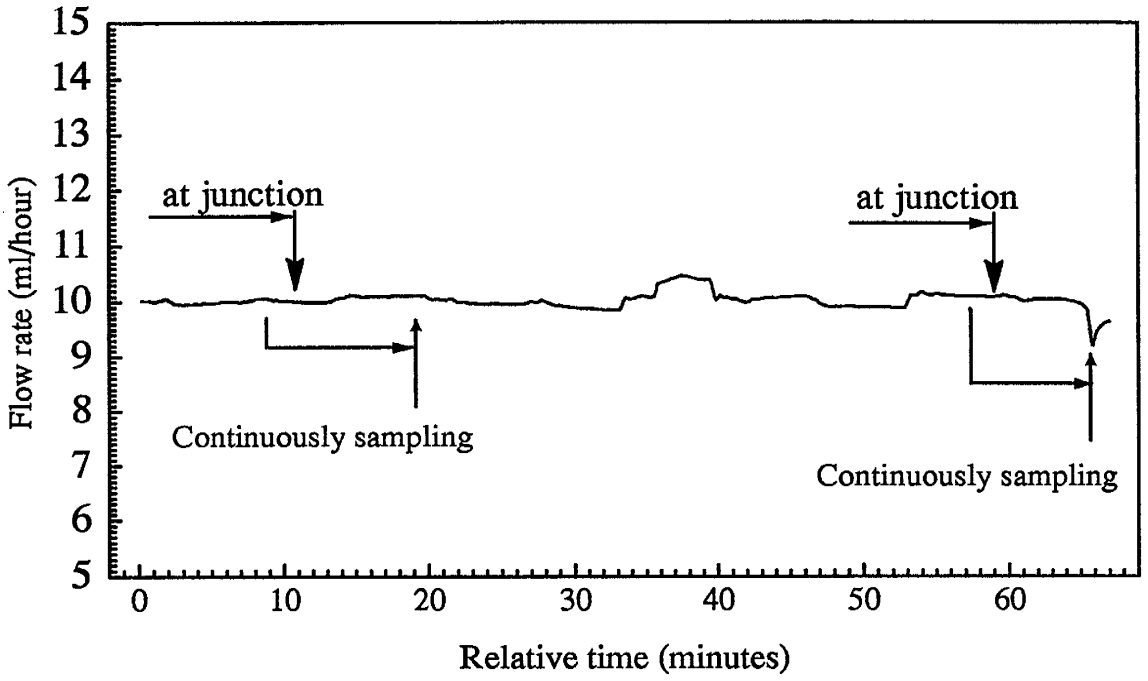

Figure B.3. Flow rate variations during the experiment at flow rate 10ml/hour. The average flow rate was 10.017ml/hour (Group–1).

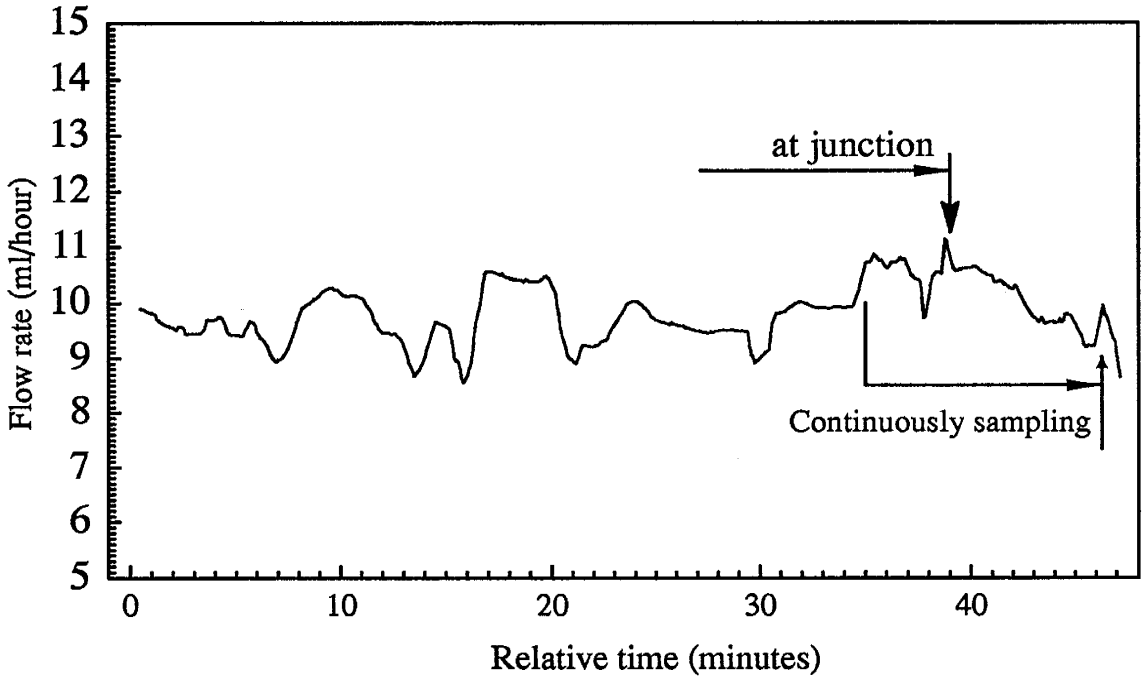

Figure B.4. Flow rate variations during the experiment at flow rate 10ml/hour. The average flow rate was 9.8054ml/hour (Group–2).

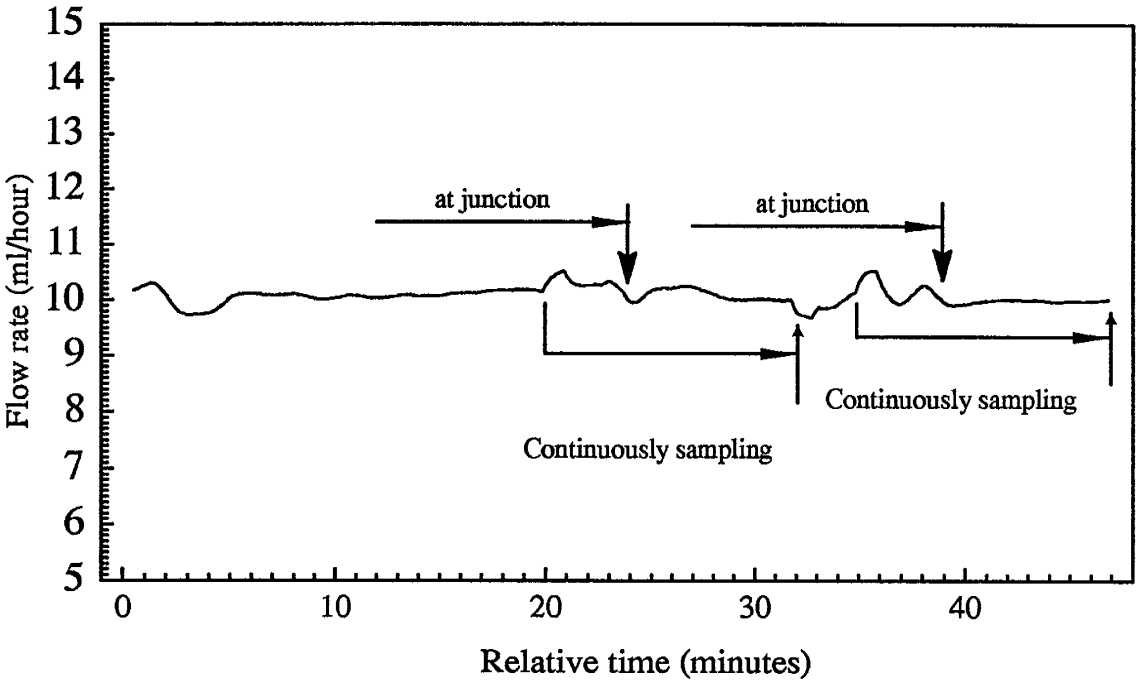

Figure B.5. Flow rate variations during the experiment at flow rate 10ml/hour. The average flow rate was 10.078ml/hour (Group-3).

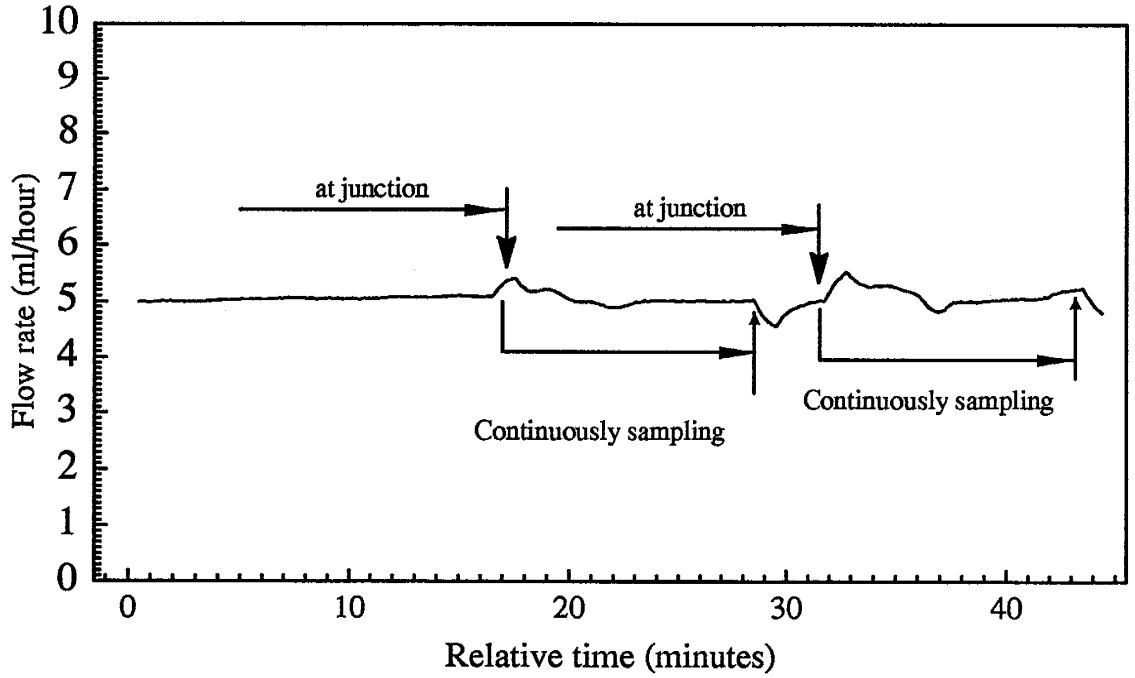

Figure B.6. Flow rate variations during the experiment at flow rate 5ml/hour. The average flow rate was 5.061ml/hour (Group-3).

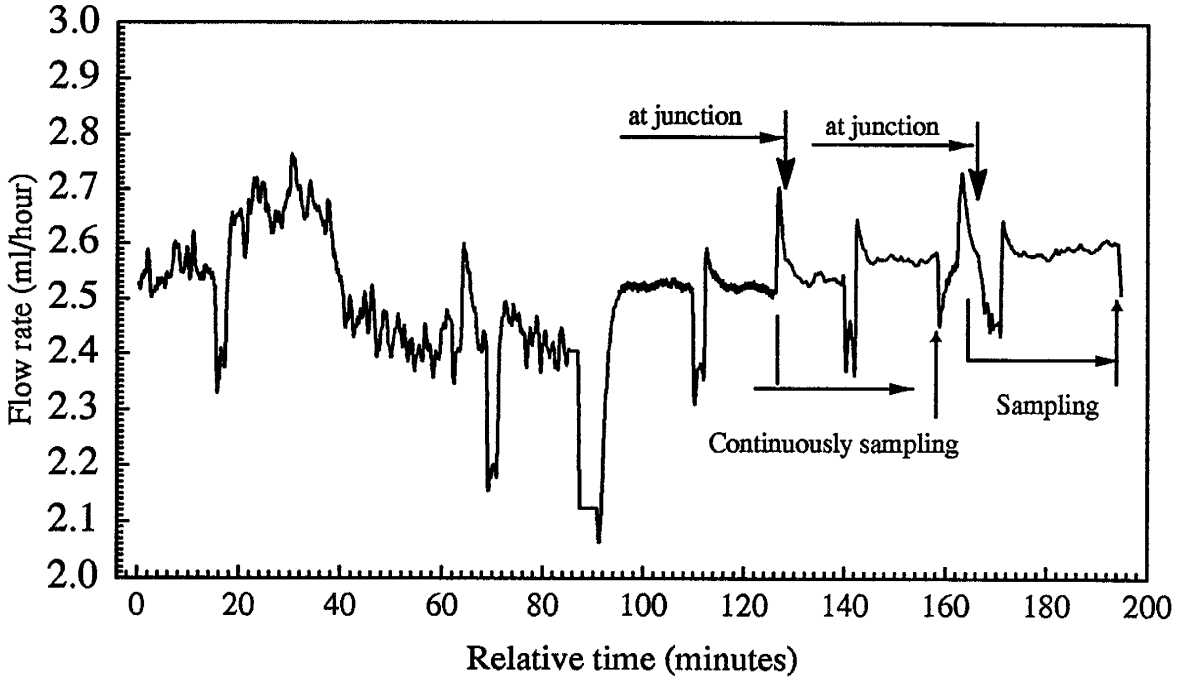

Figure B.7. Flow rate variations during the experiment at flow rate 2.5ml/hour. The average flow rate was 2.5192ml/hour (Group-1).

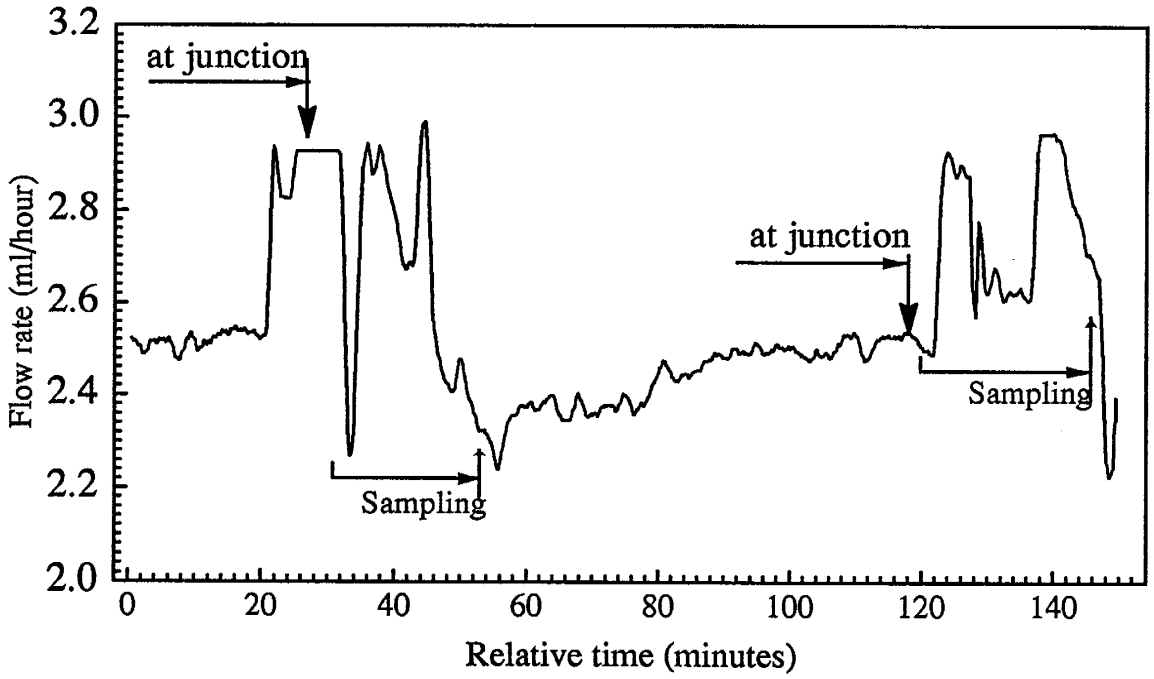

Figure B.8. Flow rate variations during the experiment at flow rate 2.5ml/hour. The average flow rate was 2.5677ml/hour (Group-3).

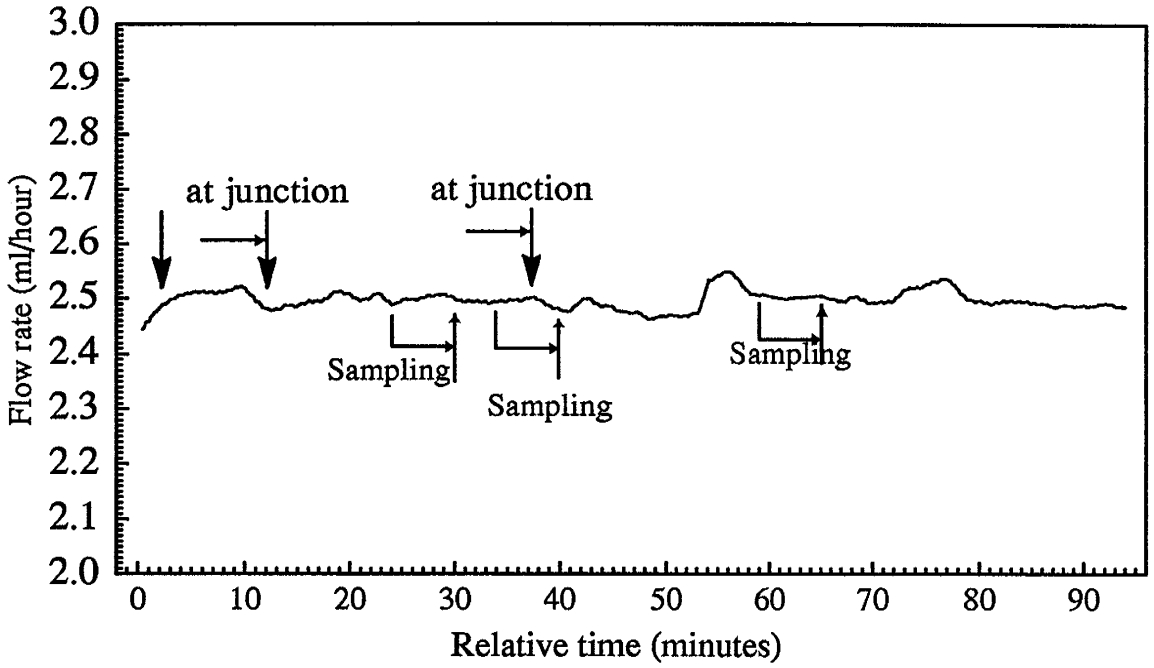

Figure B.9. Flow rate variations during the experiment at flow rate 2.5ml/hour. The average flow rate was 2.4972ml/hour (Group-6).

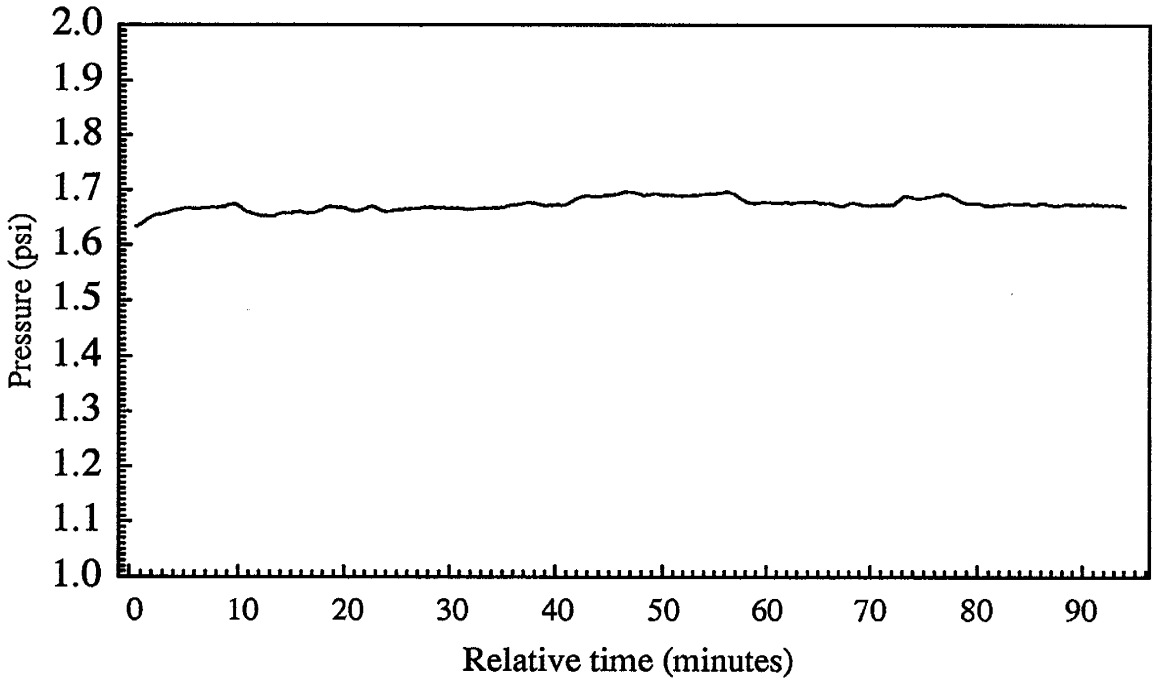

Figure B.10. Pressure variations with time during experiment at flow rate 2.5ml/hour (Group-6).

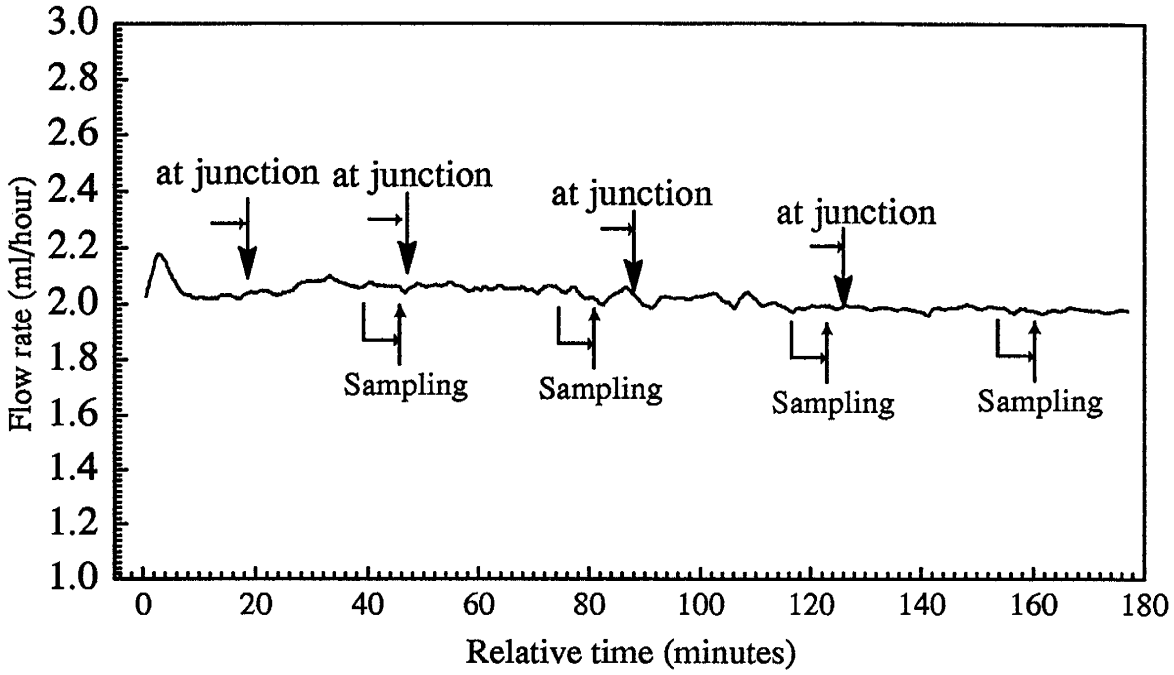

Figure B.11. Flow rate variations during the experiment at flow rate 2.0ml/hour. The average flow rate was 2.0245ml/hour (Group-5).

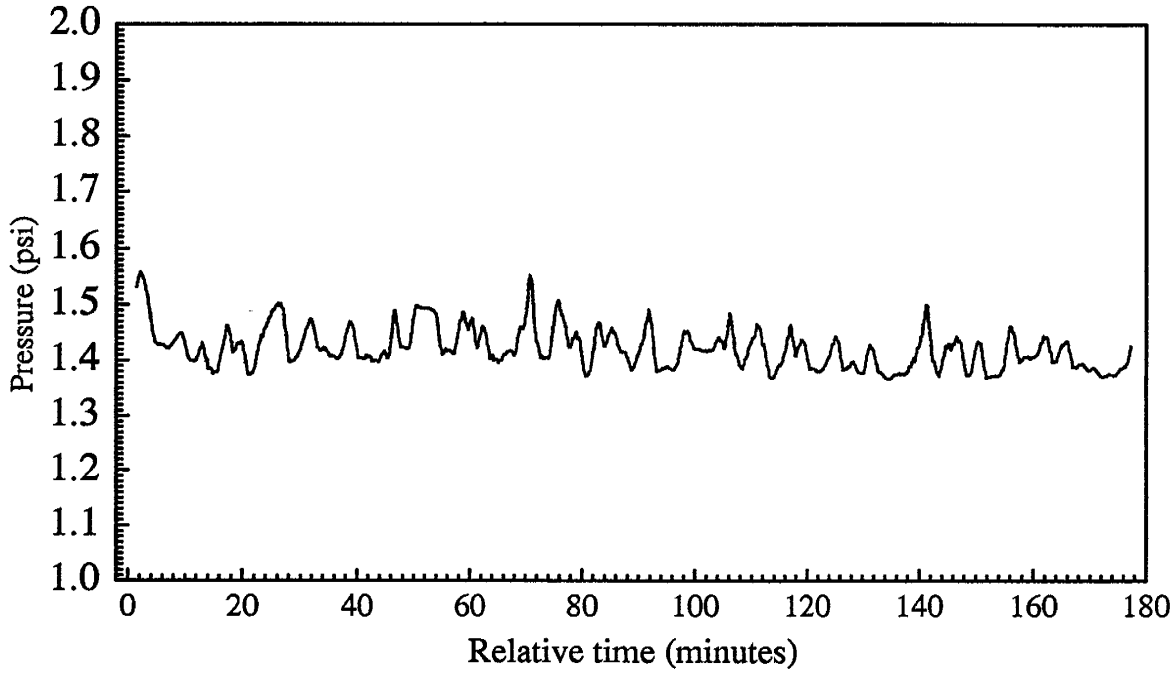

Figure B.12. Pressure variations with time during the experiment at flow rate 2.0ml/hour (Group-5).

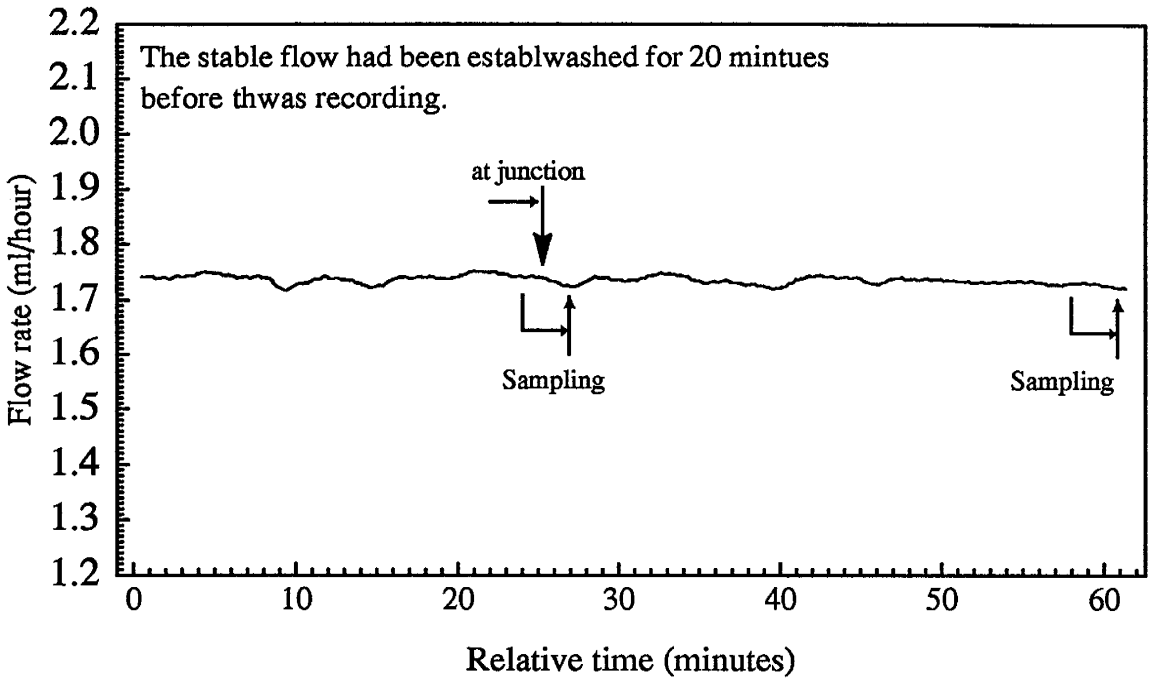

Figure B.13. Flow rate variations during the experiment at flow rate 1.75ml/hour. The average flow rate was 1.726ml/hour (Group-5).

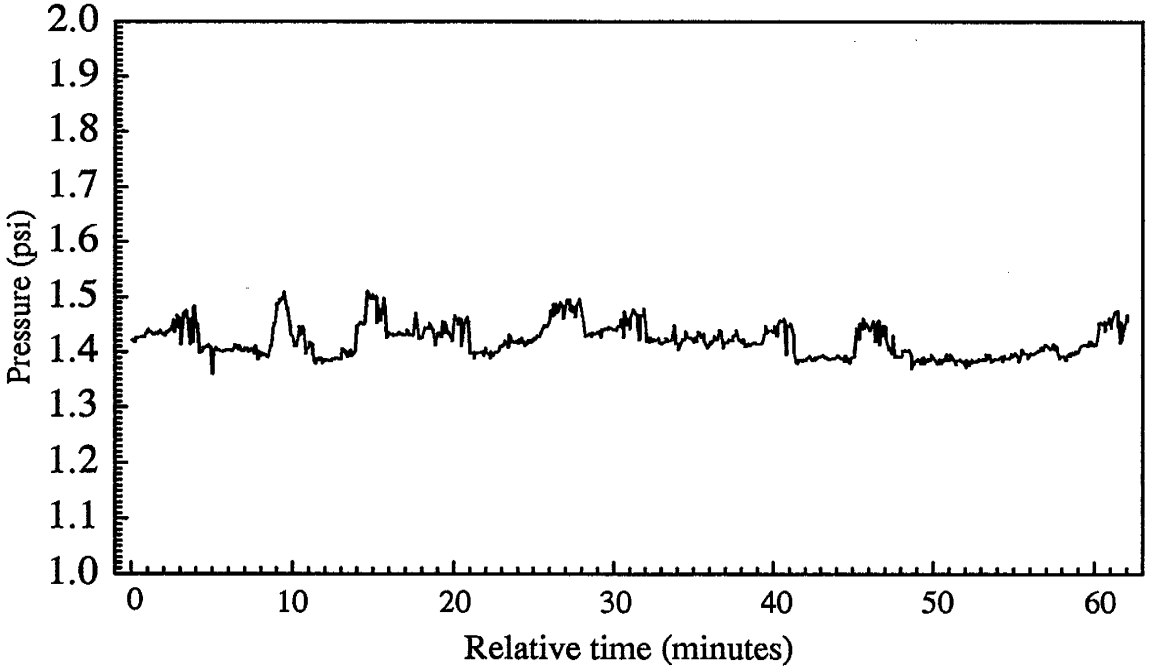

Figure B.14. Pressure variations with time during the experiment at flow rate 1.75ml/hour (Group-5).

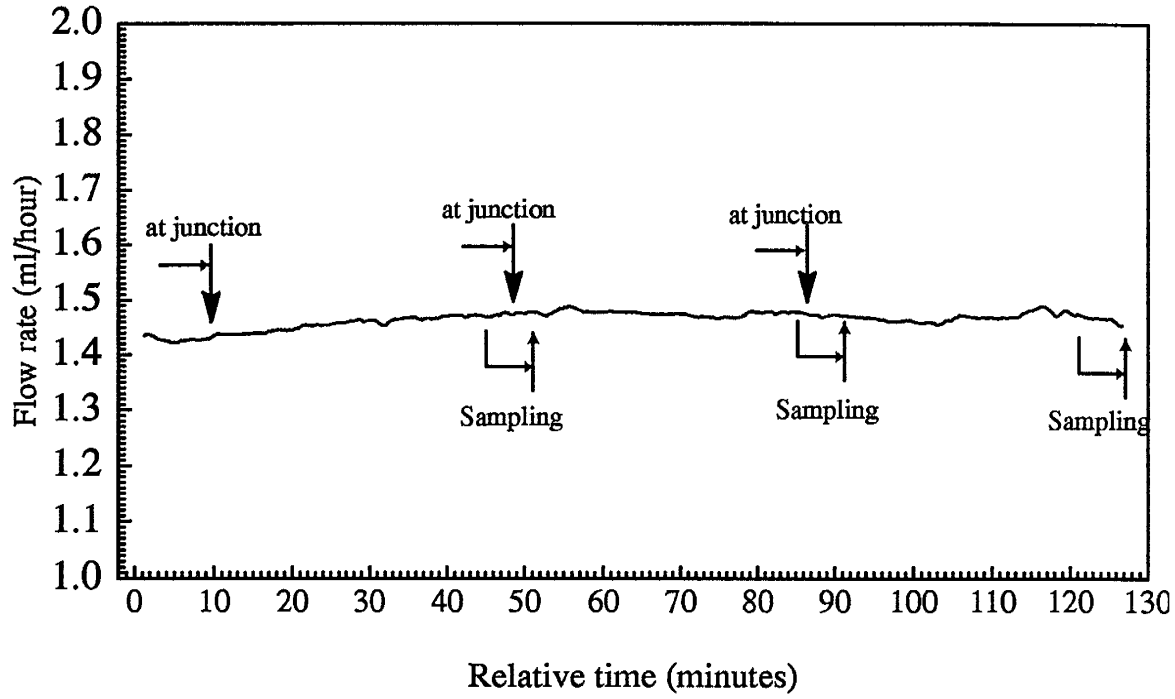

Figure B.15. Flow rate variations during the experiment at flow rate 1.5ml/hour. The average flow rate was 1.46ml/hour (Group-5).

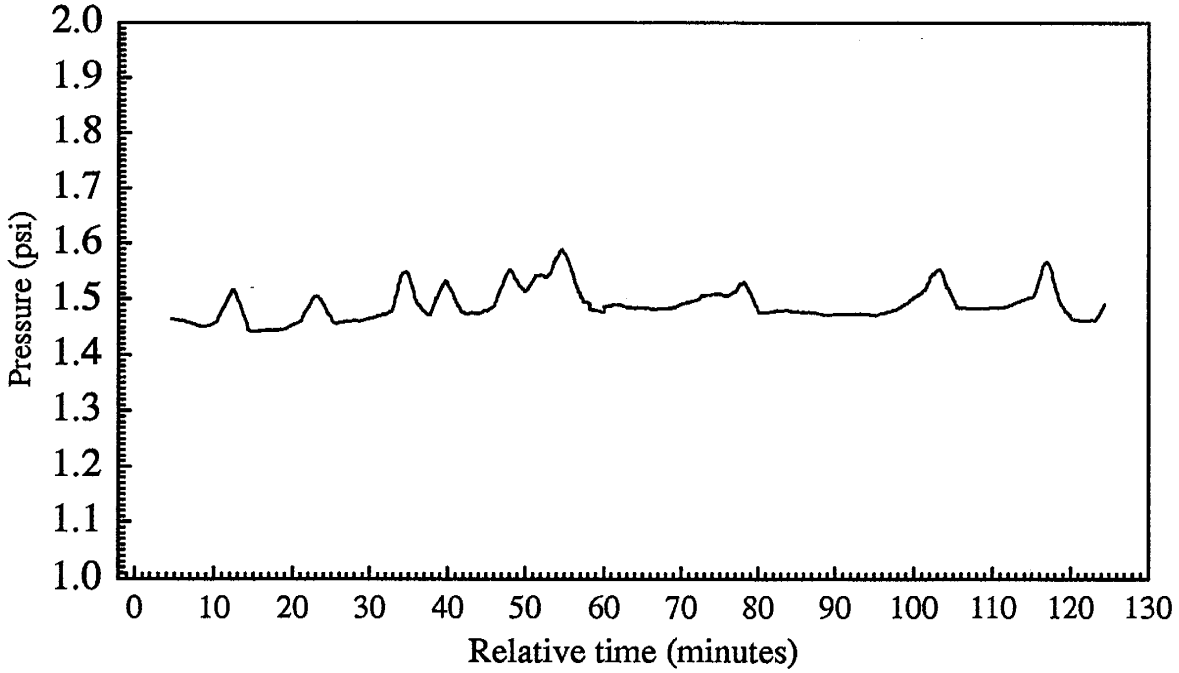

Figure B.16. Pressure variations with time during the experiment at flow rate 1.5ml/hour (Group-5).

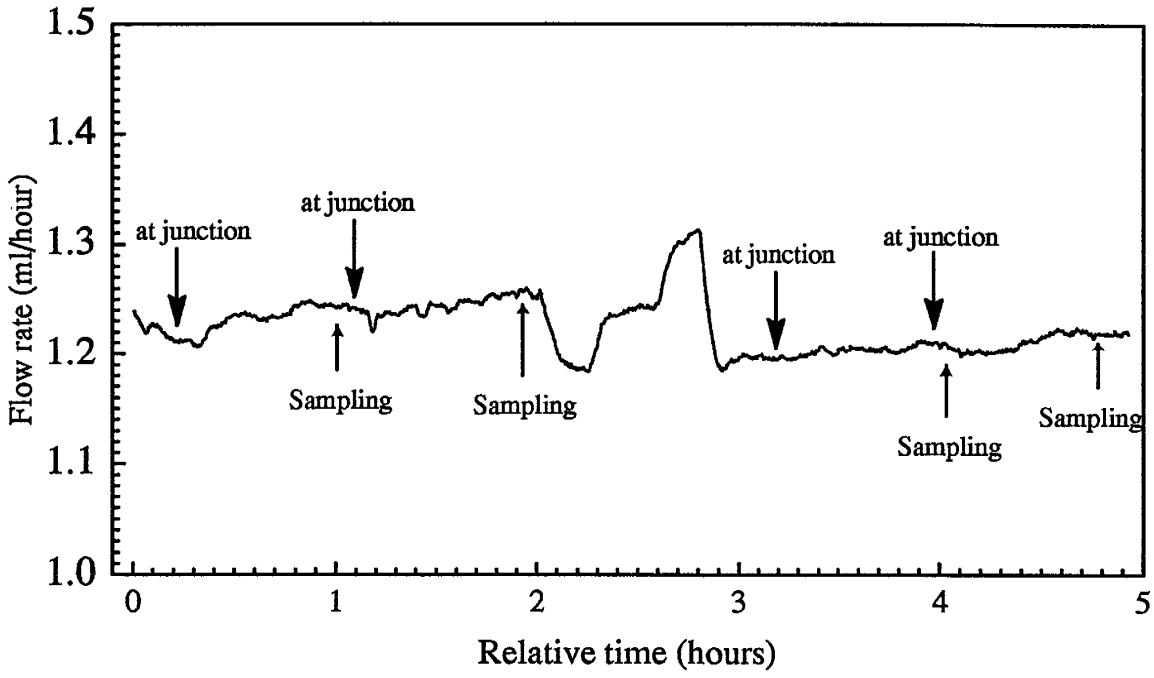

Figure B.17. Flow rate variations during the experiment at flow rate 1.25ml/hour. The average flow rate was 1.2208ml/hour (Group-5).

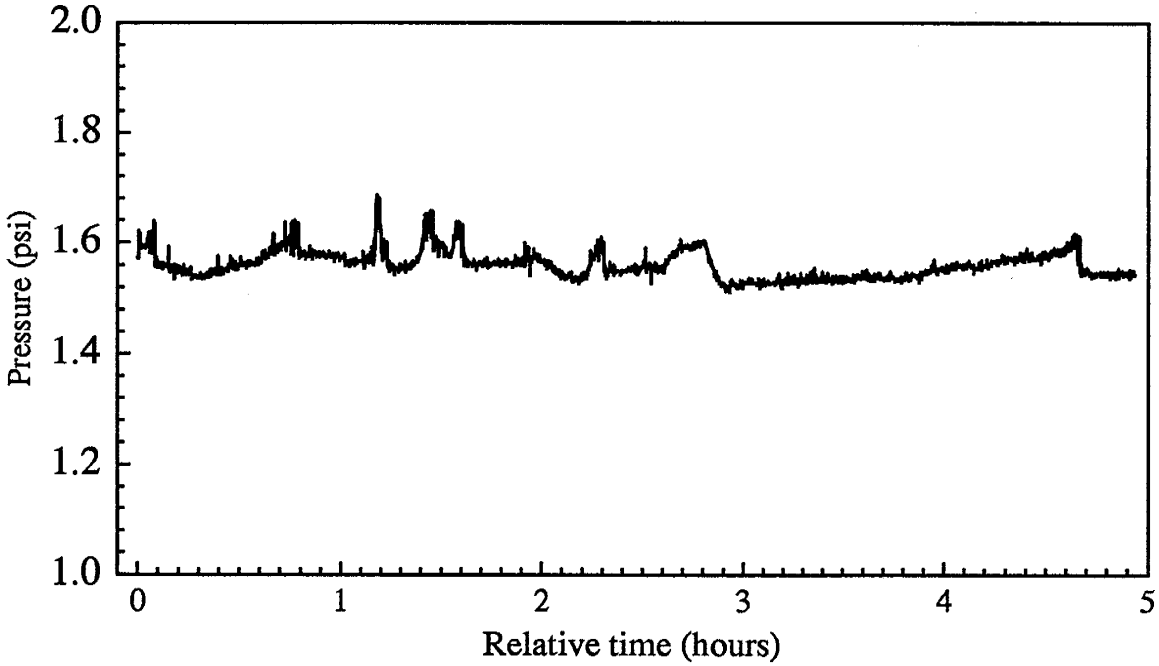

Figure B.18. Pressure variations with time during the experiment at flow rate 1.25ml/hour (Group-5).

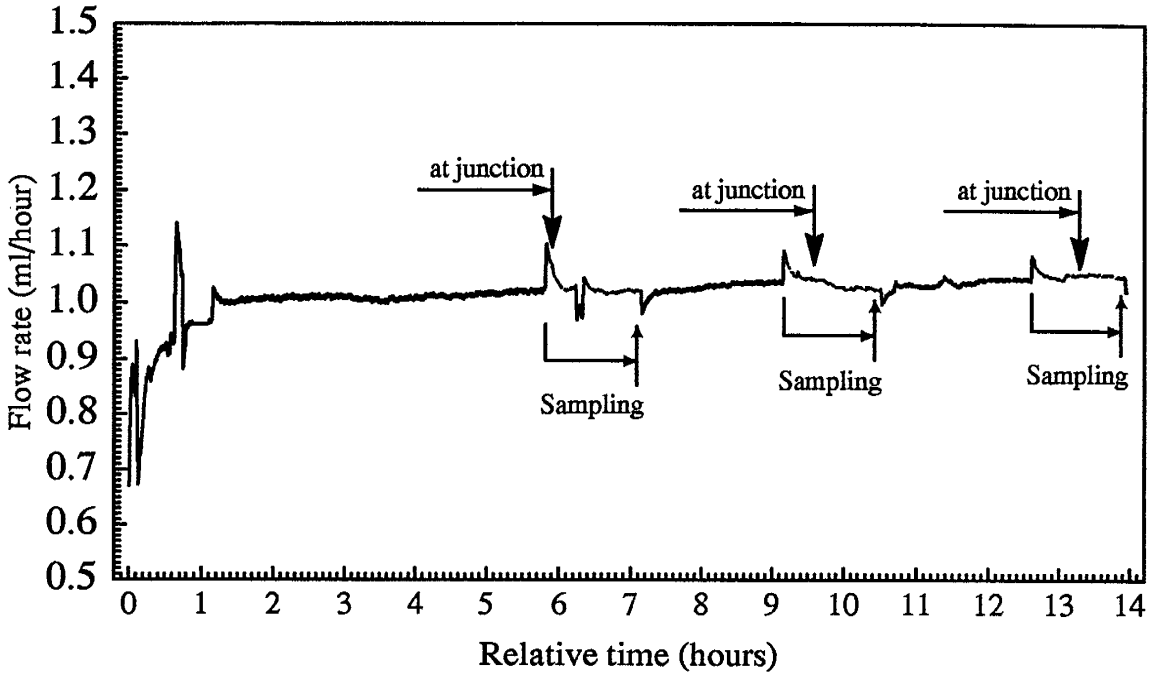

Figure B.19. Flow rate variations during the experiment at flow rate 1.0ml/hour. The average flow rate was 1.0251ml/hour (Group-1).

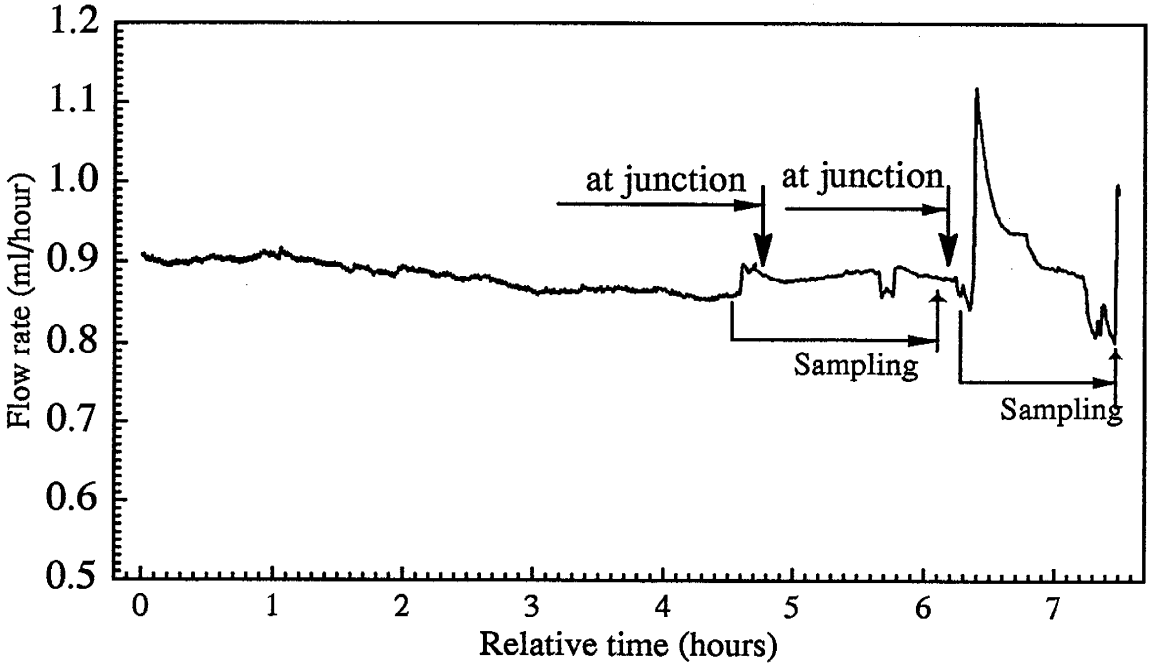

Figure B.20. Flow rate variations during the experiment at flow rate 0.9ml/hour. The average flow rate was 0.8871ml/hour (Group-1).

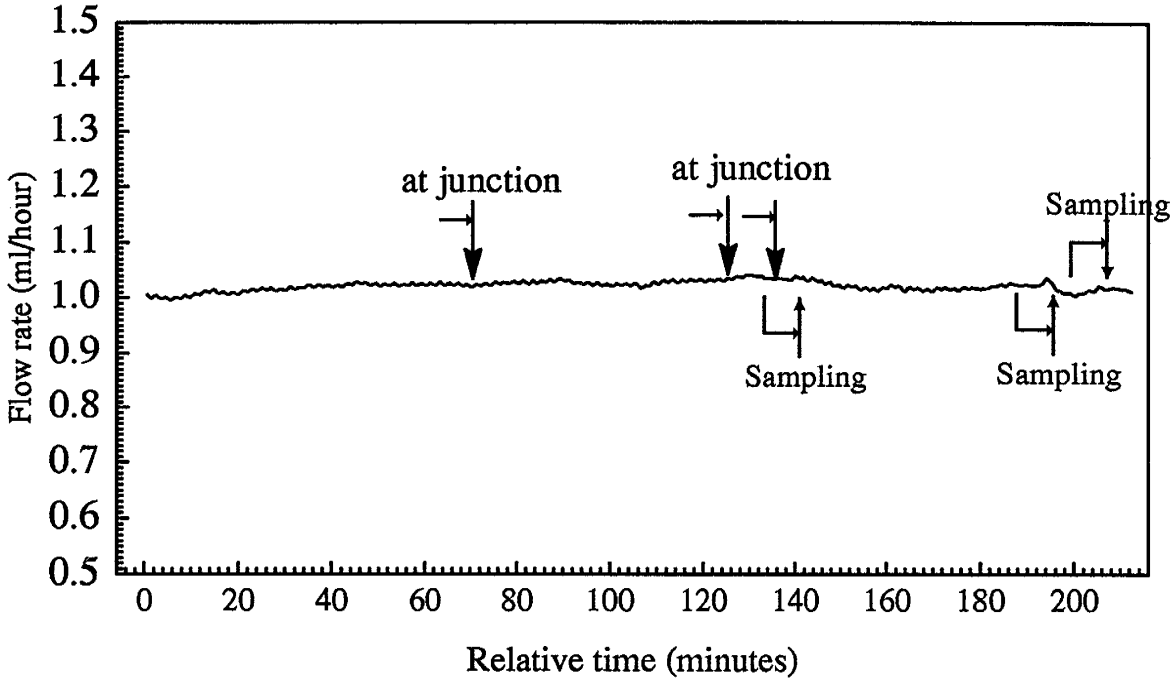

Figure B.21. Flow rate variations during the experiment at flow rate 1.0ml/hour. The average flow rate was1.0314ml/hour (Group-6).

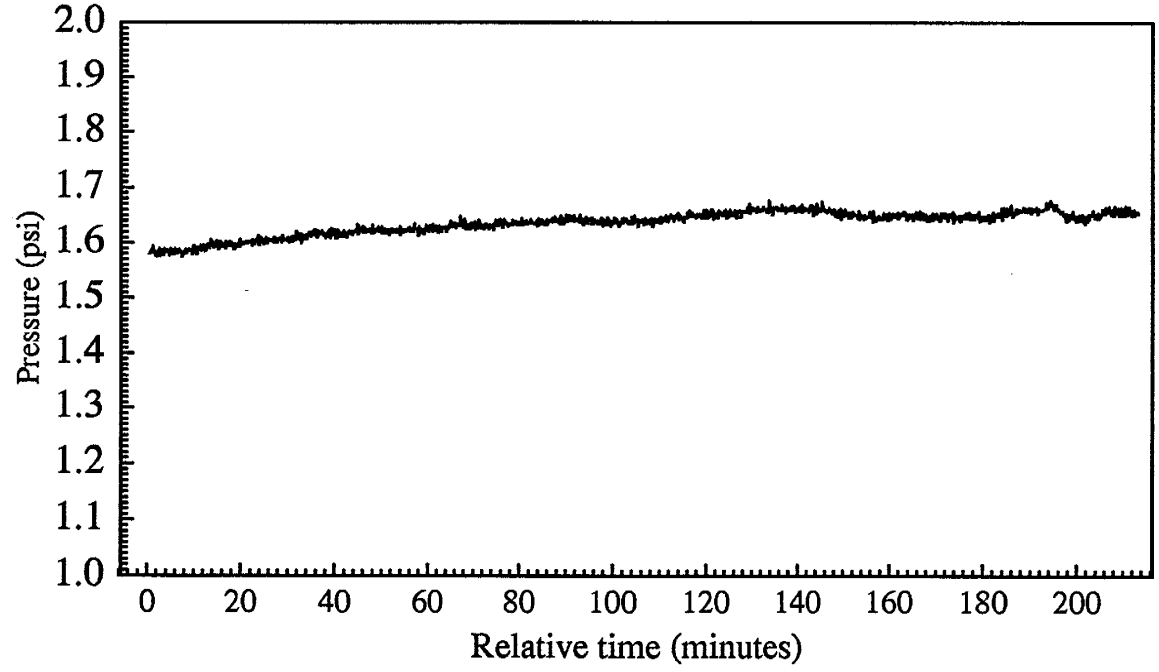

Figure B.22. Pressure variations with time during the experiment at flow rate 1.00ml/hour (Group-6).

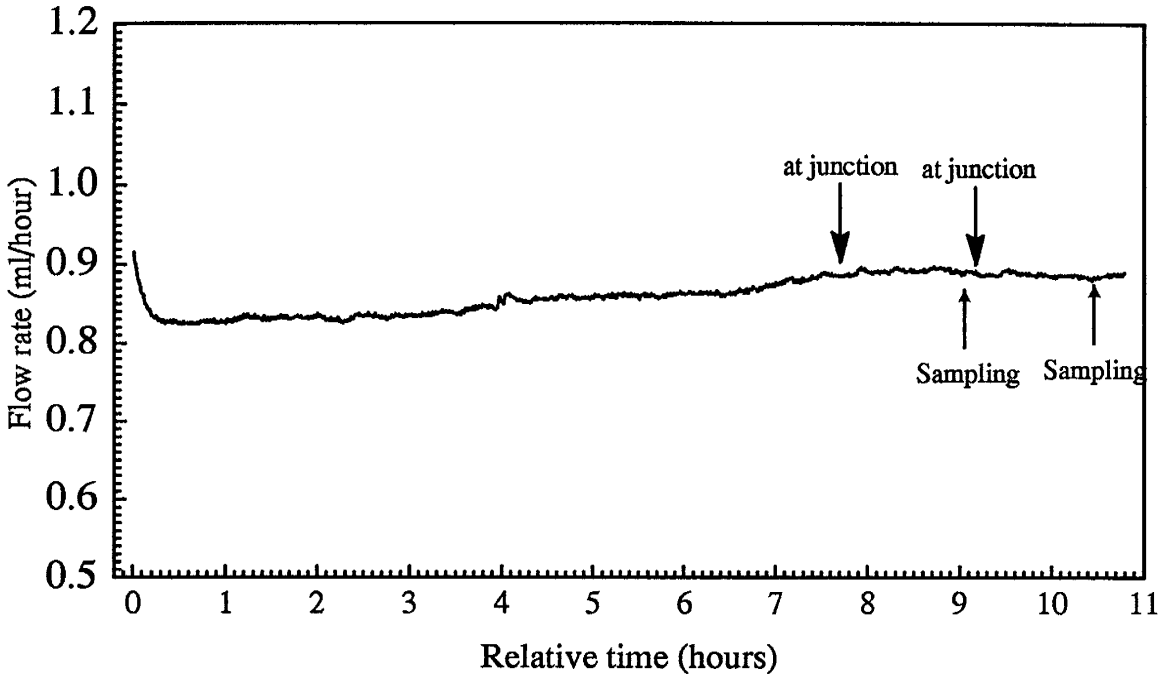

Figure B.23. Flow rate variations during the experiment at flow rate 0.9ml/hour. The average flow rate was 0.8857ml/hour (Group-6).

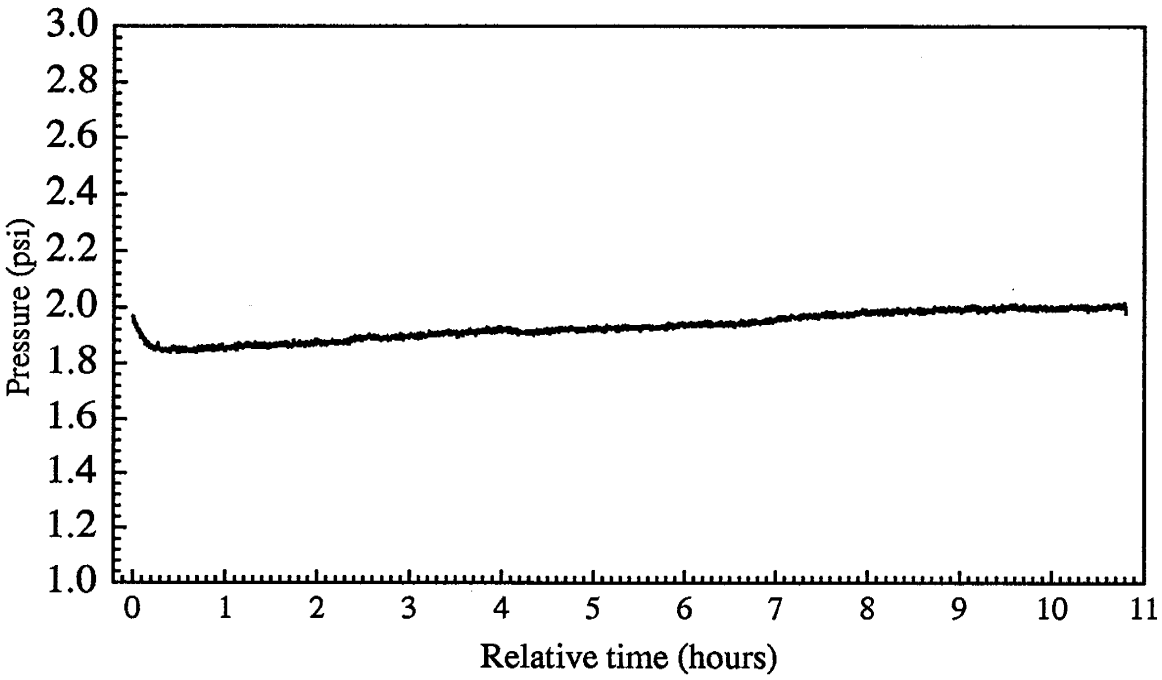

Figure B.24. Pressure variations with time during the experiment at flow rate 0.90ml/hour (Group-6).

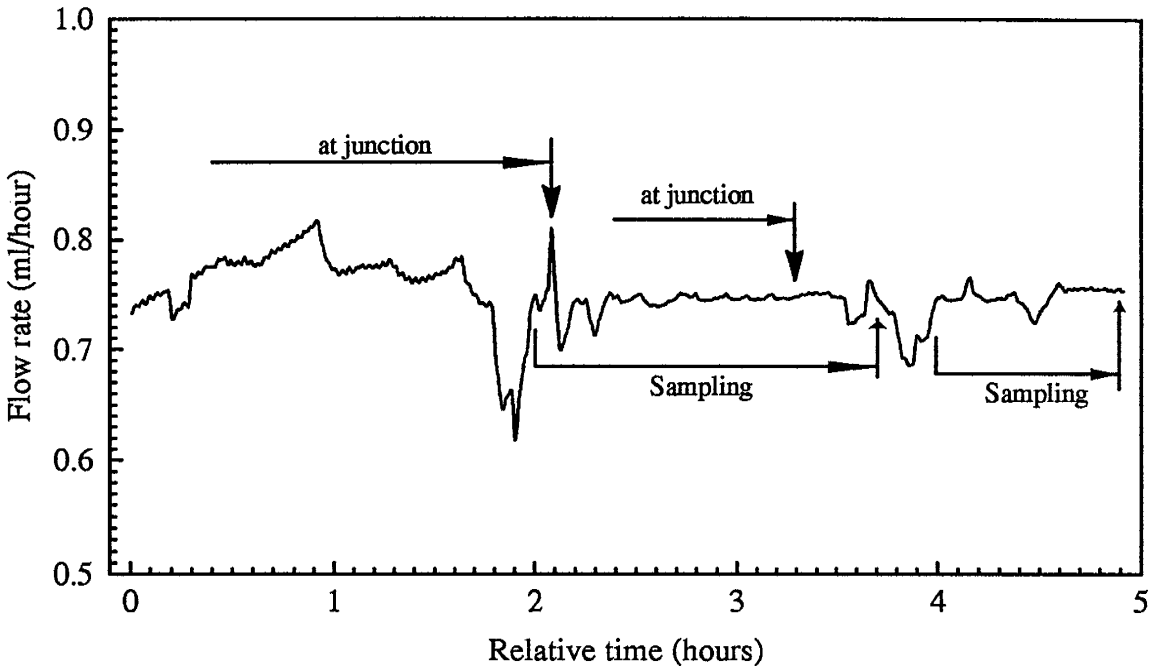

Figure B.25. Flow rate variations during the experiment at flow rate 0.75ml/hour. The average flow rate was 0.7505ml/hour (Group–2).

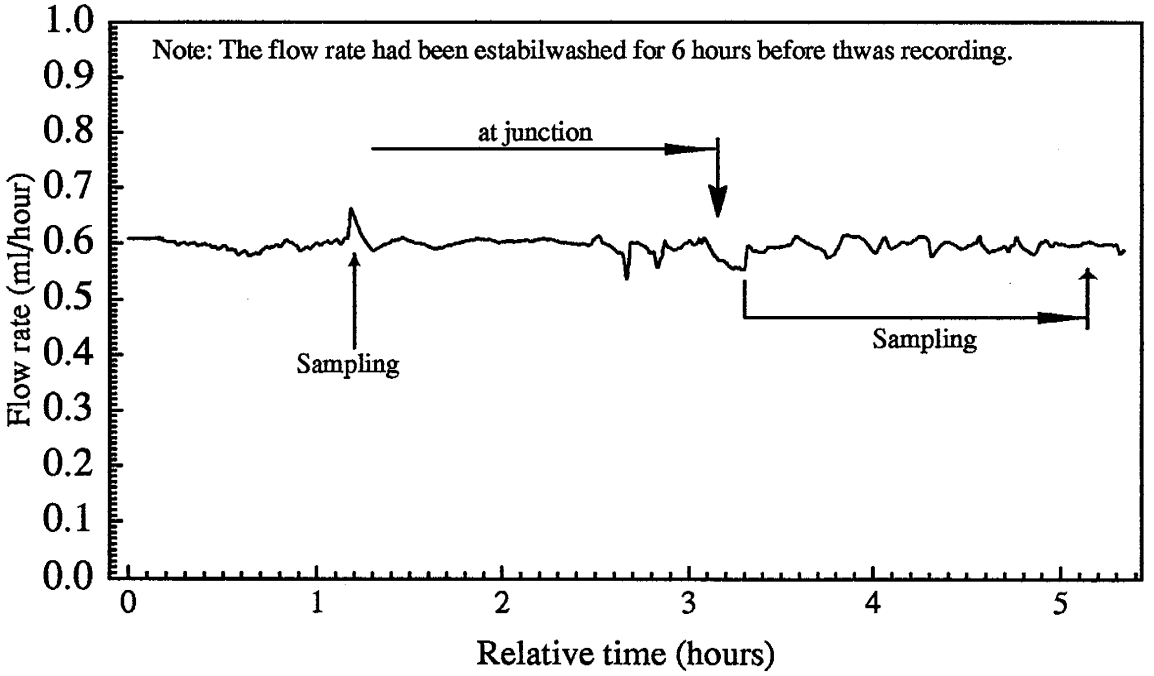

Figure B.26. Flow rate variations during the experiment at flow rate 0.60ml/hour. The average flow rate was 0.5975ml/hour (Group–3).

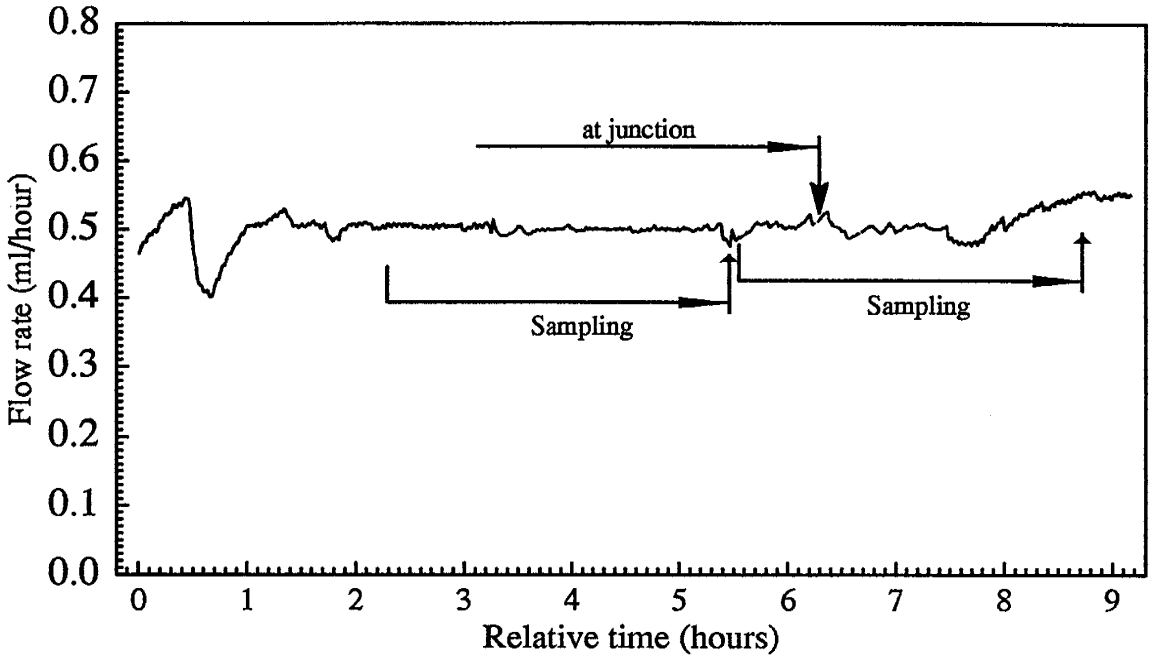

Figure B.27. Flow rate variations during the experiment at flow rate 0.50ml/hour. The average flow rate was 0.4997ml/hour (Group–4).

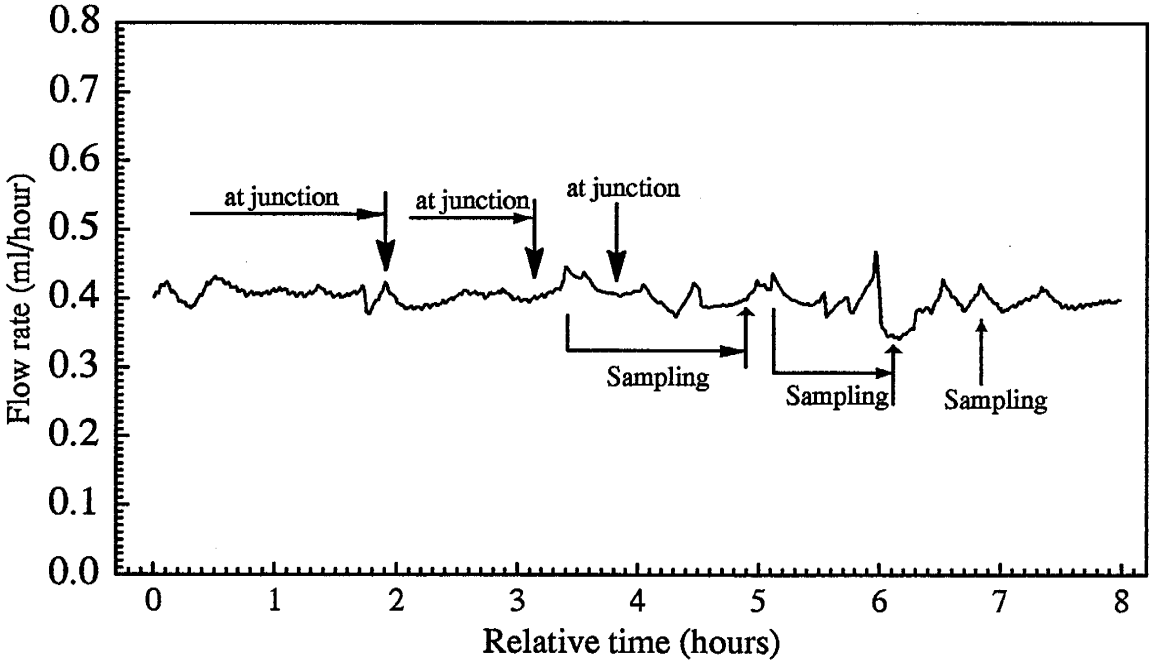

Figure B.28. Flow rate variations during the experiment at flow rate 0.40ml/hour. The average flow rate was 0.4015ml/hour (Group–4).

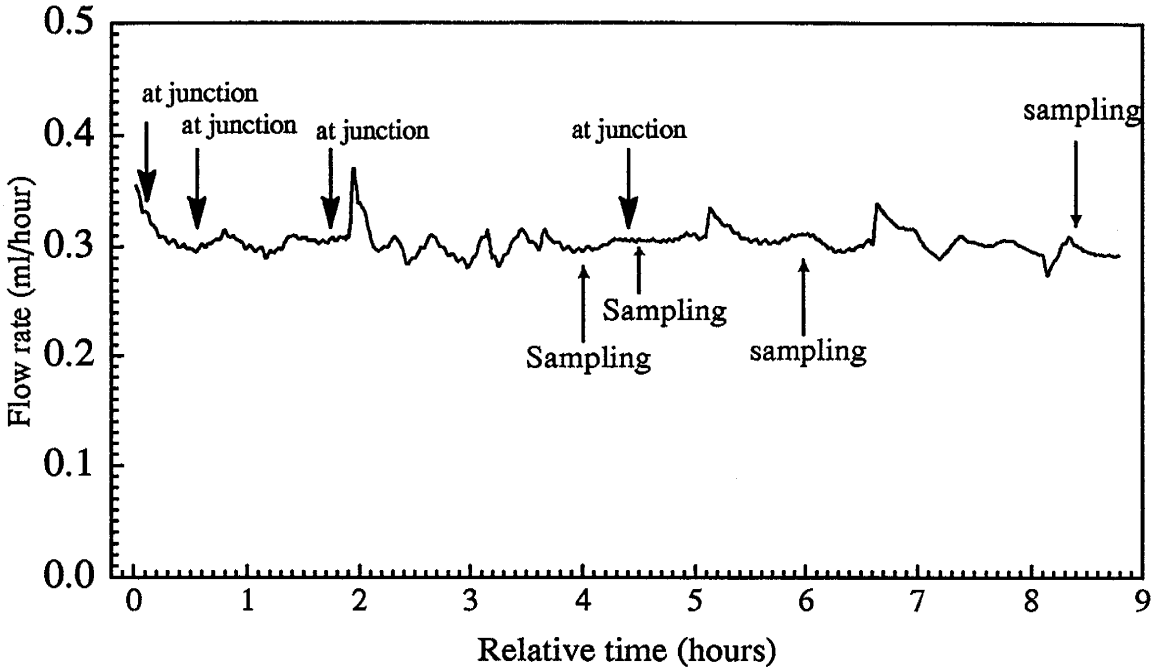

Figure B.29. Flow rate variations during the experiment at flow rate 0.30ml/hour. The average flow rate was 0.3049ml/hour (Group–4).

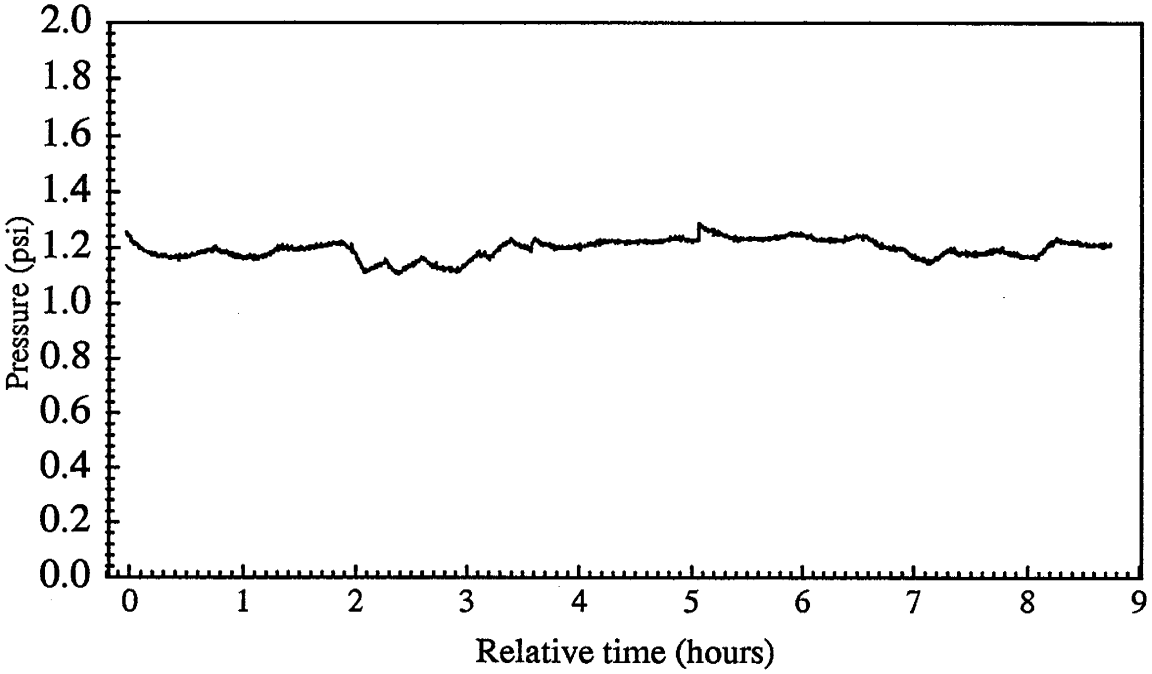

Figure B.30. Pressure variations with time during the experiment at flow rate 0.30ml/hour (Group–4).

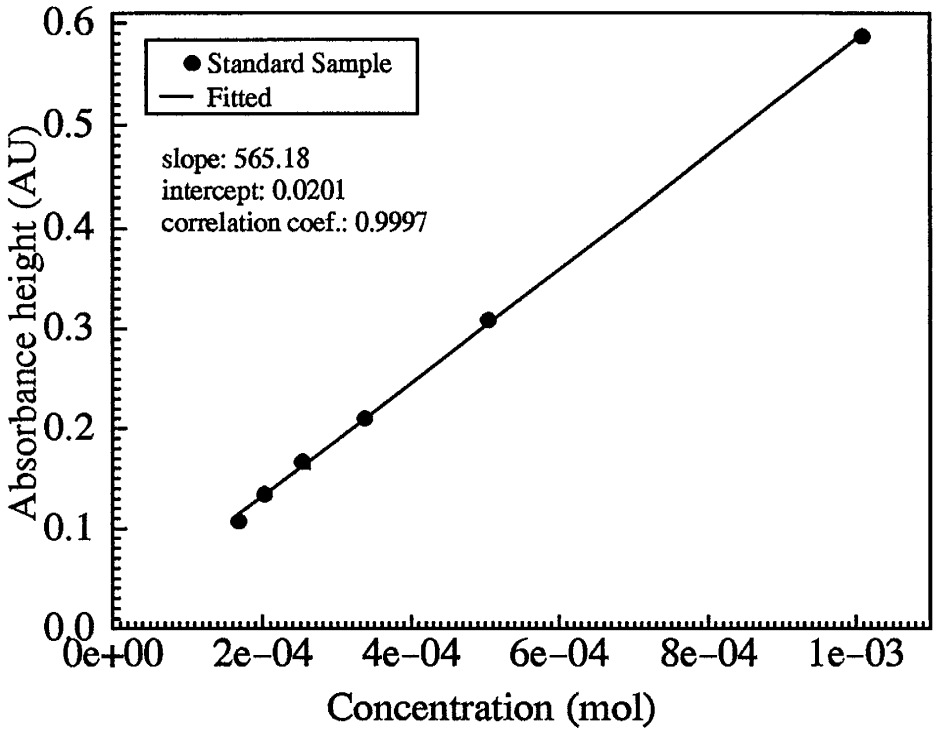

Figure B.31. Relationship between UV absorbance and KBr molar concentrations (Group-1).

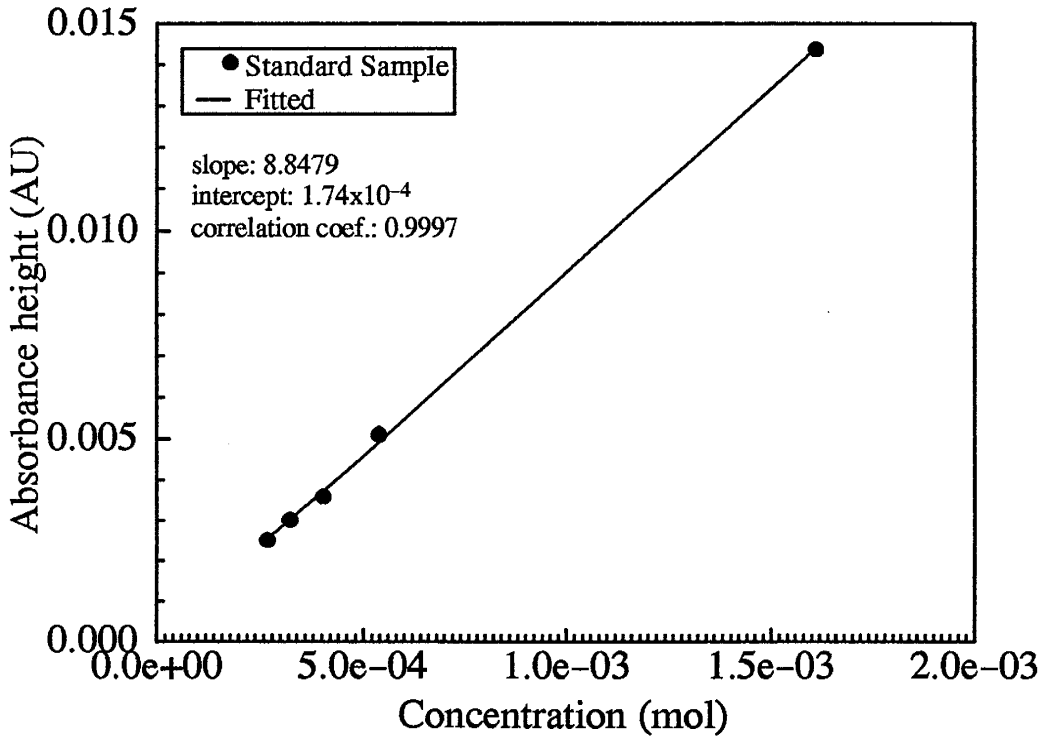

Figure B.32. Relationship between UV absorbance and KCl molar concentrations (Group-1).

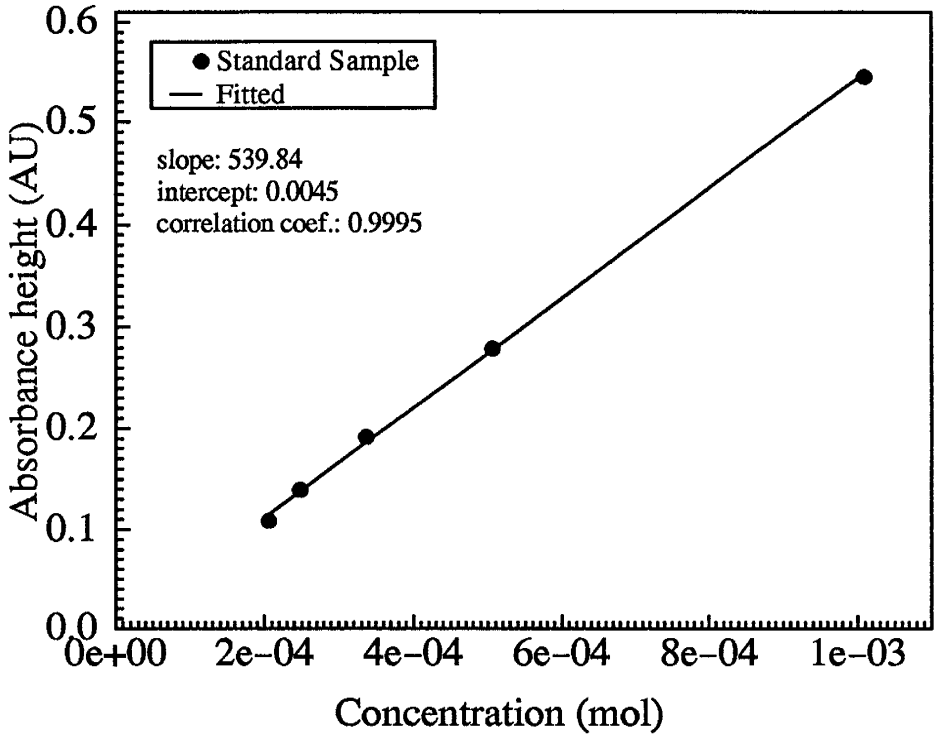

Figure B.33. Relationship between UV absorbance and KBr molar concentrations (Group-2).

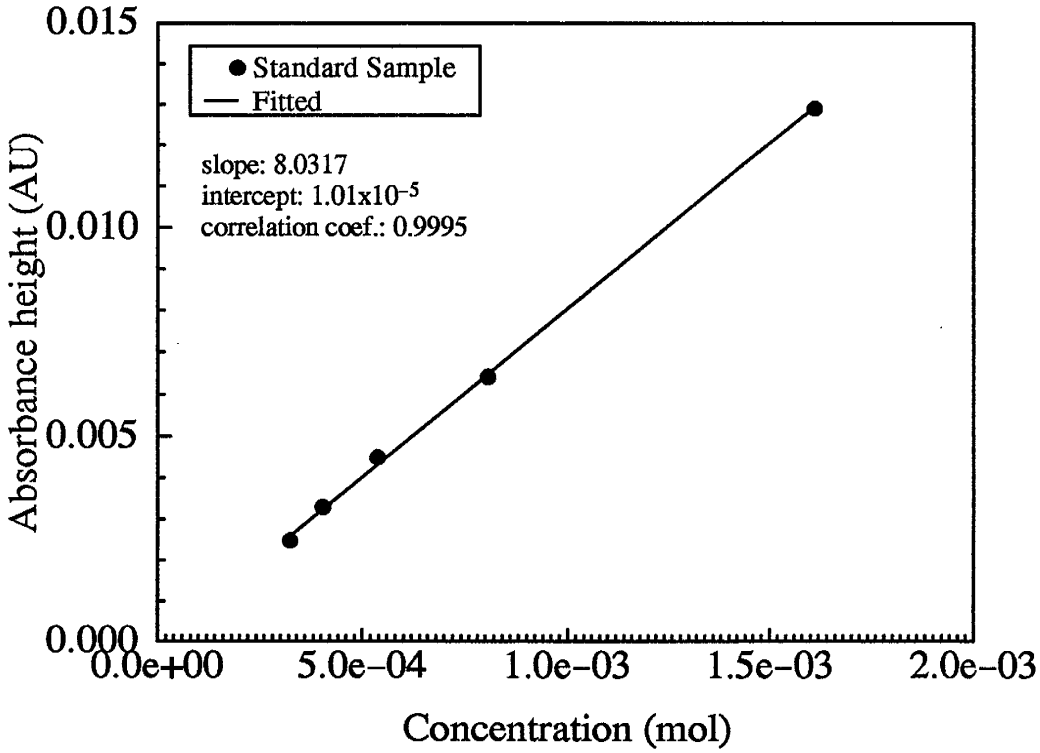

Figure B.34. Relationship between UV absorbance and KCl molar concentrations (Group-2).

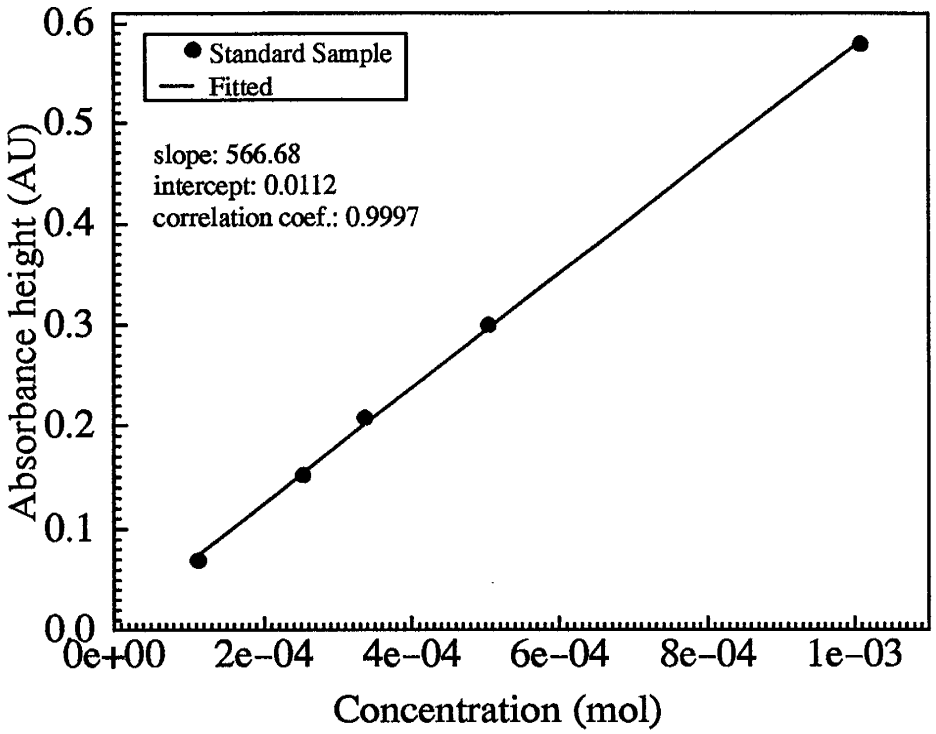

Figure B.35. Relationship between UV absorbance and KBr molar concentrations (Group-3).

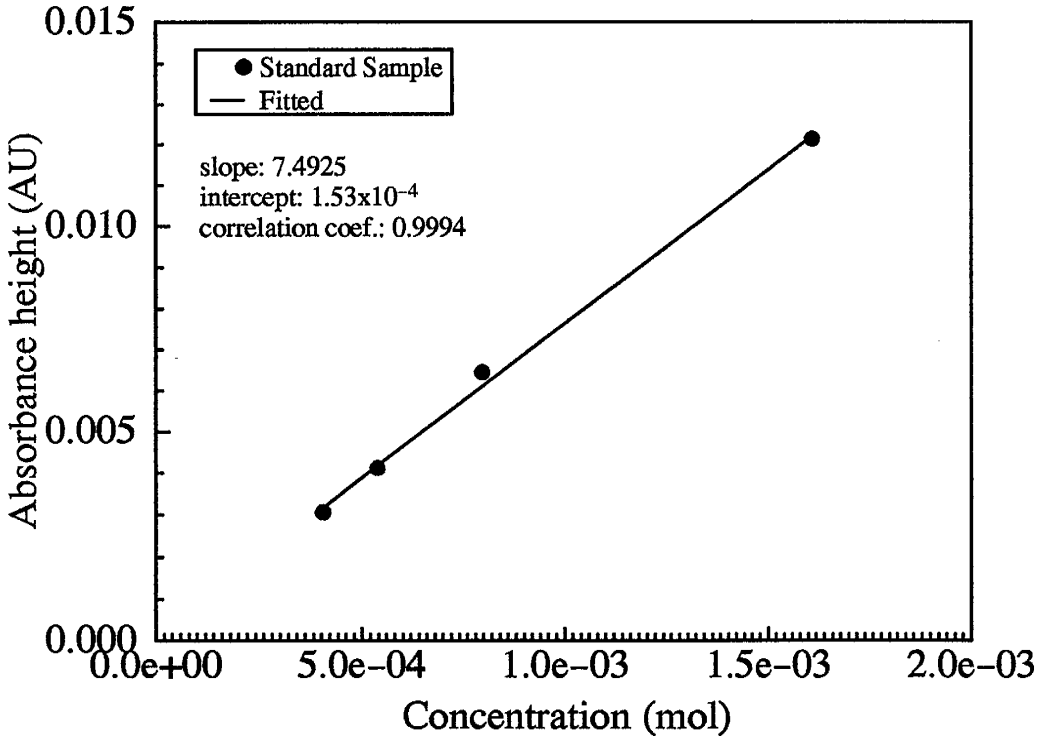

Figure B.36. Relationship between UV absorbance and KCl molar concentrations (Group-3).

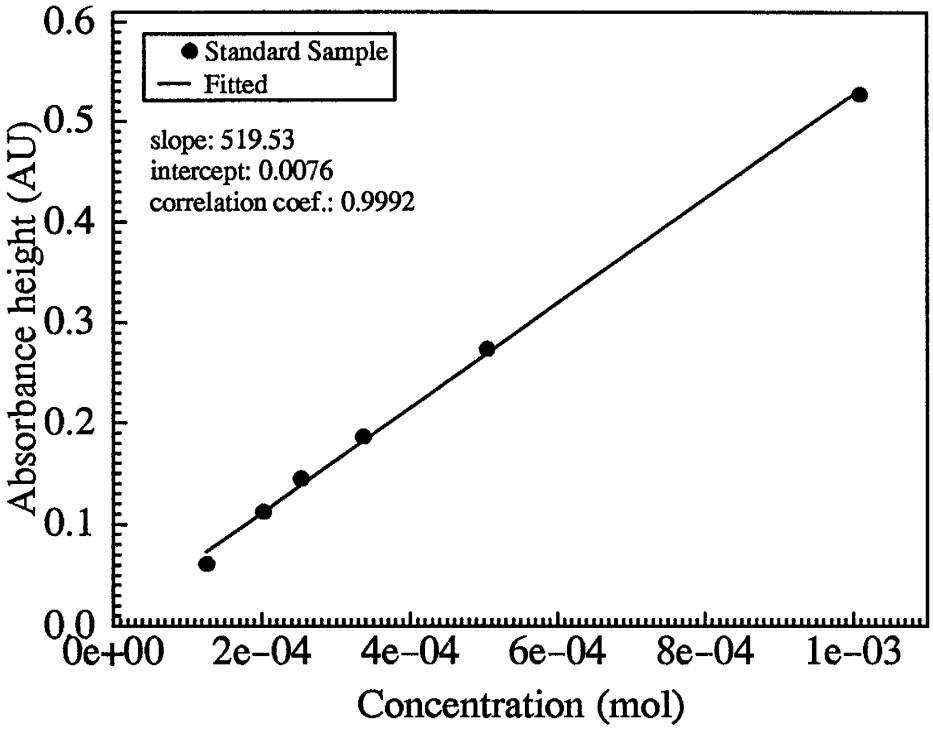

Figure B.37. Relationship between UV absorbance and KBr molar concentrations (Group-4).

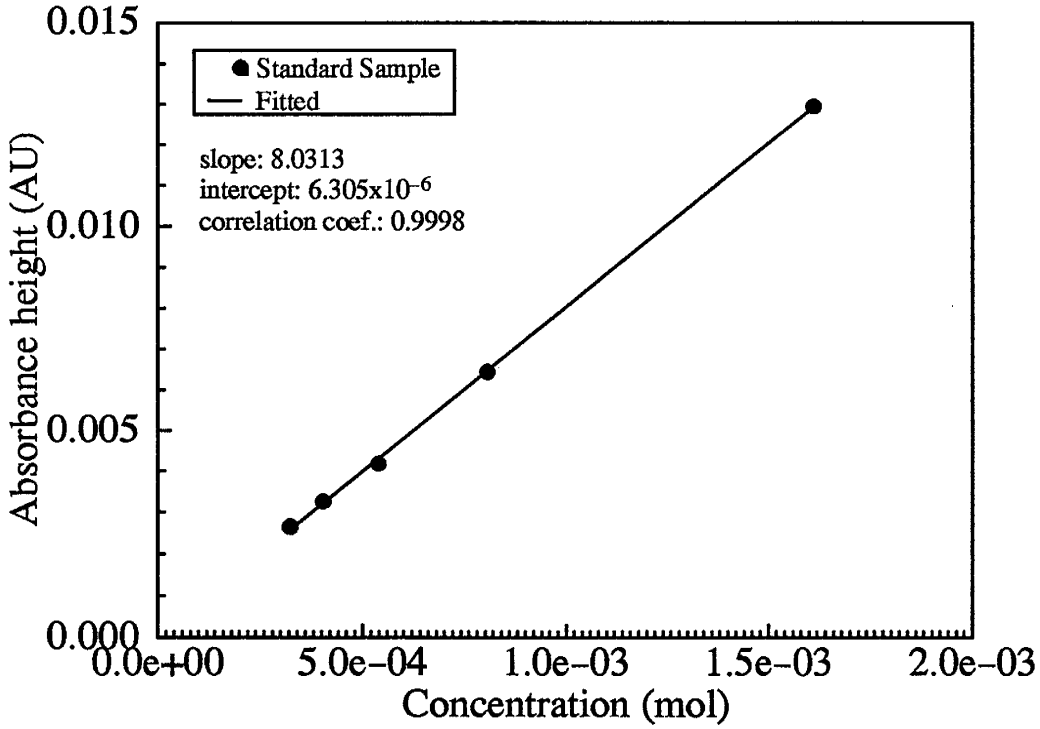

Figure B.38. Relationship between UV absorbance and KCl molar concentrations (Group-4).

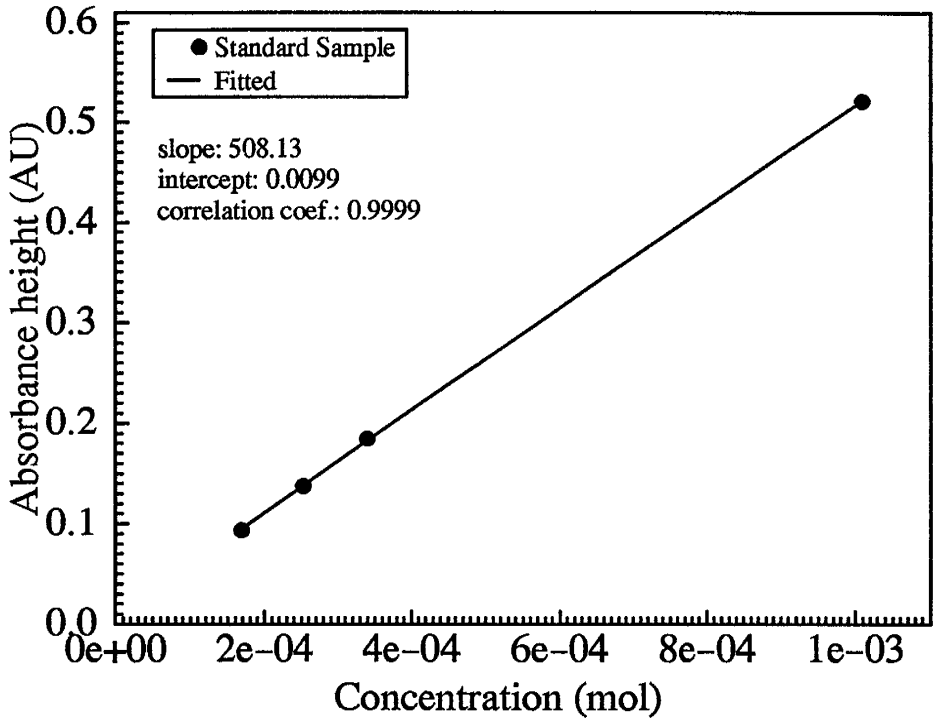

Figure B.39. Relationship between UV absorbance and KBr molar concentrations (Group-5).

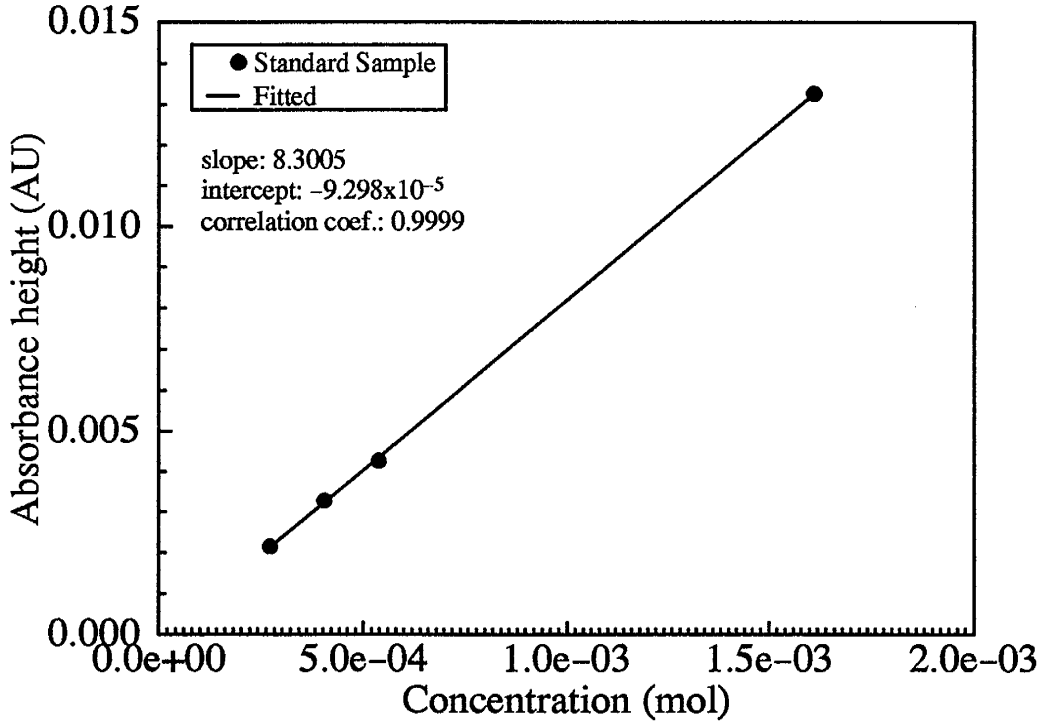

Figure B.40. Relationship between UV absorbance and KCl molar concentrations (Group-5).

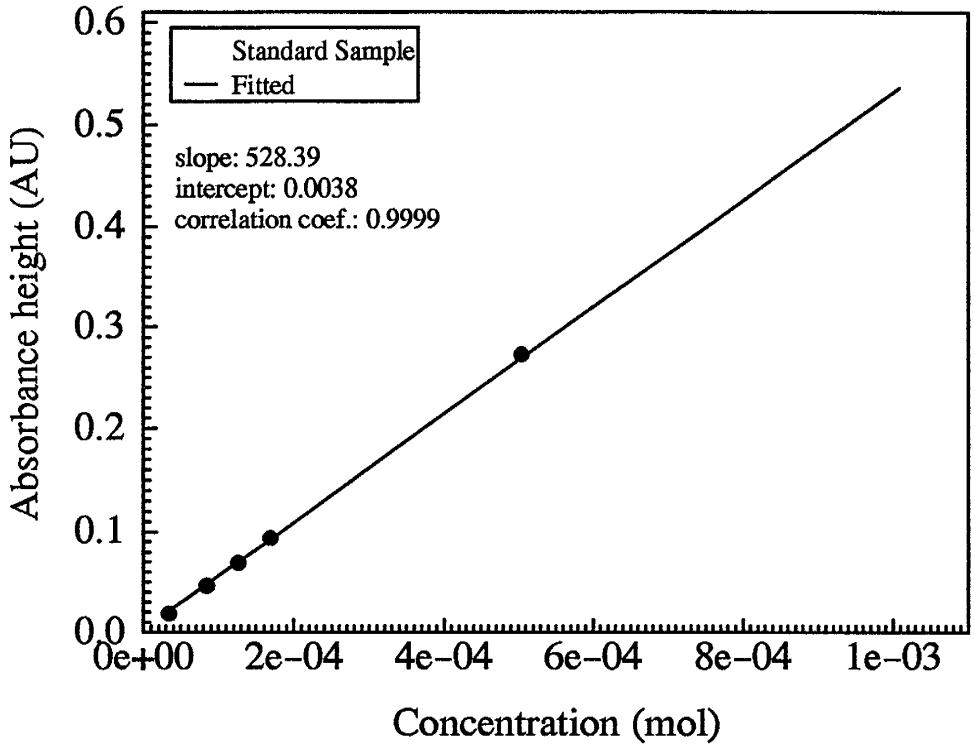

Figure B.41. Relationship between UV absorbance and KBr molar concentrations (Group-6).

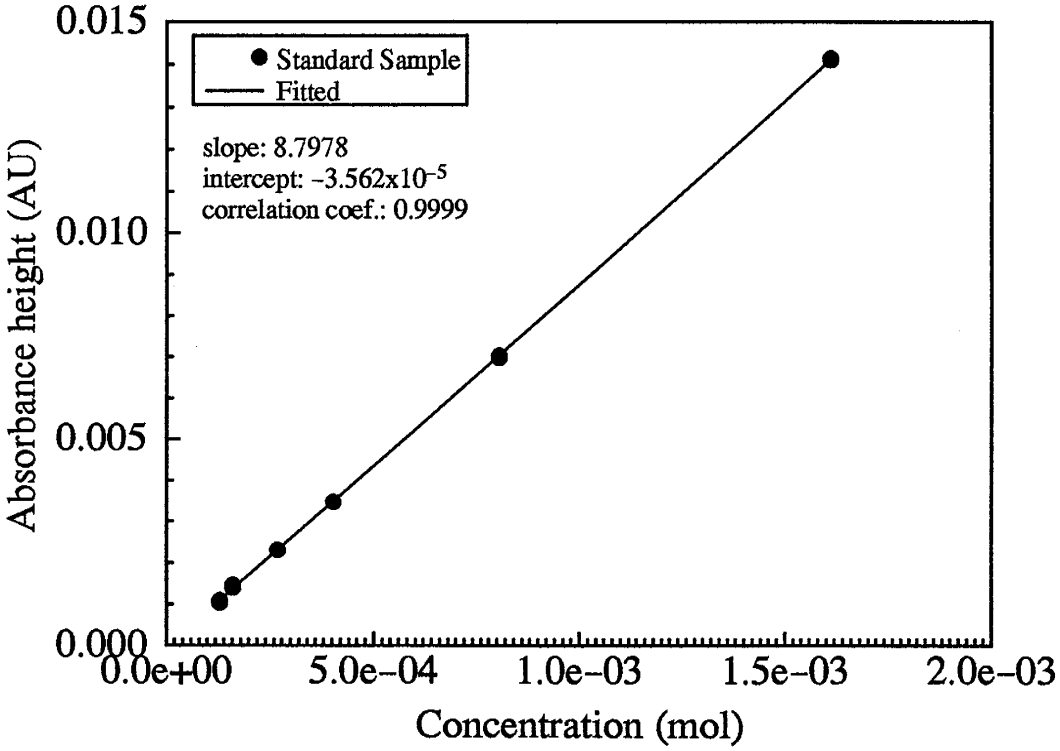

Figure B.42. Relationship between UV absorbance and KCl molar concentrations (Group-6).

A total of 6 group of experiments were performed. The raw data are listed in Table B.1. The following notations are used in Table B.1:

Gd: Group ID.

Sample_name: The name of the sample. For example, s3b2330–1 standards for sample from fracture 3 taken on b (Feburary) 23, flow rate was 30, this is the 1 st sample.

Tracer: Name of the tracer.

Set_Q: Pump flow rate.

Real_Q: Flow rate in fracture. It was measured by the flow meter.

AU_height: UV absorbance height for the specified tracer.

measured_peak: Occasionally the integrator failed to integrate the UV absorbance height. In case that occurs, the UV absorbance height was measured on the figure.

Table B.1. Raw data from the physical experiments.

Gd	Sample_name	Tracer	Set_Q ml/h	Real_Q ml/h	AU_height	Note
6	s3b2330-1	Br	30	29.988	0.05247	
6	s3b2330-1	Cl	30	29.988	0.01237	
6	s4b2330-1	Br	30	29.892	0.49256	
6	s4b2330-1	Cl	30	29.892	0.00122	
6	s3b2330-2	Br	30	29.988	0.05217	
6	s3b2330-2	Cl	30	29.988	0.01270	
6	s4b2330-2	Br	30	29.892	0.49459	
6	s4b2330-2	Cl	30	29.892	0.00119	
6	s3b2330-3	Br	30	29.988	0.05123	
6	s3b2330-3	Cl	30	29.988	0.01276	
6	s4b2330-3	Br	30	29.892	0.49403	
6	s4b2330-3	Cl	30	29.892	0.00120	
2	s3a2610-1	Br	10	9.9455	0.064	air in the model.
2	s3a2610-1	Cl	10	9.9455	0.010846	
2	s4a2610-1	Br	10	9.9835	0.48384	
2	s4a2610-1	Cl	10	9.9835	0.00169	
2	s3a2610-2	Br	10	9.805	0.08698	flow rate not stable
2	s3a2610-2	Cl	10	9.805	0.01027	
2	s4a2610-2	Br	10	9.805	0.49124	
2	s4a2610-2	Cl	10	9.805	0.00111	
1	s3a2210-1	Br	10	9.9	0.07128	
1	s3a2210-1	Cl	10	9.9	0.01225	
1	s4a2210-1	Br	10	10.0	0.47180	
1	s4a2210-1	Cl	10	10.0	0.00222	
1	s3a2210-2	Br	10	9.92733	0.07312	
1	s3a2210-2	Cl	10	9.92733	0.01226	
1	s4a2210-2	Br	10	9.88867	0.72181	
1	s4a2210-2	Cl	10	9.88867	0.00327	
3	s3a2910-1	Br	10	10.063	0.07671	
3	s3a2910-1	Cl	10	9.8495	0.01086	
3	s4a2910-1	Br	10	9.8495	0.51705	
3	s4a2910-1	Cl	10	9.8495	0.00160	
3	s3a2910-2	Br	10	10.260	0.07820	
3	s3a2910-2	Cl	10	10.260	0.01066	
3	s4a2910-2	Br	10	9.8095	0.51748	
3	s4a2910-2	Cl	10	9.8095	0.00134	

3	s3a295-1	Br	5	5.0835	0.09308	
3	s3a295-1	Cl	5	5.0835	0.01026	
3	s4a295-1	Br	5	4.89	0.49627	
3	s4a295-1	Cl	5	4.89	0.00180	
3	s3a295-2	Br	5	4.9065	0.09821	
3	s3a295-2	Cl	5	4.9065	0.01020	
3	s4a295-2	Br	5	4.9115	0.50193	
3	s4a295-2	Cl	5	4.9115	0.00173	
1	s3a235-1	Br	5	5.0896	0.09912	
1	s3a235-1	Cl	5	5.0896	0.01073	
1	s4a235-1	Br	5	4.8752	0.45390	
1	s4a235-1	Cl	5	4.8752	0.00197	
1	s3a235-2	Br	5	5.0896	0.10467	
1	s3a235-2	Cl	5	5.0896	0.01116	
1	s4a235-2	Br	5	4.8752	0.47528	
1	s4a235-2	Cl	5	4.8752	0.00150	measured peak
6	s3b252.5-2	Br	2.5	2.475	0.10871	measured flow
6	s3b252.5-2	Cl	2.5	2.475	0.01146	
6	s4b252.5-2	Br	2.5	2.443	0.44941	measured flow
6	s4b252.5-2	Cl	2.5	2.443	0.00259	
6	s3b252.5-3	Br	2.5	2.478	0.10985	measured flow
6	s3b252.5-3	Cl	2.5	2.478	0.01163	
6	s4b252.5-3	Br	2.5	2.429	0.44828	measured flow
6	s4b252.5-3	Cl	2.5	2.429	0.00260	
5	s3b202_1	Br	2	1.9152	0.14196	flow not stable
5	s3b202_1	Cl	2	1.9152	0.01608	
5	s4b202_1	Br	2	2.0076	0.44582	
5	s4b202_1	Cl	2	2.0076	0.00296	measured peak
5	s3b202-2	Br	2	1.972	0.11259	
5	s3b202-2	Cl	2	1.972	0.01085	
5	s4b202-2	Br	2	1.978	0.42646	
5	s4b202-2	Cl	2	1.978	0.00294	
5	s3b202-3	Br	2	2.001	0.11606	
5	s3b202-3	Cl	2	2.001	0.01061	
5	s4b202-3	B r	2	1.949	0.42647	
5	s4b202-3	Cl	2	1.949	0.00311	
5	s3b202_4	Br	2	2.042	0.12337	measured peak
5	s3b202-4	Cl	2	2.042	0.01088	
5	s4b202-4	Br	2	1.936	0.43727	

5	s4b202-4	Cl	2	1.936	0.00282	
5	s3b201.75_1	Br	1.75	1.752	0.12217	
5	s3b201.75_1	Cl	1.75	1.752	0.01065	measured peak
5	s4b201.75-1	Br	1.75	1.738	0.41402	
5	s4b201.75-1	Cl	1.75	1.738	0.00308	
5	s3b201.75-2	Br	1.75	1.725	0.12577	
5	s3b201.75-2	Cl	1.75	1.725	0.010575	measured peak
5	s4b201.75-2	Br	1.75	1.76	0.43384	measured peak
5	s4b201.75-2	Cl	1.75	1.76	0.00306	
5	s3b201.5-1	Br	1.5	1.439	0.13991	
5	s3b201.5-1	Cl	1.5	1.439	0.01044	
5	s4b201.5-1	Br	1.5	1.496	0.42445	
5	s4b201.5-1	Cl	1.5	1.496	0.00315	
5	s3b201.5-2	Br	1.5	1.451	0.13009	
5	s3b201.5-2	Cl	1.5	1.451	0.01025	
5	s4b201.5-2	Br	1.5	1.48	0.41503	
5	s4b201.5-2	Cl	1.5	1.48	0.00325	
5	s3b201.5-3	Br	1.5	1.458	0.13416	
5	s3b201.5-3	Cl	1.5	1.458	0.01033	
5	s4b201.5-3	Br	1.5	1.464	0.42093	
5	s4b201.5-3	Cl	1.5	1.464	0.00326	
5	s3b201.25_1	Br	1.25	1.148	0.13895	
5	s3b201.25-1	Cl	1.25	1.148	0.00997	
5	s4b201.25-1	Br	1.25	1.281	0.40934	
5	s4b201.25-1	Cl	1.25	1.281	0.00353	
5	s3b201.25-2	Br	1.25	1.152	0.13831	
5	s3b201.25-2	Cl	1.25	1.152	0.01008	
5	s4b201.25-2	Br	1.25	1.285	0.40682	
5	s4b201.25-2	Cl	1.25	1.285	0.00352	
5	s3b201.25-3	Br	1.25	1.176	0.14817	measured flow
5	s3b201.25-3	Cl	1.25	1.176	0.01050	
5	s4b201.25-3	Br	1.25	1.228	0.40797	measured flow
5	s4b201.25-3	Cl	1.25	1.228	0.00350	
5	s3b201.25-4	Br	1.25	1.183	0.13550	
5	s3b201.25-4	Cl	1.25	1.183	0.00971	
5	s4b201.25-4	Br	1.25	1.263	0.41374	
5	s4b201.25-4	Cl	1.25	1.263	0.00350	
1	s3a231-1	Br	1.0	0.9788	0.19974	
1	s3a231-1	Cl	1.0	0.9788	0.00828	

1	s4a231-1	Br	1.0	1.0059	0.35268	
1	s4a231-1	Cl	1.0	0.9788	0.00490	
1	s3a231-2	Br	1.0	0.9563	0.20978	
1	s3a231-2	Cl	1.0	0.9563	0.00871	
1	s4a231-2	Br	1.0	1.0116	0.35263	
1	s4a231-2	Cl	1.0	1.0116	0.00483	
1	s3a231-3	Br	1.0	0.9284	0.20865	
1	s3a231-3	Cl	1.0	0.9284	0.00853	
1	s4a231-3	Br	1.0	1.0235	0.34708	
1	s4a231-3	Cl	1.0	1.0235	0.00496	
6	s3b251-1	Br	1.0	0.999	0.16724	measured flow
6	s3b251-1	Cl	1.0	0.999	0.01031	
6	s4b251-1	Br	1.0	0.947	0.41301	measured flow
6	s4b251-1	Cl	1.0	0.947	0.00400	
6	s3b251-3	Br	1.0	0.966	0.16644	
6	s3b251-3	Cl	1.0	0.966	0.01012	
6	s4b251-3	Br	1.0	1.034	0.41496	
6	s4b251-3	Cl	1.0	1.034	0.00408	
6	s3b250.9-1	Br	0.9	0.886	0.17077	
6	s3b250.9-1	Cl	0.9	0.885	0.01023	
6	s4b250.9-1	Br	0.9	0.914	0.40054	
6	s4b250.9-1	Cl	0.9	0.914	0.00418	
6	s3b250.9-2	Br	0.9	0.886	0.17077	
6	s3b250.9-2	Cl	0.9	0.885	0.01023	
6	s4b250.9-2	Br	0.9	0.914	0.40054	
6	s4b250.9-2	Cl	0.9	0.914	0.00418	
6	s3b250.9-3	Br	0.9	0.885	0.16826	
6	s3b250.9-3	Cl	0.9	0.885	0.01001	
6	s4b250.9-3	Br	0.9	0.915	0.40072	
6	s4b250.9-3	Cl	0.9	0.915	0.00408	
2	s3a270.75-1	Br	0.75	0.7754	0.19957	
2	s3a270.75-1	Cl	0.75	0.7754	0.00899	
2	s4a270.75_1	Br	0.75	0.7754	0.38649	measured peak
2	s4a270.75-1	Cl	0.75	0.7245	0.00425	
2	s3a270.75-2	Br	0.75	0.7549	0.20684	
2	s3a270.75-2	Cl	0.75	0.7549	0.00914	
2	s4a270.75-2	Br	0.75	0.704	0.37665	
2	s4a270.75-2	Cl	0.75	0.704	0.00403	
3	s3a290.6-1	Br	0.6	0.6028	0.21979	

3	s3a290.6-1	Cl	0.6	0.6028	0.00778	
3	s4a290.6-1	Br	0.6	0.5743	0.38440	
3	s4a290.6-1	Cl	0.6	0.5743	0.00420	
3	s3a290.6-2	Br	0.6	0.5961	0.20882	measured peak
3	s3a290.6-2	Cl	0.6	0.5961	0.00764	
3	s4a290.6-2	Br	0.6	0.5765	0.38846	
3	s4a290.6-2	Cl	0.6	0.5765	0.00431	
4	s3a290.5-1	Br	0.5	0.5261	0.20493	
4	s3a290.5-1	Cl	0.5	0.5261	0.00810	
4	s4a290.5-1	Br	0.5	0.4726	0.34467	
4	s4a290.5-1	Cl	0.5	0.4726	0.00467	measured peak
4	s3b20.5-2	Br	0.5	0.5237	0.21113	
4	s3b20.5-2	Cl	0.5	0.5237	0.00809	
4	s4b20.5-2	Br	0.5	0.4688	0.35502	
4	s4b20.5-2	Cl	0.5	0.4688	0.00467	
4	s3b50.4-2	Br	0.4	0.4093	0.22287	
4	s3b50.4-2	Cl	0.4	0.4093	0.00789	
4	s4b50.4-2	Br	0.4	0.3832	0.33182	
4	s4b50.4-2	Cl	0.4	0.3832	0.00496	
4	s30.4-4	Br	0.4	0.4093	0.23878	
4	s30.4-4	Cl	0.4	0.4093	0.00864	
4	s40.4-4	Br	0.4	0.3832	0.37389	
4	s40.4-4	Cl	0.4	0.3832	0.0066	
4	s30.3-1	Br	0.3	0.2845	0.278750	
4	s30.3-1	Cl	0.3	0.2845	0.00890	
4	s40.3-1	Br	0.3	0.3213	0.38740	
4	s40.3-1	Cl	0.3	0.3213	0.00649	
4	s3b50.3-2	Br	0.3	0.2845	0.24815	
4	s3b50.3-2	Cl	0.3	0.2845	0.00847	
4	s4b50.3-2	Br	0.3	0.3213	0.35725	
4	s4b50.3-2	Cl	0.3	0.3213	0.00648	
4	s3b50.3-3	Br	0.3	0.2845	0.23113	
4	s3b50.3-3	Cl	0.3	0.2845	0.00777	
4	s4b50.3-3	Br	0.3	0.3213	0.32517	
4	s4b50.3-3	Cl	0.3	0.3213	0.00550	
4	s3b70.2-1	Br	0.2	0.1972	0.27286	
4	s3b70.2-1	Cl	0.2	0.1972	0.00803	
4	s4b70.2-1	Br	0.2	0.2000	0.33237	
4	s4b70.2-1	Cl	0.2	0.2000	0.00638	

4	s3b70.2-2	Br	0.2	0.1972	0.26976	
4	s3b70.2-2	Cl	0.2	0.1972	0.00803	
4	s4b70.2-2	Br	0.2	0.2000	0.34136	
4	s4b70.2-2	Cl	0.2	0.2000	0.00666	
4	s3b70.2-3	Br	0.2	0.1972	0.27328	
4	s3b70.2-3	Cl	0.2	0.1972	0.00796	
4	s4b70.2-3	Br	0.2	0.2000	0.34934	
4	s4b70.2-3	Cl	0.2	0.2000	0.00667	
4	s3b70.2-4	Br	0.2	0.1972	0.27400	
4	s3b70.2-4	Cl	0.2	0.1972	0.00810	
4	s4b70.2-4	Br	0.2	0.2000	0.34376	
4	s4b70.2-4	Cl	0.2	0.2000	0.00687	
4	s3b70.2-5	Br	0.2	0.1972	0.25323	
4	s3b70.2-5	Cl	0.2	0.1972	0.00728	
4	s4b70.2-5	Br	0.2	0.2000	0.31051	
4	s4b70.2-5	Cl	0.2	0.2000	0.00580	

Table B.2. Final mixing ratio data determined from the concentration data of Br^-.

GD	Sample Name	Tracer	Set_Q ml/h	Real_Q ml/h	UV Height	Peclet Number	Mixing Ratio	Sum
6	s3b2330-1	Br	30.0	29.988	0.05247	166.154	0.091	
6	s4b2330-1	Br	30.0	29.892	0.49256	166.154	0.914	1.005
6	s3b2330-2	Br	30.0	29.988	0.05217	166.154	0.091	
6	s4b2330-2	Br	30.0	29.892	0.49459	166.154	0.918	1.009
6	s3b2330-3	Br	30.0	29.988	0.05123	166.154	0.089	
6	s4b2330-3	Br	30.0	29.892	0.49403	166.154	0.917	1.006
1	s3a2210-1	Br	10.0	9.900	0.07128	55.385	0.124	
1	s4a2210-1	Br	10.0	9.900	0.47180	55.385	0.819	0.943
1	s3a2210-2	Br	10.0	9.927	0.07312	55.385	0.127	
1	s4a2210-2	Br	10.0	9.889	0.72181	55.385	1.252	1.379
3	s3a2910-1	Br	10.0	10.063	0.07671	55.385	0.115	
3	s4a2910-1	Br	10.0	9.849	0.51705	55.385	0.872	0.987
3	s3a2910-2	Br	10.0	10.260	0.07820	55.385	0.120	
3	s4a2910-2	Br	10.0	9.809	0.51748	55.385	0.869	0.989
3	s3a295-1	Br	5.0	5.083	0.09308	27.692	0.146	
3	s4a295-1	Br	5.0	4.890	0.49627	27.692	0.830	0.976
3	s3a295-2	Br	5.0	4.906	0.09821	27.692	0.149	
3	s4a295-2	Br	5.0	4.911	0.50193	27.692	0.844	0.993
6	s3b252.5-2	Br	2.5	2.475	0.10871	13.846	0.195	
6	s4b252.5-2	Br	2.5	2.443	0.44941	13.846	0.817	1.012
6	s3b252.5-3	Br	2.5	2.478	0.10985	13.846	0.197	
6	s4b252.5-3	Br	2.5	2.429	0.44828	13.846	0.811	1.008
5	s3b202-2	Br	2.0	1.972	0.11259	11.077	0.197	
5	s4b202-2	Br	2.0	1.978	0.42646	11.077	0.804	1.001
5	s3b202-3	Br	2.0	2.001	0.11606	11.077	0.207	
5	s4b202-3	Br	2.0	1.949	0.42647	11.077	0.792	0.999
5	s3b201.75_1	Br	1.8	1.752	0.12217	9.692	0.219	
5	s4b201.75-1	Br	1.8	1.738	0.41402	9.692	0.783	1.002
5	s3b201.75-2	Br	1.8	1.725	0.12577	9.692	0.223	
5	s4b201.75-2	Br	1.8	1.760	0.43384	9.692	0.832	1.055
5	s3b201.5-1	Br	1.5	1.439	0.13991	8.308	0.243	
5	s4b201.5-1	Br	1.5	1.496	0.42445	8.308	0.807	1.050
5	s3b201.5-2	Br	1.5	1.451	0.13009	8.308	0.227	
5	s4b201.5-2	Br	1.5	1.480	0.41503	8.308	0.780	1.007
5	s3b201.5-3	Br	1.5	1.458	0.13416	8.308	0.236	
5	s4b201.5-3	Br	1.5	1.464	0.42093	8.308	0.783	1.018

5	s3b201.25-2	Br	1.25	1.152	0.13831	6.923	0.231	
5	s4b201.25-2	Br	1.25	1.285	0.40682	6.923	0.796	1.027
5	s3b201.25-3	Br	1.25	1.176	0.14817	6.923	0.254	
5	s4b201.25-3	Br	1.25	1.228	0.40797	6.923	0.763	1.017
6	s3b251-1	Br	1.0	0.999	0.16724	5.538	0.306	
6	s4b251-1	Br	1.0	0.947	0.41301	5.538	0.727	1.034
6	s3b251-3	Br	1.0	0.966	0.16644	5.538	0.295	
6	s4b251-3	Br	1.0	1.034	0.41496	5.538	0.798	1.093
6	s3b250.9-1	Br	0.9	0.886	0.17077	4.985	0.309	
6	s4b250.9-1	Br	0.9	0.914	0.40054	4.985	0.756	1.065
6	s3b250.9-2	Br	0.9	0.886	0.17077	4.985	0.309	
6	s4b250.9-2	Br	0.9	0.914	0.40054	4.985	0.756	1.065
6	s3b250.9-3	Br	0.9	0.885	0.16826	4.985	0.304	
6	s4b250.9-3	Br	0.9	0.915	0.40072	4.985	0.757	1.061
3	s3a290.6-1	Br	0.6	0.603	0.21979	3.323	0.367	
3	s4a290.6-1	Br	0.6	0.574	0.38440	3.323	0.625	0.992
3	s3a290.6-2	Br	0.6	0.596	0.20882	3.323	0.344	
3	s4a290.6-2	Br	0.6	0.576	0.38846	3.323	0.634	0.978
4	s3b20.5-2	Br	0.5	0.524	0.21113	2.769	0.407	
4	s4b20.5-2	Br	0.5	0.469	0.35502	2.769	0.622	1.029
4	s3b50.3-2	Br	0.3	0.285	0.24815	1.662	0.435	
4	s4b50.3-2	Br	0.3	0.321	0.35725	1.662	0.715	1.150
4	s3b50.3-3	Br	0.3	0.285	0.23113	1.662	0.405	
4	s4b50.3-3	Br	0.3	0.321	0.32517	1.662	0.649	1.054
4	s3b70.2-1	Br	0.2	0.197	0.27286	1.108	0.499	
4	s4b70.2-1	Br	0.2	0.200	0.33237	1.108	0.620	1.119
4	s3b70.2-2	Br	0.2	0.197	0.26976	1.108	0.493	
4	s4b70.2-2	Br	0.2	0.200	0.34136	1.108	0.637	1.130
4	s3b70.2-3	Br	0.2	0.197	0.27328	1.108	0.500	
4	s4b70.2-3	Br	0.2	0.200	0.34934	1.108	0.652	1.152
4	s3b70.2-4	Br	0.2	0.197	0.27400	1.108	0.501	
4	s4b70.2-4	Br	0.2	0.200	0.34376	1.108	0.642	1.143
4	s3b70.2-5	Br	0.2	0.197	0.25323	1.108	0.462	
4	s4b70.2-5	Br	0.2	0.200	0.31051	1.108	0.578	1.040

Table B.3. Final mixing ratio data determined from the concentration data of Cl^-.

GD	Sample Name	Tracer	Set_Q ml/h	Real_Q ml/h	UV Height	Peclet Number	Mixing Ratio	Sum
6	s3b2330-1	Cl	30.0	29.988	0.01237	166.154	0.873	
6	s4b2330-1	Cl	30.0	29.892	0.00122	166.154	0.086	0.959
6	s3b2330-2	Cl	30.0	29.988	0.01270	166.154	0.896	
6	s4b2330-2	Cl	30.0	29.892	0.00119	166.154	0.084	0.980
6	s3b2330-3	Cl	30.0	29.988	0.01276	166.154	0.901	
6	s4b2330-3	Cl	30.0	29.892	0.00120	166.154	0.084	0.985
1	s3a2210-1	Cl	10.0	9.900	0.01225	55.385	0.852	
1	s4a2210-1	Cl	10.0	9.900	0.00222	55.385	0.154	1.006
1	s3a2210-2	Cl	10.0	9.927	0.01226	55.385	0.855	
1	s4a2210-2	Cl	10.0	9.889	0.00327	55.385	0.227	1.082
3	s3a2910-1	Cl	10.0	9.849	0.01086	55.385	0.874	
3	s4a2910-1	Cl	10.0	9.849	0.00160	55.385	0.118	0.993
3	s3a2910-2	Cl	10.0	10.260	0.01066	55.385	0.894	
3	s4a2910-2	Cl	10.0	9.809	0.00134	55.385	0.096	0.990
3	s3a295-1	Cl	5.0	5.083	0.01026	27.692	0.852	
3	s4a295-1	Cl	5.0	4.890	0.00180	27.692	0.134	0.985
3	s3a295-2	Cl	5.0	4.906	0.01020	27.692	0.817	
3	s4a295-2	Cl	5.0	4.911	0.00173	27.692	0.128	0.946
6	s3b252.5-2	Cl	2.5	2.475	0.01146	13.846	0.801	
6	s4b252.5-2	Cl	2.5	2.443	0.00259	13.846	0.179	0.980
6	s3b252.5-3	Cl	2.5	2.478	0.01163	13.846	0.814	
6	s4b252.5-3	Cl	2.5	2.429	0.00260	13.846	0.178	0.992
5	s3b202-2	Cl	2.0	1.972	0.01085	11.077	0.801	
5	s4b202-2	Cl	2.0	1.978	0.00294	11.077	0.218	1.018
5	s3b202-3	Cl	2.0	2.001	0.01061	11.077	0.794	
5	s4b202-3	Cl	2.0	1.949	0.00311	11.077	0.227	1.021
5	s3b201.75_1	Cl	1.8	1.752	0.01065	9.692	0.798	
5	s4b201.75-1	Cl	1.8	1.738	0.00308	9.692	0.229	1.027
5	s3b201.75-2	Cl	1.8	1.725	0.01058	9.692	0.780	
5	s4b201.75-2	Cl	1.8	1.760	0.00306	9.692	0.230	1.011
5	s3b201.5-1	Cl	1.5	1.439	0.01044	8.308	0.750	
5	s4b201.5-1	Cl	1.5	1.496	0.00315	8.308	0.235	0.985
5	s3b201.5-2	Cl	1.5	1.451	0.01025	8.308	0.742	
5	s4b201.5-2	Cl	1.5	1.480	0.00325	8.308	0.240	0.982
5	s3b201.5-3	Cl	1.5	1.458	0.01033	8.308	0.751	
5	s4b201.5-3	Cl	1.5	1.464	0.00326	8.308	0.238	0.990

5	s3b201.25-2	Cl	1.2	1.152	0.01008	6.923	0.695	
5	s4b201.25-2	Cl	1.2	1.285	0.00352	6.923	0.271	0.966
5	s3b201.25-3	Cl	1.2	1.176	0.01050	6.923	0.739	
5	s4b201.25-3	Cl	1.2	1.228	0.00350	6.923	0.257	0.997
6	s3b251-1	Cl	1.0	0.999	0.01031	5.538	0.727	
6	s4b251-1	Cl	1.0	0.947	0.00400	5.538	0.267	0.995
6	s3b251-3	Cl	1.0	0.966	0.01012	5.538	0.690	
6	s4b251-3	Cl	1.0	1.034	0.00408	5.538	0.298	0.988
6	s3b250.9-1	Cl	0.9	0.885	0.01023	4.985	0.710	
6	s4b250.9-1	Cl	0.9	0.914	0.00418	4.985	0.300	1.010
6	s3b250.9-2	Cl	0.9	0.885	0.01023	4.985	0.710	
6	s4b250.9-2	Cl	0.9	0.914	0.00418	4.985	0.300	1.010
6	s3b250.9-3	Cl	0.9	0.885	0.01001	4.985	0.695	
6	s4b250.9-3	Cl	0.9	0.915	0.00408	4.985	0.293	0.988
3	s3a290.6-1	Cl	0.6	0.603	0.00778	3.323	0.635	
3	s4a290.6-1	Cl	0.6	0.574	0.00420	3.323	0.321	0.956
3	s3a290.6-2	Cl	0.6	0.596	0.00764	3.323	0.617	
3	s4a290.6-2	Cl	0.6	0.576	0.00431	3.323	0.331	0.948
4	s3b20.5-2	Cl	0.5	0.524	0.00809	2.769	0.650	
4	s4b20.5-2	Cl	0.5	0.469	0.00467	2.769	0.334	0.984
4	s3b50.3-2	Cl	0.3	0.285	0.00847	1.662	0.617	
4	s4b50.3-2	Cl	0.3	0.321	0.00648	1.662	0.532	1.148
4	s3b50.3-3	Cl	0.3	0.285	0.00777	1.662	0.565	
4	s4b50.3-3	Cl	0.3	0.321	0.00550	1.662	0.450	1.016
4	s3b70.2-1	Cl	0.2	0.197	0.00803	1.108	0.608	
4	s4b70.2-1	Cl	0.2	0.200	0.00638	1.108	0.489	1.096
4	s3b70.2-2	Cl	0.2	0.197	0.00803	1.108	0.608	
4	s4b70.2-2	Cl	0.2	0.200	0.00666	1.108	0.510	1.118
4	s3b70.2-3	Cl	0.2	0.197	0.00796	1.108	0.602	
4	s4b70.2-3	Cl	0.2	0.200	0.00667	1.108	0.511	1.113
4	s3b70.2-4	Cl	0.2	0.197	0.00810	1.108	0.613	
4	s4b70.2-4	Cl	0.2	0.200	0.00687	1.108	0.527	1.140
4	s3b70.2-5	Cl	0.2	0.197	0.00728	1.108	0.550	
4	s4b70.2_5	Cl	0.2	0.200	0.00580	1.108	0.444	0.994